

CTH-NT-207

THESIS FOR THE DEGREE OF DOCTOR OF PHILOSOPHY

# Noise Diagnostics of Stationary and Non-Stationary Reactor Processes

CARL SUNDE



Nuclear Engineering  
Department of Applied Physics  
Chalmers University of Technology  
S-412 96 Göteborg, Sweden 2007

Noise Diagnostics of Stationary and Non-Stationary Reactor Processes  
CARL SUNDE  
ISBN 978-91-7291-902-0

©Carl Sunde, 2007

Doktorsavhandling vid Chalmers tekniska högskola  
Ny serie nr 2583  
ISSN 0346-718X

Nuclear Engineering  
Department of Applied Physics  
Chalmers University of Technology  
S-412 96 Göteborg  
Sweden  
Telephone +46 (0)31 772 1000

Cover: Wavelet coherence of detector signals from Ringhals-1. Also shown in Fig. 4.6.

Chalmers Reproservice  
Göteborg, Sweden 2007

# Noise Diagnostics of Stationary and Non-Stationary Reactor Processes

CARL SUNDE

Nuclear Engineering

Department of Applied Physics

Chalmers University of Technology

## ABSTRACT

This thesis concerns the application of noise diagnostics on different problems in the area of reactor physics involving both stationary and non-stationary core processes. Five different problems are treated, divided into three different parts.

The first problem treated in the first part is the classification of two-phase flow regimes from neutron radiographic and visible light images with a neuro-wavelet algorithm. The algorithm consists of wavelet pre-processing and of an artificial neural network. The result indicates that the wavelet pre-processing is improving the training of the neural network. Next, detector tubes which are suspected of impacting on nearby fuel-assemblies in a boiling water reactor (BWR) are identified by both a classical spectral method and wavelet-based methods. It was found that there is good agreement between the different methods as well as with visual inspections of detector tube and fuel assembly damage made during the outage at the plant. The third problem addresses the determination of the decay ratio of a BWR from the auto-correlation function (ACF). Here wavelets are used, with some success, both for de-trending and de-noising of the ACF and also for direct estimation of the decay ratio from the ACF.

The second part deals with the analysis of beam-mode and shell-mode core-barrel vibrations in pressurised water reactors (PWRs). The beam-mode vibrations are analysed by using parameters of the vibration peaks, in spectra from ex-core detectors. A trend analysis of the peak amplitude shows that the peak amplitude is changing during the fuel cycle. When it comes to the analysis of the shell-mode vibration, 1-D analytical and numerical calculations are performed in order to calculate the neutron noise induced in the core. The two calculations are in agreement and show that a large local noise component is present in the core which could be used to classify the shell-mode vibrations. However, a measurement made in the PWR Ringhals-3 shows that it is impossible to use this local component due to practical reasons, i.e. due to the limitations of the possible detector positions.

In the third and final part the validity of the break-frequency method for the estimation of the reactivity in a subcritical system is investigated. A numerical calculation of the neutron noise in a 2-D subcritical system corresponding to a power reactor during loading conditions is performed. From the auto power spectral density of the numerically calculated neutron noise, the reactivity is estimated by the break-frequency method. The result indicates that the break-frequency method yields only a rough, although conservative, estimate of the reactivity.

*Keywords:* noise diagnostics, spectral analysis, wavelet analysis, two-phase flow, detector tube impacting, decay ratio, core-barrel vibrations, break-frequency method



## Appended papers

This thesis is an introduction to and a summary of the work published in the following papers

### PAPER I

C. Sunde, S. Avdić and I. Pázsit, "Classification of two-phase flow regimes via image analysis and a neuro-wavelet approach"  
*Progress in Nuclear Energy*, **46**, 348 (2005).

### PAPER II

C. Sunde and I. Pázsit, "Investigation of detector tube impacting in the Ringhals-1 BWR"  
*International Journal of Nuclear Energy Science and Technology*, **2**, 189 (2006).

### PAPER III

C. Sunde and I. Pázsit, "Wavelet techniques for the determination of the Decay Ratio in Boiling Water Reactors"  
*Kerntechnik*, **72**, 7 (2007).

### PAPER IV

C. Sunde, C. Demazière and I. Pázsit, "Calculations of the neutron noise induced by shell-mode core-barrel vibrations in a 1-D, two-group, two-region slab reactor model"  
*Nuclear Technology*, **154**, 129 (2006).

### PAPER V

C. Sunde, C. Demazière and I. Pázsit, "Investigation of the neutron noise induced by shell-mode core-barrel vibrations in a reflected reactor"  
*Proc. Int. Top. Mtg. on Mathematics and Computing, Supercomputing, Reactor Physics and Nuclear and Biological Applications (M&C2005)*, Avignon, France, September 12-15, 2005, American Nuclear Society (2005).

### PAPER VI

M. Pázsit, C. Sunde and I. Pázsit, "Beam mode core-barrel vibrations in the PWRs Ringhals 2-4", *Proc. Int. Top. Mtg. on Advances in Nuclear Analysis and Simulations (PHYSOR2006)*, Vancouver, Canada, September 10-14, 2006, American Nuclear Society (2006)

### PAPER VII

C. Sunde, C. Demazière and I. Pázsit, "Investigation of the validity of the point-kinetics approximation and of the break-frequency method in 2-D subcritical systems", *Proc. Joint Int. Top. Mtg. on Mathematics and Computing and Supercomputing in Nuclear Applications (M&C + SNA 2007)*, Monterey, California, April 15-19, 2007, American Nuclear Society (2007)



## Related work not included in this thesis

C. Sunde and V. Arzhanov, "Calculations of the neutron noise induced by shell-mode core-barrel vibrations in a 1-D 2-group 2-region slab reactor" CTH-RF-173, Chalmers University of Technology (2003)

C. Demazière, C. Sunde, V. Arzhanov and I. Pázsit, "Final Report on the Research Project Ringhals Diagnostics and Monitoring, stage 8, CTH-RF-177/RR-10, Chalmers University of Technology, (2003)

C. Sunde, S. Avdić and I. Pázsit, "Classification of two-phase flow regimes via image analysis by a neuro-wavelet approach", *Applied Computational Intelligence, Proc. of the 6th international FLINS Conference*, Blankenberge, Belgium, September 1-3 (2003)

C. Sunde and I. Pázsit, "Investigation of detector tube impacting in the BWR Ringhals-1", *Proc. 29th Informal Mtg. on Reactor Noise (IMORN-29)*, Budapest, Hungary, May 17-19, 2004 (2004)

C. Demazière, I. Pázsit, C. Sunde and J. Wright, "Research and Development Program in Reactor Diagnostics and Monitoring with Neutron Noise Methods, Stage 10. Final report", SKI Report 2004:57, Statens Kärnkraftsinspektion (2004)

C. Sunde, "Wavelet and Spectral Analysis of Some Selected Problems in Reactor Diagnostics", Licentiate Thesis, CTH-RF-183, Chalmers University of Technology, (2004)

C. Demazière, C. Sunde and I. Pázsit, "Final Report on the Research Project Ringhals Diagnostics and Monitoring, stage 9, CTH-RF-187/RR-11, Chalmers University of Technology, (2005)

C. Sunde, C. Demazière, J. Wright and I. Pázsit, "Final Report on the Research Project Ringhals Diagnostics and Monitoring, stage 10, CTH-RF-194/RR-12, Chalmers University of Technology (2005)

C. Sunde, C. Demazière, I. Pázsit, B. Dahl and L. Mileshina, "Research and Development Program in Reactor Diagnostics and Monitoring with Neutron Noise Methods, Stage 11-12. Final report", SKI Report 2006:34, Statens Kärnkraftsinspektion (2006)

C. Sunde, C. Demazière and I. Pázsit, "Final Report on the Research Project Ringhals Diagnostics and Monitoring, stage 11, CTH-NT-206/RR-13, Chalmers University of Technology (2007)

C. Demazière and C. Sunde, "Calculation of the eigenfunctions and corresponding eigenvalues of the 2-group diffusion equation in heterogeneous systems", *Proc. Joint Int. Top. Mtg. on Mathematics and Computing and Supercomputing in Nuclear Applications (M&C + SNA 2007)*, Monterey, California, April 15-19, 2007, American Nuclear Society (2007)

<b>1</b>	<b>Introduction</b>	<b>1</b>
1.1	Noise diagnostics . . . . .	1
1.2	Outline of the thesis . . . . .	2
<b>2</b>	<b>Wavelets</b>	<b>5</b>
2.1	Time and frequency . . . . .	5
2.2	One-dimensional wavelet transform . . . . .	6
2.3	Two-dimensional wavelet transform . . . . .	10
<b>3</b>	<b>Classification of two-phase flow</b>	<b>13</b>
3.1	Flow images . . . . .	13
3.2	Wavelet pre-processing . . . . .	14
3.3	The classification algorithm . . . . .	15
3.4	Results from the classification . . . . .	16
<b>4</b>	<b>Detector tube impacting in BWRs</b>	<b>19</b>
4.1	Physical model . . . . .	19
4.2	Analysis methods . . . . .	21
4.2.1	Spectral method . . . . .	21
4.2.2	Discrete wavelet method . . . . .	23
4.2.3	Continuous wavelet method . . . . .	24
4.3	Analysis of the measurements . . . . .	25
4.4	Conclusions of the detector tube impacting . . . . .	28
<b>5</b>	<b>Decay ratio estimation in BWRs</b>	<b>31</b>
5.1	General principles of the estimation of the decay ratio . . . . .	31
5.2	De-trending and de-noising using discrete wavelets . . . . .	33
5.3	Using the continuous wavelet transform for estimating the DR . . . . .	34
5.4	Testing of the methods on Ringhals Benchmark . . . . .	37
<b>6</b>	<b>Core barrel vibrations in PWRs</b>	<b>39</b>
6.1	General description of the core-barrel vibrations . . . . .	39
6.2	Analysis of beam-mode vibrations . . . . .	41
6.2.1	Curve-fitting of the data . . . . .	41
6.2.2	Trend analysis . . . . .	42
6.3	Shell-mode vibrations . . . . .	43

## Contents

---

6.3.1	Description of the model . . . . .	44
6.3.2	Space-frequency dependent solution . . . . .	45
6.3.3	Results . . . . .	46
<b>7</b>	<b>The break-frequency method</b>	<b>49</b>
7.1	Derivation of the neutron noise . . . . .	49
7.2	Definition of the source . . . . .	50
7.3	Neutron noise in the frequency domain . . . . .	51
7.4	Break-frequency method . . . . .	52
7.5	Definition of the system . . . . .	53
7.6	Estimation of the reactivity . . . . .	54
<b>8</b>	<b>Concluding remarks</b>	<b>57</b>
	<b>Acknowledgements</b>	<b>59</b>
	<b>References</b>	<b>61</b>
	<b>Papers I-VII</b>	<b>65</b>

# CHAPTER 1

## INTRODUCTION

The topic of this thesis is noise diagnostics which has been used in nuclear power plants (NPPs) since the earliest days of reactor physics, [1–4], beginning fifty years ago with the start of the first reactor. Noise diagnostics has been a part of the research at the Department of Nuclear Engineering at Chalmers University of Technology for more than 15 years and have resulted in a number of PhD theses [5–8]. This thesis is a continuation and development of the previous work done at the Department and has been performed during the last five years. Noise diagnostics problems in both pressurised water reactors (PWRs) and boiling water reactors (BWRs) are treated in this thesis. The main concepts of noise diagnostics will be explained in this introduction together with an outline of the thesis.

### 1.1 Noise diagnostics

In ordinary life, noise is considered to be something unwanted or disturbing, the noise in radio broadcasting or disturbing noise which can occur when speaking in a cell-phone. In order to get a clear, noise-free signal, the noise is often filtered away. However, in noise diagnostics it is the other way around, the static signal is filtered out and the noise is considered as the important part of the signal. Thus, the noise is extracted rather than filtered away. What is the use of the noise? Take, again, the cell-phone as an example. When calling to someone, there may be some disturbances (noise) in the voice transmitted over the phone. Based on the noise it could be possible to draw the conclusion that the person you are calling for example is driving a car, which is an example of a simple form of noise diagnostics. Hence, the noise is used to draw conclusions about a system, which can be very useful.

In reactor noise diagnostics, the noise, i.e the fluctuations of the stationary signal, from detectors placed inside and outside the reactor core is used to diagnose the reactor. Compared to the simple cell-phone example the situation is of course significantly more involved when diagnosing a reactor. First, the magnitude of the noise can be a couple of powers of ten lower compared to the mean value (static part) of the signal itself. Second, it is possible to have more than one noise-source. Third, it is not always easy to get a simple response; you can not simply

ask a reactor whether it is driving a car or not! Rather, continuing with the same example, it is like finding out in which of New York's thousands of streets the car is in, what speed it has etc.

The purpose of reactor noise diagnostics is mainly to have a surveillance and monitoring of the reactor and to make sure everything is working properly. However, if something starts deteriorating, the on-line diagnostics of the reactor should detect the error and if necessary alert the operator, who in return may initiate some correction action, i.e. a shut-down. The off-line diagnostics of the reactor means mainly to investigate the behaviour of the reactor and to give information about the reactor status, e.g. find components that may need maintenance or understand trends, unexpected phenomena etc. Hence, the diagnostics must be as reliable as possible. One does not want to stop the reactor by false alarm or maintain a working component, since, it is time consuming to restart the reactor and, of course, there is a financial loss if the reactor is not operating. Hence, it is important to understand and develop noise diagnostic methods, which are reliable. The methods developed in this thesis are not for on-line use in power producing nuclear plants, but more of an understanding level of the processes in a reactor and for off-line use.

## 1.2 Outline of the thesis

The summary part of the thesis is divided into three parts. The first part, which is treated in Chapters 3-5 and is based on **Papers I-III**, uses wavelet technique for the noise diagnostics. The following three problems are dealt with: two-phase flow identification, detector tube impacting and decay ratio estimation. The second part of the thesis is summarised in Chapter 6, which is based on **Papers IV-VI**. In this part beam-mode and shell-mode core barrel vibrations in the three PWR units at the Ringhals NPP are analysed with noise diagnostic methods. Finally, part three, described in Chapter 7, treats the estimation of reactivity in sub-critical systems. This part is a summary of **Paper VII**. Since a major part of the thesis uses wavelets, which is a relatively new tool in reactor physics, a short introduction to wavelet theory is given in Chapter 2.

One major objective with the work included in the thesis has been to test all developed algorithms and methods on real data, i.e. on measurements. Because it is one thing to find methods which work perfectly fine on simulated data and it is a completely different story to apply them on real measurements. In the author's opinion a method which works on simulated data but not on measurements is useless. In all parts, except for the last part (Chapter 7) of this thesis, the algorithms and methods developed have indeed been tested on real measurements and data. Measurements from all four units at the Swedish nuclear power plant Ringhals, located on the west coast of Sweden, have been analysed in the different parts of this thesis. Unit 1 is a BWR with 840 MWe and units 2, 3 and 4 are

PWRs with 870, 1040 and 910 MWe, respectively [9]. All the measurements were carried out by plant personnel.

Most of the work in the thesis has been done by the author. However, in **Paper I** the Neural Network was developed by one of the co-authors and in **Paper IV** the simulations made with the numerical noise simulator were also performed by one of the co-authors.



## CHAPTER 2

## WAVELETS

One goal of this thesis and the research within the project is to use wavelet techniques in noise diagnostics. Wavelets are still considered to be a new field in signal processing, even though they have been in use for two decades since they were first introduced in the mid-80s. The real development started in the early 90's, [10], and has continued ever since by the use of wavelets in different scientific areas such as fluid dynamics, medicine, finance, physics and geophysics [11]. This Chapter gives a very short introduction to both one- and two-dimensional wavelets and their application. A more mathematical detailed explanation can be found in Refs. [10–14].

### 2.1 Time and frequency

The classical Fourier transform can be used to map a time signal into the frequency domain, as illustrated in Fig. 2.1. Since the Fourier transform uses an infinitely long sinusoidal function as the analysing tool it can only be applied on stationary signals, where there are no changes in frequency over the time interval of interest. Thus, if the signal to be analysed is non-stationary, the Fourier transform cannot be used. In that case a windowing of the signal can be done, using the so-called windowed Fourier transform or short time Fourier transform (STFT). The STFT maps a time signal into a two-dimensional signal of both time and frequency. Hence, it is possible to get information about both when and at what frequency a certain event occurs. However, there is one drawback with the STFT, namely that the time resolution is the same for all frequencies. Often there is a need for better resolution in time at higher frequencies. Hence, one would like to have a tool which can map a time signal both into time and into frequency but with different resolution for different frequencies. The wavelet transform is able to cope with this requirement, even though it is mapping the signal into time-scale or time-level rather than time-frequency. However, there is a connection between scale, level and frequency. The better resolution in time at high frequencies is achieved by reducing the resolution in frequency and vice versa, as is illustrated in Fig. 2.1.

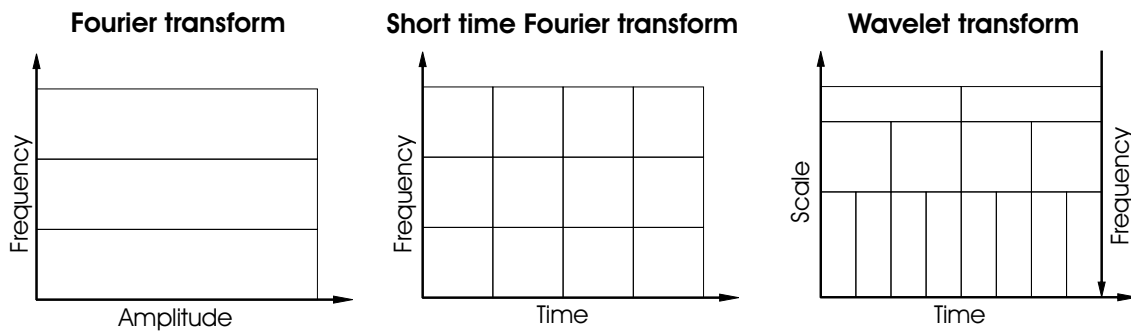


**Figure 2.1:** Schematic picture of the Fourier, short time Fourier and wavelet transforms.

Instead of the sinusoidal analysing function of the Fourier transform, the wavelet transform uses a small, localised wave function (see Fig. 2.2) as the analysing tool, hence the name wavelet. The use of localised functions makes the wavelet transform well suited for analysing non-stationary signals such as transients and intermittent signals. The wavelet displayed in Fig. 2.2 is the so-called *Daubechies 4* wavelet (*db4*), [10]. The *db4* wavelet has the characteristic features of a wavelet such as orthogonality and compact support. Hence, in the remainder of this Chapter the *db4* wavelet will be used to illustrate some of the features of wavelets and their applications.

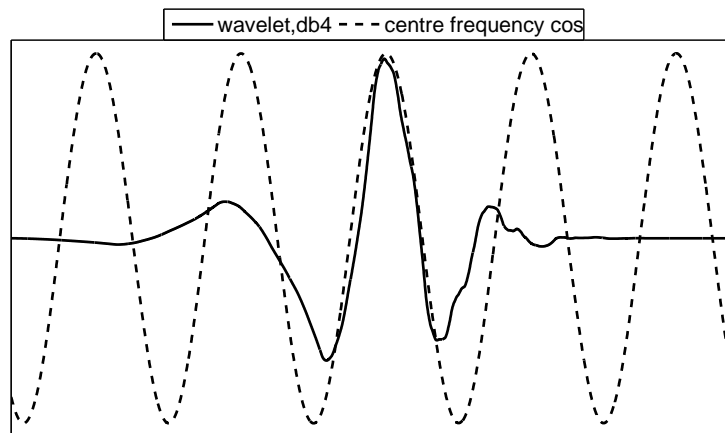


**Figure 2.2:** The *db4* wavelet has the form of a small localised wave, hence the name wavelet. The dotted curve is a cosine function with the same frequency as the centre frequency of the *db4* wavelet.

## 2.2 One-dimensional wavelet transform

It is possible to use the wavelet transform on one- or two-dimensional data. In this Section the one-dimensional transform is described and in the next a short

description of the two-dimensional wavelet transform is given.

There are two ways of performing the one-dimensional transform: continuous with continuous scales or levels (frequencies), or discrete with discrete scales or levels (frequencies). Here only the discrete transform will be described.

The wavelet transform is based on a so-called mother-wavelet,  $\psi$ , which can be dilated and translated (see Fig. 2.3), with the parameters  $a$  and  $b$ .

$$\psi_{a,b}(t) = \frac{1}{\sqrt{a}}\psi\left(\frac{t-b}{a}\right) \quad (2.1)$$

At each scale  $a$  there is a characteristic frequency,  $F_a$ , which can be calculated through the so-called centre-frequency of the mother-wavelet,  $F_c$ , and the sampling period,  $\Delta t$ , of the analysed signal:

$$F_a = \frac{F_c}{a\Delta t}. \quad (2.2)$$

The centre-frequency is the characteristic frequency of the mother-wavelet which is illustrated by showing a cosine function (dashed line) with the centre-frequency of the wavelet in Fig. 2.2, i.e.  $\cos(F_c 2\pi t)$ . Hence, the central part of the mother wavelet has the same oscillating behaviour as a cosine function which is oscillating with the centre-frequency of the wavelet.

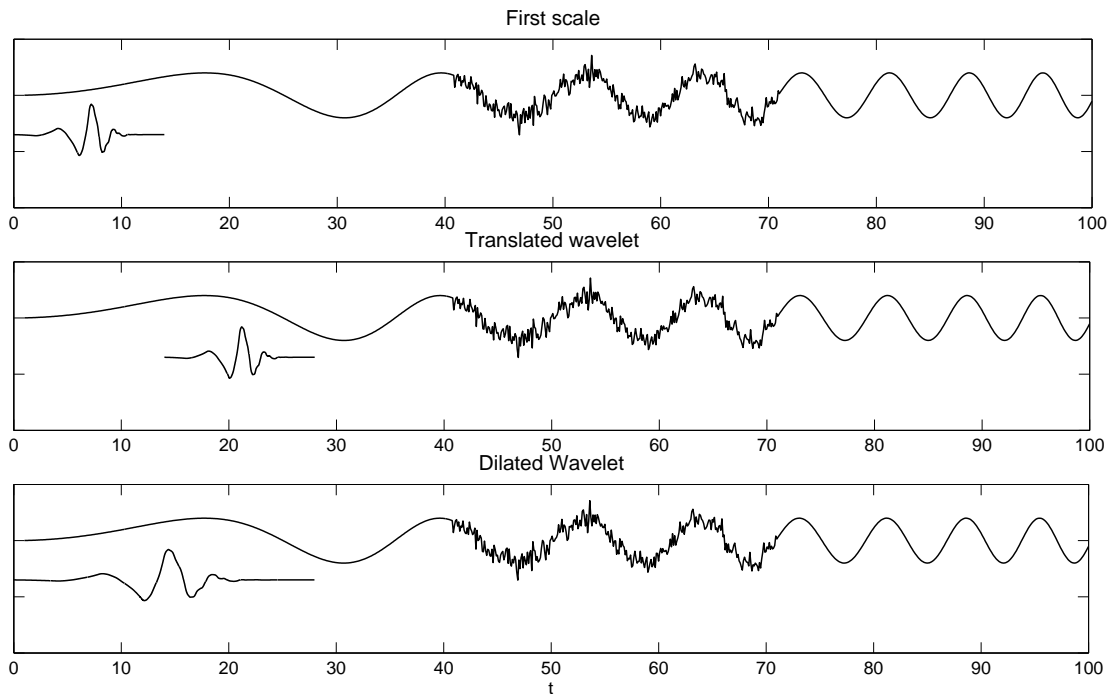


**Figure 2.3:** The *db4* mother wavelet with translated and dilated version, analysing a signal.

One way of choosing the parameters in Eq. (2.1) are,  $a = a_0^m$  and  $b = nb_0a_0^m$  where  $m$  is called the level. The most common choice of  $a_0$  and  $b_0$  are 2 and 1, respectively. This gives the discrete one-dimensional wavelet transform of the signal  $x(t)$  as:

$$T_{m,n} = \int_{-\infty}^{\infty} x(t) \frac{1}{\sqrt{2^m}} \psi(2^{-m}t - n) dt. \quad (2.3)$$

Here  $T_{m,n}$  are called the detail wavelet coefficients. They contain information about the details of the signal  $x$ . The coefficients  $T_{m,n}$  are calculated by translating and dilating the mother wavelet along the signal, illustrated in Fig. 2.3, and performing the integration at each step. The transform is performed at each discrete level  $m$ , i.e. the signal is convolved with the wavelet at each discrete point  $n$  at each level  $m$ .

With each wavelet there is an associated scaling-function,  $\phi$ . The wavelet and the scaling functions are orthogonal and have the following relation:

$$\psi(t) = \sum_k (-1)^k c_{1-k} \phi(2t - k). \quad (2.4)$$

Here  $c$  is a scaling coefficient. The scaling functions can be used to calculate approximation coefficients,  $S_{m,n}$  of the signal,  $x(t)$ , in the same way as the calculation of the detail coefficients,  $T_{m,n}$ :

$$S_{m,n} = \int_{-\infty}^{\infty} x(t) \frac{1}{\sqrt{2^m}} \phi(2^{-m}t - n) dt. \quad (2.5)$$

The approximation coefficients contain information about the mean behaviour of the signal. With the use of both the detail coefficients and the approximation coefficients the original signal can be perfectly reconstructed as:

$$x(t) = x_{m_0}(t) + \sum_{m=-\infty}^{m_0} d_m(t) \quad (2.6)$$

where the detail,  $d_m(t)$  of the signal, at level  $m$ , is defined as:

$$d_m(t) = \sum_{n=-\infty}^{\infty} T_{m,n} \frac{1}{\sqrt{2^m}} \psi(2^{-m}t - n) \quad (2.7)$$

and the approximation of the signal at level,  $m_0$  is:

$$x_{m_0}(t) = \sum_{n=-\infty}^{\infty} S_{m_0,n} \frac{1}{\sqrt{2^{m_0}}} \phi(2^{-m_0}t - n). \quad (2.8)$$

The reconstruction of the signal is the inversion of the wavelet transform and the complete original signal is recovered.

The detail coefficients  $T_{m,n}$  contain the same information as the reconstructed details,  $d_m(t)$ , and the same is valid for the approximation coefficients  $S_{m_0,n}$  and the reconstructed approximation,  $x_{m_0}(t)$ . Hence it is possible to use either the coefficients or the reconstructed approximation and details when analysing the signal. The advantage with the coefficients is that the size of them are decreasing with a factor of two at each level, compared with the reconstructed signals which have the same size as the original signal.

If the input signal,  $x_0$ , is discrete and of finite length, e.g  $N = 2^M$ ,  $m$  and  $n$  are also finite and it is possible to rewrite the above formulae as follows:

$$\begin{aligned}
 x_0(t) &= x_M(t) + \sum_{m=1}^M d_m(t), \\
 x_M(t) &= S_{M,n} \frac{1}{\sqrt{2^M}} \phi(2^{-M}t - n), \\
 d_m(t) &= \sum_{n=0}^{2^{M-m}-1} T_{m,n} \frac{1}{\sqrt{2^m}} \psi(2^{-m}t - n).
 \end{aligned} \tag{2.9}$$

Here  $x_M$  is the mean of the signal. From these equations it is possible to get a relation between approximation and detail at one level and the approximation at the next level:

$$x_{m-1}(t) = x_m(t) + d_m(t). \tag{2.10}$$

With the above choice of  $a$  and  $b$  the decomposition of the signal into details and approximation is called the wavelet *multiresolution* analysis. From the multiresolution it is clear that the wavelets, used in the discrete transform, consist of an orthogonal set of basis functions in which an arbitrary function can be expanded.

As an example of the multiresolution analysis take a chirp signal, shown at the top in Fig. 2.4a, with some white noise added. It is decomposed into details and approximations at different levels using the *db4* wavelet in the *MatLab Wavelet Toolbox*, [14]. The details at each level represent the content of the signal at that level (frequency). Hence it is possible to extract information about both when and at what frequency a certain event happens. As expected, the noise is present in the lowest level (highest frequency) details 1-3, see Fig. 2.4b. The high frequency components of the regular chirp signal are visible at the middle levels, 5-6, to the right in Fig. 2.4b. The low frequency components of the regular chirp signal are visible to the left at higher levels, 7-8, in the same figure. An almost noise free chirp signal is visible at approximation level 4,  $x_4(t)$  in Fig. 2.4a.

From Fig. 2.4 it is possible to draw the conclusion that wavelets can be used to de-noise a noisy signal. By taking the approximation at level 4 of the signal, an almost noise-free chirp signal can be obtained. However, all information from the details at levels 1 to 4 is neglected, when using this approximation. One way of performing a better de-noising is to use some information from the lowest levels (highest frequencies). This can be done by thresholding the detail coefficients,

in this example details at level 1-4. When reconstructing the signal, the approximation and the thresholded detail coefficients are used to calculate a de-noised representation of the signal. Also it is seen that the noise can be extracted through the details. By using the three first levels of details in Fig. 2.4b) it is possible to almost completely extract the time-limited white noise. An application where this could be of use is the possibility to extract short intermittent parts of a signal, so-called spikes. This technique will be used in the analysis of detector tube vibrations in Chapter 4.

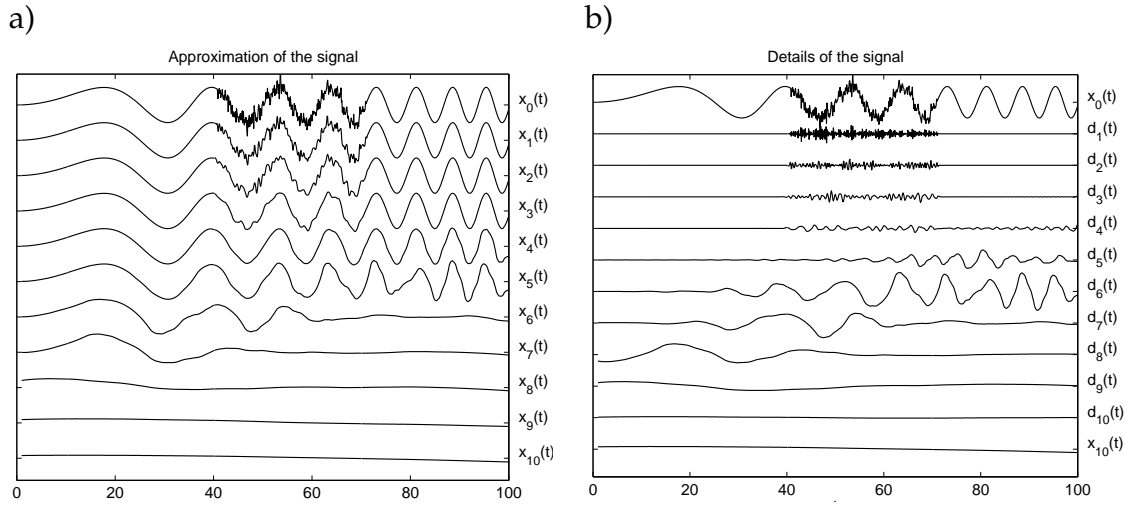


**Figure 2.4:** In a) approximation  $x_m$  and in b) details  $d_m$  are shown at ten different levels of the wavelet transform using the *db4* wavelet. The original signal  $x_0$  is at the top in both figures.

## 2.3 Two-dimensional wavelet transform

If the input data is two-dimensional, i.e. it is an image, it is possible to use a two-dimensional wavelet transform. The principles of the transformation are the same as for the one-dimensional transform, but instead of having one detail at each level there are three. The information in each of the three details are from three directions of the two-dimensional input data, horizontal, vertical and diagonal details. The first equation in Eq. (2.9) can be rewritten for the two-dimensional case as

$$x_0(x, y) = x_M(x, y) + \sum_{m=1}^M d_m^h(x, y) + d_m^v(x, y) + d_m^d(x, y). \quad (2.11)$$

This is the reconstruction (inversion) for the two-dimensional discrete wavelet transform. The details, the detail coefficients, the approximations and the approximation coefficients are calculated in the same way as for the one-dimensional transform, except that different two-dimensional wavelets are used for the different directions and a two-dimensional scaling function is used. All the two-

dimensional wavelet and scaling functions can be calculated from the one-dimensional ones as

$$\begin{aligned}\psi^h(x, y) &= \phi(x)\psi(y), \\ \psi^v(x, y) &= \psi(x)\phi(y), \\ \psi^d(x, y) &= \psi(x)\psi(y), \\ \phi(x, y) &= \phi(x)\phi(y).\end{aligned}\tag{2.12}$$

Figs. 2.5b-e show the reconstructed approximation and details at the first level (highest frequency) of a two-dimensional wavelet transform, using the *db4* wavelet, on the original image in Fig. 2.5a. In c), where the horizontal details are shown, the vertical high frequency parts (sharp transitions) are clearly visible, e.g. the line in the middle. In the same way the horizontal high frequency parts (the trees) are clearly visible in d), showing the vertical detail. There are no clear features in the diagonal details e), since the original images have no sharp diagonal transitions. The two-dimensional transform can be used to characterise an image by identifying different features of the image at different detail levels (scales) and/or different directions. This method is used in Chapter 3 where two-phase flow regimes are classified.

For further information on wavelet theory and applications the interested reader is referred to Refs. [10–14]. All the mathematical details, which are left out in this thesis, can be found there.

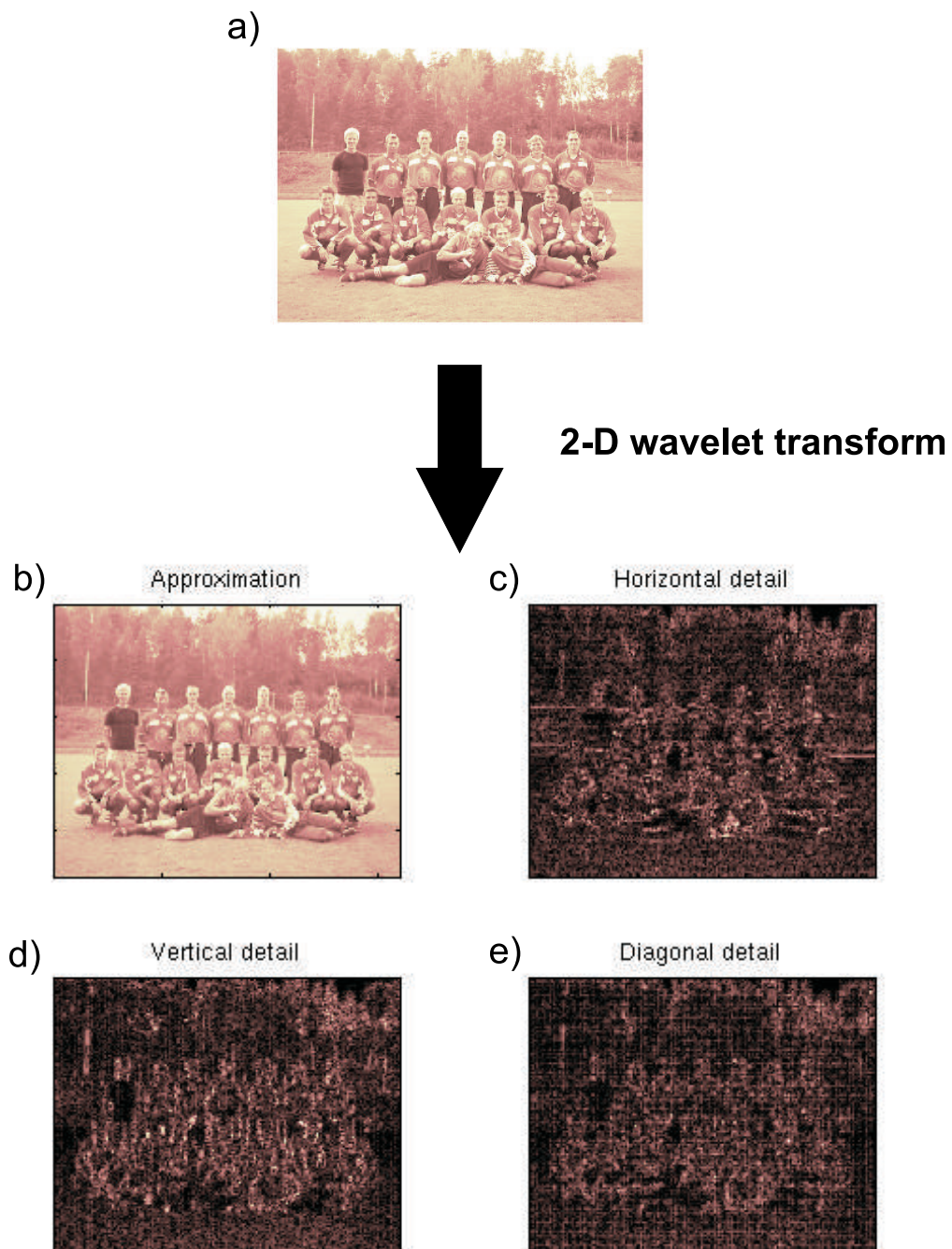


**Figure 2.5:** In a) the original image is shown. In b) the approximation, and c)-e) the details from a two-dimensional wavelet transform, using *db4* wavelet, at the first level are shown.

## CHAPTER 3

# CLASSIFICATION OF TWO-PHASE FLOW

The first application of wavelet techniques in this thesis is in the area of two-phase flow identification. It is important to classify the different flow regimes in a BWR, since they have quite different flow properties. Before using a flow equation, the regime must be determined in order for the right expression to be chosen for e.g. the interfacial shear coefficient or some other coefficients like the heat transfer coefficient. The task at hand is to classify two-phase flow regimes with image analysis.

The approach in this Chapter is to use wavelets to pre-process flow images and then extract statistical features to use as inputs to an artificial neural network (ANN), see Fig. 3.1. The use of dynamic images as the "signal" from the flow means that the method is non-intrusive. Both non-intrusive methods, wavelets and ANN have been used previously when classifying two-phase flow regimes [15–20]. However, they have not been used in combination before. A more detailed description of the two-phase flow identification algorithm is found in **Paper I**.

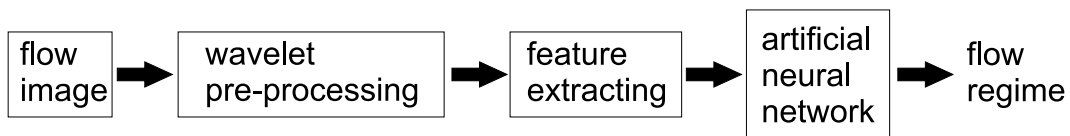


**Figure 3.1:** Outline of the two-phase flow classification algorithm.

### 3.1 Flow images

Two different sets of flow images were analysed. The first set included dynamic neutron radiographic images of two-phase flow within a metallic water loop, see Fig. 3.2a. This experiment was performed at the Kyoto University Reactor Research Institute (KURRI) [21]. By continuously increasing the heating of the water in the loop, all four flow regimes were created in sequence.

The second set of images, recorded at our department with the use of an ordinary digital camcorder, used visible light instead of neutron radiography. In the

experiment the two-phase flow was simulated by injecting air into a thin transparent rectangular duct filled with coloured water, see Fig. 3.2b. Due to the simple set-up it was only possible to simulate bubbly and slug flow. On the other hand, a much better image quality was achieved as compared to the neutron radiographic images.

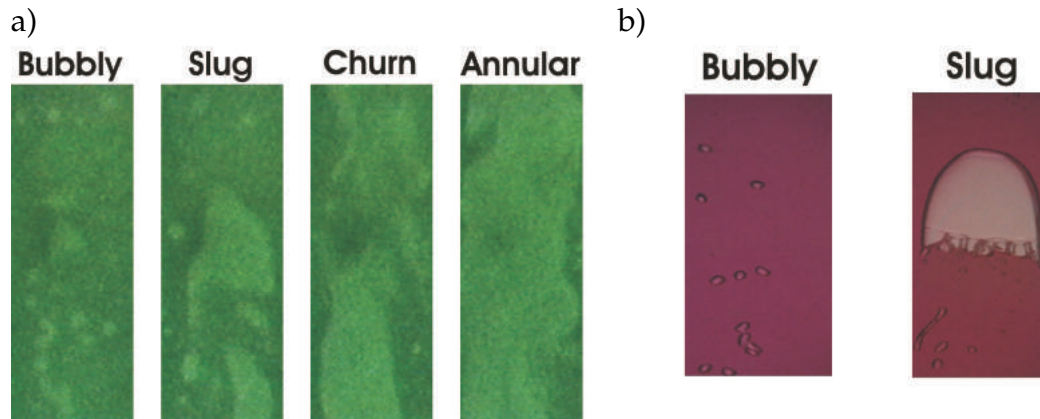


**Figure 3.2:** a): Images of the four different flow regimes from neutron radiography, flicker noisy images. b): Images of bubbly and slug flow regimes from visible light and coloured water, rather clear images with good contrast.

## 3.2 Wavelet pre-processing

Before extracting inputs for the ANN, the images (2-D matrix with gray scale pixel intensity) are pre-processed with the two-dimensional wavelet transform, since wavelets are suitable to highlight features of different length scales (frequencies) in an image. It is also possible to extract information about features in different directions in an image, see Fig. 2.5 in Section 2.3. The different flow regimes are assumed to have different features at different length scales in different directions.

The idea with the wavelet pre-processing is to use some features of the transformed wavelet coefficients which are characteristic for each regime. One such possible feature is the energy content of the detail coefficients. In this case the detail coefficients of the first level are considered and one way of expressing the energy content is given in Ref. [11] as:

$$E_1^x = \sum_i |T_{1,i}^x|^2. \quad (3.1)$$

Here  $x$  stands for the different directions (horizontal, vertical and diagonal) in the two-dimensional transform, see Section 2.3 for details. This energy feature was used to characterise the visible light images. Unfortunately, using the energy feature did not work in the case of the radiographic images, probably due to

the flicker noise and poor contrast of the images. Instead, the mean value of the first level approximation coefficients was used. Another possible feature, which could be used, is the variance of the very same coefficients. Hence, one value for the neutron radiographic images, the variance of the approximation coefficients, and three values for the visible light images, one for the details coefficients in each direction, are used. This gives a total of two features extracted for the radiographic images and six features for the visible light images. These features are, in the next step of the classification process, used as inputs for an ANN.

### 3.3 The classification algorithm

The classification task is solved by using an ANN with the wavelet pre-processed features as inputs. The principle of an ANN is to have a set of inputs with known output values. The ANN is fed with these inputs which propagate through the nodes of the network. The output is compared with the known output values and some error parameters are calculated which are used to change the weight of the nodes in the ANN. There are different ways in changing the nodes, i.e. different training procedures. The training is repeated until some pre-defined minimal criterion of the error is reached. Each repetition is called an epoch. After the training it is possible to feed the ANN with inputs whose outputs are to be determined. A properly trained ANN will generate the correct output values. For the two-phase flow classification the flow regime type is searched.

The ANN used in this thesis is constructed with the use of the *Neural Network Toolbox* in *MatLab* [22]. Different types of networks and training algorithms were tested and by trial and error the best combination was selected for the task at hand. A feed-forward network with an input layer, an output layer and one hidden layer trained with the resilient backpropagation (BP) algorithm was found to be the most effective one. The number of input nodes used depends on which type of flow images that are to be analysed. Two input nodes were used for the radiographic images and six for the visible light images. The number of nodes in the output layer also depends on the type of flow images, e.g. one output for each flow regime that is classified. Hence, four output nodes were used for the radiographic ones and two for the visible light images. The *log-sigmoid* transfer function was used for the output layer, giving values between 0 and 1. For both types of images 40 hidden nodes with *tan-sigmoid* transfer functions were used. The training target values were set to 0.9 for the correct regime and 0.1 for the other outputs.

The input data consist of 200 images from each of the flow regimes in the case with neutron radiography and 75 images from each of the two regimes in case of the visible light. A 5-fold cross-validation over the training data was used, i.e. 1/5 of the input data was used as a test set to verify the classification success of the network trained with the remaining 4/5 of the inputs. This was repeated five

times by using different images in the test set. All images were used only one time in the test set. When classifying the test set, the outputs were thresholded in order to get either 1 for the right flow and 0 for the wrong ones. If more than one output is 1 or none is 1 the image is classified as having unknown flow regime.

### 3.4 Results from the classification

To investigate the advantage with the wavelet pre-processing, the mean value and the variance from the raw image pixel intensity were also fed in to the network, and the results were compared to those with the wavelet pre-processed input data. Six different discrete wavelets were used for the pre-processing, *Haar*, *Daubechies 8*, *Coiflet 4*, *Symmlet 6* and *Biorthogonal 3.1*, all available in the *Wavelet Toolbox* in *MatLab* [14]. In the case of the noisy radiographic images, the success ratio of the classification was around 95% for the test set of images for all the different wavelets and the same for the raw data input. In Fig. 3.3 the result for the input pre-processed with the *Daubechies 8* wavelet is shown. When using the visible light images the success ratio was even higher, around 99%, for both the pre-processed and the raw inputs. Hence, there is no advantage, from the point of view of success ratio, in pre-processing the images.

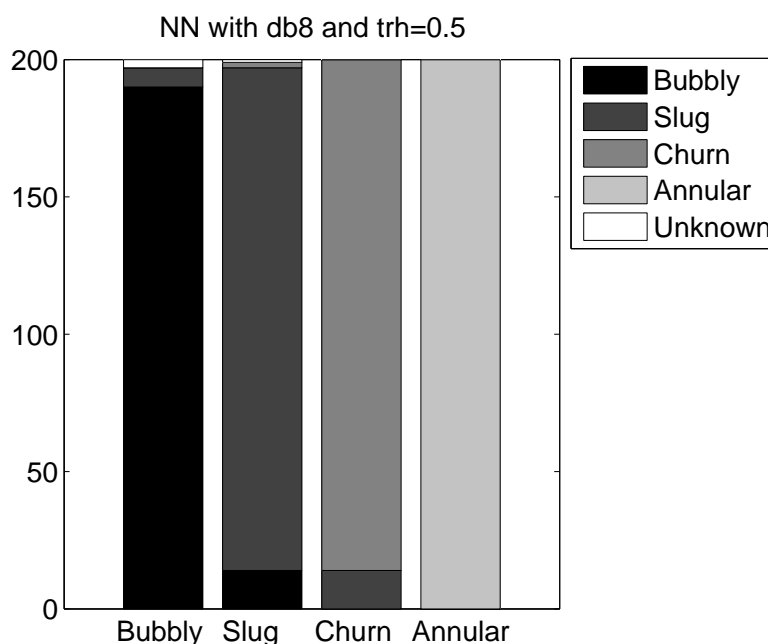


**Figure 3.3:** Classification ratio of the neutron radiographic images using a threshold of 0.5 after the ANN and the *Daubechies 8* wavelet for the pre-processing. A total of 200 images from each regime were classified and the average success ratio was 95%.

However, the number of epochs used during the training procedure is reduced with a factor of 100 when using wavelet pre-processing. For the raw data

input the maximum number of epochs, set to 30 000, was always reached before the target value of the Mean Square Error (MSE), set to  $10^{-3}$  was reached. In the pre-processed case the MSE target was reached within approximately 300 training epochs. Hence, the use of wavelet pre-processing has large advantages from the practical point of view.

Also worth mentioning is that 100 % of the annular flow images were classified correctly in the neutron radiographic case. As expected, the slug flow and the churn flow were the ones most likely to be mixed up, i.e. classified wrong or as unknown.



## CHAPTER 4

# DETECTOR TUBE IMPACTING IN BWRs

In this Chapter the second topic using wavelet techniques will be treated. The Chapter is a summary of **Paper II** with some recent results also included [23–26].

Methods for detection of detector tube impacting in BWRs with noise diagnostic methods, applied to signals from neutron detectors, have been used for a long time. The first method used was based on classical Fourier analysis [3, 4, 27]. In this method the auto power spectral density (APSD), coherence and phase curves are used to identify impacting tubes.

At our Department a new method, based on discrete wavelet analysis, has been developed. First, simulations and measurements from the Swedish nuclear power plant Barsebäck-2 were analysed with the wavelet method [28]. Later, measurements taken from Oskarshamn-2 were analysed and the result was compared with visual inspections made before the analysis [29–31]. Between the two different analyses the wavelet algorithm was modified.

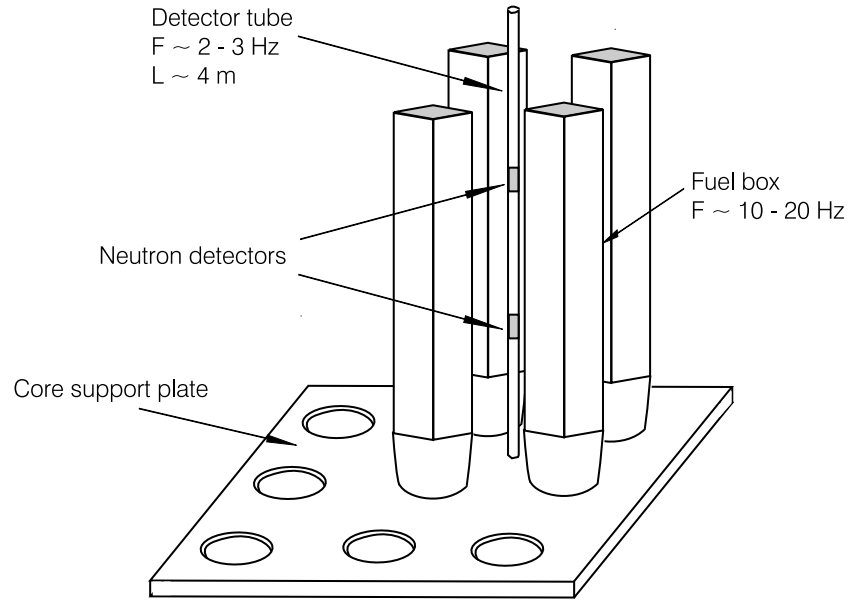
This Chapter is a continuation of these analyses. Here, measurements from Ringhals-1 are analysed both with the traditional spectral method and the new discrete wavelet based method. Also one method based on the continuous wavelet transform is included in the analysis. Measurements from 4 consecutive fuel cycles from 2002 to 2005 of Ringhals-1 are analysed.

### 4.1 Physical model

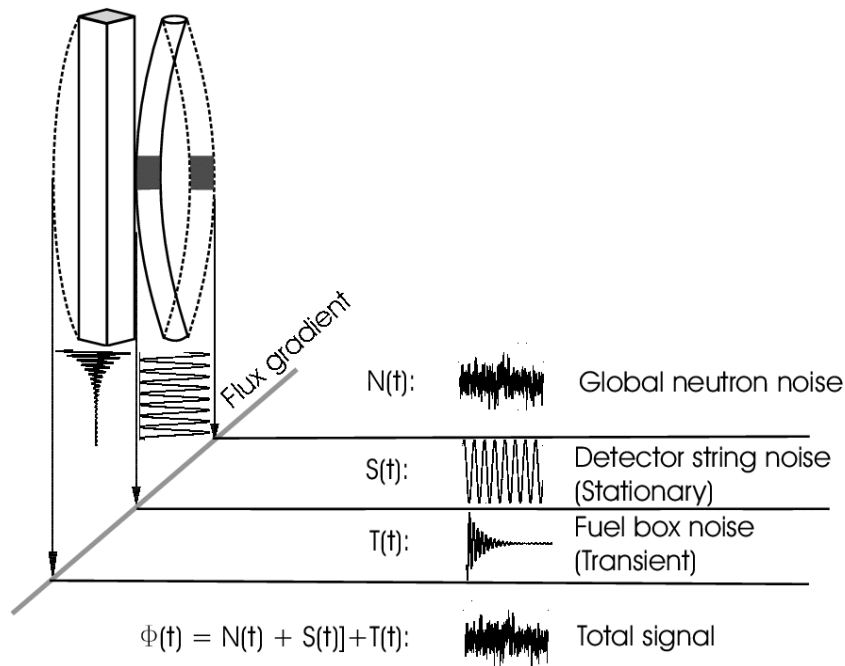
The task is to identify detector tubes which not only vibrate but also impact on the neighbouring fuel assemblies. If a detector tube hits a fuel assembly it can damage the fuel box which may cause also damage to the fuel cladding. Also the detector itself can be damaged. Any such event must be avoided in an operating plant.

Fig. 4.1 shows a general outline of the physical setup of a detector tube together with the surrounding fuel assemblies. The vibrations arise from the strong flow of coolant water in the reactor and the fact that the detector tubes, which are roughly four metres long, are fixed only in their ends. The typical eigenfrequency of a detector tube in flowing water is around 2 Hz [3]. If the vibration amplitude is

large enough, the tube may impact on the nearby fuel assemblies, which in return will execute a short, damped oscillation after each hit, with an eigenfrequency of 10 to 20 Hz. In addition, the detector itself might execute similar transient vibrations in the guide tube.



**Figure 4.1:** Illustration of a detector tube in a BWR core with four surrounding fuel assemblies. Some typical data of interest are also shown.



**Figure 4.2:** Schematic view of the signal,  $S(t)$ , from a detector vibrating in a flux gradient with background noise,  $N(t)$ , and fuel box vibration,  $T(t)$ .

The signals from vibrating and impacting detector tubes are assumed to contain three parts, see Fig. 4.2. The first is a global part with some broad-band noise,  $N(t)$ , including the boiling noise, i.e. from the generation and transport of bubbles past the detector. The second part is a regularly oscillating part from the detector tube vibration,  $S(t)$ , and thirdly an intermittent part due to the vibration of the fuel-assembly,  $T(t)$ . The intermittent structure is due to the damped, randomly occurring vibration of the fuel-assembly, due to each impacting.

In general, the amplitude or the root mean square value of  $T(t)$  is much smaller than that of  $N(t) + S(t)$ . Therefore, in a spectral analysis, the effect of  $T(t)$  is not visible. Hence, the classical spectral method focuses on the vibration of the detector tubes, i.e. the changes of the auto-spectra and phase of the coherence due to increase of amplitude and confinement of motion, which are indirect indications of impacting. On the other hand the wavelet methods are suitable for identification of the intermittent signal from the fuel assembly vibrations and hence direct indication of the impacting events.

## 4.2 Analysis methods

The three different analysis methods of detecting detector tube impacting, such as the spectral method, the discrete wavelet method and the continuous wavelet method will be described in the following subsections.

### 4.2.1 Spectral method

The spectral method is based on the features of the APSD, the coherence, and the phase between two detectors in the same tube. The following four criteria are used to classify a detector tube as an impacting one [27]. First, broadening of the eigenfrequency peak in the APSD compared to a vibrating but non-impacting tube. Second, multiple peaks in the APSD, especially at the double eigenfrequency. Third, high coherence at the eigenfrequency, and finally, distorted (zero) phase over a large frequency range. The decision of whether a tube is impacting or not is made by qualitatively taking all four criteria into account. This makes the method a more or less relative method, which requires expertise judgement.

Fig. 4.3 shows the APSD, coherence and phase from signals of detector tube 2, LPRM 2.2 and LPRM 2.4, from a measurement made in 2003 at the Ringhals-1 BWR. LPRM stands for local power range monitor and is the notation of the neutron detectors used. LPRM 2.4 is the upper detector and LPRM 2.2 is the lower one. This tube was not suspected for impacting since the APSD is smooth without any vibrations peaks. The phase is linear up till 4 Hz and where the phase is zero there is a high coherence, showing the upward flow of bubbles in the core. Hence, this tube is used as a reference tube showing a non-vibrating and non-impacting tube.

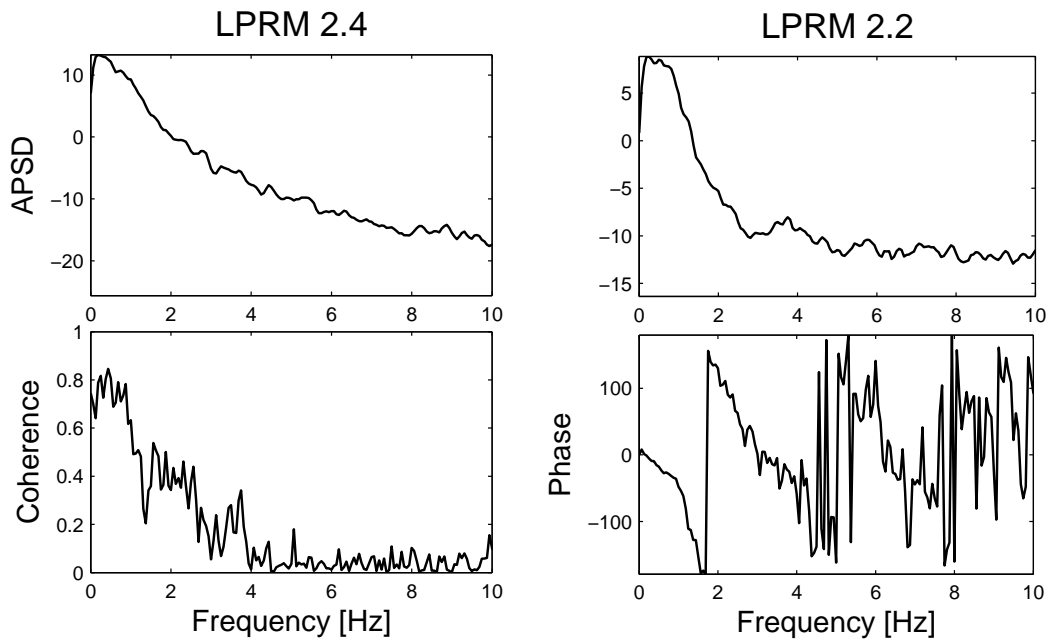


**Figure 4.3:** Autospetra (APSD), coherence and phase for the detectors at position 2 from a measurement made at the BWR Ringhals-1 in 2003.

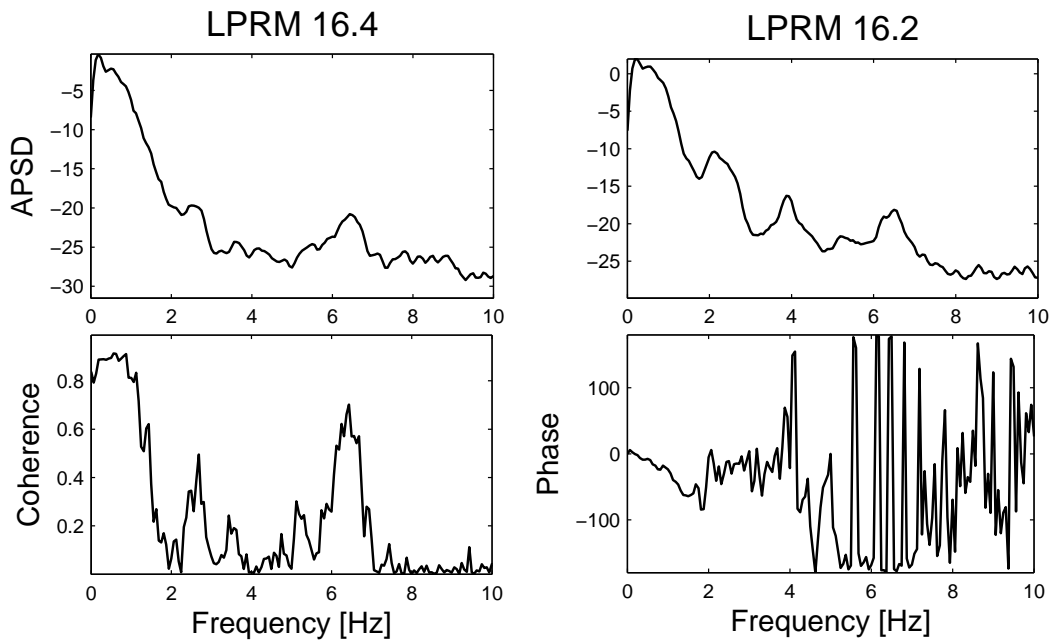


**Figure 4.4:** Autospetra (APSD), coherence and phase for the detectors at position 16 from a measurement made at the BWR Ringhals-1 in 2003.

Fig. 4.4 shows the APSD, coherence and phase from detector tube 16, LPRM 16.2 and LPRM 16.4, from the same measurement as above. Clearly there is a broad peak in the APSD around the expected eigenfrequency of the detector tubes (2 Hz). Multiple peaks are also visible in the APSD. The coherence is high at the very same frequency and the characteristic distortion of the phase is present (non-linear and almost zero). Hence, this detector position was classified as one of the most likely ones to impact in this measurement.

## 4.2.2 Discrete wavelet method

The idea with the wavelet method is to calculate a so-called impact rate index (IR-index) [31]. The IR-index is assumed to give the number of intermittent signals per unit time due to the fuel assembly vibration. A high value means severe impacting. By using the IR-index, there is no need for an expert judgment which is the case for the spectral method. Hence, the wavelet method is an absolute method.

The IR index is calculated by first assuming that the detector signals consist of three parts (see Fig 4.2):

$$\phi(t) = N(t) + S(t) + T(t). \quad (4.1)$$

Here  $N(t) + S(t)$  is analysed in the spectral case, described above, and  $T(t)$ , e.g. the fuel-box vibration, is the part which the discrete wavelet tries to extract.

To reduce the high frequency noise present in the signal, a wavelet de-noising is performed. The de-noising is done by applying a level-dependent threshold to each of the detail coefficients,  $T_{m,n}$  as described in Chapter 2, in a multiresolution analysis of  $\phi(t)$ . The wavelet decomposition is made down to a level,  $M$ , corresponding to the lowest assumed value of eigenfrequency of the fuel assemblies,  $\sim 10$  Hz. The de-noised details are then reconstructed by using the thresholded detail coefficients in Eq. (2.9), giving  $Denoise(d_m(t))$ . From the de-noised details the intermittent signal from the fuel assembly vibration can be calculated as,

$$V(t) = \sum_{m=N}^M Denoised(d_m(t)) \approx T(t). \quad (4.2)$$

Here the level  $N$  corresponds to frequencies around 25 Hz and level  $M$ , as mentioned, above corresponds to about 10 Hz. The IR-index is calculated as the number of peaks in  $V(t)$  divided by the length of the measurement. Each peak corresponds to the start of an intermittent fuel assembly vibration. In order to use the wavelet method, a value of the eigenfrequency of the fuel assemblies has always to be given to perform the de-noising to the correct level (frequency band).

As is commonly known when using wavelets, it is not easy to know which kind of wavelet to use for a certain analysing task. Using the *Meyer* wavelet in

the *MatLab Wavelet Toolbox*, [14], gave best agreement with the result from the spectral method.

In Fig. 4.5a the detector signal from LPRM 16.4 (the same measurement as is used as an example in Fig. 4.4) is shown and  $V(t)$  calculated from equation Eq. 4.2 is shown in Fig. 4.5b. As can be seen, several spikes are visible in  $V(t)$  and the IR-index in this case is 4.6 impacts/min. Hence, this detector tube was pointed out as most likely to impact by the discrete wavelet method for this certain measurement.

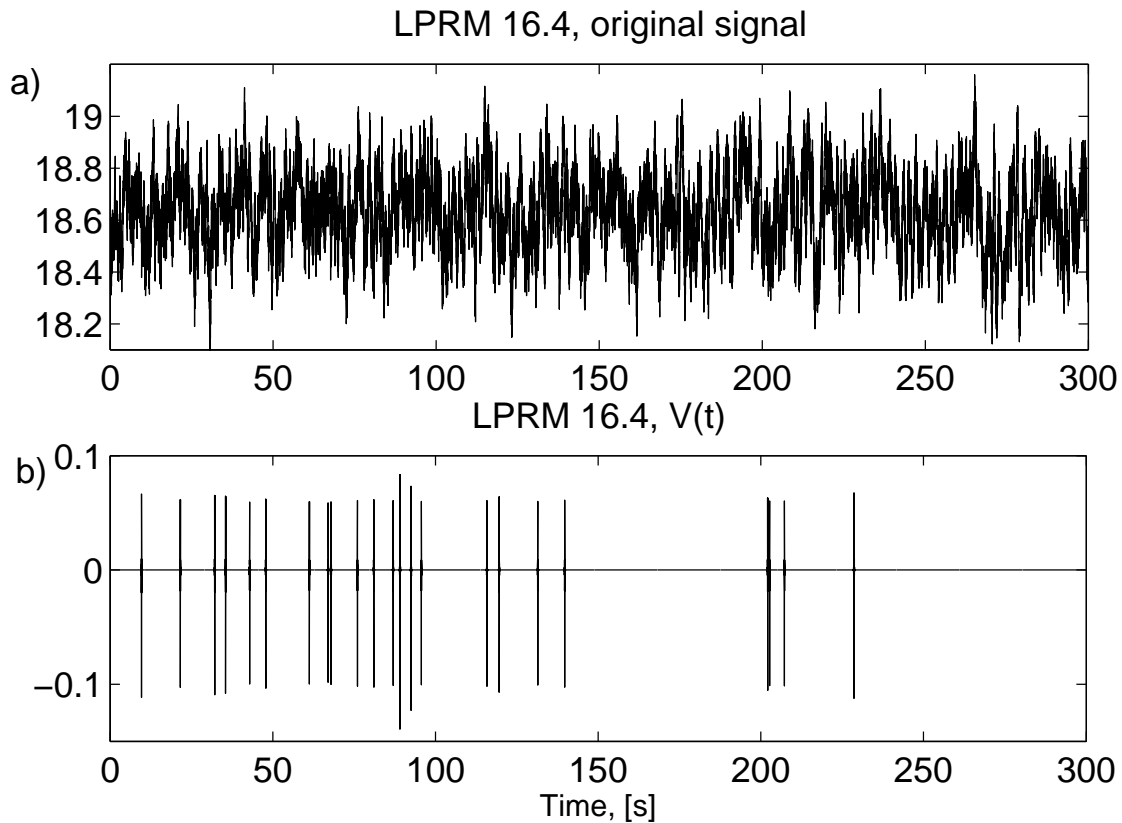


**Figure 4.5:** Signal from LPRM 16.4 from a measurement made at the BWR Ringhals-1 in 2003. In a) the original signal is shown. In b) the intermittent signal,  $V(t)$ , after the wavelet analysis of the detector is shown. The spikes indicating impacting are clearly visible.

### 4.2.3 Continuous wavelet method

The continuous wavelet method is based on the calculation of the so-called wavelet coherence  $\gamma_{g,h}^w(a,b)$ , [11,32], between two detector signals  $g$  and  $h$  from the same tube,

$$\gamma_{g,h}^w(a,b) = \frac{|C_{g,h}^w(a,b)|}{\sqrt{C_{g,g}^w(a,b)C_{h,h}^w(a,b)}}. \quad (4.3)$$

Here

$$C_{g,h}^w(a,b) = \int_{b-T/2}^{b+T/2} T_g^*(a,b')T_h(a,b')db' \quad (4.4)$$

is an averaging of the wavelet scalogram,  $T_g^*(a,b)T_h(a,b)$ , where  $T_x(a,b)$  is the continuous wavelet transform of signal  $x(t)$ . It should be noted that  $a$  is corresponding to frequency and  $b$  to time, hence it is possible to convert  $\gamma_{g,h}^w(a,b)$  into  $\gamma_{g,h}^w(f,\tau)$ . Fig. 4.6 shows the wavelet coherence for detector tube 16 from the same measurement as in the two previous subsections.

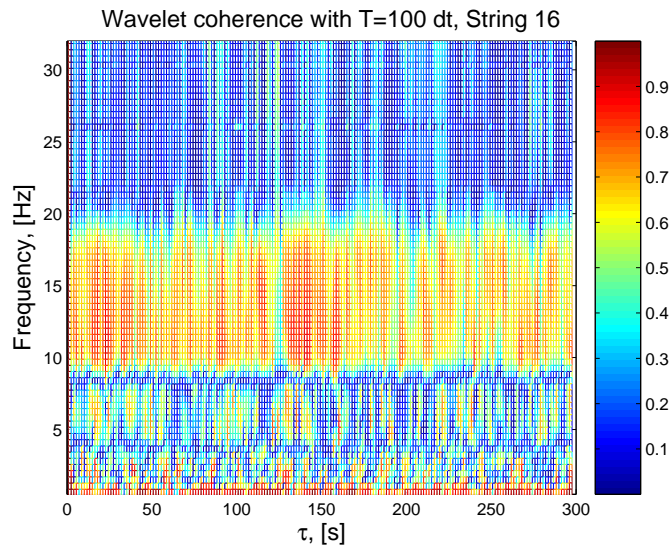


**Figure 4.6:** Wavelet coherence for detector tube 16 from a measurement made at the BWR Ringhals-1 in 2003.

The presence of the large values in the wavelet coherence around 10-20 Hz is an indicator of impacting. The exact mechanism of generating high coherence in this frequency region through impacting is not fully understood. By empirical evidence it can be claimed that it is the fuel assembly vibrations that are seen. Detector positions pointed out by the discrete wavelet method as impacting also display large values in the frequency band between 10 and 20 Hz in the wavelet coherence. Even though the result from the continuous wavelet transform is not fully understood, it implies that further use may turn out to be of interest when investigating detector tube impacting.

### 4.3 Analysis of the measurements

The methods described above were applied to four measurements made during the start-up of four consecutive fuel cycles at the BWR Ringhals-1. The measurements were taken during full power ( $\sim 109\%$ ) and full core flow ( $\sim 11\,000$  kg/s) from 2002 to 2005 in cooperation with plant personnel. The detectors are placed

at four different axial levels in the detector tube. However, only signals from two of the four detectors in each tube were available in these measurements. There are 36 detector tubes evenly distributed in the core giving a total of 72 signals in this case.

In the following of this Chapter the measurements will be referred to as measurements 1-4 with the measurement from 2002 being measurement 1. In **Paper II** measurements 1 and 2 are analysed, in Ref. [25] measurement 3 and in Ref. [26] measurement 4 is analysed.

The measurements are summarised in Table 4.1. In measurement 1 the sampling frequency was too low, 12.5 Hz, for the wavelet method to be used. This is because the maximum frequency which can be analysed is half the sampling frequency and the wavelet methods are using frequencies up to 25 Hz. Hence, in order for the wavelet methods to be applicable, the sampling frequency must be at least 50 Hz.

Name	Year	Sampling frequency, [Hz]	Duration, [min]
measurement 1	2002	12.5	11
measurement 2	2003	64	5
measurement 3	2004	200	33
measurement 4	2005	200	33

**Table 4.1:** Summary of the measurements made at the BWR Ringhals-1.

The target of the analysis of the measurements was to make a judgment of which tubes that are most likely to impact in each measurement case. Since measurement 1 was not suited for wavelet analysis, the judgment on which tubes that may impact on the fuel assemblies is based mainly on the spectral method in that case.

After the analysis of measurement 1 was performed, the plant personnel made visual inspections of some fuel assemblies, which were pointed out by the analysis, during the outage of the plant in August 2003. They inspected fuel assemblies around detector tube positions 1, 9, 10 and 22 out of which position 1 had been classified as non-vibrating in the analysis and the three others were the ones that was judged most likely to impact. The result of the analysis and the inspection is presented in Table 4.2.

Status	By spectral analysis	By visual inspection
most likely impacting	9, 10 and 22	10 and 22
probably impacting	4, 8, 16 and 24	—
small chance of impacting	11, 12, 30 and 33	—

**Table 4.2:** Results of the analysis of measurement 1.

As can be seen, tube positions 10 and 22 were pointed out by the visual in-

spection. They showed some wear marks on the corner of the fuel boxes. This is in good agreement with the prediction from the analysis.

In the analysis of measurements 2 to 4 all three analysis methods were used and compared with each other. However, this times no visual inspections were made. Hence, the spectral method is used as a reference since the validity of that method was verified in measurement 1.

The results of the analysis of measurements 2-4 are presented in Table 4.3 - 4.5.

Status	By spectral analysis	By discrete wavelet analysis	By continuous wavelet analysis
most likely impacting	15, 16, 24 and 35	16, 23 and 2	4, 9, 16, 23 and 35
probably impacting	12 and 34	4, 34 and 35	24 and 34
small chance of impacting	27 and 32	—	—

Table 4.3: Results the analysis of measurement 2.

Status	By spectral analysis	By discrete wavelet analysis	By continuous wavelet analysis
most likely impacting	16, 24, 30 and 35	4, 16, 26 and 35	4, 16, 23, 34 and 35
probably impacting	4, 5, 9 and 34	6, 14, 17, 23, 24, 33 and 34	9 and 24
small chance of impacting	10, 11, 22, 23 and 29	—	—

Table 4.4: Results the analysis of measurement 3.

Status	By spectral analysis	By discrete wavelet analysis	By continuous wavelet analysis
most likely impacting	16, 24, 9 and 34	5	16, 24 and 36
probably impacting	2, 22, 23, 30 and 36	3, 8, 17, 24 and 28	2, 7 and 34
small chance of impacting	1, 4, 10 and 31	—	1, 9, 15, 17 and 29

Table 4.5: Results the analysis of measurement 4.

## 4.4 Conclusions of the detector tube impacting

In Table 4.6 the results from the four measurements are summarised. The tubes listed in the top row are pointed out for impacting in all measurements analysed. In the case of the spectral analysis, four measurements were analysed and for the wavelet methods three measurements were analysed. In the second row the tubes which are pointed out in all but one of the measurements are listed. For the spectral case this means that they are pointed out three times out of four and for the wavelet methods two times out of three. The spectral method is in good agreement with visual inspections and the wavelet based methods are, to some extent, in agreement with the spectral one.

Number of times suspected	By spectral analysis	By discrete wavelet analysis	By continuous wavelet analysis
4/4 or 3/3	16 and 24	24	9, 16, 24 and 34
3/4 or 2/3	4, 9, 10, 22, 30 and 34	4, 16, 17, 23, 34 and 35	4, 23 and 35

**Table 4.6:** Trend analysis of measurements 1-4. 4/4 means that the tubes are suspected for impacting in four out of four measurements.

In Fig. 4.7 the four tubes which are pointed out in all or in all but one of the measurements by all methods are marked with circles. These are the tubes which are most likely to be impacting. Probably some of the fuel assemblies around these tubes will be visually inspected during the outage in 2007.

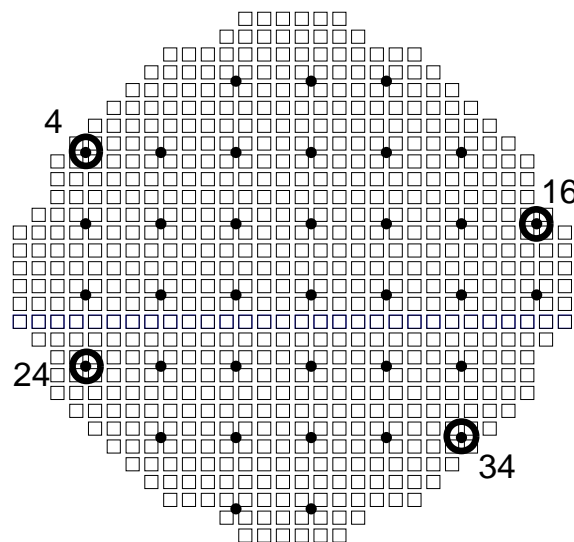


**Figure 4.7:** The four tubes which are most likely to be impacting on fuel-assemblies in Ringhals-1.

One may wonder if there is a need for a new method if a working one already exists (spectral). However, the advantage, especially with the discrete wavelet method is that there is no need for comparison with a non-vibrating sample. It is an absolute method compared to the more relative spectral method, and its use requires no expertise, in contrast to the spectral based method, which cannot be performed e.g. by the control room personnel. The three methods can also be seen as complements to each other. Hence, a judgment of which tubes who are most likely to be impacting based on all three methods together is more reliable compared to the case when only one analysis method is used.

Finally, it should be mentioned that the discrete wavelet method has been tested on measurements from three Swedish plants, Barsebäck, Oskarshamn and Ringhals. It worked satisfactorily in all three cases, even though it had to be modified between its use in different plants.



## CHAPTER 5

# DECAY RATIO ESTIMATION IN BWRs

This Chapter, which is a brief summary of **Paper III**, is the last one where wavelet techniques were used in the area of noise diagnostics.

Two principally different uses of wavelet techniques for estimating the decay ratio (DR) in BWRs from the auto-correlation function (ACF) are explored. The first part consists of investigating whether wavelet de-noising and de-trending techniques can help to improve the accuracy of the traditional parametric methods of determining the DR. This study was inspired by an early paper on wavelet applications by Domis and Tambouratzis [33].

The second line of applications consists of the use of the continuous wavelet transform for the determination of the DR. This is a relatively new method, which was suggested by Espinosa-Paredes et al. [34], where they calculated the instantaneous decay ratio. It is a promising method that can be used to real-time monitoring of the instantaneous DR, as well as to detect, under some circumstances, the coexistence of two different DRs.

First, the methods will be developed on simulated signals and then tested on real measurements from the Swedish BWR Ringhals-1.

### 5.1 General principles of the estimation of the decay ratio

The dynamic behaviour of a BWR core in the stable region, i.e. when no limit cycle behaviour can be observed, is often described as a second-order system. This means that the flux fluctuations,  $\delta\phi(t)$ , obey a second-order equation driven by a random (white) force  $f(t)$  as

$$\delta\ddot{\phi}(t) + 2\xi\omega_0\delta\dot{\phi}(t) + \omega_0^2\delta\phi(t) = f(t), \quad (5.1)$$

where  $\xi$  is the damping parameter and  $\omega_0$  is the eigenfrequency (resonant frequency, usually 0.5 Hz) of the system. Here, both  $\phi(t)$  and  $f(t)$  are assumed to be stationary ergodic processes. It is easy to confirm that the ACF of  $\delta\phi(t)$  is given as [35]

$$ACF(\tau) = Ce^{-\xi\omega_0\tau}[\cos(\omega_0\tau) + \xi \sin(\omega_0\tau)]. \quad (5.2)$$

This represents a periodic oscillation with an exponentially decaying envelope, illustrated in Fig. 5.1a. From the ACF the decay ratio can be calculated by taking the ratio between  $B2$  and  $B1$ , illustrated in Fig. 5.1a [36]. It is even better to use the 2nd, 3rd and 4th maxima and 2nd and 3rd minima, i.e.  $B3/B2$ , since the first maxima can contain the effect of white noise in the signal, in form of a sharp peak. This method will be called the peak-to-peak method in the continuation of this Chapter. If the ACF contains a trend, the use of peak-to-peak method will give a better estimation of the decay ratio than the maxima expression. This latter was the case in the measurements taken at the Swedish nuclear power plant Ringhals-1 in 1990, [37,38], see Fig. 5.1b.

The DR can also, under some simplifications, be estimated from (5.2) as

$$DR = e^{-\xi 2\pi}. \quad (5.3)$$

Here, the parameter  $\xi$  can be obtained by least-square fitting of Eq. (5.2) to a measured ACF [39]. This method has the advantage that, in contrast to the peak-to-peak method, it makes use of the whole ACF and not only a few maxima and minima.

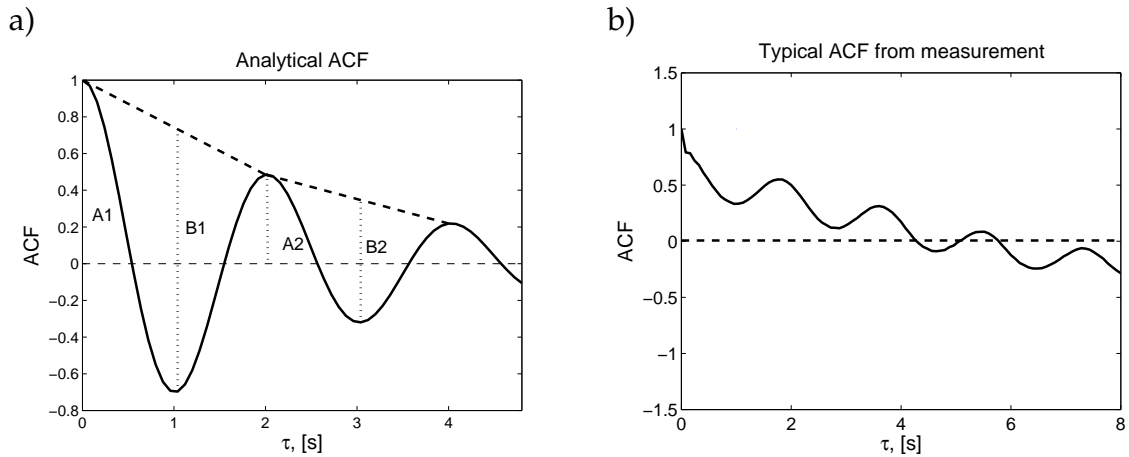


**Figure 5.1:** In a) an analytical ACF is shown where the decay ratio can be defined as either  $DR=A2/A1$  or  $DR=B2/B1$ . In b) a typical ACF, which is linearly disturbed, from one measurement taken at Ringhals-1 in 1990 is shown.

In Fig. 5.1b a typical ACF from a measurement is shown. As can be seen, the ACF contains a linear trend which can effect the estimation of the DR. Hence, it could be useful to pre-process the ACF before the estimation algorithm is applied. The ACF from measurements could also contain bit-noise or some irregularities due to finite sample length etc., which can be interpreted as white noise. Hence, wavelets could be used to de-noise and de-trend the ACF before the DR is estimated in order to improve the estimation.

## 5.2 De-trending and de-noising using discrete wavelets

Discrete wavelet techniques will in this Section be used to pre-process a noisy ACF before the estimation of the DR is made. Both random white noise and trends will be added to a simulated ACF (ideal ACF) before the pre-processing is made. The properties of the discrete wavelet transform were described in Chapter 2.

A signal can be reconstructed (inversion of the wavelet transform) from the wavelet transform by using the approximation and details according to Eq. (2.6). The approximation contains the low frequencies of the signal, hence it is possible to make a de-trending of a signal by simply not using the approximation in the reconstruction. Moreover, the details are representing different frequency components of the signal. Hence, if one chooses the right details corresponding to the frequency range of interest, it is possible to obtain a de-noising of the signal as well.

In the case of an ACF from a BWR the characteristic frequency is around 0.5 Hz and the sampling frequency of measurements made at the plants is 12.5 Hz. Based on this information it is possible to calculate which details to be used for a certain wavelet by using Eq. (2.2). First, however the wavelet to be used in the analysis need to be chosen. There are no rigorous criteria on which one could base a unique decision, rather the choice of which wavelet to use is rather arbitrary. For this case the *discrete Meyer* wavelet seems to be a good choice. Other wavelets did perform well too during tests, such as higher order *Daubechies* wavelets.

Now, it can be concluded that details at level 4,  $d_4(t)$ , of the *discrete Meyer* wavelet, correspond to a frequency of about 0.5 Hz and level 5,  $d_5(t)$ , to a frequency of about 0.25 Hz. Both of these details will be used in the reconstruction of the ACF, since they are close to the frequency of interest which is around 0.5 Hz, i.e. the frequency of the oscillations in a BWR. Hence, the de-noised and de-trended ACF,  $deACF(t)$ , will be calculated as

$$deACF(t) = d_4(t) + d_5(t). \quad (5.4)$$

In **Paper III** some other different ways of de-nosing and de-trending of the signal are also investigated but they did not work as well as the above described method.

In order to simulate an ACF which has more or less the same trend as an ACF from a measurement and which also contains some white noise,  $n(\tau)$ <sup>1</sup> the

<sup>1</sup> $n(\tau)$  is a "white noise" of the ACF and not that of the process, which would give  $n(\tau) = \delta(\tau)$

following expression is used

$$ACF_{noisy}(\tau) = \frac{ACF_{ideal}(\tau) + 0.1(2 - \tau) + e^{-0.5\tau} + 1 + n(\tau)}{ACF_{noisy}(\tau = 0)}. \quad (5.5)$$

In Fig. 5.2a  $ACF_{noisy}$  is shown, together with  $ACF_{ideal}$  (idealistic ACF calculated by Eq. (5.2)) as well as the de-trended and de-noised ACF. In Fig. 5.2b the absolute value of the errors of the estimated decay ratios for some ACFs with different DRs are shown; the peak-to-peak and curve-fitting (CF) methods are used on the de-noised and de-trended ACF. The curve fitting method is also used on  $ACF_{noisy}$  as a reference. The peak-to-peak method was not applied on  $ACF_{noisy}$  because it is cumbersome to apply that method to a noisy signal.

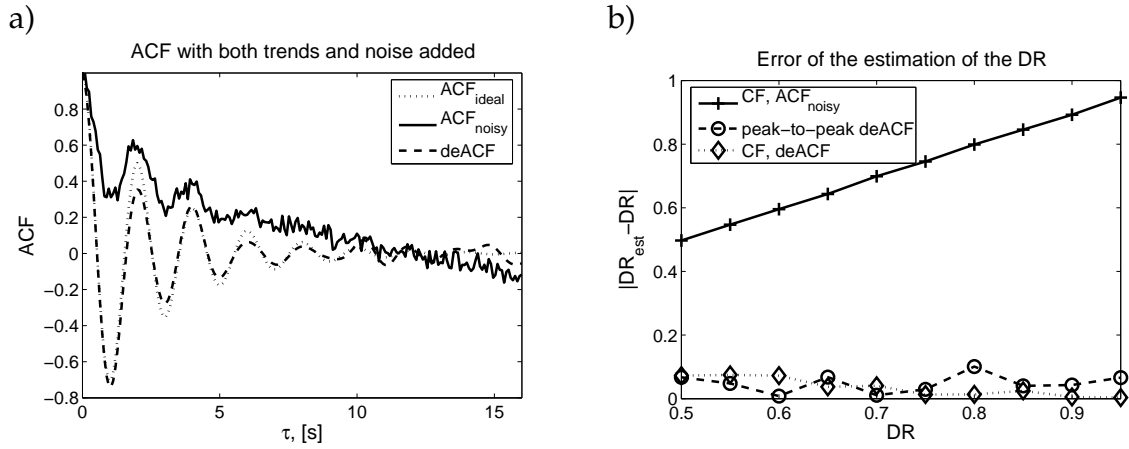


**Figure 5.2:** In a) an ACF with both trends and white noise are shown together with the original ACF and the de-noised ACF. In b) the absolute value of the error for the estimation of the decay ratio is shown.

Applied on the wavelet pre-processed ACF, both the CF and the peak-to-peak methods supply a much more accurate value of the DR than the curve-fitting performed on  $ACF_{noisy}$  containing both trends and noise. This improvement is achieved despite the fact that the form of the wavelet de-trended and de-noised ACF does not agree very well with the form of  $ACF_{ideal}$ . Since real-world ACFs taken from measurements are likely to be affected both by trends and scatter of data, the wavelet pre-processing could prove useful in improving the quality of the estimation of the DR.

### 5.3 Using the continuous wavelet transform for estimating the DR

Wavelet techniques can also be used for the determination of the DR directly from the raw time series signals or from the ACF. In this section the continuous wavelet transform (CWT) will be used for the determination of the DR from the ACF.

The essence of the method can be summarised as follows. First, a progressive CWT (containing no negative frequencies) is applied to the ACF, such as the *complex Morlet* wavelet. The modulus of the CWT of the analytical ACF from Eq. (5.2) can be approximated as [40,41]

$$|W(ACF)(a, b)| \approx \frac{1}{2} A_0 e^{-\xi \omega_0 b} |G(a \omega_0)|. \quad (5.6)$$

Here,  $W(f)(a, b)$  is the continuous wavelet transform of  $f$  and  $G$  is the Fourier transform of the analysing wavelet.

The next step is to take the logarithm of Eq. (5.6) at the ridge of the transform, i.e. at  $a = a_0$  corresponding to the maximum value of the modulus of transform,

$$\ln |W(ACF)(a_0, b)| \approx -\xi \omega_0 b + \ln\left(\frac{1}{2} A_0 |G(a_0 \omega_0)|\right). \quad (5.7)$$

The second term on the right hand side is a constant at  $a_0$ , hence  $\xi \omega_0$  can be calculated from the slope of this curve. Further,  $\omega_0$  can be approximated with  $2\pi f_0$ . Therefore the decay ratio can be calculated as:

$$DR = \exp\left(\frac{\frac{d}{db} \ln |W(ACF)(a_0, b)|}{\omega_0} 2\pi\right) = \exp\left(\frac{\frac{d}{db} \ln |W(ACF)(a_0, b)|}{f_0}\right). \quad (5.8)$$

To illustrate the method, some applications are shown with simulated ACFs. An ideal ACF is used for this purpose with  $DR = 0.6$  and  $f_0 = 0.5$  Hz. The logarithm of the modulus of the CWT for this ACF is shown in Fig. 5.3a, and the corresponding ridge at  $a_0$  is plotted in Fig. 5.3b. For better visibility the ridge is marked with a white line in Fig. 5.3a. Fig. 5.3b shows that for  $b$  between 10 and 25 s the curve has a linear slope. Hence the derivative in Eq. (5.8) can be estimated as the constant slope of the ridge between these values of  $b$ . By using the expression in Eq. (5.8) the DR is estimated to 0.60.

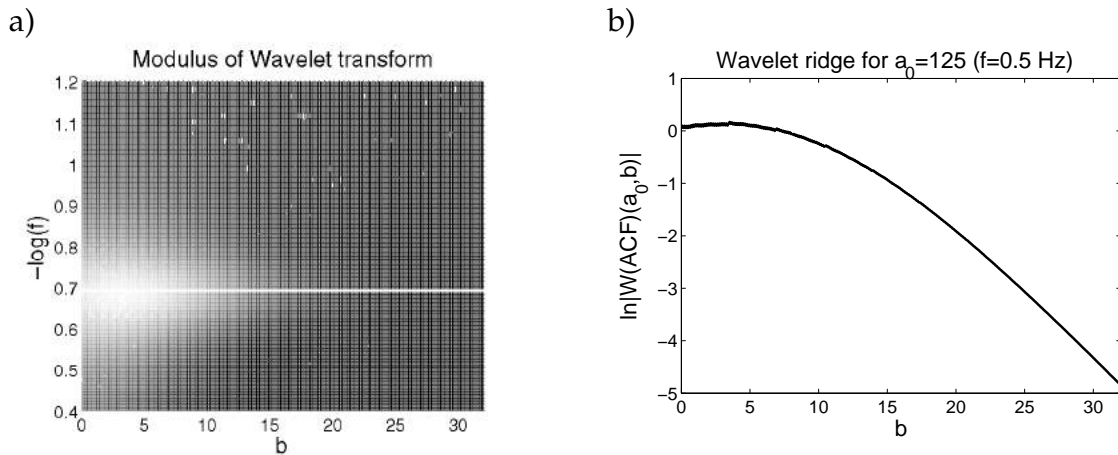


**Figure 5.3:** a): The modulus of the wavelet transform of an ACF with  $DR=0.6$  and  $f_0=0.5$  Hz with a white line showing the ridge. b): The ridge corresponding to the white line in a).

Two different wavelets will be used in the test of the CWT-method for determining the DR. Both of the wavelets will be of the type *complex Morlet* wavelets, namely the *cmor1 – 2* and *cmor1 – 5* wavelets.

First, the case of dual oscillations with the same frequency is investigated. For this an ideal ACF in the form

$$ACF(\tau) = \frac{S_1 e^{-\xi_1 \omega_0 \tau} [\cos(\omega_0 \tau) + \xi_1 \sin(\omega_0 \tau)] + S_2 e^{-\xi_2 \omega_0 \tau} [\cos(\omega_0 \tau) + \xi_2 \sin(\omega_0 \tau)]}{S_1 + S_2} \quad (5.9)$$

is considered. Here  $\xi_i$  and  $S_i$ ,  $i = 1, 2$ , correspond to the two simultaneous processes,  $S_i$  being the amplitude. In the quantitative work,  $\xi_i$  is chosen such that one has DR=0.6 for the first process (stable) and DR=0.9 for the second (unstable). The relative weight of the signals is determined by the ratio  $S_1/S_2$ . The result of the estimation of the DR with the continuous wavelet transform is shown in Fig. 5.4 where the ratio between the processes varies between 1 to 10. The two different wavelets yield a relatively good estimate of the unstable DR of 0.9 for all ratios, even when the amplitude of the stable signal is 10 times higher than that of the unstable one. In this respect the CWT method yields DR values closer to the unstable one than the traditional peak-to-peak method and the curve-fitting method, with the wavelet *cmor1 – 2* proving to be the better one of the two wavelets. This is advantageous in applications where the discovery and quantification of the unstable process is the main concern.

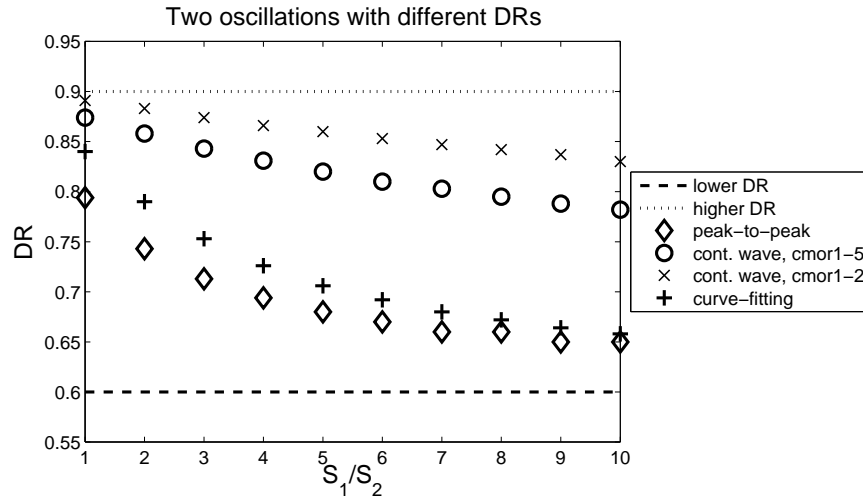


**Figure 5.4:** Signal with two DR:s at the same time. Estimation of the DR with peak-to-peak, curve-fitting and complex wavelet methods. The ratio  $S_1/S_2$  indicates the relation of the strength between the two different DRs.

As long as the two simultaneous oscillations occur with exactly the same frequency, the CWT-based method has no chance to determine both of the two different DRs. However, if the frequencies of the two oscillations slightly differ, one can observe two ridges in the modulus maxima of the wavelet transform, and hence there is a possibility to determine the two different DRs. Results of a

quantitative investigation of two simultaneous DRs are shown in Table 5.1. The DR values for the two oscillations are 0.6 and 0.9, but the frequency difference between the two oscillations is varying. These calculations were made with the  $cmor1 - 5$  wavelet, since with the  $cmor1 - 2$  it was not possible to resolve frequencies as close as 0.05 Hz. This is expected since higher centre frequency of the analysing wavelet will give better frequency resolution [41]. The results displayed in Table 5.1 show that whereas the higher DR is estimated correctly for all frequency differences, the accuracy of the estimation of the low DR deteriorates fast when the two frequencies approach each other. This study suggests that if the frequencies are not closer than 0.03 Hz, it is possible to detect two ridges in the modulus of the wavelet transform. If the difference is 0.04 Hz or larger, it is also possible to estimate both decay ratios with good accuracy.

Low DR			High DR		
$f_{0,low}$	$DR_{low}$	$DR_{est}$	$f_{0,high}$	$DR_{high}$	$DR_{est}$
0.45	0.6	0.71	0.5	0.9	0.89
0.46	0.6	0.70	0.5	0.9	0.90
0.47	0.6	0.84	0.5	0.9	0.90

**Table 5.1:** Results of estimation, using the  $cmor1 - 5$  wavelet, with two frequencies and two DRs.

## 5.4 Testing of the methods on Ringhals Benchmark

In order to test the two different wavelet methods, data from the Ringhals-1 benchmark were analysed [38]. The benchmark consists of 9 measurements at different power and core flow levels taken at beginning of cycle 14(BOC-14). Here 4 of these measurements are analysed. In Fig. 5.1b it is clear that the ACF from the measurements has some linear trend. Hence, the wavelets will be used in order to de-trend the ACF. In two of the analysed measurements it was confirmed that global and regional oscillations with different DR occurred at the same time, hence the CWT-method is used in order to identify the highest DR. Therefore, both of the methods can be tested on the same data set.

In Table 5.2 the result from the de-trending is shown. Both the peak-to-peak and the curve-fitting methods are used in the estimation. Since there are signals from 72 detectors in each measurement the estimated DR is a mean-value of the DRs estimated from all signals. The uncertainties are simply the standard deviation of the estimated DRs.

Clearly, the higher the decay ratio is, the better the de-trending is working. If the decay ratio is low, then the oscillations are mistaken as "noise" by the de-trending algorithm and the de-trending does not work well.

Operating point	reference DR		curve fitting	peak-to-peak
	global	regional		
A	0.30		$0.20 \pm 0.031$	—
D	0.72	0.83	$0.63 \pm 0.20$	$0.77 \pm 0.079$
G	0.99		$0.98 \pm 0.025$	$0.97 \pm 0.027$
H	0.7	0.94	$0.75 \pm 0.094$	$0.79 \pm 0.058$

**Table 5.2:** Decay ratio estimated with the *dmey* wavelet and 200 points of the ACF using *deACF* from measurements taken at BOC-14, Ringhals-1.

In Table 5.3 the results from the estimation of the DR by using the CWT-method are shown. For the cases with dual oscillations (operating points D and H) both of the wavelets estimate the DR to be closer to the regional DR (higher value) than the global DR (lower value). However, the regional DR is slightly underestimated which is in agreement with analysis of the simulations shown in Fig. 5.4.

Operating point	reference DR		mean DR	
	global	regional	<i>cmor1 - 2</i>	<i>cmor1 - 5</i>
A	0.30		$0.433 \pm 0.101$	$0.824 \pm 0.051$
D	0.72	0.83	$0.784 \pm 0.110$	$0.794 \pm 0.043$
G	0.99		$0.992 \pm 0.002$	$0.989 \pm 0.003$
H	0.7	0.94	$0.864 \pm 0.038$	$0.895 \pm 0.015$

**Table 5.3:** Comparison between DR calculated by the CWT-method and reference value. Measured signals from Ringhals-1 BOC-14.

The conclusion from these investigations is that the results from the simulations are in agreement with the results from the analysis of the measurements for both the de-trending and CWT-method. Both methods can improve the estimation of the DR from an ACF under some circumstances. Moreover, the CWT-method can be used to separate two oscillations under some circumstances.

# CHAPTER 6

## CORE BARREL VIBRATIONS IN PWRs

This Chapter is a summary of **Papers IV-VI**, which are treating both the beam-mode and the shell-mode core barrel vibrations in PWRs. The beam-mode vibrations are analysed by trend analysis of measurements made at the three PWR units at Ringhals, R-2, R-3 and R-4. For the shell-mode vibrations, analytical and numerical calculations are performed for both the in-core and ex-core neutron noise. The calculations are compared with measurements from one of the PWR units at Ringhals, R-3.

### 6.1 General description of the core-barrel vibrations

The core barrel of a PWR can vibrate in different modes, the two first mechanical modes and hence the most important ones are the beam-mode and the shell-mode, see Fig. 6.1. The eigenfrequency of the beam-mode is around 8 Hz, this

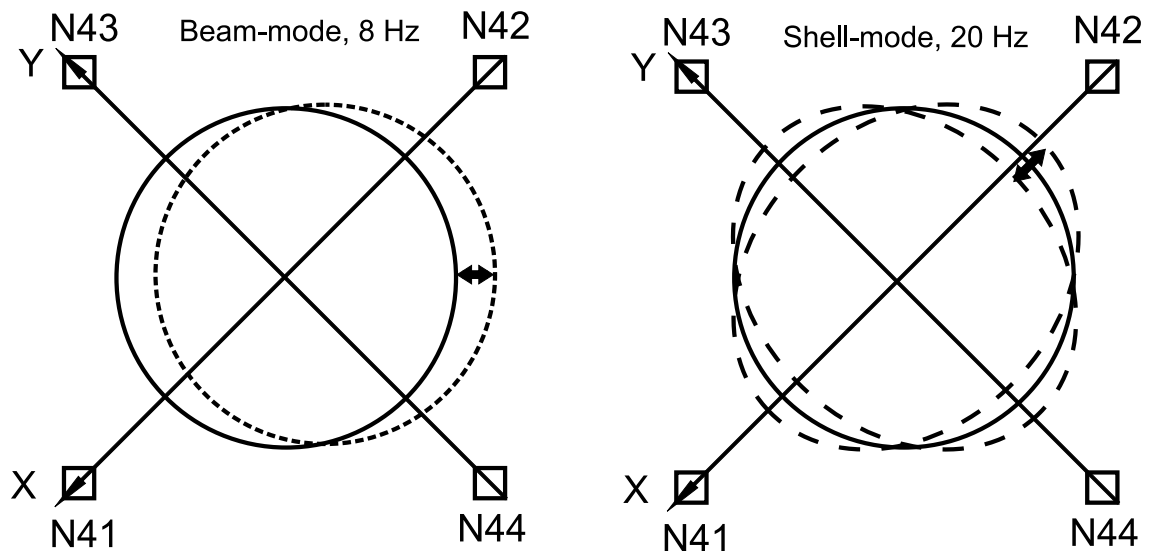


**Figure 6.1:** Illustration of the beam- and shell-mode core barrel vibrations. The ex-core detectors are shown as squares with the numbering N4i, i=1..4.

vibration mode is sometimes also called the pendulum-mode. For the shell-mode

vibration the eigenfrequency is about 20 Hz. As is illustrated in Fig. 6.1 the beam-mode has a 180 degrees rotational symmetry and the shell-mode has 90 degrees rotational symmetry.

In Ref. [42] a procedure was suggested to extract the beam-mode and shell-mode components from the ex-core detector signals as

$$\begin{cases} \mu x(t) = \frac{1}{2}(\delta\phi_1(t) - \delta\phi_2(t)) \\ \mu y(t) = \frac{1}{2}(\delta\phi_3(t) - \delta\phi_4(t)) \end{cases} \quad \text{beam-mode} \quad (6.1)$$

and

$$D(t) = \frac{1}{4}(\delta\phi_1(t) + \delta\phi_2(t) - \delta\phi_3(t) - \delta\phi_4(t)) \quad \text{shell-mode.} \quad (6.2)$$

Here  $\delta\phi_i$  are the signals from ex-core detector  $N4i$ ,  $i = 1..4$ . By using the so-called  $k - \alpha$  model for 2-D random anisotropic vibrations, [42], it is possible to write the auto spectra of the  $x$  and  $y$  components of the beam-mode signal as:

$$\begin{cases} S_{xx}(f) = |S(f)|^2(1 + k \cos 2\alpha), \\ S_{yy}(f) = |S(f)|^2(1 - k \cos 2\alpha). \end{cases} \quad (6.3)$$

Here  $\alpha$  is an azimuthal angle on the 2-D vibration plane of the preferred direction of the vibrations, and  $k$  is the anisotropy parameter ranging from zero to one. Isotropic vibration corresponds to  $k = 0$ , in which case  $\alpha$  is undetermined. From this it is possible to extract the beam-mode spectrum,  $S(f)$  as

$$APSD_{beam}(f) = \frac{S_{xx}(f) + S_{yy}(f)}{2} = |S(f)|^2. \quad (6.4)$$

The shell-mode spectrum is simply calculated from  $D(t)$  in Eq. (6.2).

In Fig. 6.2 a typical spectrum from ex-core detectors is shown, together with the extracted beam-mode and shell-mode spectra. The beam-mode peak at 8 Hz and the shell-mode peak at 20 Hz are clearly visible in the respective spectra. By analysing the spectra one can make conclusions about the behaviour of the beam- and shell-mode vibrations. It is for example possible to monitor the change in vibration amplitude over time for the beam-mode vibration.

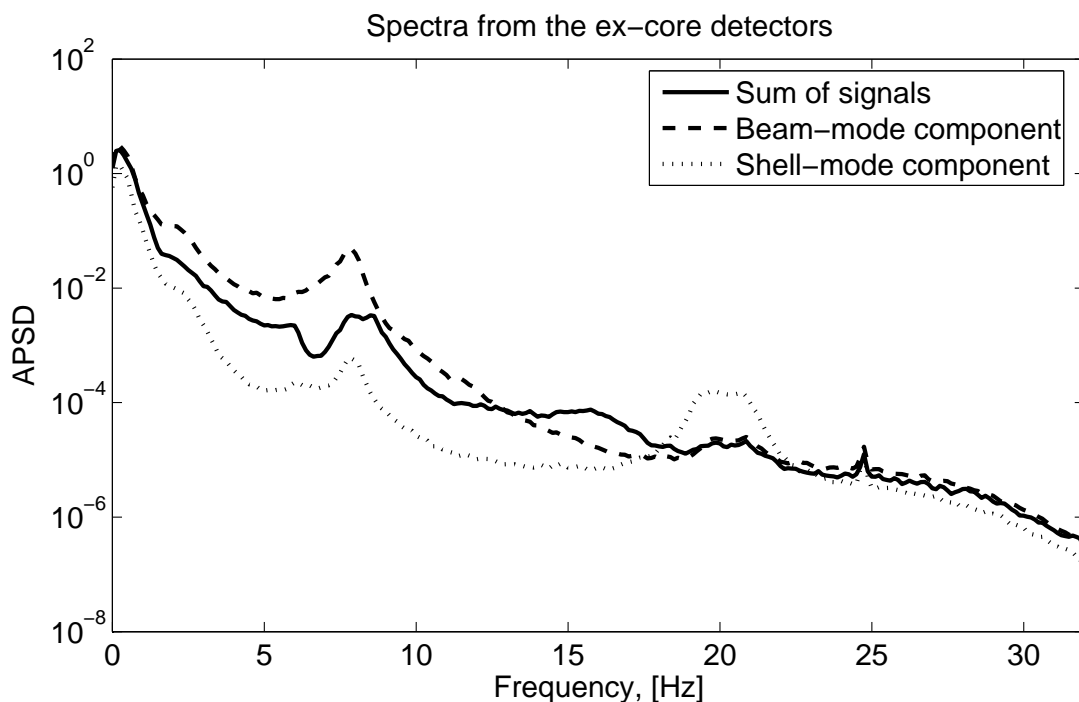


**Figure 6.2:** Spectra from ex-core detector signals from a measurement made at the PWR Ringhals-3. The beam-mode and shell-mode components are shown separately.

## 6.2 Analysis of beam-mode vibrations

In **Paper VI** the beam-mode core barrel vibrations at the units R-2, R-3 and R-4 at the Ringhals NPP are studied. The work in this paper has three different objectives. The first objective is to follow up the development of the vibration characteristics in form of a trend analysis. The trend analysis will be important in the future to monitor the change of vibrations due to the planned power up-rate in Ringhals 2-4. The second objective is to investigate the changes of the properties of the core-barrel vibrations before and after the outage in the summer of 2005 in R-3. During the outage the hold-down springs were replaced to decrease the vibration amplitude. Thirdly a curve-fitting procedure was developed to better extract the information from the vibration peak by removing the influence of the background of the APSD. The curve-fitting also allows to calculate the width of the peak which will give another parameter that can be used for characterising material conditions.

### 6.2.1 Curve-fitting of the data

An analytical expression of a peak can be fitted to the beam-mode vibration peak in the spectrum from measured signals from ex-core detectors. From the fitting it is possible to calculate the amplitude of the peak, the peak frequency and the

width of the peak.

The mechanical vibrations of the core barrel are assumed to follow the oscillations of a linear damped oscillator, driven by a white noise force,  $F(t)$ . Then the time-dependent equation for the induced noise,  $\delta\phi(t)$ , can be written as

$$\delta\ddot{\phi}(t) + 2D\omega_0\delta\dot{\phi}(t) + \omega_0^2\delta\phi(t) = F(t). \quad (6.5)$$

By performing a Fourier transform, using the Wiener-Khinchin theorem and the fact that the APSD from a white noise is a constant, [35], one ends up with the following expression for the APSD of the neutron noise:

$$APSD_{\delta\phi}(f) = \frac{C^2}{(f^2 - f_0^2)^2 + 4D^2 f^2 f_0^2}. \quad (6.6)$$

Here,  $f_0$  is the eigenfrequency,  $D$  is the damping coefficient and  $C$  is a parameter proportional to the vibration amplitude. These three parameters are used as the fitting parameters in a least-square fitting. However, inspection of the measured spectra shows that the peaks are superimposed on a background that decreases with increasing frequency quite markedly. Hence one can expect to get a better estimate of the parameters if the actual fitting is done by including linear and constant terms. Since the beam-mode peak is at around 8 Hz, the fitting is applied to the spectrum between 4 to 10 Hz. Once the parameters have been estimated it is possible to calculate the peak frequency,  $f_{peak}$ , the full width at half maximum (FWHM) and the peak height,  $A_{peak}$ , according to the following expressions:

$$\begin{aligned} f_{peak} &= \sqrt{f_0^2(1 - 2D^2)}, \\ f_{FWHM} &= f_0\sqrt{(1 - 2D^2) \pm 2D\sqrt{1 - D^2}}, \\ FWHM &= \Delta f_{FWHM}, \\ A_{peak} &= \frac{C^2}{4f_0^4 D^2 (1 - D^2)}. \end{aligned} \quad (6.7)$$

### 6.2.2 Trend analysis

The trend analysis consists of measurements from 1991, 1993, 1994, 1998, 2005 and 2006 from Ringhals 2-4. The results from the parameter estimation by curve-fitting are shown in Fig 6.3. It can be concluded that the vibration amplitudes have increased for all units during the interval 1991 to spring 2005. After the re-fueling in 2005 the amplitude decreased for both unit 3 and 4, even though only unit 3 replaced its hold-down spring. However, in 2006 the amplitude was found to be almost back at the same level as before the re-fueling in 2005. This behaviour is not fully understood but it points to the fact that there is an increase of

the vibration peaks in the spectra during the cycle, which is repeated periodically for the consecutive cycles. Work is going on to further investigate the problem, i.e. more measurements are under way to find out if it is a real increase of the vibration amplitude, or only that of the scaling factor. The influence of the change of the boron concentration during the cycle on the amplitude could be one reason for this behaviour, since the boron concentration is effecting the leakage of neutrons from the core to ex-core detectors.

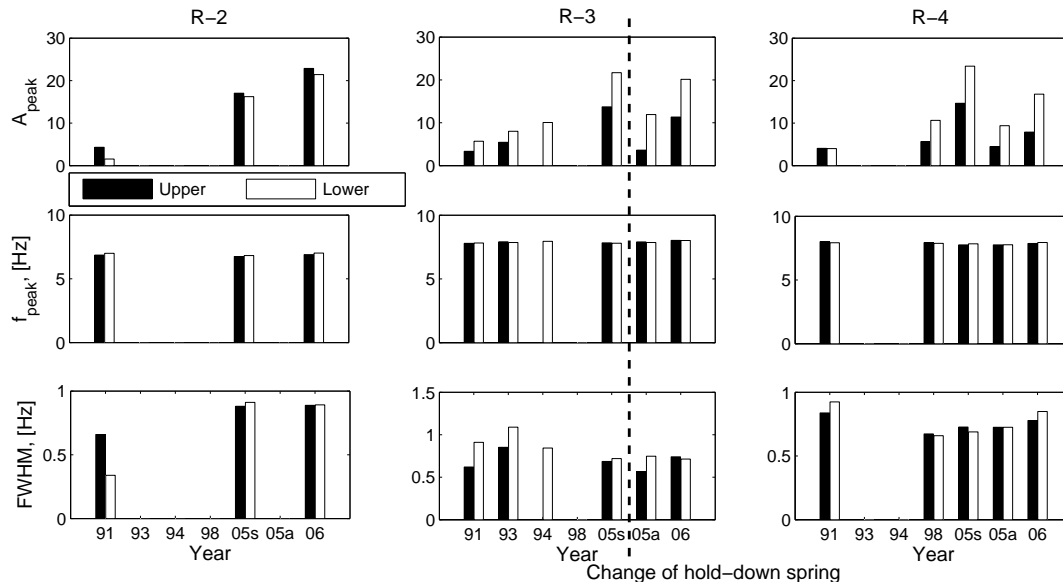


**Figure 6.3:** Results from the parameter estimation. 05s denotes spring in 2005 and 05a denotes fall, after re-fueling, in 2005.

## 6.3 Shell-mode vibrations

The shell-mode core barrel vibrations are treated in **Papers IV** and **V**. There is some overlap between the two papers, but **Paper IV** has a more detailed mathematical description whereas in **Paper V** the results from one measurement are reported on. This Section will be a summary of both papers.

In earlier work it has been noticed that the shell-mode vibrations may lead not only to ex-core neutron noise but also to in-core noise which can be used to analyse the vibrations [23]. When analysing the shell-mode vibrations, the use of in-core noise could be especially important in Westinghouse reactors, since all the ex-core detectors carry the same information, due to the  $90^\circ$  spacing. Therefore, the amplitude and the direction of the vibrations cannot be determined at the same time.

For this reason, in-core detectors were included in the analysis of the shell-mode vibrations within a research project in cooperation with the Ringhals NPP, [23]. However, the small number of in-core detectors hindered confirmation of

the theory as well as use of the result. In order to have consistent interpretations it was necessary to assume that noise from in-core and ex-core detectors lying on the same azimuthal position have opposite phase. To better model and calculate the in-core and ex-core neutron noise, a 1-dimensional analytical calculation of the noise will be performed in this Section. A comparison between the analytical results and the results from a numerical simulator, developed at the department, [43], is also made. Finally, the calculations will be compared with a measurement.

### 6.3.1 Description of the model

A 1-dimensional 2-group 2-region model is used with the boundary of the core set to  $b = 161.25$  cm and the boundary of the reflector set to  $a = 279.5$  cm, the size of the PWR Ringhals-4. The reactor parameters, e.g. cross-sections, are also calculated from the material data of the Ringhals-4 core, using the in-core fuel management code SIMULATE-3 (homogenisation from 3-D to 1-D). The fluxes are assumed to be symmetrical around the centre of the core.

Since a 1-D 2-group 2-region diffusion model is used, there are two diffusion equations in the core region,  $c$ , and two diffusion equations in the reflector region,  $r$ , for the static fluxes. One in each region for the fast flux, 1, and one for the thermal flux, 2.

$$\left\{ \begin{array}{l} D_1^c \frac{d^2}{dx^2} \phi_1^c(x) - (\Sigma_{a,1}^c + \Sigma_R^c) \phi_1^c(x) + \frac{1}{k} (\nu \Sigma_{f,2}^c \phi_2^c(x) + \nu \Sigma_{f,1}^c \phi_1^c(x)) = 0 \\ D_2^c \frac{d^2}{dx^2} \phi_2^c(x) - \Sigma_{a,2}^c \phi_2^c(x) + \Sigma_R^c \phi_1^c(x) = 0 \end{array} \right. \quad \text{Core (6.8)}$$

$$\left\{ \begin{array}{l} D_1^r \frac{d^2}{dx^2} \phi_1^r(x) - (\Sigma_{a,1}^r + \Sigma_R^r) \phi_1^r(x) = 0 \\ D_2^r \frac{d^2}{dx^2} \phi_2^r(x) - \Sigma_{a,2}^r \phi_2^r(x) + \Sigma_R^r \phi_1^r(x) = 0 \end{array} \right. \quad \text{Reflector (6.9)}$$

The cross-section notations are standard, i.e.  $a$  stands for absorption,  $f$  for fission and  $R$  for removal (scattering) from the fast group to the thermal. All the cross-sections and the diffusion coefficients are assumed to be constant within each region. The first step in calculating the phase behaviour of the noise, induced by shell-mode vibrations, is to solve the static equations (k-eigenvalue equations). That is easily done by using the symmetry, the interface (continuous fluxes and currents) and boundary (zero flux) conditions. Once a normalised and critical solution of the static fluxes is obtained, the noise can be calculated. Criticality is achieved by adjusting the fission cross-sections.

### 6.3.2 Space-frequency dependent solution

The noise from the shell-mode vibration is calculated by writing the static cross-sections, in both the core and reflector region, as:

$$\Sigma(x) = \{1 - H(x - b)\}\Sigma^c + H(x - b)\Sigma^r. \quad (6.10)$$

Here  $H(x)$  is the unit step function. A similar symmetrical expression is valid for  $x < 0$ . With a vibrating boundary  $b = b + \epsilon(t)$ , the time-dependent cross-sections are written as

$$\Sigma(x, t) = \{1 - H(x - b - \epsilon(t))\}\Sigma^c + H(x - b - \epsilon(t))\Sigma^r. \quad (6.11)$$

Splitting the cross-sections into a static and a time-dependent part and making a Taylor expansion, assuming a small vibration, gives:

$$\Sigma(x, t) \approx \Sigma(x) + \epsilon(t)\delta(x - b)\delta\Sigma, \quad \delta\Sigma = \Sigma^c - \Sigma^r. \quad (6.12)$$

By using this expression for the time-dependent cross-sections, linearise the dynamic equations for the flux and the precursors and removing the static equations, the equations for the neutron noise, in the frequency domain, can be written in a condensed form as

$$\begin{aligned} \hat{L}^c(x, \omega)\overrightarrow{\delta\phi}^c &= \epsilon(\omega)\delta(x - b)\hat{S}(x)\overrightarrow{\phi}^{static}(x), \\ \hat{L}^r(x, \omega)\overrightarrow{\delta\phi}^r &= \epsilon(\omega)\delta(x - b)\hat{S}(x)\overrightarrow{\phi}^{static}(x). \end{aligned} \quad (6.13)$$

Here the vector fluxes in respective regions represent both the fast and thermal fluxes. The matrices  $\hat{S}$  and  $\hat{L}$  are given in **Paper IV**. The perturbation at  $x = -b$  is taken into account by claiming that the noise is an even function of  $x$ . On the right hand side in Eq. (6.13) it is not indicated if the static flux is taken from the core or the reflector. But since they are equal at the interface,  $x = b$ , it does not matter which one is used. The solution to Eq. (6.13), taking into account the symmetry of the solution, is given as:

$$\begin{cases} \overrightarrow{\delta\phi}^r(x, \omega) = \tilde{A}_3 \begin{bmatrix} 1 \\ \tilde{C}_\kappa(\omega) \end{bmatrix} \frac{\sinh(\tilde{\kappa}_1(|x| - a))}{\sinh(\tilde{\kappa}_1(b - a))} + \tilde{A}_4 \begin{bmatrix} 1 \\ 0 \end{bmatrix} \frac{\sinh(\tilde{\kappa}_2(|x| - a))}{\sinh(\tilde{\kappa}_2(b - a))} \\ \overrightarrow{\delta\phi}^c(x, \omega) = \tilde{A}_1 \begin{bmatrix} 1 \\ \tilde{C}_\mu(\omega) \end{bmatrix} \cos(\tilde{\mu}x) + \tilde{A}_2 \begin{bmatrix} 1 \\ \tilde{C}_\eta(\omega) \end{bmatrix} \frac{\cosh(\tilde{\eta}x)}{\cosh(\tilde{\eta}b)} \end{cases} \quad (6.14)$$

The boundary conditions of zero fluxes at the extrapolated boundaries  $x \pm a$  have been used and the coefficients,  $\tilde{A}$ , are determined from the following matrix equation:

$$\overrightarrow{A} = \epsilon(\omega)\hat{M}^{-1} \begin{bmatrix} 0 \\ 0 \\ S_{11}\phi_1^c(b) + S_{12}\phi_2^c(b) \\ S_{21}\phi_1^c(b) + S_{22}\phi_2^c(b) \end{bmatrix}. \quad (6.15)$$

The matrix  $\hat{M}$  consists of the interface conditions and is given in **Paper IV**. Hence, now the neutron noise induced by the shell-mode core barrel vibration, in both the core and reflector is readily calculated.

The neutron noise has also been calculated by using a numerical simulator developed at our department [43]. Hence, the induced neutron noise is calculated both analytically and numerically.

### 6.3.3 Results

The thermal noise from the space-frequency dependent analytical solution, Eq. (6.14), and from the numerical simulator is shown in Fig. 6.4. The phase behaviour is very much the same in both cases, but there is some deviation in the absolute values. The difference in the absolute value is probably due to the fact that the numerical simulator uses nodes instead of continuous space. Hence, the perturbation at the boundary is spread out over a whole node rather than existing in a point (Dirac-delta function). The good agreement between the two methods is a verification of the accuracy of the calculations. The most interesting feature is

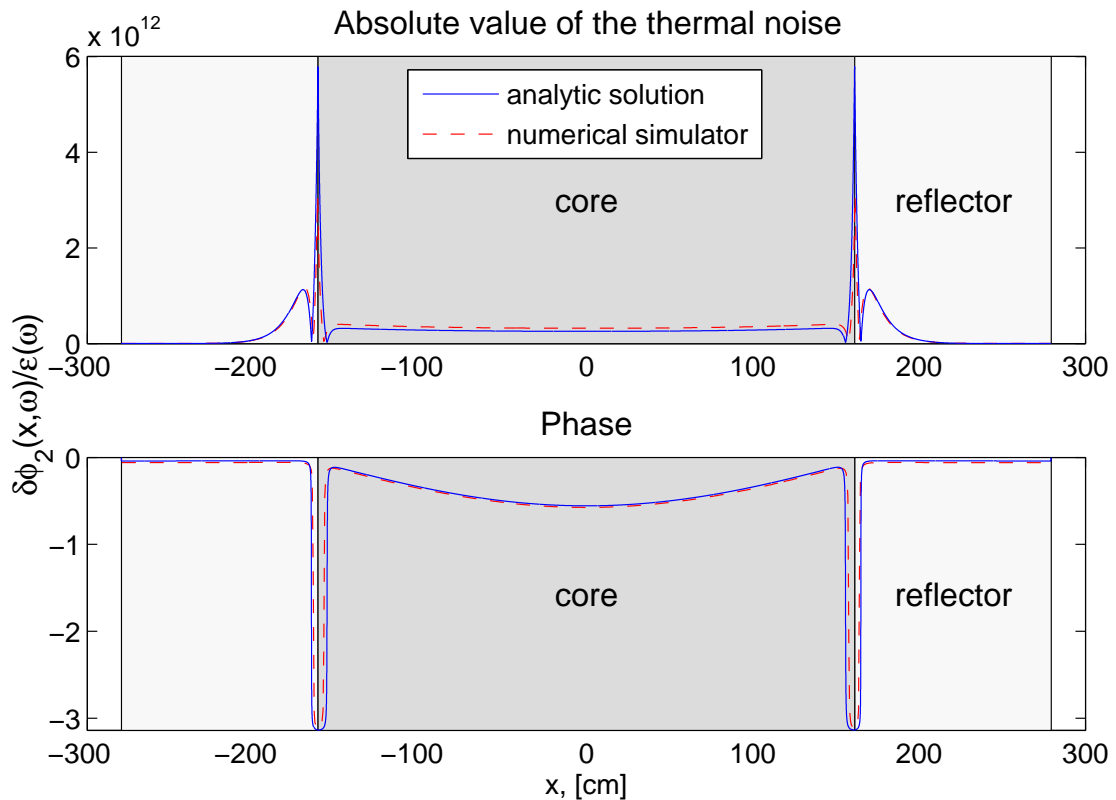


**Figure 6.4:** Absolute value in upper figure and phase in lower figure of the thermal noise from shell-mode core-barrel vibrations. The dashed line is calculated with the numerical simulator and the full line represents the analytical solution.

the large local out-of-phase behaviour close to the boundary, where the noise also has a large absolute value. The out-of-phase behaviour means that the thermal noise close to the interface has an opposite value as in the rest of the system, i.e. a decrease of the flux at the interface and an increase in the rest of the reactor. The global increase is due to the increase in reactivity,  $\delta\rho > 0$ . The decrease at the interface arises from the fact that fission material is added into the reflector region giving more absorption of thermal neutrons, and moderator material is removed, causing less slowing down of fast neutrons to thermal ones. Hence, the local decrease of the thermal flux in the calculations can be explained.

In Fig. 6.5 a measurement made at Ringhals-3 in March 2005 is compared with the analytical solution of the in-core thermal neutron noise. Even though the calculations have been performed with cross-section data from Ringhals-4, it is possible to make a quantitative comparison between calculations and measurements since the two units are similar in construction. Unfortunately only five in-core detectors can be used at the same time. Hence, the resolution of the measurement in the radial direction is rather poor.

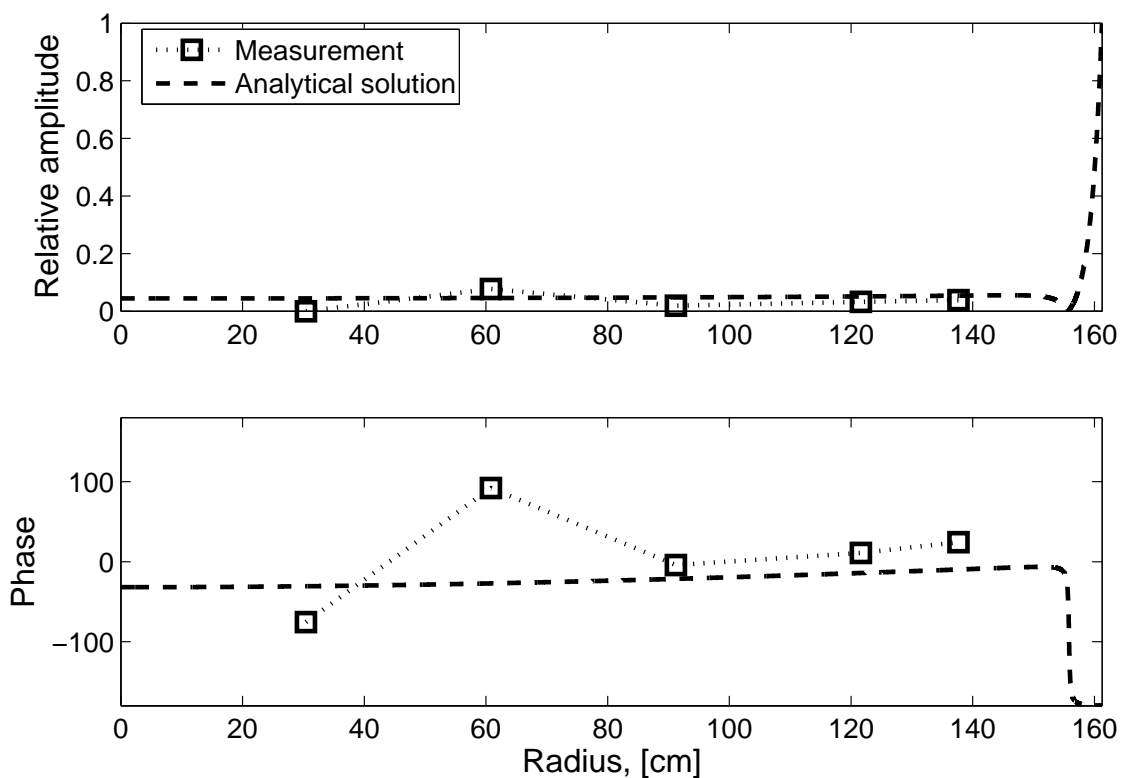


**Figure 6.5:** Comparison between in-core measurement and analytical calculation.

The analysis of the measurements shows that it is not possible to detect the large local component of induced in-core noise. This is due to the fact that it is not possible to place a detector close enough to the boundary where the local

component is present. Hence, it is unfortunately not possible to use the in-core noise when classifying the shell-mode core-barrel vibrations in the PWRs at Ringhals.

# CHAPTER 7

## THE BREAK-FREQUENCY METHOD

The final part of this thesis is a summary of **Paper VII** which deals with the break-frequency method for reactivity estimation. The validity of different methods for determining the reactivity in subcritical systems has been studied in 1-D one-group models and the methods are often based on the point-kinetic approximation. However, in 2-D, 2-group reflected systems much less is known about both the validity of methods for determining the reactivity and about the point-kinetic approximation. In this Chapter the break-frequency method, [44], will be used to estimate the reactivity in subcritical systems such as power reactors during loading. The method estimates the so-called break-frequency from the reactor transfer function and from the break-frequency, the reactivity can be calculated. The advantage with the break-frequency method compared to other reactivity estimation methods is that there is no need for an external source. Instead an inherent source in the reactor can be used, e.g. the neutrons from decay of fission products.

### 7.1 Derivation of the neutron noise

The system used in this study is a 2-group subcritical system in the diffusion approximation including one group of delayed neutrons with a source in the fast group. The system will be used to model a power reactor in two dimensions. The starting point is the time-dependent diffusion equations for the fast group:

$$\begin{aligned} \frac{1}{v_1} \frac{\partial \phi_1}{\partial t}(\mathbf{r}, t) = \nabla \cdot [D_1(\mathbf{r}) \nabla \phi_1(\mathbf{r}, t)] + \nu \Sigma_{f,2}(\mathbf{r})(1 - \beta_{eff}) \phi_2(\mathbf{r}, t) \\ + \lambda C(\mathbf{r}, t) + \left[ \nu \Sigma_{f,1}(\mathbf{r})(1 - \beta_{eff}) - \Sigma_{a,1}(\mathbf{r}) - \Sigma_{rem}(\mathbf{r}) \right] \phi_1(\mathbf{r}, t) + S_1(\mathbf{r}, t), \end{aligned} \quad (7.1)$$

for the thermal group:

$$\frac{1}{v_2} \frac{\partial \phi_2}{\partial t}(\mathbf{r}, t) = \nabla \cdot [D_2(\mathbf{r}) \nabla \phi_2(\mathbf{r}, t)] - \Sigma_{a,2}(\mathbf{r}) \phi_2(\mathbf{r}, t) + \Sigma_{rem}(\mathbf{r}) \phi_1(\mathbf{r}, t) \quad (7.2)$$

and for the precursor density:

$$\frac{\partial C}{\partial t}(\mathbf{r}, t) = \beta_{eff} \left[ \nu \Sigma_{f,1}(\mathbf{r}) \phi_1(\mathbf{r}, t) + \Sigma_{f,2}(\mathbf{r}) \phi_2(\mathbf{r}, t) \right] - \lambda C(\mathbf{r}, t). \quad (7.3)$$

Here subscript 1 denotes the fast group and subscript 2 the thermal group. All quantities have their usual meaning. Hence,  $\phi_1(\mathbf{r}, t)$  is the fast flux,  $\Sigma_x(\mathbf{r})$  is the cross-section corresponding to reaction type  $x$  and  $S_1(\mathbf{r}, t)$  is the time-dependent source in the fast group.

In order to solve these equations it is first assumed that it is possible to split the flux into an amplitude factor,  $P(t)$ , and a shape function,  $\psi(\mathbf{r}, t)$  with an additional normalisation condition due to the new function,  $\psi$ , which is introduced [45]. Then, all the time-dependent terms are divided into their mean values,  $X_0(\mathbf{r})$  and a fluctuating part,  $\delta X(\mathbf{r}, t)$ . If second-order terms are neglected, the neutron noise can be written as:

$$\begin{bmatrix} \delta\phi_1(\mathbf{r}, t) \\ \delta\phi_2(\mathbf{r}, t) \end{bmatrix} = \begin{bmatrix} \delta\phi_1^{pk}(\mathbf{r}, t) \\ \delta\phi_2^{pk}(\mathbf{r}, t) \end{bmatrix} + P_0 \times \begin{bmatrix} \delta\psi_1(\mathbf{r}, t) \\ \delta\psi_2(\mathbf{r}, t) \end{bmatrix}. \quad (7.4)$$

Here the point-kinetic term is expressed as:

$$\begin{bmatrix} \delta\phi_1^{pk}(\mathbf{r}, t) \\ \delta\phi_2^{pk}(\mathbf{r}, t) \end{bmatrix} = \frac{\delta P(t)}{P_0} \times \begin{bmatrix} \phi_1(\mathbf{r}) \\ \phi_2(\mathbf{r}) \end{bmatrix}. \quad (7.5)$$

Hence, the point-kinetic term has the same spatial dependence as the static flux,  $\phi_i(\mathbf{r})$  ( $i = 1, 2$ ), of the subcritical system driven by a source.

## 7.2 Definition of the source

Before the neutron noise is calculated, the properties of the source term need to be specified. Since a power reactor core during loading conditions is modelled, it is assumed that there is an inherent source present in the system. The inherent source neutrons are assumed to be due to the decay of fission products and transuranium elements which are produced during the static operation of the reactor. Hence, the simple assumption is made that the fission products, and thus the source, are distributed according to the static critical thermal flux,  $\phi_2^{cr,c}(\mathbf{r})$ , in the core. Furthermore it is assumed that all the source neutrons are born in the fast group. Hence, the source is assumed to have the following properties:

$$S_1(\mathbf{r}, t) = \phi_2^{cr,c}(\mathbf{r}) + \delta S_1(\mathbf{r}, t). \quad (7.6)$$

where  $\delta S_1(\mathbf{r}, t)$  has random white noise properties which cannot be given explicitly in the space-time domain.

However, it is possible to form the cross-power spectral density (CPSD) of the source fluctuation  $\delta S_1(\mathbf{r}, t)$ . First, one assumes that the space-time correlations can be factorised into a temporal and a spatial component, where the temporal component is given by  $\delta(\tau)$ . For the spatial part, one also assumes that it can be further factorised into a fast decaying component as a function of the distance between two space points,  $e^{-\frac{|\mathbf{r}-\mathbf{r}'|}{l}}$ , and a much slower varying shape function,  $\sigma^2(\mathbf{r})$ .

A more detailed derivation of the CPSD for such a random white noise can be found in Ref. [46] where the final CPSD is given as

$$\begin{aligned} CPSD_{\delta S_1}(\mathbf{r}', \mathbf{r}'', \omega) &= \langle \delta S_1^*(\mathbf{r}', \omega) \delta S_1(\mathbf{r}'', \omega) \rangle \simeq \\ &\sigma^2(\mathbf{r}) e^{\frac{|\mathbf{r}-\mathbf{r}'|}{l}} \simeq \sigma^2(\mathbf{r}) \delta(\mathbf{r}' - \mathbf{r}'') \end{aligned} \quad (7.7)$$

with

$$\mathbf{r} = \frac{\mathbf{r}' + \mathbf{r}''}{2}. \quad (7.8)$$

In the last step in the above equation it is assumed that the noise source is totally uncorrelated in space, hence  $e^{\frac{|\mathbf{r}-\mathbf{r}'|}{l}}$  is replaced with a  $\delta$ -function. As mentioned above we assume the noise source to be distributed as the critical thermal flux, hence

$$\sigma^2(\mathbf{r}) \sim (\phi_2^{cr,c})^2(\mathbf{r}). \quad (7.9)$$

Now, when the properties of the source are known, it is possible to calculate the neutron noise in the frequency domain.

## 7.3 Neutron noise in the frequency domain

The neutron noise can be derived in the frequency domain by subtracting the static solution from the dynamic equations, Eqs. (7.1-7.3), and performing a temporal Fourier transform. Next the expression for the precursors is inserted into the two equations for the flux. If all this is done one ends up with the following expression for the neutron noise in the frequency domain

$$[\nabla \cdot \bar{\bar{D}}(\mathbf{r}) \nabla + \bar{\bar{\Sigma}}_{dyn}(\mathbf{r}, \omega)] \times \begin{bmatrix} \delta \phi_1(\mathbf{r}, \omega) \\ \delta \phi_2(\mathbf{r}, \omega) \end{bmatrix} = - \begin{bmatrix} \delta S_1(\mathbf{r}, \omega) \\ 0 \end{bmatrix} \quad (7.10)$$

with

$$\bar{\bar{\Sigma}}_{dyn}(\mathbf{r}) = \begin{bmatrix} -\Sigma_1(\mathbf{r}, \omega) & \nu \Sigma_{f,2}(\mathbf{r}) \times \left(1 - \frac{i\omega \beta_{eff}}{i\omega + \lambda}\right) \\ \Sigma_{rem}(\mathbf{r}) & -\left(\Sigma_{a,2}(\mathbf{r}) + \frac{i\omega}{v_2}\right) \end{bmatrix} \quad (7.11)$$

and

$$\Sigma_1(\mathbf{r}, \omega) = \Sigma_{a,1}(\mathbf{r}) + \frac{i\omega}{v_1} + \Sigma_{rem}(\mathbf{r}) - \nu \Sigma_{f,1}(\mathbf{r}) \times \left(1 - \frac{i\omega \beta_{eff}}{i\omega + \lambda}\right). \quad (7.12)$$

The numerical noise simulator used in Chapter 6 is able to numerically solve this matrix-equation, on a nodal grid, for the neutron noise, [43]. However, it is only possible to solve the matrix-equation if the temporal Fourier transform of the

noise source can be given explicitly which is not the case here. Thus, the CPSD properties of the source need to be utilised.

In order to solve Eq. (7.10) and utilising the CPSD properties of the source, the technique of Green's function is used. For a system of differential equations the Green's operator,  $\mathbf{G}$ , is used and the solution to Eq. (7.10) can formally be written as

$$\begin{bmatrix} \delta\phi_1(\mathbf{r}, \omega) \\ \delta\phi_2(\mathbf{r}, \omega) \end{bmatrix} = \int \mathbf{G}(\mathbf{r}, \mathbf{r}', \omega) \times \begin{bmatrix} \delta S_1(\mathbf{r}', \omega) \\ 0 \end{bmatrix} d\mathbf{r}'. \quad (7.13)$$

Here  $\mathbf{G}$  is the solution of:

$$\mathbf{M} \times \mathbf{G} = -\mathbf{I}. \quad (7.14)$$

Here  $\mathbf{I}$  is the identity matrix and  $\mathbf{M}$  is the matrix on the left hand side in Eq. (7.10). By using Eq. (7.13) and the CPSD properties of the source, it is possible to calculate the APSD of the neutron noise as

$$\begin{bmatrix} APSD_{\delta\phi_1}(\mathbf{r}, \omega) \\ APSD_{\delta\phi_2}(\mathbf{r}, \omega) \end{bmatrix} = \begin{bmatrix} \delta\phi_1^*(\mathbf{r}, \omega)\delta\phi_1(\mathbf{r}, \omega) \\ \delta\phi_2^*(\mathbf{r}, \omega)\delta\phi_2(\mathbf{r}, \omega) \end{bmatrix} = \begin{bmatrix} \int G_{11}^*(\mathbf{r}, \mathbf{r}', \omega)G_{11}(\mathbf{r}, \mathbf{r}', \omega)(\phi_2^{cr,c})^2(\mathbf{r}') d\mathbf{r}' \\ \int G_{12}^*(\mathbf{r}, \mathbf{r}', \omega)G_{12}(\mathbf{r}, \mathbf{r}', \omega)(\phi_2^{cr,c})^2(\mathbf{r}') d\mathbf{r}' \end{bmatrix}. \quad (7.15)$$

The noise simulator is also able to calculate the Green's function and the static and adjoint static flux needed for the calculation of the APSD. Hence, this tool is used to numerically calculate the APSD of the neutron noise, i.e. Eq. (7.15).

In **Paper VII** an analytical expression for the point-kinetic APSD is also derived as:

$$\begin{bmatrix} APSD_{\delta\phi_1^{pk}}(\mathbf{r}, \omega) \\ APSD_{\delta\phi_2^{pk}}(\mathbf{r}, \omega) \end{bmatrix} = \left( \frac{\rho_0}{G_0^{-1}(\omega) - \rho_0} \right)^* \left( \frac{\rho_0}{G_0^{-1}(\omega) - \rho_0} \right) \begin{bmatrix} \phi_1^2(\mathbf{r}) \\ \phi_2^2(\mathbf{r}) \end{bmatrix}. \quad (7.16)$$

Here  $G_0 = 1/(i\omega(\Lambda_0 + \beta_{eff}/(i\omega + \lambda)))$  is the zero-power reactor transfer function. Hence, the analytical point-kinetic APSD can be compared with the APSD calculated for different detector positions in the system by the numerical simulator. From the numerically calculated APSD the reactivity can be estimated by using the break-frequency method which will be described in the following Section.

## 7.4 Break-frequency method

The frequency-dependence of the APSD for the point-kinetic part is governed by

$$G_\rho(\omega) = \frac{1}{G_0^{-1}(\omega) - \rho_0} = \frac{1}{i\omega\left(\Lambda_0 + \frac{\beta_{eff}}{i\omega + \lambda}\right) - \rho_0} \quad (7.17)$$

according to Eq. (7.16). At high frequencies where  $\omega \gg \lambda$  one can write

$$G_\rho(\omega) \approx \frac{1}{i\omega\Lambda_0 + \beta_{eff} - \rho_0} = \frac{\Lambda_0}{i\omega + \frac{\beta_{eff} - \rho_0}{\Lambda_0}} = \frac{\Lambda_0}{i\omega + \omega_{break}} \quad (7.18)$$

Here  $\omega_{break} = (\beta_{eff} - \rho_0)/\Lambda_0$  is the so-called break-frequency and if one can estimate the break-frequency the reactivity can be estimated as

$$\rho_0 = \beta_{eff} - \omega_{break}\Lambda_0. \quad (7.19)$$

Both  $\beta_{eff}$  and  $\Lambda_0$  are given by the material properties of the system.

It is possible to get an estimate of the break-frequency by using curve-fitting methods. If  $\sqrt{APSD_{\delta\phi_2}(\mathbf{r}, \omega)/\phi_2^2(\mathbf{r})}$  is plotted against the frequency, one can fit  $H(\omega) = |A/(\omega_{break} + i\omega)|$  to the high frequency part of the curve and get a good estimate of the break-frequency, if the system is behaving according to point-kinetics, see Fig. 7.1 for illustration.

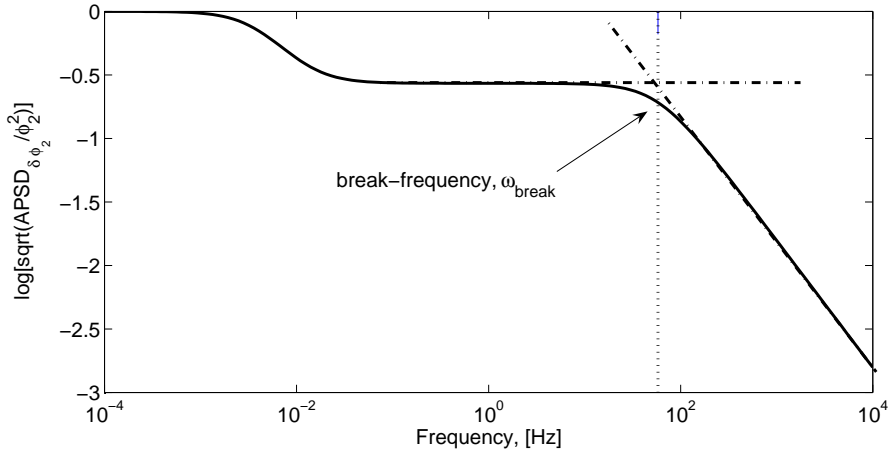


**Figure 7.1:** Illustration of the break-frequency method for reactivity estimation from the reactor transfer function.

## 7.5 Definition of the system

The diffusion approximation is used in a 2-group, 2-region system in 2 dimensions. This type of system can be handled numerically by the noise simulator. The nodalisation of the system used by the noise simulator is shown in Fig. 7.2. The size of the system is 32 by 32 nodes, each node is 10.75 cm wide. The input data for the noise simulator are taken from a SIMULATE-3 model of a conventional light water PWR.

Also a smaller system with 1/3 of the size of the above described system is modelled in order to investigate if the system size is effecting the accuracy of the estimation of the reactivity.

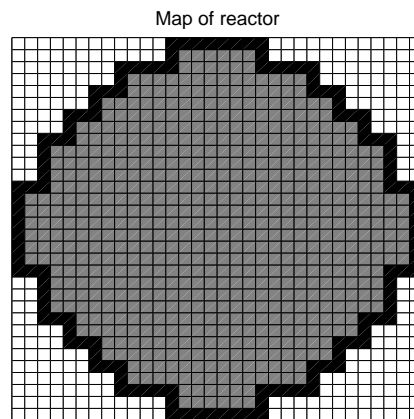


**Figure 7.2:** Nodal map of the system used by the noise-simulator. Gray squares denotes core nodes and black square denotes reflector nodes.

## 7.6 Estimation of the reactivity

By using the system described above, the break-frequency method was used to estimate the reactivity from the APSD of the neutron noise. In order to investigate the validity of the break-frequency method for different subcriticalities the subcriticality of the system is modified by adjusting the fission cross-section. Four different subcriticalities were investigated, namely, -200 pcm, -1395 pcm, -6205 pcm and -12278 pcm. These subcriticalities correspond to the following values of  $k_0$ : 0.99801, 0.98624, 0.94158 and 0.89065 respectively.

To map the radial behaviour, 16 different detector positions placed radially in the system are modelled by simply taking the calculated thermal neutron noise at the corresponding nodal position as an estimate of the detector signal. In each position the reactivity is estimated by using the break-frequency method.

In Fig. 7.3 the results from the estimation of the reactivity with the break-frequency method are shown for the large system corresponding to a conventional power reactor and the smaller system with 1/3 of the size. For the large system in a), it can be noted that at some point in between the centre and the reflector the estimation is almost perfect. However, this position is changing with the reactivity. Hence, it is not possible to use this position for placing a detector for determination of the reactivity.

The quantitative results show that the break-frequency method supplies relatively rough estimates of the subcritical reactivity when used in large power reactors during loading conditions. One reason for this is the fact that the point-kinetic approximation is not valid in large loosely coupled systems. However, in a large part of the core, it overestimates the reactivity, i.e. it yields conservative values, which is advantageous from the safety point of view. For the smaller system the result is appreciably better, even if the desired accuracy is higher than

what is achieved.

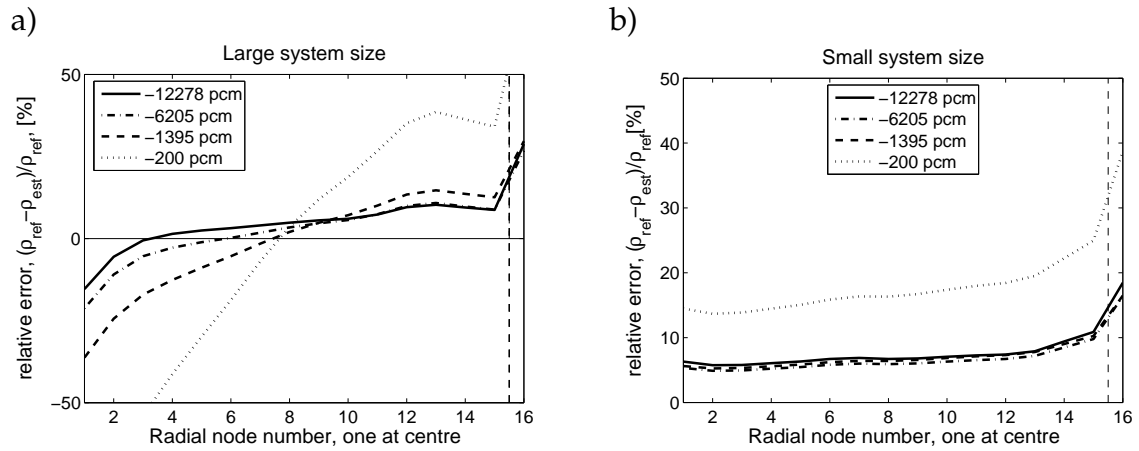


**Figure 7.3:** Relative error of the estimation of the reactivity using the break-frequency method. In a) the result for the large system is shown and in b) the result for the small system is shown. Node 16 is in the reflector and node 1 is at the centre of the core.



## CHAPTER 8

### CONCLUDING REMARKS

In this thesis five different research projects were treated and the results and conclusions of each area are found in each Chapter. Here some of the conclusions will be summarised and also some future plans for the research areas will be touched upon.

- The major finding of the wavelet pre-processing and neural network method for the identification of two-phase flow regimes is that the time of the training procedure is reduced with a factor of 100 if wavelet pre-processing is used.
- Concerning the detector tube impacting, all three methods used (spectral, discrete and continuous wavelet) are in agreement with each other. The validity of the spectral method was also investigated by a visual inspection. A fifth measurement was already made in 2006 and the analysis is under way. Hopefully there will also be a visual inspection in the autumn of 2007 where the tubes to be inspected will be based on the analysis made in this thesis. The new visual inspections are of major importance for the validation of the methods.
- The investigation of using wavelet techniques to improve the estimation of the decay ratio from ACF lead to the conclusion that the results from the simulations are to some extent in agreement with the results from the analysis of measurements taken at the BWR Ringhals-1. Both methods can improve the estimation of the DR from an ACF under some circumstances. However, the improvement is not universally valid. The CWT-method shows some promising results for separating two processes with different frequencies.
- Regarding the core-barrel vibrations, it is shown that the in-core neutron noise cannot be used in order to classify the shell-mode vibrations due to practical reasons. What regards the beam-mode vibrations, new measurements have already been made and more measurements are planned in the near future. An investigation on the behaviour of the amplitude change during the fuel-cycle is under way and hopefully, a numerical model of the reactor can be used to calculate the influence of the boron concentration on

the amplitude as well. The ultimate goal is to calculate a conversion factor between the detector signal and the real movement in *mm* of the core-barrel.

- The only topic within this thesis which has not been tested on measured data is the use of the break-frequency method for determination of the reactivity of a subcritical system. Here the main finding is that the break-frequency method has a relatively large, but conservative inaccuracy in the estimation of the reactivity for a system corresponding to a PWR under loading conditions.

The trouble with choosing the "correct" wavelet to use for a certain problem has been experienced in this thesis, as many other researchers also have reported on. Even if different wavelets seem to have the same features and properties they can generate quite different results.

One final remark about the work done in this thesis is that whenever it is possible one should always try to apply the developed algorithms and methods on real signals and data. Even though everything seems to work perfectly fine on simulations and in theory, the reality is something different! In this respect the cooperation with the Ringhals plant has been of major importance. Both since they have provided us with measurements and interesting comments on the work. But, also since we sometimes even were allowed to suggest measurement set-up which could be performed in the operating reactors to test our models. The cooperation between the academic world and the industry is very important for the development of research. Both since the developed methods can be tested and implemented in a realistic environment and also because problems which are unknown for the academic world can be emphasised by the industry.

---

## ACKNOWLEDGEMENTS

First of all I would like to thank my supervisor Professor Imre Pázsit for his support and technical knowledge about everything in reactor physics and noise diagnostics. He is also thanked for his endless supply of stories about everything from his first trip to Sweden to why Hungary lost the World Cup final in 1954. Associate Professor Christophe Demazière is acknowledged for always answering my endless questions about reactor physics and for the work with our joint papers. I would also like to thank my other co-authors to different papers Dr. Senada Avdic, Dr. Vasily Arzhanov and Maria Pázsit.

My present and former roommates Johanna, Andreas and Valentin: thank you for the company and all the fun and interesting discussions about everything! All the present and former colleagues of the Department of Nuclear Engineering are acknowledged for everything ranging from help with computers to allowing me to win the go-cart competition: Anders, Eva, Berit, Nils Göran, Lennart, Lasse, Lembit, Joska, Håkan, Farshid, Elisabeth, Larisa, Mathias, Viktor, Chiara, Katti and Davide.

The personnel of the NPP Ringhals is acknowledged for providing neutron measurement data for us. Kyoto University Reactor Research Institute is acknowledged for the neutron radiographic images of the two-phase flow. Svenskt Kärntekniskt Centrum (SKC) is acknowledged for the financial support.

Friends, family and Malin: Tack!



---

## REFERENCES

- [1] J. A. Thie, "Reactor Noise", ANS, Rowman and Littlefield, Inc., New York (1963)
- [2] M. M. R. Williams, "Random Processes in Nuclear Reactors", Pergamon Press, Oxford (1974)
- [3] J. A. Thie, "Core motion monitoring", *Nuclear Technology*, **45**, 5-41 (1979)
- [4] J. A. Thie, "Power Reactor Noise", ANS, La Grange Park (1981)
- [5] J. K.-H. Karlsson, "Development and Application of Reactor Noise Diagnostics", PhD Thesis, Chalmers University of Technology (1999)
- [6] Z. F. Kuang, "The Diversity and Unity of Reactor Noise Theory", PhD Thesis, Chalmers University of Technology (2001)
- [7] V. Arzhanov, "Power Reactor Noise Studies and Applications", PhD Thesis, Chalmers University of Technology (2002)
- [8] C. Demazière, "Development of a Noise-Based Method for the Determination of the Moderator Temperature Coefficient of Reactivity (MTC) in Pressurized Water Reactors (PWRs)", PhD Thesis, Chalmers University of Technology (2002)
- [9] [www.ringhals.se](http://www.ringhals.se), 2007-03-14
- [10] I. Daubechies, "Ten lectures on wavelets", CBMS 61, Society for Industrial and Applied Mathematics, Philadelphia, US (1992)
- [11] P. S. Addison, "The Illustrated Wavelet Transform Handbook", Institute of Physics Publishing, Bristol and Philadelphia, US (2002)
- [12] S. Mallat, "A Wavelet Tour of Signal Processing", Academic Press, London, UK (1998)
- [13] J. Bergh, F. Ekstedt and M. Lindberg, "Wavelets", Studentlitteratur, Lund, Sweden (1999)
- [14] Wavelet toolbox, Users guide, The Math Works Inc.

- [15] M. A. Vince and R. T. Lahey, "Development of an optical digital interferometer", *International Journal of Multiphase Flow*, **8**, 93-124 (1982)
- [16] A.M.C. Chan and D. Bzovey, "Measurement of mass flux in high temperature pressure steam-water two-phase flow using a combination of Pitot tubes and a gamma densitometer", *Nuclear Engineering and Design*, **122**, 95-104 (1990)
- [17] M. Balasko, E. Svab, L. Cser, "Simultaneous Dynamic Neutron And Gamma-radiography", *NDT International*, **20**, 157-160 (1987)
- [18] K. Mishima, T. Hibiki, Y. Saito, H. Nakamura and M. Matsubayashi, The review of the application of neutron radiography to thermal hydraulic research, *Nuclear Instruments and Methods A*, **424**, 66-72 (1999)
- [19] H. Wu, F. Zhou and Y. Wu, "Intelligent identification system of flow regime of oil-gas-water multiphase flow", *International Journal of Multiphase Flow*, **27**, 459-475 (2001)
- [20] R. Ulbrich, M. Krotkiewicz, N. Szmolke, S. Anweiler, M. Masiukiewicz and D. Zajac, "Recognition of two-phase flow patterns with the use of dynamic image analysis", *Proc. Inst. Mechanical Engineers Part E -Journal of Proc. Mech. Engineering*, **216**, 227-233 (2002)
- [21] K. Mishima and T. Hibiki, "Development of high-frame-rate neutron radiography and quantitative measurement method for multiphase flow research", *Nuclear Engineering and Design*, **184**, 183-201 (1998)
- [22] Neural Network Toolbox, Users guide, The Math Works Inc.
- [23] C. Demazière, C. Sunde, V. Arzhanov and I. Pázsit, "Final Report on the Research Project Ringhals Diagnostics and Monitoring, Stage 8", CTH-RF-177/RR10, Chalmers University of Technology, Göteborg, Sweden. (2003)
- [24] C. Demazière, C. Sunde and I. Pázsit, "Final Report on the Research Project Ringhals Diagnostics and Monitoring, Stage 9", CTH-RF-187/RR11, Chalmers University of Technology, Göteborg, Sweden. (2003)
- [25] C. Sunde, J. Wright, C. Demazière and I. Pázsit, "Final Report on the Research Project Ringhals Diagnostics and Monitoring, Stage 10", CTH-RF-194/RR12, Chalmers University of Technology, Göteborg, Sweden. (2005)
- [26] C. Sunde, C. Demazière and I. Pázsit, "Final Report on the Research Project Ringhals Diagnostics and Monitoring, Stage 11", CTH-NT-206/RR13, Chalmers University of Technology, Göteborg, Sweden. (2007)
- [27] I. Pázsit and O. Glöckler, "BWR instrument tube vibrations: Interpretations of measurements and simulations", *Annals of Nuclear Energy*, **21**, 759-786 (1993)
- [28] A. Rácz and I. Pázsit, "Diagnostics of detector tube impacting with wavelet techniques", *Annals of Nuclear Energy*, **25**, 387-400 (1997)

- 
- [29] I. Pázsit, C. Demazière, V. Arzhanov, and N. S. Garis, "Research and Development Program in Reactor Diagnostics and Monitoring with Neutron Noise Methods. Stage 7. Final Report", SKI Report 01:27, Statens Kärnkraftsinspektion (Swedish Nuclear Power Inspectorate), Stockholm, Sweden. (2001)
- [30] I. Pázsit, C. Demazière, and V. Arzhanov, "Research and Development Program in Reactor Diagnostics and Monitoring with Neutron Noise Methods. Stage 8. Final Report2, SKI Report 2003:08, Statens Kärnkraftsinspektion (Swedish Nuclear Power Inspectorate), Stockholm, Sweden. (2003)
- [31] V. Arzhanov and I. Pázsit, "Detecting Impacting of BWR Instrument Tubes with Wavelet Techniques", *Power Plant Surveillances and Diagnostics - Applied Research with Artificial Intelligence*, Editors Da Ruan and Paolo F. Fantoni, Springer, Physica Verlag XIV, pp. 157-174 (2002)
- [32] G. Pokol and G. Por, "ALPS Loose Parts Monitoring System and wavelet analysis" *International Journal of Nuclear Energy Science and Technology*, **2**, 241-252 (2006)
- [33] M. Antonopoulos-Domis and T. Tambouratzis, "System identification during a transient via wavelet multiresolution analysis followed by spectral techniques", *Annals of Nuclear Energy*, **25**, 465 (1998)
- [34] G. Espinosa-Paredes, A. Prieto-Guerrero, A. Núñez-Carrera and R. Amador-García, "Wavelet-based method for instability analysis in boiling water reactors", *Nuclear Technology*, **151**, 250 (2005)
- [35] I. Pázsit, "Determination of reactor stability in case of dual oscillations", *Annals of Nuclear Energy*, **22**, 377 (1995)
- [36] T. H. J. J. van der Hagen, I. Pázsit, O. Thomson and B. Melkerson, "Methods for determination of the in-phase and out-of-phase stability characteristics of a boiling water reactor" *Nuclear Technology*, **107**, 193 (1994)
- [37] I. Pázsit (editor), "Investigation of regional instability in Ringhals-1", CTH-RF-100/RR-1, Chalmers University of Tehcnology 1993
- [38] T. Lefvert, "Ringhals 1 stability benchmark, Final report", NEA/NSC/DOC(96)22 (1996)
- [39] K. Behringer and D. Henning, "A novel auto-correlation function method for the determination of the decay ratio in BWR stability analysis", *Annals of Nuclear Energy*, **29**, 1483 (2002)
- [40] R. A. Carmona, W. L. Hwang and B. Torrésani, "Characterization of Signal by the Ridges of Their Wavelet Transforms", *IEEE Transactions on Signal Processing*, **45**, 2586 (1997)

## References

---

- [41] N. Delprat, B. Escudié, P. Guillemain, R. Kronland-Martinet, P. Tchamitchian and B. Torrèsani, "Asymptotic Wavelet and Gabor Analysis: Extraction of Instantaneous Frequencies", *IEEE Transactions on Information Theory*, **28**, 644 (1992)
- [42] I. Pázsit, J. Karlsson and N. S. Garis, "Some developments in core-barrel vibration diagnostics", *Annals of Nuclear Energy* **25**, 1079-1093 (1998)
- [43] C. Demazière, "Development of a 2-D 2-group neutron noise simulator", *Annals of Nuclear Energy*, **31**, 647-680 (2004)
- [44] J. T. Mihalczo, E. D. Blakeman, G.E. Ragan, E. B. Johnson and Y. Hachiya, "Dynamic Subcriticality Measurements Using the  $^{252}\text{Cf}$ -Source-Driven Noise Analysis Methods", *Nuclear Science and Engineering*, **104**, 314-338 (1989)
- [45] G. I. Bell and S. Glasstone, "Nuclear Reactor Theory", Van Nostrand-Reinhold, New York (1970)
- [46] C. Demazière and I. Pázsit, "Theoretical investigation of the MTC noise estimate in 1-D homogenous systems", *Annals of Nuclear Energy*, **29**, 75-100 (2002)

# Paper I

*Classification of two-phase flow regimes via image analysis and a neuro-wavelet approach*

C. Sunde, S. Avdić and I. Pázsit

Progress in Nuclear Energy **46**, 348 (2005).





## CLASSIFICATION OF TWO-PHASE FLOW REGIMES VIA IMAGE ANALYSIS AND A NEURO-WAVELET APPROACH

CARL SUNDE<sup>1,\*</sup>, SENADA AVDIC<sup>2</sup> AND IMRE PÁZSIT<sup>1</sup>

<sup>1</sup>Department of Reactor Physics, Chalmers University of Technology,  
SE - 412 96 Göteborg, Sweden

<sup>2</sup>Faculty of Sciences, Department of Physics, University of Tuzla  
75 000 Tuzla, Bosnia-Herzegovina

\*[kalle@nephy.chalmers.se](mailto:kalle@nephy.chalmers.se)

### ABSTRACT

A non-intrusive method of two-phase flow identification is investigated in this paper. It is based on image processing of data obtained partly from dynamic neutron radiography recordings of real two-phase flow in a heated metal channel, and partly by visible light from a two-component mixture of water and air. Classification of the flow regime types is performed by an artificial neural network (ANN) algorithm. The input data to the ANN are some statistical moments of the wavelet pre-processed pixel intensity data of the images. The pre-processing used in this paper consists of a one-step multiresolution analysis of the 2-D image data. The investigations of the neutron radiography images, where all four flow regimes are represented, show that bubbly and annular flows can be identified with a high confidence, but slug and churn-turbulent flows are more often mixed up in between themselves. The reason for the faulty identifications, at least partially, lies in the insufficient quality of these images. In the measurements with air-water two-component mixture, only bubbly and slug flow regimes were available, and these were identified with nearly 100% success ratio. The maximum success ratio attainable was approximately the same whether the raw data was used without wavelet preprocessing or with a wavelet preprocessing of the input data. However, the use of wavelet preprocessing decreased the training time (number of epochs) with about a factor 100.

### KEYWORDS

Two-phase flow classification; Image analysis; Neural networks; Wavelet analysis.

© 2005 Elsevier Ltd. All rights reserved

## 1. INTRODUCTION

Two-phase flow patterns are usually classified into four classical so-called flow regime types. These are 1) bubbly, 2) slug, 3) churn-turbulent, and 4) annular flow regimes (see Fig. 1.). Recognition and, possibly control, of the flow regime types is essential in numerous practical applications. For instance, in two-phase flow calculations, in order to use the correct algorithm in a fluid dynamics code, the regime type in question must be known in advance, so that the right expression can be chosen for e.g. the interfacial shear coefficient or some other coefficients like the heat transfer coefficient.

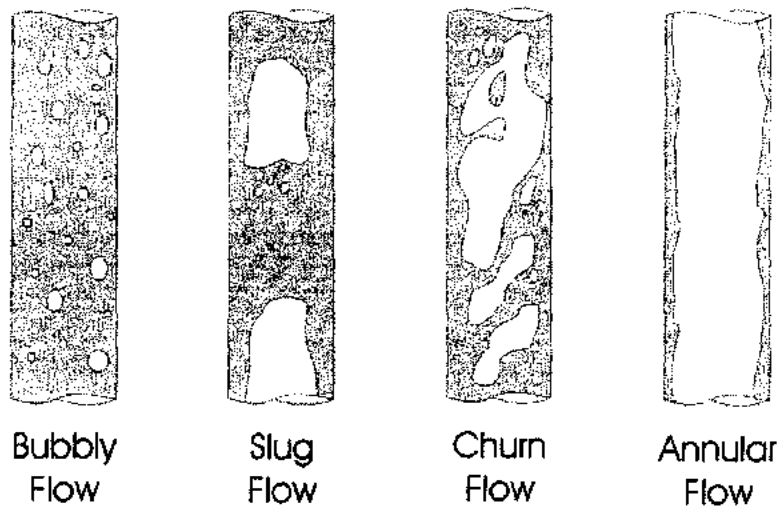


Fig. 1. Schematic drawings of the different phases of vertical two-phase flow

Although the flow classification can be done reliably in fully instrumented channels in which thermocouples, pressure transducers, flow-meters etc. are available, a more challenging alternative would be to use non-intrusive methods. In this field, the availability of the methods is much more limited. Non-intrusive methods so far have been based on radiation attenuation measurements, such as X-rays (Vince and Lahey, 1982) or gamma-rays (Chan and Banerjee, 1981; Chan and Bzovey, 1990; Kok et al., 2001). These methods are usually based on the detection of collimated rays penetrating the flow, and the processing of the variation of the intensity, modulated by the flow, by various statistical methods (probability distributions, auto- and cross-correlations and spectra).

A qualitatively different approach, which will be pursued in this paper, is to use image analysis, in combination with a neural network based identification method with a wavelet pre-processor. After all, the concept of flow regime arises from an intuitive judgement of the topology of the flow, based on visual observation. Correspondingly, image analysis, although not combined with so-called intelligent computing methods, has quite recently been recognised as one possible avenue of flow identification (Ulbrich et al., 2002; Kashdan et al. 2004a, b). Images of two-phase flow are though not easy to produce for real high-pressure high-temperature flows. Ulbrich et al. (2002) used a water-air two-component flow with visible light, and this is one of the alternatives that will also be investigated in this paper. Kashdan et al. (2004b) investigated particle beam in air. Images of a flow can be produced in transparent pipes easily with visible light, but in metal pipes, needed for real two-phase flow, neither X-rays or gamma-rays are applicable. X-rays do not penetrate the wall, and gamma-rays can not, in general, be produced with desired intensity such that an image with good contrast and dynamics can be achieved.

However, in the past one and a half decade, dynamic neutron radiography has been developed to the extent that it can produce dynamic images of two-phase flow in metal pipes. Such measurements require a thermal reactor as a neutron source, and hence this method is not suitable for in-situ applications, only for laboratory work. On the other hand, this is the only method of visualisation of high-pressure, high-

temperature two-phase flow in metal pipes without disturbing the flow. It is therefore very suitable to provide data on real two-phase flows for developing flow pattern recognition methods.

Such measurements were made at the Kyoto University Research Reactor Institute (Mishima et al., 1982). Some of these measurements were made available for us, and were used in the present analysis. However, the quality of these recordings turned out to be insufficient for the purpose of effective image analysis. Hence we have set up model experiments with coloured water - air loop in a plexiglas slab pipe. In these experiments visible light and an ordinary digital video camcorder was used. This way images with much better contrast and sharpness could be obtained. The purpose of these latter experiments was to check the algorithms, elaborated first in connections with the radiography images, and see if the improvement in the input data quality led to improvement in the flow regime classification. More details on the data acquisition and some image examples will be shown in the next section.

The image analysis, leading to the flow regime identification, is based on wavelet transform, i.e. multiresolution analysis, and neural identification. Such methods have been used for two-phase flow identification (Wu et al., 2001), but the input signals were simple process signals and not images. Multiresolution analysis is capable of extracting information from a one- or two-dimensional structure, corresponding to different scales. Such a procedure leads also to the reduction of the dimensionality of the information represented by the image, and can be used as input data to an Artificial Neural Network (ANN) for the classification. This requires training samples (images) being available to train the network, where the flow regime type is known. The trained network can be fed by similar, but unknown type, images as input, and used to classify the type or regime. It is this program that has been performed in the present paper and which will be described more in detail below.

## 2. THE FLOW IMAGES

Two different types of images were used. The first one was obtained with neutron radiography, and it comprises all four flow regimes (Fig. 2). The second one was obtained with visible light of only bubbly and slug flow (Fig. 3).

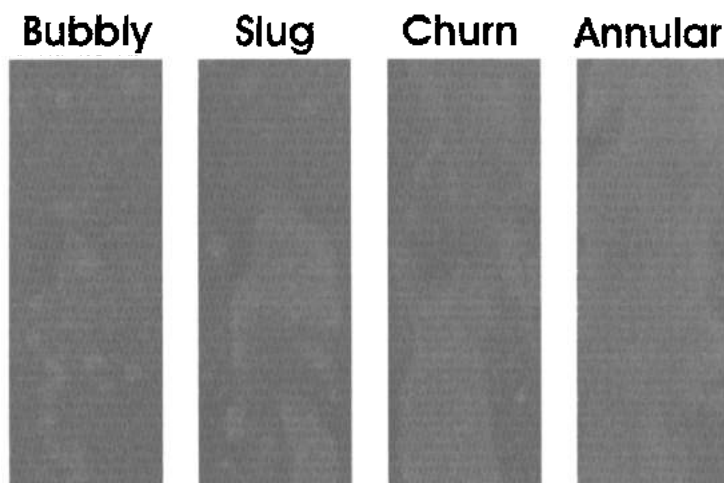


Fig. 2. Images of two-phase flow using neutron radiography

The way of producing dynamic neutron radiographic images, and in particular for two-phase flow, can be found in the literature (Mishima et al. 1988, 1999a; Balasko et al., 1987, 1999). The essence is to use a collimated beam of thermal neutrons from a reactor to illuminate the object, in this case the two-phase flow in the pipe. After penetrating the pipe and the flow, where some neutrons are removed by scattering and absorption in the sample, the beam is directed to a neutron converter, which converts the neutron beam into

visible light. This light, after a reflection by a mirror (in order to filter out gamma-rays that accompany the neutrons for most neutron sources) are recorded with an ordinary CCD video camera.

The images used in this work were recorded at the Kyoto University Reactor Research Institute (KURRI), by the Division of Nuclear Engineering (Mishima et al., 1998). During the experiment, the water was circulated in a loop with an overflow tank, and was heated up. The experiment started with pure water in the loop, and the heating was increased. With increasing heating, all four flow regimes occurred in sequence. The measurement results were available for us in form on an analogue VHS recording in NTSC format. From the whole sequence, four sections, corresponding to the four different regimes, were selected, and for each regime a number of individual frames were selected. Each frame was then saved as an individual tiff file.

Although, by a visual inspection of the video, the various flow regimes can be clearly seen, the contrast and sharpness of the static images obtained by the above procedure was relatively poor. Some examples are shown in Fig. 2. One reason for the poor quality is the digitization of the original analogue recording, the fact that the pictures were not recorded with digital technology leads to a high level of background noise.

To obtain better quality images, a simpler experiment was set up at our department. In this case a thin transparent plastic pipe, filled with coloured water, was used to generate the images. The images were recorded with a digital video camera. The two-phase flow was simulated by injecting air in the bottom of the pipe. By this way only two-component flow could be created, with only bubbly and slug flow regimes. The same way as with the radiography recordings, the number of frames corresponding to the (now only two) available regime types were selected, and converted as individual tiff files. Some examples are shown in Fig. 3. It is seen that due to the digital signal handling throughout, and the better contrast and sharpness of the original image to be recorded, the image quality of these files is much superior to the radiography ones.

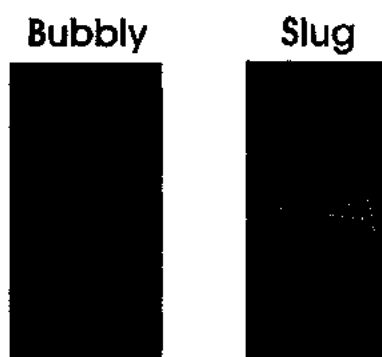


Fig. 3. Images of two-phase flow using visible light and coloured water

It has to be noted that the difficulty we encountered with the neutron radiography images is not due to the technique itself. Very high quality images of two-phase flow, and even steam explosions, have been produced lately with pulsed reactors and/or high speed digital cameras (Mishima et al., 1999b). It is the intention of the present authors to repeat the analysis presented here also on better quality radiography images when and if they will become available for us.

In the present study, from the neutron radiographic images a total of 200 frames from each of the four regimes were used for the identification and classification process, whereas 75 frames from each of the two regimes were used from the experiment with visible light.

### 3. WAVELET DATA PROCESSING

The information in each image in the digital (tiff) files is contained in approximately 60,000 pixels. Naturally, this information content needs to be reduced in dimension before using it as input to the neural network. Wavelet transform is known to often be an effective tool to achieve this goal (Addison, 2002; Bergh et al., 1999). Apart from data compression, wavelet transform coefficients are also often better (more sensitive) features in pattern recognition tasks than the original data. What regards two-phase flow, the four flow regimes have structures that show up spatial variations at different scales. Hence, wavelet coefficients from a multi-resolution analysis (or the original input data, but reduced by a one-step wavelet multiresolution analysis) seem to be suitable input data.

In order to improve the classification process of the flows, it is advisable to pre-process the images using wavelet techniques before extracting the input data for the Artificial Neural Networks (ANNs), (Hazarakia et al., 1997; Fadhel and Bhattacharyya, 1999; Verma et al., 2002; Kandaswamy et al., 2003). The advantages using wavelet transform include some noise reduction and feature extracting at different scales and directions of the images.

The one-dimensional wavelet transform maps a time signal into a time and frequency signal at different frequency levels,  $N$ , (Addison, 2002; Bergh et al., 1999; Mallat, 1999). At each level the signal is decomposed into an approximation and a detail. It is possible to do both a discrete (with discrete frequency levels), and a continuous (with continuous frequency levels), transform. In the case with an image, one uses the two-dimensional wavelet transform, which maps a two-dimensional signal (image), in spatial rather than time coordinates, into the two coordinates at different frequency (wave number) levels. The two-dimensional transform can also be done both discrete and continuous in the frequency coordinate or level.

At the first level of a 2-D discrete wavelet transform, the coarsest level of approximation coefficients,  $A_1$  contains 25% of the information of the original image,  $S_0$ . The approximation coefficients,  $A_1$ , at level 1, can be used to make a reconstruction of an approximation,  $S_1$ , of the original image. In the same way the detail coefficients,  $T_1^h$ ,  $T_1^v$  and,  $T_1^d$  (Fig. 4) containing the high frequency information of the image, at level 1 can be used to reconstruct horizontal,  $D_1^h$ , vertical,  $D_1^v$ , and diagonal,  $D_1^d$ , details of the original image. Adding the details to the approximation one can reconstruct the original image completely without any loss of information.

$$S_0(x, y) = S_1(x, y) \oplus D_1^h(x, y) \oplus D_1^v(x, y) \oplus D_1^d(x, y) \quad (1)$$

It is possible to do the transformation into lower levels were the details at each level contain the information of the signal corresponding to the frequency of that level. But in this work, only the first level of transformation was found to be useful to apply. The coefficients and the corresponding reconstructed images contain the same information, hence it is possible to use the coefficients when extracting input data for the ANNs. The reconstructed images are useful when displaying the transform.

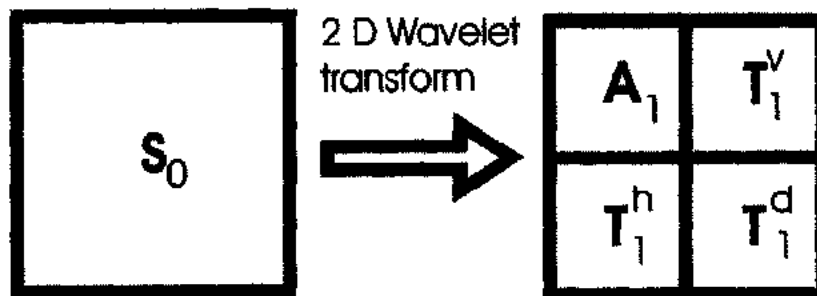


Fig. 4. First level of the 2 D wavelet transform.  $S_0$  is original image or data,  $A_1$  is the set of the first level approximation coefficients and  $T_1$  are the first level detail coefficients in each of the three directions, vertical, horizontal and diagonal

### 4. IDENTIFICATION WITH ANNS

As mentioned above, it is possible to improve the classification if the input data are pre-processed with wavelets before using them in the ANN. With the wavelets it is possible to extract features which are not visible in the original data. One set of features, mentioned in Hazarika et al. (1997), is the mean and variance of the first level approximation coefficients. Another possibility would be to use the energy of the different wavelet details,  $T_1^h$ ,  $T_1^v$  and,  $T_1^d$ . The energy of each detail is defined as the sum of the square of the absolute value of the detail coefficients, (Addison, 2002).

$$E_1^\alpha = \sum_{i,j} |T_{1,i,j}^\alpha|^2, \quad \alpha = \{h, v, d\} \tag{2}$$

Here  $T_{1,i,j}^\alpha$  denotes the matrix elements of the detail matrix,  $T_1^\alpha$ . In the first run, the neutron radiography images were analysed. Input data from the raw images were extracted and compared with the wavelet pre-processed input data. In this case the mean and variance from both the raw images and the first level approximation coefficients were used first, as reference input data. It turned out that, due to the poor image quality, no other features could be successfully used in the classification procedure.

In the second case the images produced with visible light, which had much better quality, were used. Again the mean and variance of the raw data were used as reference. Here, however, wavelet transform pre-processing did lead to improvement. With the wavelet pre-processing, the energy of the first level of detail coefficients and their variances were used, giving a total of 6 inputs for the ANN (see Fig 5).

As usual with wavelet analysis, the choice of the right wavelet for the task at hand is not self-obvious. One guideline of choosing a suitable wavelet is to select one, which has the same features as the data analysed. For this classification task the following wavelets were tested: Daubechies of order 8 (db8), Symmlet of order 6 (sym6), Coiflet of order 4 (coif4), Daubechies of order 1 (Haar) and biorthonormal (bior3.1). These are all available in the Wavelet Toolbox in MatLab (Anon, 2000).

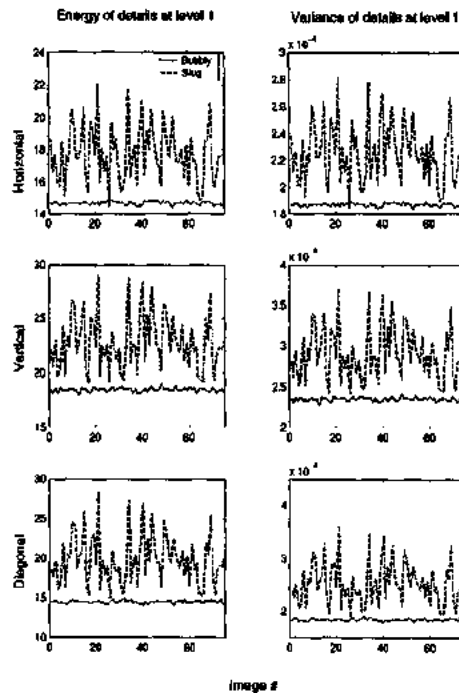


Fig. 5. Input data of the images made with visible light after wavelet pre-processing

#### 4.1 Classification using artificial neural networks

ANNs are capable to tackle very complicated tasks, including non-linear classification problems. The backpropagation (BP) algorithm is the most frequently used algorithm for the training of such networks (Pazsit and Kitamura, 1997). We have used the multi-layered perceptron (or simply the feed-forward network) consisting of an input layer, an output layer and one hidden layer. The network receives input through the nodes in the input layer, from which the signals propagate forward to the nodes of the consecutive layer and output signals are produced in the output layer. In the backward phase, error signals are propagated backward through the network and some parameters are adjusted in reference to the error signals.

The performance of ANNs depends on the proper choice of the input parameters. We have investigated the performance of the ANN for various input parameter sets. The number of the input and output nodes is defined by the problem itself. For the radiographic images, the number of input nodes was 2 and for the visible light images it was 6, as mentioned before. All the input feature vectors were normalized so that they fall in the range  $[-1,1]$ . For each type of flow, a corresponding output class is associated. The ANN has 4 output nodes for the radiographic case and 2 output nodes for the visible light case, corresponding to the 4 or 2 different flow types (Fig. 6). The target value, during training, for each class contains value of 0.9 for the correct category and three or one dummy variables with value of 0.1.

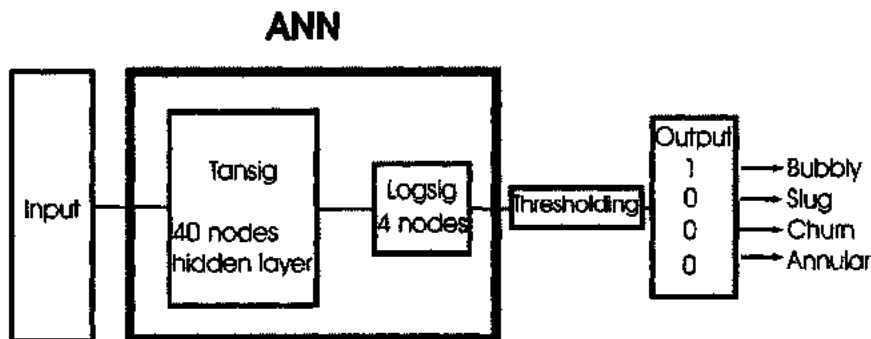


Fig. 6. The Artificial Neural Network used in the classification process of the neutron radiographic images. The thresholding is only used during testing

Since the output layer chosen for this classification task has a *log-sigmoid* transfer function, the output values range from 0 to 1, and thresholding has to be performed on the output data, to get 0 or 1, when classifying. Two different threshold levels were used, 0.5 and 0.7. All output values larger than the threshold are set to unity and all other to zero. If the output data, after the thresholding, are all four zeros, the corresponding image is classified as unknown or unclassified flow regime. The same applies for the case of more than one non-zero value. The choice of the threshold level is somewhat arbitrary and it is partly based on trial and error. A too high threshold avoids ambiguous identifications (where more than one output has a value equal to 1; but leads to a higher number of unsuccessful identification (when all four outputs are zero). With a low threshold value, the situation is the opposite, there will be few unsuccessful identifications, but many of them will be ambiguous. The most plausible choice, 0.5 was selected first; however, a higher threshold of 0.7 was also tested. The best classification results were achieved with the lower threshold value of 0.5,

The optimal number of nodes in the hidden layer, the training algorithm and the activation functions were determined by trial and error. *Tan-sigmoid* function was used for the hidden layer and *log-sigmoid* for the output layer. A few of the modified backpropagation (BP) algorithms such as adaptive learning rate, resilient BP, scaled conjugate gradient and gradient descent algorithm with momentum were examined for training the ANN. Cross-validation was used to estimate which learning ANN model will perform the best on the problem at hand. For each of the models a 5-fold cross-validation over the training set was used, which means that 1/5th of the training data was used as a validation set and the process was repeated with

non-overlapping rotations. In the case of the neutron radiographic images, each learning model was trained with 640 samples for the four various types of flow, and then they were tested on one subset of 160 samples which was not used during training. For the visible light images, the training set consisted of 120 samples and the test subset of 30 samples (Fig. 5). The resilient backpropagation (RP) algorithm was found to have the highest average test set score. Namely, the classification efficiency with RP algorithm was 100% (the percentage of the flows that were correctly classified) when the recall test was performed on the training set, and 95% when the recall test was made on the subset not used during training. The best performance was obtained for the training and validation test set with an ANN structure consisting of one hidden layer having 40 nodes. The default performance function for feedforward networks was the mean square error, i.e. the average squared error between the network outputs and the target outputs. The ANN training was performed until the maximum number of epochs, set to 30000, was reached or the mean square error, MSE, target value of  $10^{-3}$  was achieved. All calculations were carried out by using the toolboxes available with the technical computing software MATLAB (Anon, 2000).

## 5. RESULTS AND DISCUSSION

### 5.2 Neutron Radiographic images

The performance of different wavelets, db8, sym6, coif4, haar and bior3.1, on the classification efficiency has been investigated. The classification efficiency is defined as the percentage ratio of the number of flow pictures correctly classified to the total number of pictures corresponding to one type of flow. Average efficiency of the flow classification for each type of the chosen wavelets by using ANN with mean values and variance as input and for threshold levels of 0.5 and of 0.7, is depicted in Fig. 7. The average efficiency is shown with error bars (standard deviation). Almost the same result is achieved independent of which wavelet type that is used. Though, coif4 has a slightly lower percent of correct classified regimes and Haar has the best classification efficiency.

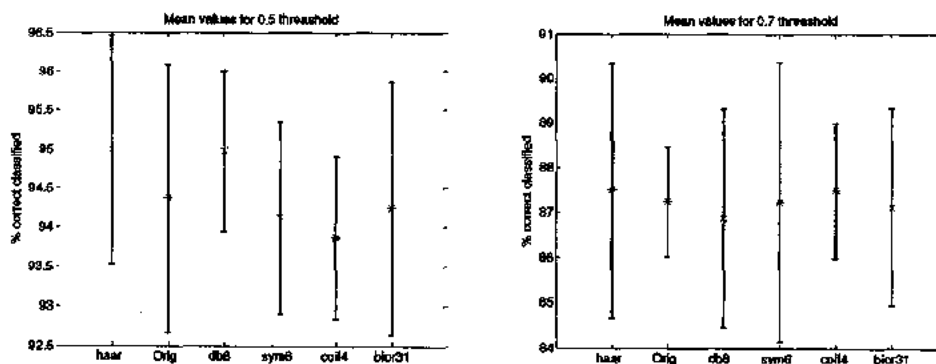


Fig. 7. Classification efficiency for the different wavelets and the original data, threshold 0.5 to the left and 0.7 to the right

Clearly a threshold of 0.5, with accuracy of about 95%, is better than a threshold of 0.7, which only has about 87% correctly classified images. But even by using the mean and variance of the original image values, the efficiency is the same. So there is not much improvement, in classification, using the wavelet transform in this case.

All of the different wavelets classified the annular flow with 100% efficiency, which is also the case for the original data. In Fig. 8 each bar represents the 200 images from each flow and the different colours show which regime the images were identified with. White is for unknown or unclassified images. As it is seen, a very few images turn out to be unclassified for a threshold of 0.5. The most difficult regimes to

classify for both the wavelet and the original data are the slug and churn flow. This is of course due to the fact that these flows have similar features.

The maximum number of epochs, 30 000, were used in the training process, meaning that the *MSE* target value of  $10^{-3}$  was not reached.

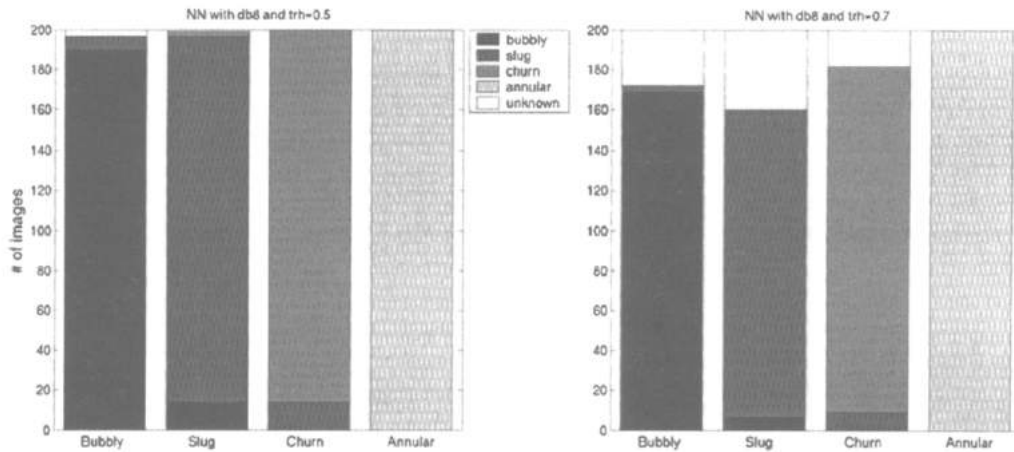


Fig. 8. Result of the classification of the neutron radiographic two-phase flow images using input data pre-processed with the db8 wavelet, with a threshold of 0.5 to the left and 0.7 to the right

### 5.3 Visible light images

The same five wavelets as above were used also in the case with visible light images. The results are partly similar to the radiography images. Namely, there is not much increase of the classification efficiency when using wavelets compared to the features of the raw images. However, in this case there is a large improvement in the number of epochs (iterations) used when training the ANN. When using the wavelet pre-processed data, the number of epochs is reduced with a factor of 100, compared to the raw data input (Fig. 9). With the raw data, the number of epochs always exceed the maximum number of 30 000, before reaching the *MSE* target values of  $10^{-3}$ .

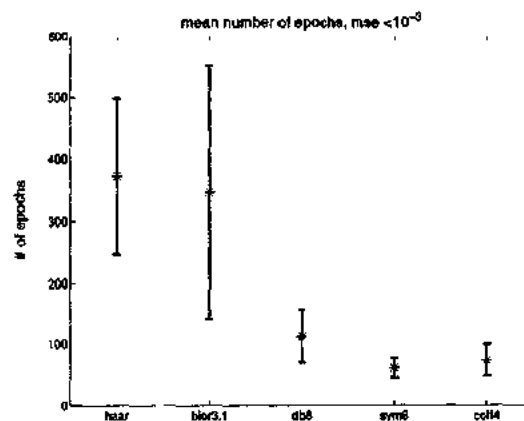


Fig. 9. Depicted is the number of epochs used when training the network. The input data are wavelet pre-processed visible light images

The classification efficiency is also slightly better in this case, compared to the neutron radiographic case. This is presumably also attributed to the better quality of the images. For the wavelet pre-processed data one slug flow image was classified as bubbly and the rest were correctly classified. That is, 149/150=99.33% for wavelet pre-processing, whereas success ratio of classification with the raw image inputs was 146/150=97.33%. The result was the same for all wavelets with a threshold of 0.7.

## 6. CONCLUSIONS

The methodology used in this paper appears to be suitable to classify two-phase flow regimes by image analysis, in a non-intrusive way. The original idea was to use data from dynamic neutron radiography of two-phase flow in a heated metal pipe. Such measurements have been performed and by now good quality images can be obtained. Unfortunately no such measurements were available to us, only old analogue recordings. However, a proof-of-principle investigation was made of the applicability of the image analysis method, with positive outcome. The potential of the method were then investigated by using experiments with visible light on a water-air mixture. In this experiment only a few basic flow structures could be achieved, but the images had better quality. Hence it was possible to prove the extended efficiency of the wavelet pre-processing of the data before the neural identification. The two different measurements together show that on-line, non-intrusive identification of two-phase flow in a metal pipe can be achieved with processing dynamic neutron radiography images with a neuro-wavelet approach.

## 7. ACKNOWLEDGEMENT

This work was supported by the Swedish Centre for Nuclear Technology, and the Swedish Nuclear Power Inspectorate.

## 8. REFERENCES

- Addison P.S. (2002) *The Illustrated Wavelet Transform Handbook*, Institute of Physics Publishing, Bristol and Philadelphia.
- Anon (2000) *Users manual MatLab*. The Math Works Inc., Natick, MA US.
- Bergh J., Ekstedt F. and Lindberg M. (1999) *Wavelets*, Studentlitteratur, Lund, Sweden.
- Balasko M, Svab E, Cser L (1987) Simultaneous Dynamic Neutron And Gamma-radiography. *NDT International* 20, 157-160
- Balasko M, Korosi F, Svab E, Eordogh I (1999) A novel type epithermal neutron radiography detecting and imaging system. *Nucl. Instr. Methods A* 424, 263-269
- Chan A.M.C. and Banerjee S (1981) Design aspects of gamma densitometers for void fraction measurements in small scale two-phase flows, *Nuclear Instruments & Methods* 190, 135.
- Chan A.M.C. and Bzovey D. (1990), Measurement of mass flux in high temperature pressure steam-water two-phase flow using a combination of Pitot tubes and a gamma densitometer, *Nuclear Engineering and Design* 122, 95.
- Fadhel E.A. and Bhattacharyya, P. (1999), Application of a Steerable Wavelet Transform using Neural Network for Signature Verification, *Pattern Analysis & Applications* 2, 184.
- Hazarika N., Chen J. Z., Tsoi A. C. and Sergejew, A. (1997), Classification of EEG signals using the wavelet transform, *Signal Processing* 59, 61.
- Kandaswamy A., Sathish Kumar C., Ramanathan R. P., Jayaraman S. and Malmurugan N. (2003), Neural Classification of Lung Sounds using wavelet coefficients, *Computers in Biology and Medicine* 6, 523.

- Kashdan JT, Shrimpton JS, Whybrew A (2004a) Two-phase flow characterization by automated digital image analysis. Part 1: Fundamental principles and calibration of the technique. *Particle & Particle Systems Characterization* 20, 387-397
- Kashdan JT, Shrimpton JS, Whybrew A (2004b) Two-phase flow characterization by automated digital image analysis. Part 2: Application of PDIA for sizing sprays. *Particle & Particle Systems Characterization* 21, 15-23
- Kok H.V., van der Hagen T.H.J.J., Mudde R.F. (2001) Subchannel void-fraction measurements in a 6 x 6 rod bundle using a simple gamma-transmission method. *International Journal Of Multiphase Flow* 27, 147-170
- Mallat S. (1999), *A wavelet tour of signal processing*, Academic Press, USA.
- Mishima K., Fujine S., Yoneda K., Yonebayashi K., Kanda K. and Nishihara H. (1988) Proc. 3rd Japan-US Seminar on Two-Phase Flow Dynamics, Ohtsu, Japan.
- Mishima K, Hibiki T, Saito Y, Nakamura H, Matsubayashi M (1999a) The review of the application of neutron radiography to thermal hydraulic research. *Nucl. Instr. Methods A* 424, 66-72
- Mishima K, Hibiki T, Saito Y, Sugimoto J, Moriyama K (1999b) Visualization study of molten metal-water interaction by using neutron radiography. *Nucl. Eng. Design* 189 391-403
- Pazsit, I. and Kitamura, M. (1997), The Role of Nuclear Networks in Reactor Diagnostics and Control, *Advances in Nuclear Science and Technology* 24, 95.
- Verma M. S., Pratt L., Ganesh C. and Medina C. (2002), Hair-MAP: a prototype automated system for forensic hair comparison and analysis, *Forensic Science International* 129, 168.
- Vince M. A. and Lahey R. T. (1982) *International Journal of Multiphase Flow* 8, 93
- Ulbrich R, Krotkiewicz M, Szmolke N, Anweiler S, Masiukiewicz M, Zajac D (2002) Recognition of two-phase flow patterns with the use of dynamic image analysis. *Proc. Inst. Mechanical Engineers Part E-Journal of Proc. Mech. Engng* 216 227-233
- Wu H., Zhou F and Wu Y (2001) Intelligent identification system of flow regime of oil-gas-water multiphase flow. *Int. J. Multiphase Flow* 27, 459-47



# Paper II

*Investigation of detector tube impacting in the Ringhals-1 BWR*

C. Sunde and I. Pázsit

International Journal of Nuclear Energy Science and Technology **2**,189 (2006).



---

## **Investigation of detector tube impacting in the Ringhals-1 BWR**

---

Carl Sunde\* and Imre Pázsit

Department of Nuclear Engineering  
Chalmers University of Technology  
SE-412 96 Göteborg, Sweden  
Fax: +46-31-772 3079  
E-mail: kalle@nephy.chalmers.se  
E-mail: imre@nephy.chalmers.se  
\*Corresponding author

**Abstract:** Neutron noise measurements were made in two consecutive fuel cycles in the Swedish BWR Ringhals-1 with the purpose of diagnostics of vibrations and impacting of detector strings. Two diagnostic tools were used, first a traditional spectral analysis and second a wavelet-based method. Both types of methods have been used in the past, but not simultaneously during one fuel cycle. In addition, a new method, wavelet-based coherence, was tested with success.

Based on the results of the analysis, with emphasis on the traditional method, the detector tubes were divided into three groups with respect to the severity and likelihood of impacting. For the first series of measurements, these conclusions could be checked against visual inspection of the fuel assemblies during refuelling after the cycle, in order to find impacting damage. A good correlation between the prediction of the analysis and the inspection results was found.

**Keywords:** noise analysis; neutron noise; detector impacting; spectral analysis; APSD; coherence; phase; wavelet analysis.

**Reference** to this paper should be made as follows: Sunde, C. and Pázsit, I. (2006) 'Investigation of detector tube impacting in the Ringhals-1 BWR', *Int. J. Nuclear Energy Science and Technology*, Vol. 2, No. 3, pp.189–208.

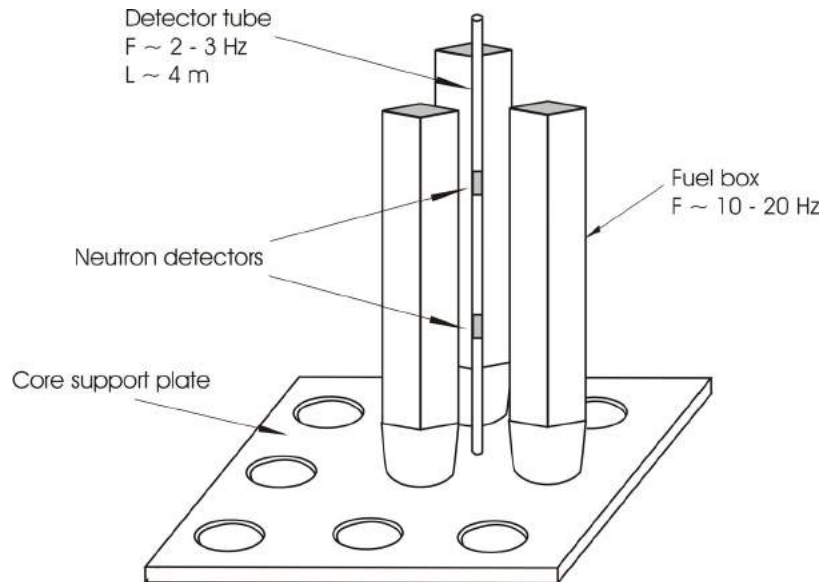
**Biographical notes:** Carl Sunde received his MSc in engineering physics from Chalmers University of Technology, Sweden, in 2002 and is working as a PhD student at the Department of Reactor Physics of Chalmers. His research interests are noise diagnostics, diagnostics of two-phase flow and intelligent computing methods including artificial neural networks and wavelet analysis.

Imre Pázsit is Professor at the Department of Reactor Physics, Chalmers University of Technology, Göteborg, Sweden. He got his PhD at the University Roland Eötvös in Budapest, Hungary in 1975 and worked in the Central Research Institute for Physics, Budapest, until 1983. After that he spent a period in Studsvik, Sweden, before he joined Chalmers in 1991. His research interests are fluctuations in neutron transport and atomic collision cascades; reactor diagnostics based on noise analysis; elaboration of inverse methods in neutron noise diagnostics; intelligent computing methods such as artificial neural networks and wavelet analysis; diagnostics of two-phase flow and fusion plasma; and recently, positron annihilation spectroscopy and positron transport. He is the Director of the Chalmers Centre for Nuclear Technology, and Head of the Section for Mathematical Physics of the Swedish Physical Society.

## 1 Introduction

Excessive vibrations and impacting of detector strings in BWRs have been a known problem for a long time (Thie, 1979; 1981; Mott *et al.*, 1976; Fry *et al.*, 1977; Pázsit *et al.*, 1988; Pázsit and Glöckler, 1994). The situation is illustrated in Figure 1. High turbulence around the detector from the bypass flow at the lower core support plate can cause strong vibrations of the detector tube (also called instrument tube, or detector string). Various methods of detecting impacting from the signals of the vibrating neutron detectors have also been elaborated and tested during the past few decades (Mott *et al.*, 1976; Fry *et al.*, 1977; Pázsit *et al.*, 1988; Pázsit and Glöckler, 1994; Thomson *et al.*, 1997; Rácz and Pázsit, 1998; Arzhanov and Pázsit, 2002).

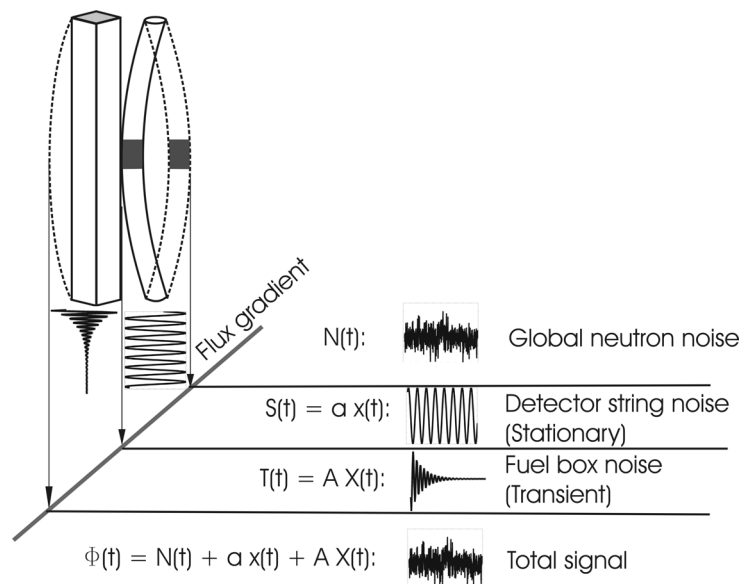
**Figure 1** Illustration of the position of the detector string in a BWR core between four fuel elements, with indication of some typical data of interest.



These methods can be divided into two categories: traditional or spectral analysis-based methods, and wavelet analysis methods. The spectral analysis methods are based on assumptions concerning how the spectral properties of the APSD, and in particular the properties of the vibration peak(s) and the phase of the cross-spectra change compared to vibrating but not impacting, or not vibrating, cases. These methods assume stationarity of the signal, and they are mostly qualitative. They have nevertheless been found to work in several cases. As is clear from the description, these methods mostly rely on the knowledge of a 'reference base', *i.e.*, vibration characteristics of vibrating but not impacting strings. In other words these methods are in need of some form of calibration. The wavelet-based methods are more absolute, *i.e.*, have less need of calibration, and supply a quantitative measure of the severity of impacting. They do not assume a stationary behaviour, rather they can handle intermittent signals as well. They are, on the other hand, based on a hypothesis, which, although being very plausible, has not been

possible so far to prove or disprove in practice. The hypothesis is that each impact of the detector string against the fuel box induces a short, damped vibration of the assembly, with a frequency that is higher than the eigenfrequency of the detector string (for an illustration, see Figure 2). The neutron noise induced by this short-lived vibration is sensed by the neutron detector as a ‘spike’ in a broadband noise, which can be extracted efficiently by wavelet filtering methods. This latter method has also been verified on measurements taken in several Swedish BWRs (Arzhanov and Pázsit, 2002; Pázsit *et al.*, 2001; Pázsit *et al.*, 2003). In addition, continuous wavelet transform methods were also tested in this work as a novel method for detecting detector impacting. A time-frequency dependent wavelet coherence was calculated, which shows high values in the frequency range of the impacting detector strings around the eigenfrequency of the damped vibrations of the fuel assemblies.

**Figure 2** Schematic view of the signal of a detector vibrating in a flux gradient with background noise and impacting. In the time domain, the components  $S(t)$  and  $T(t)$  are not visible in the total signal. For explanation see text in the paper.



When assessing the performance of the various methods, it should be noted that there is no general assessment available about the performance of the various methods at different reactors. In most cases, one kind of method was used by one diagnostic group at one type of core and corresponding instrumentation. There are also some indications that a method, which was used successfully at one reactor unit, did not perform successfully when transferred to another core. In Sweden, both spectral and wavelet-based methods, that worked well at the Barsebäck reactor, did not perform so well when transferred to measurements made on the Oskarshamn reactor (Pázsit *et al.*, 1988; Pázsit and Glöckler, 1994; Arzhanov and Pázsit, 2002; Pázsit *et al.*, 2001; Pázsit *et al.*, 2003). The reason for the varying performance of the traditional spectral analysis method in different cores was already discussed by Pázsit and Glöckler (1994). The success of this method requires

some ‘optimum’ ratio of the magnitudes of the boiling noise and the noise induced by the vibrations of the detector. The former depends on the local void fraction, and the second on the flux gradients. These are different in different cores. The wavelet-based method, on the other hand, required further development before it worked just as effectively for the Oskarshamn measurements as for the Barsebäck ones. Here, one main task is to find a proper thresholding amplitude, which can be determined by ‘tuning’ of the method when transferred from one core to another.

In other words, the experience with the transfer of methods from one core to another is relatively sparse. Therefore, it appears interesting to report on the applicability of some, already tested, methods in a new core. In Sweden, vibration analysis has been performed in the Barsebäck and Oskarshamn reactors, but this is the first case when the two methods reported on in this communication were tested on the Ringhals-1 BWR. Unfortunately, only one (the second) out of the two measurement campaigns was suitable for wavelet analysis, whereas post-cycle checking of the caused damage of impacting, which can be used for rating the performance of the diagnostics, is available only for the first measurement series.

The wavelet-based analysis indeed showed that a direct transfer of the method that worked quite effectively for the Oskarshamn measurements, is not possible, and further modifications of the method became necessary. On the other hand, the traditional spectral analysis could be performed for both cycles, and the performance of the diagnostics in the first cycle could be checked during fuel inspection during the revision. A good correlation was found between the prediction of the diagnostics and the actual damages found.

## 2 Principles of analysis

### 2.1 The spectral analysis method

This method was elaborated and first used during the analysis of the early Barsebäck measurements in 1986 by the Studsvik noise group (Pázsit *et al.*, 1988). Its principles are described thoroughly in (Pázsit and Glöckler, 1994). The essence is that in the absence of vibrations, the APSD (autospectrum) of the LPRMs, *i.e.*, the individual detectors, is a smooth function of the frequency, and the coherence and phase between any two detectors in the same string follows a characteristic pattern for propagating perturbations in the presence of a local noise component (in-core BWR noise). The phase is linear up to 10 Hz, and the coherence shows a periodic peak-sink structure, whose maxima and minima coincide with the zero- and  $\pi$ -crossings of the phase.

The presence of weak vibrations can be noticed in the appearance of a relatively narrow peak in the APSD at the fundamental frequency (eigenmode) of the detector string, usually in the range of 2–5 Hz. With an increasing amplitude of the vibrations, the fundamental peak increases; also, new peaks occur at frequencies of the higher harmonics (double and triple of the fundamental frequency). When impacting starts, the vibration peak gets broadened. Concurrently, the linear phase, and to a lesser extent also the sink structure of the coherence, get distorted with increasing vibrations. The most visible is the distortion of the phase around the vibration frequency; with increasing strength of the vibrations, the phase tends to be zero over an increasing frequency region around the vibration frequency, owing to the simultaneous movement of the two detectors. The

occurrence of the higher harmonics can be due either to the effect of the flux curvature with larger vibrating amplitudes, or to the appearance of the higher vibrating modes of the detector string, which can be induced by the impacting (Lansåker, 2004).

It is important that out of the above quantities, only the peak broadening is a clear indicator of impacting. The higher harmonics and phase distortion are, strictly speaking, only an indicator of increasing vibration amplitudes. Nevertheless, a large vibration amplitude is associated with a higher probability of impacting. Experience so far shows that the set of above indicators can be used for a quantitative classification of the probability and severity of impacting into three basic groups as follows:

- 1 No vibrations:
  - smooth structure of the APSD and the coherence, no peaks
  - linear phase between the two detectors in the same string, showing the time delay of the signal (bubble transit time).
- 2 Vibrations but no impacting:
  - a single narrow peak in the APSD and the coherence
  - linear phase distorted in the narrow frequency range of vibrations, the phase is zero there.
- 3 Indications of impacting:
  - a broad peak in the APSD
  - several peaks, mainly a second peak at the double frequency of the fundamental mode
  - phase curve distorted and zero over a large frequency range
  - The severity of the impacting can be judged by whether or not all three points are fulfilled simultaneously, and also on the quantitative value of the indicators (broadening, distortion *etc.*).

## 2.2 The wavelet-based method

The first method that has been used in several applications before, is based on discrete wavelet transform and wavelet filtering. The principles of this method are described in (Rácz and Pázsit, 1998; Arzhanov and Pázsit, 2002; Pázsit *et al.*, 2001; Pázsit *et al.*, 2003). An illustration of the assumptions is shown in Figure 2. In case of impact-free vibrations, the detector signal consists of a broadband background noise, and a narrow frequency band component, both components being stationary. The impacting induces a short, damped vibration of the fuel assembly, which is converted into a short, decaying transient in the detector signal. It is assumed that the eigenfrequency of the transient vibrations is noticeably higher than that of the detector strings, and is in the range 10–15 Hz. These transients or spikes occur in an intermittent manner, and their contribution to the signal APSD is negligible compared to the other two components, due to their small amplitude and sparse occurrence. The task of the wavelet analysis is to detect the presence of such spikes and give a measure of the frequency of their occurrence. This quantity is named the ‘impacting rate’, and is calculated in an algorithmic way by wavelet filtering.

The essence of the method is a wavelet filtering, based on the Discrete Wavelet Transform (DWT) and a thresholding of the wavelet transform coefficients before inverse transform. A usual problem in such an application is the determination of the filter threshold. Usually, the variance of the background noise is used to set the threshold in an algorithmic way. The background noise level, on its turn, is determined from the high-frequency tail of the APSD, for frequencies above the fuel assembly eigenfrequency. In the first application (Rácz and Pázsit, 1998) Haar wavelets were used, and the break frequency of the high-pass filter of the background extraction method was set in an *ad hoc* way at a frequency that was assumed above the fuel eigenfrequency.

Later this method was further developed by using scale-dependent thresholding, *i.e.*, the thresholds are different for each of the different scales in the wavelet multiscale resolution (Arzhanov and Pázsit, 2002; Pázsit *et al.*, 2001), when analysing measurements taken in Oskarshamn-2. First a global threshold is calculated (Wavelet Toolbox User's Guide, 2000; Addison, 2002; Mallat, 1999).

$$thr_g = 0.3936 + 0.1829 * \log_2(N) \quad (1)$$

where  $N$  is the length of the signal. Then a scale-dependent threshold is calculated as the median absolute deviation:

$$thr_s(a) = \text{median}(|c(a)|) / 0.6745 \quad (2)$$

where  $c(a)$  are the wavelet coefficients at scale  $a$ . The final threshold at scale  $a$  is then:

$$thr(a) = thr_g * thr_s(a) \quad (3)$$

The multiscale resolution is performed down to scales corresponding to the frequency of the fuel-box, 10 Hz. The connection between scale and frequency is given by the so-called centre frequency of the wavelet (Addison, 2002). When analysing the Oskarshamn measurements it was also noticed that, unlike in the Barsebäck case, the choice of the mother wavelet did play a role. Moreover, the algorithm had to be improved to be competitive with other, nonwavelet-based techniques. The improvement consists of a final thresholding of the difference  $V$  between the wavelet denoised signal  $Den(S)$  and the approximation at the largest scale level  $A$  in the multiscale resolution:

$$V = Den(S) - A \quad (4)$$

using the variance of the background noise.

In analysing the measurements from Ringhals-1 the discrete Meyer wavelet was used without the final thresholding of  $V$ . The result is partly a visual display of the remaining spikes that are supposed to represent the impacting effects and thus give an intuitive measure of the impacting frequency or severity, and partly a number called Impact Rate index (IR index), which is the number of spikes (impacts) in the signal per unit time.

$$IR \text{ index} = \frac{\text{number of spikes in } V}{\text{unit time}} \quad (5)$$

In addition, a new method was tested in the present measurements the first time, based on wavelet coherence. The inspiration for the test of this method was taken from a recent work by Pokol and Por (2005). Similarly to the case of the traditional spectral analysis method, the wavelet coherence was calculated between the signals of two detectors in the same instrument tube. The wavelet coherence between two signals  $f$  and  $g$  is determined as follows (Pokol and Por, 2005). First a short-term averaging integral of the wavelet transforms is calculated as:

$$C_{f,g}^w(f,t) = \int_{t-T/2}^{t+T/2} W_f^*(f,\tau)W_g(f,\tau)d\tau \quad (6)$$

Here  $W(f, \tau)$  is the continuous wavelet transform of signal  $f$  and  $g$ , respectively and  $T$  is chosen to be 100 times the sampling frequency in order to get a good averaging. Note here that, according to the character of the application, the wavelet transform is given in terms of the frequency rather than as a function of the scale. The two variables are inversely related, but the correspondence is unambiguous.

The coherence is then calculated as:

$$\gamma_{f,g}^w(f,t) = \frac{|C_{f,g}^w(f,t)|}{\sqrt{C_{f,f}^w(f,t)C_{g,g}^w(f,t)}} \quad (7)$$

This way a coherence function is obtained, which, similarly to the ordinary CWT transform, is dependent on both time and frequency. One can choose the averaging window in (6) to be of different length; if the integral is extended to the whole time interval of the measurement, one obtains a coherence function which, similarly to the FFT-based coherence, is only dependent on frequency. Even in such a case, as a rule, the information content of the wavelet coherence differs from that of the spectral coherence. As an analogy, it can be mentioned that, as is demonstrated in (Addison, 2002), the structure of the FFT-based power auto- and cross-spectra is different from that of the wavelet-based spectra, defined as in Equation (6). Our expectation is that, as was also shown in (Pokol and Por, 2005), the wavelet coherence can identify characteristics at certain frequencies that cannot be seen in the spectral functions (APSD) or the wavelet-based spectrograms of single signals.

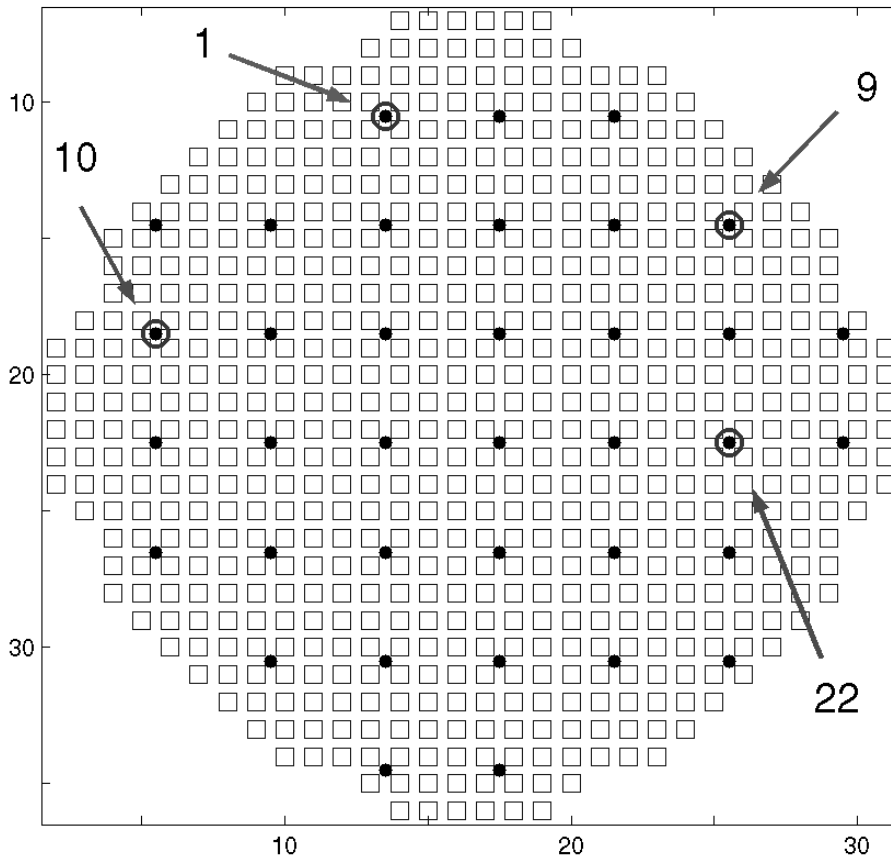
### 3 The measurements

Two different measurements are analysed. The first measurement, #1, was taken during start-up of Ringhals-1 on 3–6 September 2002 and the second measurement, #2, one year later on 27 October 2003, also during start-up. The first measurement consists of four different measurements, three at reduced core flow and reduced power, to investigate BWR stability, and one measurement at full flow and full power. The latter one is the most interesting one regarding detector tube vibrations, hence solely this measurement was used in this analysis. Signals from a total of 36 core positions were recorded, each position containing two detectors, one at a lower axial elevation (4) and another one at a higher axial elevation (2). This gives a total of 72 different signals, but the signals from one position were defect. The measurement was around 11 min long with a sampling frequency of 12.5 Hz.

After the analysis of the first measurement it was realised that the sampling frequency was too low for the wavelet-based method. A new measurement was then taken during the start-up of the following cycle in 2003. This measurement also consists of 72 signals, but with a higher sampling frequency of 60 Hz and a length of five min.

The layout of the core, with the positions of the detector strings is shown in Figure 3. The positions of the detector Strings 9, 10 and 22 that were judged in the analysis to have impacting in the first series of measurements (see Section 4), as well as String 1 which did not even indicate vibrations, are marked in the figure.

**Figure 3** The layout of the core of Ringhals-1 with the locations of the detector strings. String #1 did not show vibrations, whereas Strings 9, 10 and 22 were found to have impacting in the measurement Series #1.



## 4 Results of the analysis

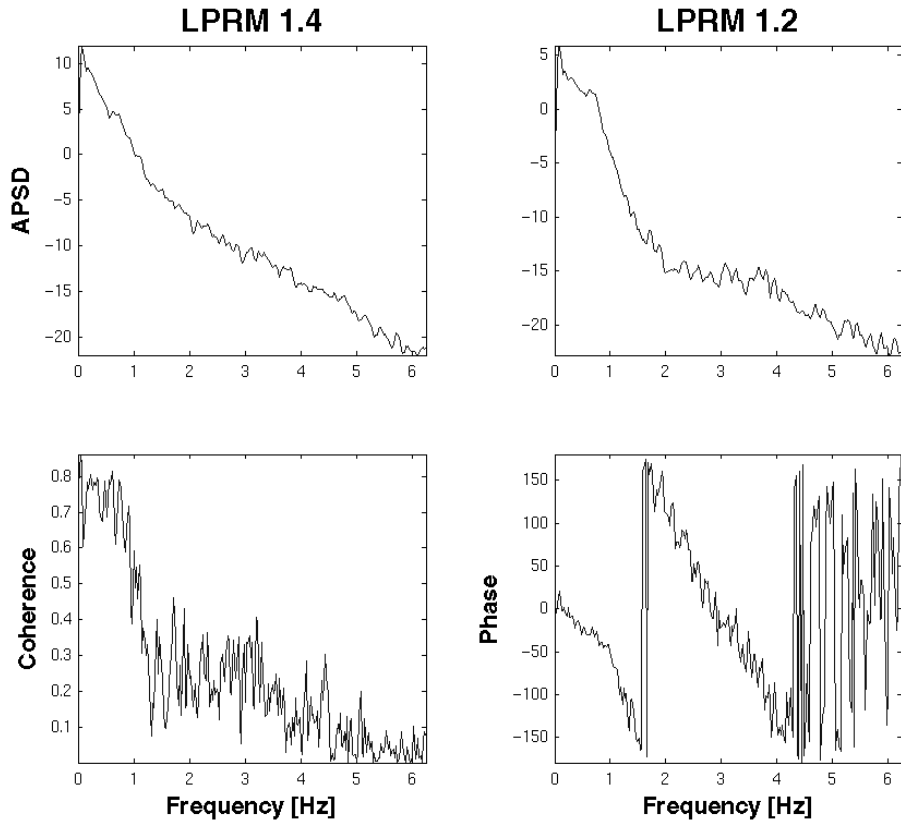
### 4.1 The measurements made in 2002 (Series #1)

Experience from earlier studies shows that classification and ranking of the probability and severity of impacting of the various strings is most effective if all cases are investigated and an internal comparison between the different strings is made. This is because the methods, at least for the traditional spectral analysis method, are not absolute, and the criteria for judgement are differing from core to core. For the first series of measurements, analysed in this section, the wavelet-based analysis was not effective, due to the low sampling frequency, hence in this section we shall concentrate on the spectral analysis.

For all strings included in the measurements, the APSD of both detectors within a string, as well as the coherence and the phase between the two detectors were taken. A complete list of these indicators, as well as the raw time signals and the APD functions (amplitude probability distributions) were listed in the internal report (Demazière *et al.*, 2003). Based on these data, the strings were classified as follows. Some strings did not show signs of vibrations and hence had no impacting at all. Some strings showed signs of mild vibrations where the probability of impacting was judged to be negligible. The next category is that of strings with definite vibrations and a non-negligible likelihood of impacting, such that the impacting was not judged to be severe. Finally some strings were judged to have severe impacting with a large confidence in the judgement, based on the experimental evidence. Examples of some of the cases, and in particular for the heavily impacting strings, will be shown below.

The spectra calculated and shown are made without normalising to the true DC component of the signals, and therefore the absolute values of the spectra are not comparable quantitatively. The magnitude of the peaks is therefore ranked in a qualitative way, namely in comparison to the smooth background. Some justification of this procedure can be given by comparing the spectra of the two detectors within the same string. Since Detector 2 in the string lies closer to the axial mid-point of the core than Detector 4 (there are altogether four detectors in one string with equal and symmetric spacing), for the fundamental frequency, which can only correspond to the fundamental mode of vibration, the vibration amplitude is larger for detector Position 2 than for detector Position 4 (assuming the same flux gradients, which is not always fulfilled). Figures 5 through 9 show that this is indeed the case, *i.e.*, the peaks at the fundamental frequency are always higher for the detectors (LPRMs, Local Power Range Monitor) at Level 2 than at Level 4 in the above sense, irrespective of the absolute value of the spectra in general.

String 1 (Figure 4) shows no signs of vibrations, hence this instrument tube has no impacting. As Figure 4 shows, the APSD has a smooth dependence on frequency, without any apparent peaks. The most convincing indicator of negligible vibrations is supplied by the phase curve. It has a clear linear shape up to 4.5 Hz, which is the maximum frequency range for Ringhals-1 where linear phase can be observed. For comparison it is interesting to notice that in Barsebäck-1 the linear phase extended well over 10 Hz, showing that the signatures are different even for nonvibrating strings for different cores. The coherence also has a structure that is associated with pure two-phase flow induced noise, with minima and maxima corresponding to the  $\pi$ - and zero-crossings of the phase, respectively.

**Figure 4** Autospectra, coherence and phase of the detectors in String 1, Measurement #1.

The strings with the largest likelihood of heavy impacting were found to be Strings 9, 10 and 22. The corresponding autospectra, coherence and phase curves are shown in Figures 5–7. These all show one or more peaks in the autospectrum, and a significantly distorted phase and coherence structure. LPRMs 9.2 and 9.4 (Figure 5) both show a broad peak at around 1.5 Hz. Here, LPRM 9.2 denotes Detector 2 in String 9 *etc.* In addition, peaks are present even at higher frequencies; in LPRM 9.2 the first higher harmonics at 3 Hz is seen, whereas 9.4 shows a peak at around 4.5 Hz, which corresponds to the second harmonics. The phase is nearly zero everywhere between 0 and 4 Hz, and the sink structure of the coherence is different from that of String 1, *i.e.*, the nonvibrating case. There is a peak in the coherence at 1.5 Hz, which is the fundamental frequency of the instrument tube vibrations.

Figure 5 Autospectra, coherence and phase of the detectors in String 9, Measurement #1

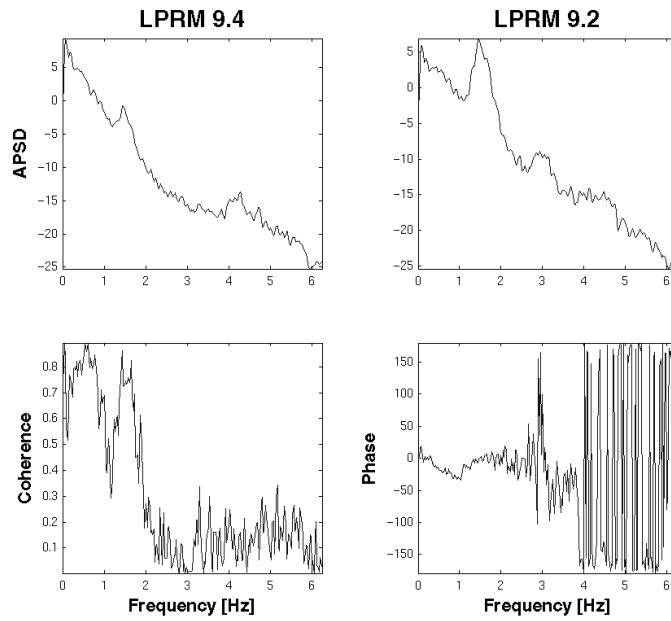
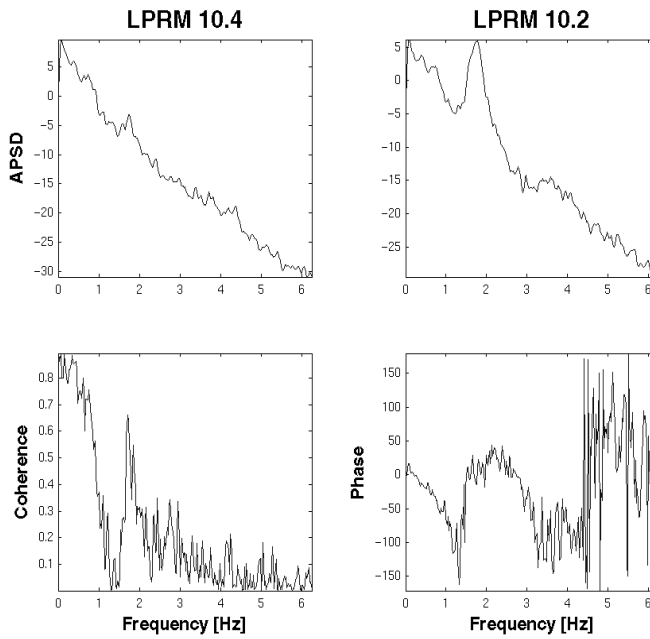
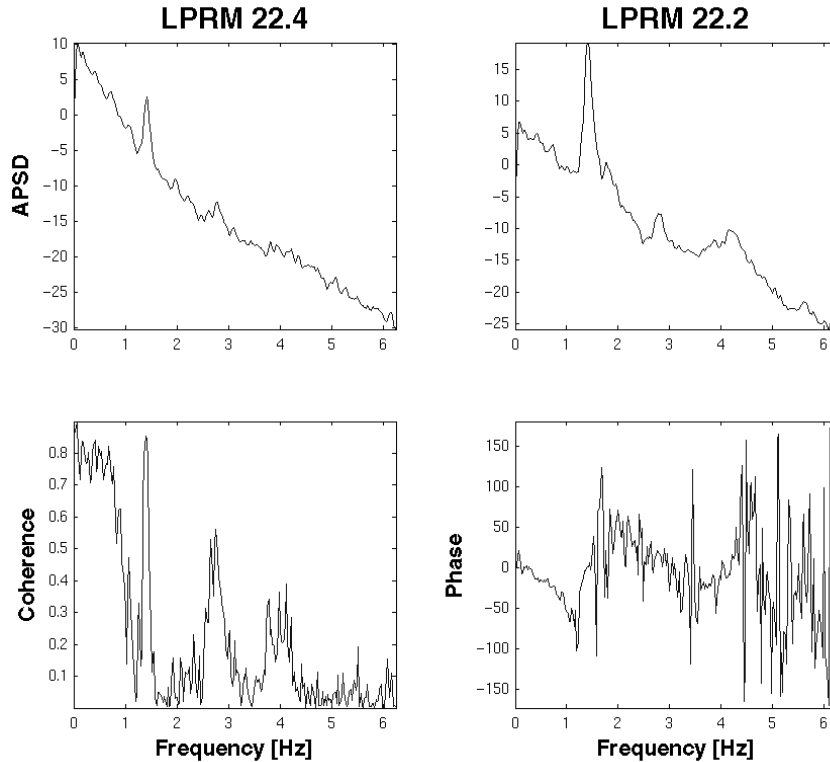


Figure 6 Autospectra, coherence and phase of the detectors in String 10, Measurement #1



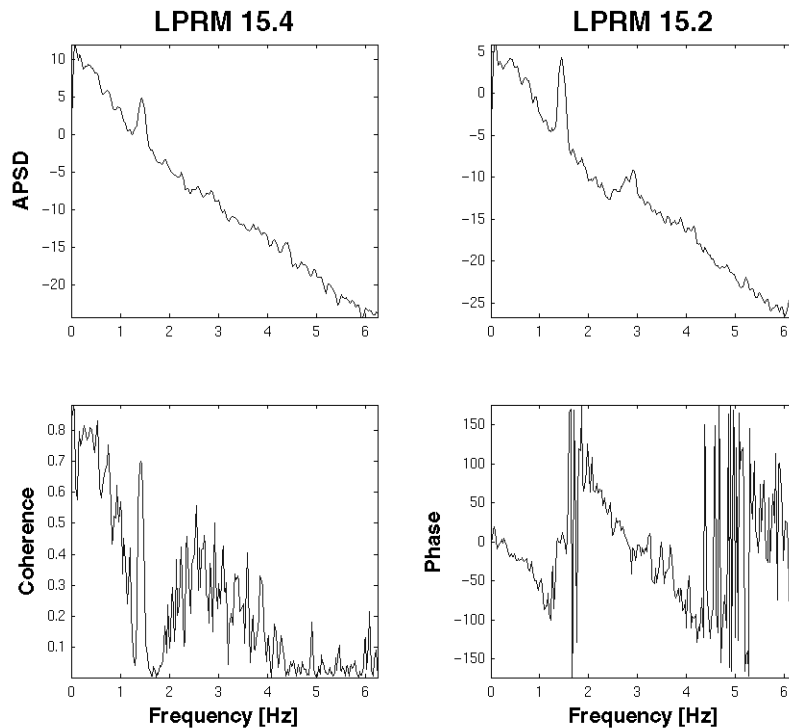
**Figure 7** Autospectra, coherence and phase of the detectors in String 22, Measurement #1

The analysis of the other two strings that were judged to have impacting goes in a similar manner. In the APSDs of the detectors in String 10 there is a broad peak at the fundamental frequency, and traces of peaks at higher frequencies. The phase starts out in a linear manner, but above 1 Hz it drops to zero. In String 22 there is a large peak at 1.5 Hz, which is not as broad as in the other two impacting strings, but several higher harmonics are seen with broad peaks. The phase and coherence are distorted, and the peak structure of the coherence is completely dictated by the positions of the peaks of the APSD, *i.e.*, the vibration eigenfrequencies.

Finally, one case is shown, String 15, with some possibility of impacting, whose likelihood and/or severity is nevertheless judged to be lower than for the above three cases (Figure 8). The same characteristic features are seen as for Strings 9, 10 and 22, but to a smaller extent. The peak at 1.5 Hz is smaller and is narrow, and the phase shows a linear dependence on frequency over a large part of the region 0–4 Hz, except at the vibration frequency. This case also illustrates the fact that there is no clear-cut separation between the cases of heavy and light impacting, and that the procedure is based on an expert evaluation of the calculated quantities. The results of the analysis of Measurement #1 are found in Table 1.

**Table 1** Results of Measurement #1

<i>Impacting status</i>	<i>By spectral analysis</i>	<i>By visual inspection</i>
Most likely impacting	9, 10 and 22	10 and 22
Probably impacting	4, 8, 16 and 24	–
Very small chance of impacts	11, 12, 30 and 33	–

**Figure 8** Autospectra, coherence and phase of the detectors in String 15, Measurement #1

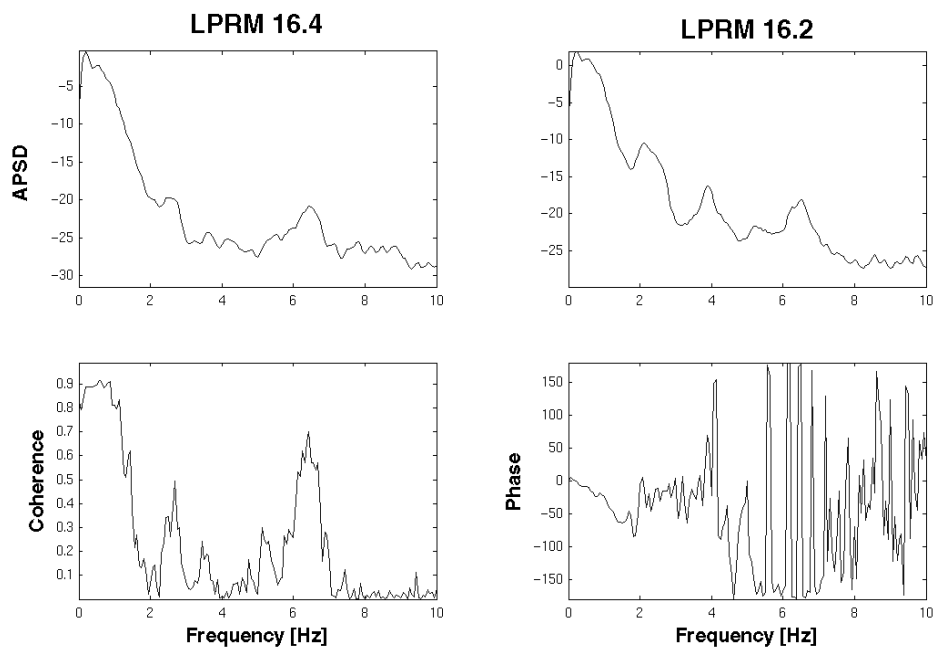
As was mentioned earlier, for this measurement, the wavelet-based impact detection algorithm was not applicable. The reason is the low sampling frequency of the measurement (which was primarily made for investigating BWR stability, whose characteristic frequency is about 0.5 Hz). The sampling frequency of 12.5 Hz means that the spectral quantities can only be calculated up to 6.25 Hz. This is sufficient to see the detector tube vibration peaks and the lowest higher harmonics. However, the damped vibrations of the fuel assemblies, induced by the impacting, are expected to lie in the range 10–15 Hz. The low sampling frequency causes two problems. First, the short transients ('spikes') in the signal, corresponding to the effect of the fuel assembly vibrations, can go undetected fully or partially. Second, the variance of the background noise, which is necessary to know in order to set the wavelet filter threshold, cannot be determined since this requires access to the high frequency tail of the APSD, above 10 Hz. For this reasons, no wavelet-based wavelet analysis of Measurement #1 was performed.

#### 4.2 The measurements made in 2003 (Series #2)

This measurement was performed with a sampling frequency of 64 Hz, which makes it suitable also for wavelet analysis. However, the analysis was first performed with the traditional spectral analysis, similarly as in the previous case. The principles are the same, therefore only a summary of the findings will be given here.

In these measurements, four strings were found to show the strongest vibrations, and these are Strings 15, 16, 24 and 35. As an illustration, the case of String 16 is shown in Figure 9. It shows the same features as those in measurement 1. There are several broad peaks at around 2, 4 and 6 Hz, *i.e.*, at the fundamental frequency and corresponding harmonics. One can note that these frequencies are somewhat higher than those in the previous measurement. The reason for this frequency change is not clear, but varying frequencies for the same strings in consecutive cycles, or in the same cycle between different strings, have been observed many times in the past in other works. One reason could be the different thermohydraulic conditions (mass flow, void fraction) and hence different magnitude of added mass in the flow-induced structural vibrations. The phase is close to zero at low frequencies up to 4 Hz and the peak structure of the coherence follows the peaks in the APSD closely. The other strings judged to execute impacting show similar features. They are not shown here for brevity. A summary of all the findings with classifications is given in the next section.

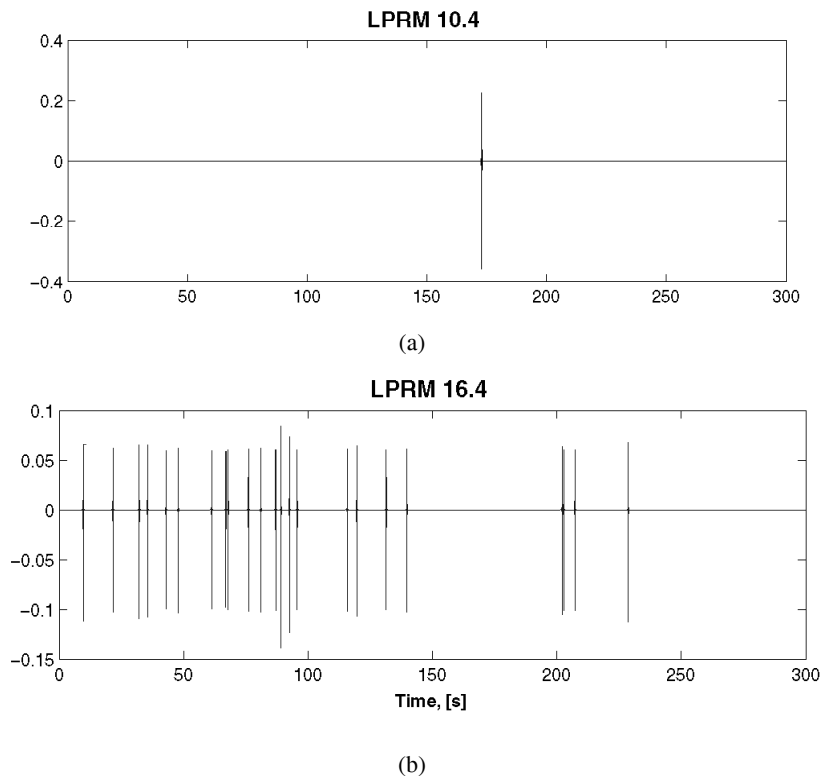
**Figure 9** Autospectra, coherence and phase of the detectors in String 16, Measurement #2



For measurement #2, the wavelet-based impact diagnostics was also possible to perform. Here, however it was noticed that the method, based on wavelet filtering and thresholding, which was also used in the evaluation of the Oskarshamn-2 measurements, had to be slightly modified. This is in line with the fact that when applying the method, originally used for Barsebäck, to the Oskarshamn measurements, also a modification was necessary before a good discrimination power of the method was achieved as follows.

The threshold given in Equation (3) was used on the wavelet coefficients of the two smallest scales, corresponding to frequencies higher than 10 Hz, of the multiscale resolution using the discrete Meyer wavelet (Wavelet Toolbox User's Guide, 2000). After the thresholding, the signal was reconstructed and the difference  $V$  (Equation 4), was examined for the possible occurrence of spikes, which are supposed to represent the intermittent fuel-box vibrations. In this measurement the best discrimination was obtained at core Level 4, *i.e.*, the lowest axial elevation. The quantity  $V$  (Equation 4) is shown in Figure 10a for LPRM 10.4, which is assumed to be non-vibrating, and in Figure 10b for LPRM 16.4, which is assumed to be impacting according to the spectral analysis. The difference between the two signals, as regards the number of impacting spikes found, is clearly visible. The IR index (Equation 5) for LPRM 16.4 is 4.6 impacts/min whereas for LPRM 10.4 it is only 0.2 impacts/min, confirming that String 16 is heavily impacting, whereas String 10 is not impacting or only extremely slightly.

**Figure 10** Difference  $V$  of the detectors at Level 4 in String 10 and String 16 showing the spikes corresponding to the fuel-box vibrations, Measurement #2.



Out of the 36 LPRM signals at Level 4, the following ones have IR index higher than two impacts/min: Strings 4, 16, 23, 24, 34 and 35. Out of these, Strings 16, 24 and 35 are identical with three of the four strings, pointed out by the spectral method to be the most probable impacting ones. String 34 is in the second highest category of impacting probability based on the spectral method. Thus the result from the wavelet-based analysis is in good agreement with the classical spectral analysis.

As was mentioned earlier, the new method of wavelet coherence was also tested on these measurements. The wavelet coherence was calculated by using a discrete real Meyer wavelet via Equations (6) and (7) for each string, using the two detector signals available per string. It was found that for certain strings a high value of the coherence was found between 10 and 20 Hz, which is the frequency range where the fuel box vibrations are expected to take place. For the other strings no such component was observed, so this analysis divided the LPRM tubes into two categories. A comparison with the results from the spectral and wavelet filtering analysis showed that the LPRM strings showing a large wavelet coherence around 15 Hz coincide with those that were pointed out as most likely impacting. An illustration is given in Figure 11, which shows four LPRM strings: two with high wavelet coherence at 15 Hz (Strings 16 and 35) and two others that have an average (low) coherence at these frequencies (Strings 1 and 17). A comparison with Table 2 confirms that these strings are suspected for strong impacting by the other two methods.

**Figure 11** Wavelet-based coherence, as a function of time, for four different detector strings. Figures on the left: Strings 1 and 17. Low coherence everywhere. Figures on the right: Strings 16 and 35. High coherence in the frequency band 10–20 Hz, indicating impacting.

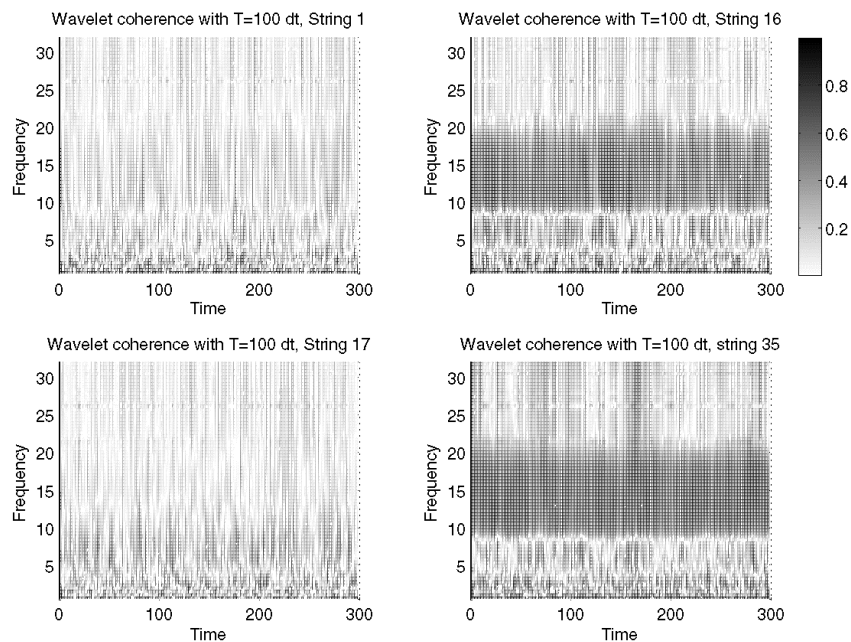


**Table 2** Results of Measurement #2

<i>Impacting status</i>	<i>By spectral analysis</i>	<i>By wavelet analysis</i>
Most likely impacting	15, 16, 24 and 35	16, 23 and 24
Probably impacting	12 and 34	4, 34 and 35
Very small chance of impacts	27 and 32	–

It is interesting to note that the ordinary FFT-based coherence has a large, sharp peak at around 15 Hz for all detector signals, with very little variation in the amplitude (Figure 12). The origin of this very narrow peak in the spectral-based coherence is not understood. Although it is in the middle of the frequency range found by the wavelet coherence method, which is attributed to the frequency of the impacting induced damped vibrations of the fuel assemblies, yet this appears to be given rise by a different physical phenomenon than flow-induced or impacting-induced vibrations. The narrow peak actually is seen even in the autospectra of the detectors, as is shown in Figure 13 for detectors at Level 2 for all four strings. Hence the peak cannot be related to impacting-induced intermittent vibrations, since those are not visible in the autospectra. One possibility would be that it corresponds to the flow induced stationary vibrations of the fuel assemblies which, like the stationary vibrations of the detector strings, are visible in the autospectra (Lansåker, 2004). However, the very narrow character of the peak makes even this assumption unlikely. Flow-induced vibrations of mechanical structures have a significant damping, and as a consequence, all vibration induced peaks have a significant width.

**Figure 12** Spectral based coherences for the four strings shown in Figure 11. In all four strings a narrow peak around 15 Hz is shown in the coherence, with somewhat lower magnitude for the strings that were not suspected as impacting by the other methods

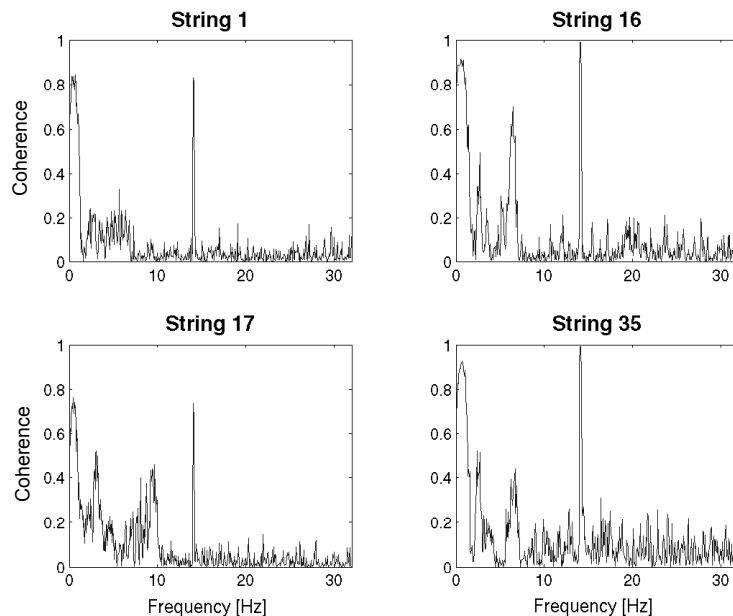
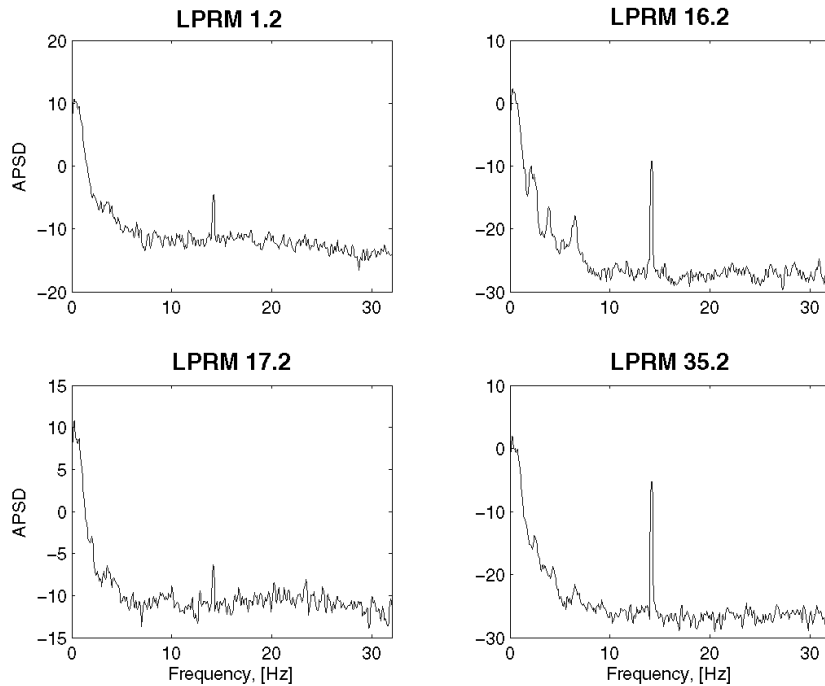


**Figure 13** APSD of Level 2 of the strings shown in Figure 12 for the whole frequency range showing a peak at 15 Hz.



The narrow peak in the spectral-based coherence, on the other hand, does not show up in the wavelet coherence, due to the fact that the frequency resolution of wavelet methods are much coarser (especially for higher frequencies) than the FFT-based methods. Hence it seems that, despite the quantitative coincidence of the frequencies where both the spectral and the wavelet coherence have peaks or high values, respectively, these correspond to physically different phenomena. It is also seen that the wavelet coherence has a much higher discrimination power for detecting impacting than the ordinary coherence. The performance of the wavelet coherence method has though to be confirmed by further tests.

## 5 Discussion

In measurement #1, only the traditional diagnostic procedure was applicable, so a comparison between the two methods was not possible. On the other hand, the predictions of the traditional spectral method could be compared to the results of visual inspection of several, but not all, fuel assemblies. The reason for the partial observation is that during an average refuelling, time constraints do not permit to inspect all four fuel assemblies around all 36 LPRM positions, only a few selected ones. One use of the vibration diagnostics is to restrict the number of inspected fuel assemblies into a limited set of suspected positions.

The result of the traditional diagnostics of measurement #1 can be summarised in Table 1. In the left side the classification of the different strings is given with respect to the probability or severity of impacts. This information was made available to the power plant as a recommendation on which LPRM positions should be inspected. In particular, the impacting Strings 9, 10, 22 and the nonvibrating String 1 (as reference) were recommended to be checked. During the refuelling in October 2003, a total of ten fuel assemblies around the four positions were inspected. Around Strings 1 and 9 no wear damages was observed, but two assemblies around LPRM 10 and one around LPRM 22 showed marks of wear (see the right column of Table 1). It is seen that a good correlation exists between the strings predicted to have impacting and the actual damage.

As regards measurement #2, no post-cycle inspections were available, since such inspections are made only in every second year. On the other hand, both the spectral and the wavelet-based analyses were possible to perform. The analysis results are summarised in Table 2 for the two methods. The Table shows that the strings pointed out as the most severely vibrating are not completely identical for the two methods, but they have a large overlap between the two groups. The Strings 16 and 24 are the ones pointed out by both methods to have the highest probability of impacting, hence they are the primary suspects for impacting. String 35 is in the highest group of the spectral method and in the second highest in the wavelet method. Finally String 34 is in the group with the second highest probability in both of the methods. Also the new method of using wavelet coherence was also tested for this measurements, and supplied results completely consistent with the findings of the spectral and wavelet filtering methods. The applicability of this latter method needs, however, to be confirmed in further measurements. It is also important to get feedback from the inspections during refuelling to confirm or deny the applicability of the methods. The inspection during a later revision will bring a very useful and important clarification regarding the performance of the two methods.

## **6 Conclusion**

Diagnostics of impacting of detector strings was shown to be possible by both spectral and wavelet-based methods. The spectral method was possible to apply to the Ringhals-1 case without any modifications compared to earlier applications. However, this method is not suitable for online monitoring by the operators; rather it requires expert judgement and works best offline. The wavelet-based method had to be modified compared to earlier applications before it turned out to be effective. This shows that the wavelet method, at least when first applied to a new core, does not fulfil the expectations of being suitable for an algorithmic, absolute (without calibration) and quantitative method that can be used for online monitoring by the operators. Nevertheless, it can be tuned to a specific core such that after tuning it can be used for online monitoring by non-experts. The tuning means finding the suitable mother wavelet form and the corresponding threshold values. It requires an analysis of all signals, and the optimum parameters are found by assuming that there are both non-impacting and impacting strings. In other words, the tuning of the method is just as subjective and based on expert knowledge as the traditional method. However, after having optimised for a given core, it fulfils the expectations of being an absolute, algorithmic method. This latter statement will be followed up in applying the wavelet method, optimised in this study, for later cycles in

the Ringhals-1 core. In addition, a new method of wavelet-based coherence was tested which, although at this point appears to be more like empirical without deep theoretical justification, seems to be directly applicable for a new core without tuning. Its applicability has though to be tested in more applications.

## Acknowledgement

This work was supported by Ringhals AB, contract Nos. 531970–003 and 543672–002.

## References

- Addison, P.S. (2002) *The Illustrated Wavelet Transform Handbook*, Bristol and Philadelphia: Institute of Physics Publishing.
- Arzhanov, V. and Pázsit, I. (2002) ‘Detecting impacting of BWR instrument tubes by wavelet analysis’, in D. Ruan and P.F. Fantoni (Eds.) *Power Plant Surveillance and Diagnostics-Applied Research with Artificial Intelligence*, Springer, Physica Verlag XIV, pp.157–174.
- Demazière, C., Sunde, C., Arzhanov, V. and Pázsit, I. (2003) ‘Final report on the research project ringhals diagnostics and monitoring, Stage 8’, *Chalmers Report CTH-RF-177/RR-10*, Chalmers University of Technology, Göteborg, Sweden.
- Fry, D.N., et al. (1977) *Summary of ORNL Investigations of In-Core Instrument Tube Vibrations in BWR-4*, ORNL/NUREG/TM-101, Oak Ridge National Laboratory.
- Lansåker, P. (2004) *Personal Communication*.
- Mallat, S. (1999) *A Wavelet Tour of Signal Processing*, Academic Press.
- Mott, J.E., Robinsson, J.C., Fry, D.N. and Brackin, M.P. (1976) ‘Detection of impacts of instrument tubes against channel boxes in BWR-4s using neutron noise analysis’, *Transactions of American Nuclear Society*, Vol. 23, p.465.
- Pázsit, I. and Glöckler, O. (1994) ‘BWR instrument tube vibrations: interpretation of measurements and simulations’, *Annals of Nuclear Energy*, Vol. 21, No. 12, pp.759–786.
- Pázsit, I., Åkerhielm, F., Bergdahl, B-G. and Oguma, R. (1988) ‘BWR instrument tube vibrations: theory of in-core detector spectra and interpretation of measurements’, *Progress in Nuclear Energy*, Vol. 21, pp.107–116.
- Pázsit, I., Demazière, C. and Arzhanov, V. (2003) ‘Research and development program in reactor diagnostics and monitoring with neutron noise methods, Stage 8’, *Final Report, SKI Report 2003:08*, Statens Kärnkraftsinspektion (Swedish Nuclear Power Inspectorate), Stockholm, Sweden.
- Pázsit, I., Demazière, C., Arzhanov, V. and Garis, N.S. (2001) ‘Research and development program in reactor diagnostics and monitoring with neutron noise methods, Stage 7’, *Final Report, SKI Report 01:27*, Statens Kärnkraftsinspektion (Swedish Nuclear Power Inspectorate), Stockholm, Sweden.
- Pokol, G. and Por, G. (2005) ‘The advanced loose parts monitoring system (ALPS) and wavelet analysis’, *International Journal of Nuclear Energy Science and Technology*, Vol. 2, No. 3, ppp. 237–248.
- Rácz, A. and Pázsit, I. (1998) ‘Diagnostics of detector tube impacting with wavelet techniques’, *Annals of Nuclear Energy*, Vol. 25, No. 6, pp.387–400.
- Thie, J.A. (1979) ‘Core motion monitoring’, *Nuclear Technology*, Vol. 45, pp.5–41.
- Thie, J.A. (1981) *Power Reactor Noise*, ANS, La Grange Park, Illinois.
- Thomson, O., Garis, N.S. and Pázsit, I. (1997) ‘Quantitative indicators of detector string impacting’, *Nuclear Technology*, Vol. 120, pp.71–80.
- Wavelet Toolbox User’s Guide (2000) ‘Wavelet toolbox user’s guide’, *The MathWorks, Inc.*

# Paper III

*Wavelet techniques for the determination of the Decay Ratio in Boiling Water Reactors*

C. Sunde and I. Pázsit

Kerntechnik **72**, 7 (2007)



C. Sunde and I. Pázsit

# Wavelet techniques for the determination of the decay ratio in boiling water reactors

The usefulness of wavelet transform and wavelet filtering techniques for the improvement of the estimation of the decay ratio (DR), characterising the stability of BWRs, is discussed. There are two distinct areas investigated. The first concerns the improvement of the quality of the traditionally used auto-correlation function (ACF) for the estimation of the DR, by trend elimination and denoising. The subsequent estimation of the DR itself is made by traditional methods such as the peak-to-peak method or curve fitting. The second area is the estimation of the DR by the use of continuous wavelet transform. The possibility of estimating two different DRs in case of dual oscillations, and in particular the finding of the higher DR, is also investigated. It was found that wavelet pre-processing does not always improve the estimation of the ACF of a non-ideal signal, compared to other methods; but for signals containing various trends and data scatter in the ACF, it brings a noticeable improvement. As an extension of the discrete wavelet methods, the continuous wavelet transform appears to be a promising candidate to determine the critical DR even in the case of two oscillations being co-existent with different stability properties. The methods investigated or developed here were also tested on measured data from Swedish BWRs.

**Wavelet-Technik zur Bestimmung der Zerfallsrate in Siedewasserreaktoren.** Der Nutzen von Wavelet-Transformations- und Wavelet-Filtertechniken zur Verbesserung der Bestimmung der Zerfallsrate, die die Stabilität von Siedewasserreaktoren charakterisiert, wird diskutiert. Dabei werden 2 getrennte Bereiche untersucht. Der erste Bereich betrifft die Verbesserung der Qualität der traditionell für die Zerfallsrate verwendeten Auto-Korrelationsfunktion durch Elimination von seriellen Abhängigkeiten oder Trends und Denoising. Die daraus folgende Bestimmung der Zerfallsrate selbst wird mit traditionellen Methoden wie z. B. der Peak-to-Peak- oder Curve Fitting-Methode durchgeführt. Der zweite Bereich ist die Bestimmung der Zerfallsrate mit Hilfe kontinuierlicher Wavelet-Transformationen. Die Möglichkeit der Bestimmung zweier verschiedener Zerfallsraten im Falle dualer Oszillationen und insbesondere die Bestimmung der höheren Zerfallsrate wird ebenfalls untersucht. Es stellte sich heraus, dass Wavelet Pre-Processing im Vergleich im anderen Methoden nicht immer die Bestimmung eines der Auto-Korrelationsfunktion eines nicht idealen Signals verbessert, aber für Signale mit verschiedenen Trends und Datenstreuung in der Auto-Korrelationsfunktion bringt es eine merkliche Verbesserung. Als Erweiterung der diskreten Wavelet-Methoden scheint die kontinuierliche Wavelet-Transformation eine aussichtsreiche Methode zur Bestimmung der kritischen Zerfallsrate, auch wenn zwei Oszillationen mit verschiedenen Stabilitätseigenschaften gleichzeitig vorhanden sind. Die hier untersuchten oder entwickelten Methoden wurden auch mit Hilfe von Messergebnissen schwedischer Siedewasserreaktoren überprüft.

## 1 Introduction

The stability of boiling water reactors (BWRs) has been a matter of interest since several decades now. The possibility of an instability of the coupled neutronic-thermohydraulic type was predicted by Thie as early as 1959 [1]. Since then, numerous cases of instability events have been observed at several plants worldwide. As experience was gained, several different modes of unstable flux oscillations became known, such as global, regional (azimuthal) and local or channel-type. In several cases, combinations of two modes occurred, making the quantification of the individual oscillations and in particular that of the most unstable one, difficult from the measurement data.

Naturally, the existence of BWR instability led to extensive research and development activity in the field. Work was pursued along three different avenues. The first of these concerns the efforts to understand the reasons for the occurrence of instability in core physics terms, identifying the root cause and the couplings and mechanisms between the various system parameters. This approach uses various simplified (from the system point of view), but non-linear models of coupled systems as their tool [2, 3]. The second avenue, conceptually overlapping with the first, concerns the numerical calculation of the most frequently used stability parameter, the so-called decay ratio (DR) from large core physics – thermal hydraulic system codes, [4–7]. The decay ratio can be successfully calculated using such codes and its correctness was seen through their agreement with measurements. At several plants this calculation of the DR is performed routinely before the start-up of the reactor after refuelling, to avoid the possibility of instability during start-up.

The third, and no doubt the largest, area concerns the actual quantitative determination of the decay ratio, from the measured in-core neutron noise. In its simplest form the DR is defined as the ratio of two consecutive maxima (in reversed order) of the autocorrelation function of the neutron noise. Even if the usefulness of the decay ratio as a measure of stability in BWRs has been questioned [8], it is still the most commonly used quantitative parameter used in practice.

During the years of BWR operation several methods for analysing the stability and determining the decay ratio have been suggested [9–16]. In these methods either a manual evaluation of the peak amplitudes of the ACF was made, or a curve fitting procedure was used. In addition to these traditional parametric methods, new algorithms and non-parametric estimation methods were also used. One such algorithm is constituted by Artificial Neural Networks, ANNs, which were successfully used to estimate the decay ratio on both simulated signals and measurements [12, 13]. Recently, Singular Value Decomposition, SVD, has also been used to calculate the decay ratio from signals from the Ringhals-1 BWR, [14]. A combination of SVD, ANNs and curve-fitting methods have been also been used to estimate the DR from the same BWR measurements with good results [15].

The subject of this paper falls into the last category above. Its purpose is the investigation of the usefulness of wavelet techniques in the determination of the decay ratio. This objective is motivated by the fact that wavelet techniques have been around as a promise under a long period with application potentials in a row of practical cases. However, the number of concrete applications and implementations is not that large as the promise would suggest. So one objective of this study was to explore whether wavelet techniques can contribute to the stability investigations in BWRs. Two principally different uses of wavelet techniques were explored. One consists of investigating whether wavelet de-noising and de-trending techniques can help to improve the accuracy of the traditional parametric methods of determining the DR. This study was inspired by an early paper on wavelet applications by Domis and Tambouratzis [17], who investigated the separation of the coloured noise, corresponding to the response of a system to a white noise input, from a trend (temporal variation) in the expected value of the signal. Similarly to their case, we will test the performance of the method on simulated (synthetic) signals, but also on real measurements. The difference in our case is that we will do the wavelet processing on the ACF, rather than on the raw signals, and will try to eliminate both a linear or an exponential trend in the signal as well as irregularities in the calculated ACF, which can be interpreted as “noisiness” of the ACF.

The second line of applications consists of the use of the continuous wavelet transform for the determination of the DR. This is a relatively new method, which was suggested by Espinosa-Paredes et al. [18], where they calculated the instantaneous decay ratio. It is a promising method that can be used to real-time monitoring of the instantaneous DR, as well as to detect, under some circumstances, the coexistence of two different DRs. This method will be described and investigated in more detail in the second last Section of the paper.

## 2 General principles

The dynamic behaviour of a BWR core in the stable region, i.e. when no limit cycle behaviour can be observed, is often described as a second-order system. This means that the flux fluctuations,  $\delta\phi(t)$ , obey a second-order equation driven by a random (white) force  $f(t)$  as

$$\delta\ddot{\phi}(t) + 2\xi\omega_0\delta\dot{\phi}(t) + \omega_0^2\delta\phi(t) = f(t) \quad (1)$$

where  $\xi$  is the damping parameter and  $\omega_0$  is the eigenfrequency (resonant frequency, usually 0.5 Hz) of the system. Here, both  $\delta\phi(t)$  and  $f(t)$  are assumed to be stationary ergodic processes. A visual inspection of the time behaviour of BWR in-core detector signals in case of an instability readily shows that the signals are not stationary (and hence not ergodic), which can explain partly the deviation of the measured ACFs from the ideal one. As is easy to confirm [11], the ACF of  $\delta\phi(t)$ , defined as

$$ACF(\tau) = \int \delta\phi^*(t + \tau) \delta\phi(t) dt \quad (2)$$

is given as

$$ACF(\tau) = Ce^{-\xi\omega_0\tau} [\cos(\omega_0\tau) + \xi \sin(\omega_0\tau)] \quad (3)$$

This represents a periodic oscillation with an exponentially decaying envelope, Fig. 1a. From this latter expression, under some simplifications, it is easy to confirm that the decay ratio is equal to

$$DR = e^{-\xi 2\pi} \quad (4)$$

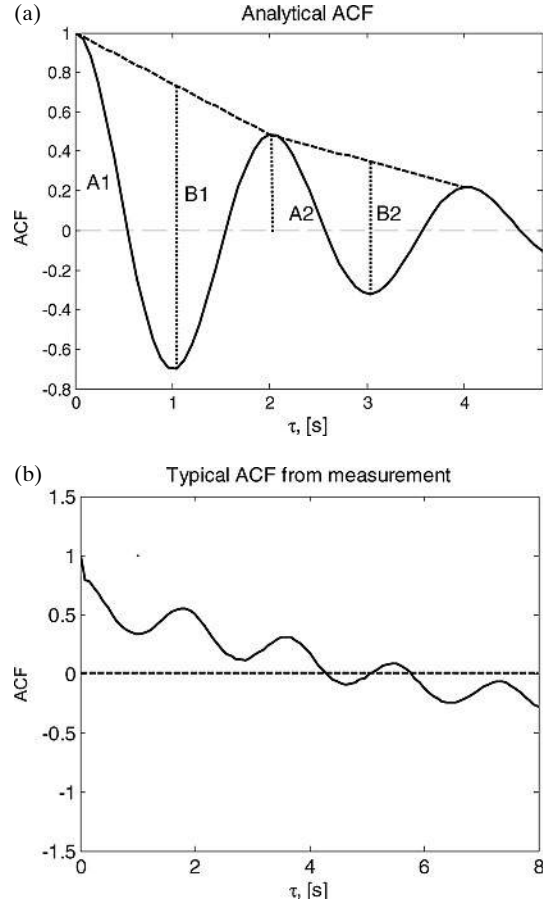


Fig. 1. In (a) an analytical ACF is shown where the decay ratio can be defined as either  $DR = A2/A1$  or  $DR = B2/B1$ . In (b) a typical ACF, which is linearly disturbed, from one measurement taken at Ringhals-1 in 1990 is shown

The parameters  $C$ ,  $\xi$  and  $\omega_0$  can be obtained from the experimentally determined ACF by means of least-square fitting [10]. This method has the advantage that, in contrast to the traditional method to be described below, makes use of the whole ACF and not only a few maxima and minima. The parameter estimation method, on the other hand, is based on the assumption of ideal second-order system behaviour. As is shown in Fig. 1b, taken from a real measurement, the experimental ACFs deviate from this behaviour, which means that the curve fitting method should be modified to incorporate also a model of the deviations. In this respect some of the simplest and earliest estimations of the DR can be more robust.

The traditional way to calculate the decay ratio is by taking the ratio between two successive maxima from the ACF, i.e.  $A2 = A1$  from Fig. 1a. In case of an ACF containing a trend, such as in Fig. 1b, a better way of estimating the decay ratio, as suggested by van der Hagen et al. [9], is to use the information from three maxima and two minima. With these, the decay ratio is estimated as  $B2 = B1$ , illustrated in Fig. 1a. It is even better to use the 2nd, 3rd and 4th maxima and 2nd and 3rd minima, i.e.  $B3 = B2$ , since the first maxima can contain the effect of a white noise in the signal, in form of a sharp peak. This method will be called the peak-to-peak method in the continuation of this paper. The use of peak-to-peak method will give a better estimation of the decay ratio than the maxima expression alone if the ACF contains a trend. This latter was the case in the measurements taken at the Swedish nuclear power plant Ringhals-1 in 1990 [19, 20], see Fig. 1b.

For an ACF which has an appearance of a decaying oscillation around a trend line instead of zero, it is a natural idea to try to eliminate the trend with some better founded algorithmic procedure than the peak-to-peak method. One possibility is to use the discrete wavelet transform to eliminate trends from the measured ACF. This possibility will be investigated in the forthcoming sections.

In short measurements, i. e. when the on-line determination of the DR is of concern, the statistics of the calculated ACF will be relatively poor. This manifests itself as if the ACF contained some “noise”. This is though only bit noise from the measurement and estimation error due to the finite length of the sample. Nevertheless such irregularities in the ACF worsen the accuracy of the estimation of the ACF. Removing such irregularities in the ACF can be performed by discrete wavelet de-noising techniques. The capability of these techniques for improving the quality of the ACF will be examined in this paper as well.

The choice of wavelet analysis is motivated by the fact that the signal pre-processing is made directly on the input to the algorithm that extracts the decay ratio, i. e. on the auto-correlation function (ACF). Investigation of the preconditioning of the raw detector signal time series was performed by Thomson et al. [21]. Such traditional, spectral filtering based methods can be performed on stationary ergodic signals. However they will not be able to eliminate the reasons leading to the deviation of the “real” ACFs from the ideal ones corresponding to a pure second-order system since those deviations are most likely due to the system not being second order, the signals being non-stationary, to the existence of interfering signal components from other noise sources etc. In addition, such methods cannot be applied on short, transient-like signals such as an ACF which, being interpreted as a signal itself, is not stationary, rather it looks like a short transient that dies away after a few oscillations.

The study that will be reported on in these investigations is empirical in character, and it will be performed as follows. We start by choosing an idealised ACF in the form of Eq. (3) with given parameters  $\zeta$  and  $\omega_0$ . Hence for each case we also know the true DR which is given by Eq. (4). Then we simulate the “real world” ACFs by adding a linear or exponentially decaying trend, and/or a “white noise” (simulating measurement inaccuracy, finite signal length etc). On these “real” signals we perform a wavelet de-trending and/or de-noising, corresponding to the type of disturbance that we added to the ideal signal. After that we calculate the DR from the pre-processed signal both by the peak-to-peak method and the curve fitting method. These results are then compared to those obtained from the disturbed ACF, without pre-processing, to see the effect of the wavelet pre-processing.

In some measurements it was observed that two instability modes co-existed with different DRs and different amplitudes, but with the same or nearly the same frequency. Due to the same or close to same frequency, those oscillations cannot be separated by frequency filtering methods. If the more unstable mode occurs in the signal of an LPRM (in-core detector) with a smaller weight than the stable mode, then the single DR extracted from the signal will be closer to that of the stable component, unless one is aware of the dual oscillations and devises a separation method to extract the higher DR. If this is not done, the operators perceive an incorrect margin to instability. Hence, it is desirable to determine both decay ratios present, or at least the one closest to instability in a correct way. This problem will also be addressed in this paper by the use of the continuous wavelet transform.

### 3 Decay ratio estimation by trend elimination and de-noising using discrete wavelet techniques

#### 3.1 Principles and choice of wavelet

The de-trending and de-noising will be performed by discrete wavelet analysis, the principles of which are described thoroughly by Addison [22]. Hence the details of this technique will not be described here, only the main steps of its application. Given a discrete wavelet  $\psi_{m,n}(t)$  and its scaling function  $\phi_{m,n}(t)$ , the signal can be decomposed into an approximation  $A_M$  by the scaling function, and a sum of details  $D_n$  by the wavelet function in the form:

$$x(t) = A_M + \sum_{n=1}^M D_n \quad (5)$$

Such a decomposition of the signal is called a multi-resolution analysis. In the above,  $n$  is the scale (dilatation index) and  $m$  the translation index. Each detail,  $D_n$ , represents the part of the signal corresponding to a scale, uniquely related to the frequency band of the wavelet. For discrete wavelets, the characteristic frequency for each  $n$  is determined by the sampling frequency of the signal and the centre frequency of the analysing wavelet.

In contrast to traditional spectral analysis, in wavelet analysis there is a freedom regarding which analysing function one should use. There are no rigorous criteria on which one could base a unique decision, rather the choice of which wavelet to use is rather arbitrary. In most cases, however, it is advantageous to choose a wavelet which has the same features as the signal being analysed. We have found that in this case the discrete Meyer wavelet is a good choice. Other wavelets did perform well too during our tests, such as higher order Daubechies wavelets. The mother wavelet for the discrete Meyer wavelet is shown in Fig. 2.

Due to the relationship between the sampling frequency of the signal, the type of the wavelet and the centre frequency of the wavelet, it is possible to calculate which frequency each level,  $n$ , represents for a given wavelet and sampling frequency. For the discrete Meyer wavelet (*dmey*), with a sampling frequency of 12.5 Hz (same frequency as the Ringhals-1 BWR measurements), the relationship between  $n$  and the frequency is given in Table 1.

From Table 1 it is seen that scale levels 4 and 5 are the closest to the generic frequency of BWR instability oscillations, 0.5 Hz. Slow trends correspond to wavelet components higher than level 4–5, whereas broadband noise in the ACF will correspond to smaller scales.

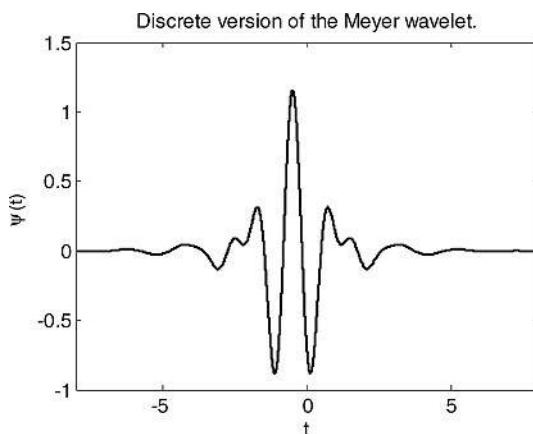


Fig. 2. Mother wavelet of the discrete Meyer wavelet

Table 1. Connection between level and frequency for *dmey*

level, n	frequency, (Hz)
1	4.1460
2	2.0730
3	1.0365
4	0.5183
5	0.2591

### 3.2 Trend elimination

Observation of experimental ACFs, such as in Fig. 1b, suggest that both linear and exponentially decaying trends can appear in the evaluated measurement of BWR in-core noise. These will be the two types of trends that we will investigate both separately and in combination. It is worth first making a brief test of how the trends themselves can be reconstructed by multi-resolution analysis by the discrete Meyer wavelet. To this order we analysed a linear function (Fig. 3a), used later to introduce a linear trend to an ideal ACF, and an exponentially decaying one (Fig. 3b) with multi-resolution analysis.

The best agreement between the trends and the wavelet approximations are at level 4 and level 5. The linear trend is estimated better than the exponential one, since the exponen-

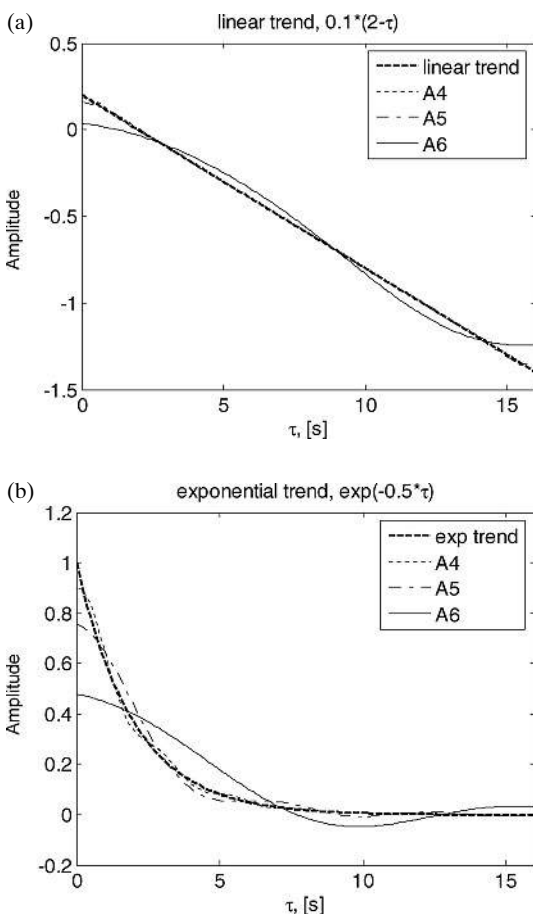


Fig. 3. In (a) a linear trend and approximations at different levels are shown. Level 5 and 6 have the best agreement with the trend. In (b) an exponential trend and approximations at different levels are shown. Level 5 has the best agreement with the exponential trend

tial trend contains a number of different frequencies, hence some parts of the exponential trend are found at lower level details. Although both trends appear to be best approximated at level 4, in the trend elimination we shall use level 5 as the approximation level. The reason is that, as mentioned above, the main subject of the investigation, the instability around 0.5 Hz, corresponds partly to level 4, hence elimination of this level would interfere with the unfolding of the information about the decay ratio by multi-resolution analysis.

For the analysis, the “real” (realistic) signal was constructed from the “ideal” one through the relationship

$$ACF_{real}(\tau) = \frac{ACF_{ideal}(\tau) + trend(\tau)}{ACF_{real}(\tau = 0)} \quad (6)$$

Here and in the remainder of the paper  $ACF_{ideal}$  is calculated according to Eq. (3). Based on the considerations above regarding the relationships between the levels, wavelet frequency and the frequency of the BWR oscillations, the de-trending of the real ACF can be performed by two slightly different methods. In the first method the ACF is estimated as the difference between the real ACF and its approximation at level 5:

$$detrend1(\tau) = ACF_{real}(\tau) - A_5(\tau) \quad (7)$$

In the second method the ACF is reconstructed by simply using the details at level 4 and 5,

$$detrend2(\tau) = D_4(\tau) + D_5(\tau) \quad (8)$$

The difference between the two methods is that the second one does not make use of information from details at levels 1–3. After the de-trending, the extracted ACF is re-normalised to unity at zero time-lag, in order that the extracted curves shall correspond to the analytical ones.

These two methods were investigated quantitatively for the cases of a “real” (simulated) signal, containing a linear and an exponential trend, respectively. The results are shown in Fig. 4. The effect of the de-trending on the signal shape is shown in Fig. 4a for the linear trend, and in Fig. 4b for an exponential trend. It is seen that the original (ideal) signal shape is reconstructed very well for the case with the linear deviation from the ideal signal in the real ACF, and somewhat worse when the real signal contains an exponential term. There is no large difference in the performance of the two different de-trending methods.

The important question is, however, how much the de-trending improved the possibilities to unfold the decay ratio from the de-trended signal as compared to the raw (real) signal. The results are seen in Fig. 4c–d which show the absolute error between the estimated decay ratios and the analytical decay ratios for a number of different decay ratios. The decay ratio from the de-trended signal was estimated by the curve-fitting method (CF) and the peak-to-peak method. The DR as calculated from the real signals was performed by the peak-to-peak method, which served as a reference for the performance of the traditional methods. The accuracy of all DRs obtained was compared to the true value of the DR, known from the analytical form of the ACF.

The results of this analysis are somewhat surprising. For the case of the linear trend in the real signal, where the reconstruction of the original (ideal) form of the ACF from the real one appeared to be rather successful, it turns out that the traditional method of determining the DR from the real signal gave a more accurate estimation than the evaluation of the DR from the de-trended signal. Especially for high decay ratios, which is the most important case for the diagnostics, the evaluation of the real ACF lead to much smaller errors than

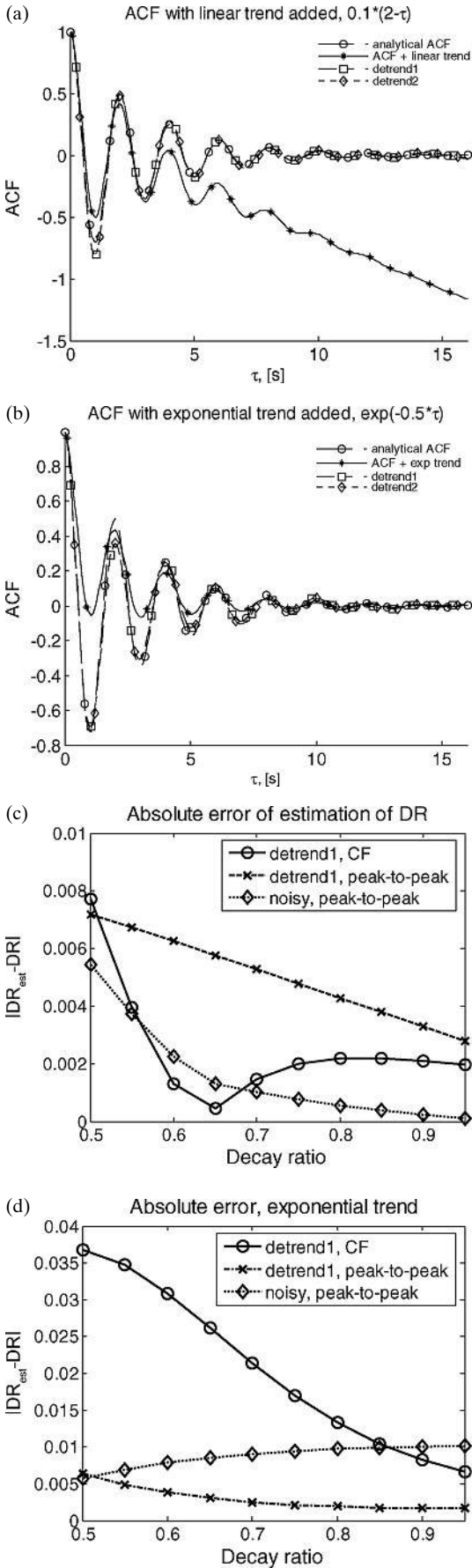


Fig. 4. Real ACF and de-trended ACF with a linear trend (a) and an exponential trend (b) added, DR = 0.6 and  $f = 0.5$  Hz. In (c) the absolute error of estimated DRs for the linear trend added are shown and in (d) the same is shown for an exponential trend

that of the de-trended signal. Due to the similar performance of the two de-trending methods, only results corresponding to the method *detrend1* are shown. The curve fitting (CF) method performs better than the peak-to-peak method when applied to the de-trended signal. Even the analysis of the case with the exponential trend in the real ACF gave similarly counterintuitive results. Although the reconstruction of the ideal shape of the ACF was less successful than in the case of the linear trend, the decay ratios determined from the de-trended signal here are superior in accuracy to that of the traditional method.

Even in this case the two de-trending methods perform similarly; but regarding the unfolding of the DR, now it is the peak-to-peak method which performs better. Finally, we have also investigated the case when a mixture of a linear and an exponential trend exists in the ACF, again based on the experience from the measurement in Ringhals-1. In that case the “real” ACF was assumed to have the form

$$ACF_{real}(\tau) = \frac{ACF_{ideal}(\tau) + 0.1(2 - \tau) + e^{-0.5\tau} + 1}{ACF_{real}(\tau = 0)} \quad (9)$$

Fig. 5a shows the disturbed (“real”) signal, the ideal (analytical) one and the de-trended ACFs. Again, the agreement between the de-trended and the analytical ACF is not perfect. However, similarly to the case of the pure exponential trend, the estimation of the decay ratio is improved noticeably, at least for values of the DR higher than 0.6, for the de-trended signal as compared to that of the real signal, as is seen in Fig. 5b.

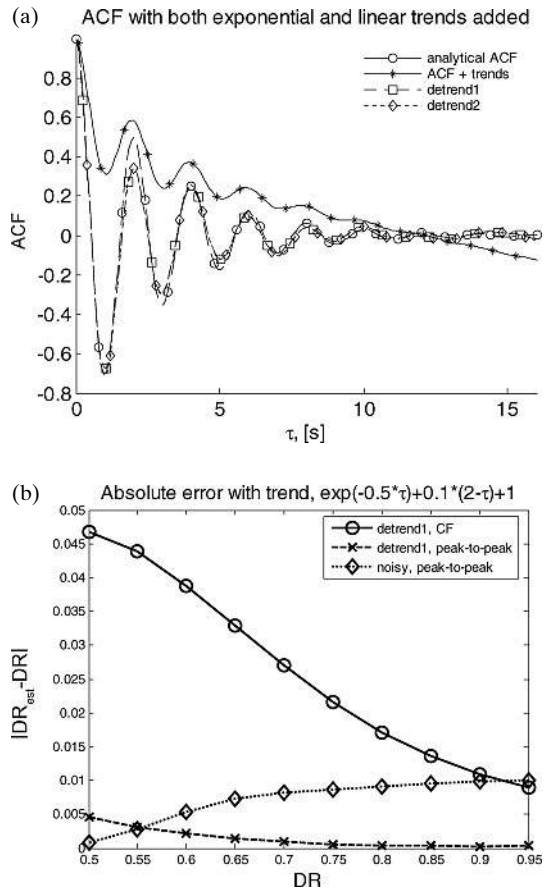


Fig. 5. ACF and de-trended ACF with a linear and an exponential trend (a) added, DR = 0.6 and  $f = 0.5$  Hz. In (b) the absolute error of estimated DRs for different values of decay ratio in the ACF

The conclusion is that under some circumstances, wavelet pre-processing of the ACF can help improving the accuracy of the determination of the DR, but the result is not universally valid. It can be summarised that since a pure linear trend is unlikely to occur in practice, the wavelet pre-processing should be useful in general, since it worked well for cases containing more complicated trends than a simple linear one. However, the value of this statement should be investigated with real signals. It is a more important observation that a better similarity between the pre-processed signal to the ideal one, as compared to the real signal, does not guarantee a better estimation of an underlying parameter of the ideal curve. Similar observations were made also in other parameter estimation studies, such as determining the reactivity from a pulsed Feynman-alpha measurement with curve fitting [24].

The results presented here warrant some caution on the uncritical use of wavelet methods in parameter estimation. The usefulness of the wavelet methods, especially in de-noising, manifests itself by the removing of unwanted terms, the success of which process is confirmed visually. However, often the final goal is to extract a certain parameter with some algorithm by knowing the theoretical form of the process signal or its derived quantities (spectra, correlations, cumulated counts etc). The chances of better parameter estimation, as seen above, are not always improved by seemingly improving the agreement between the measured (real) and the ideal curve (such as an ACF).

3.3 Signal de-noising (eliminating parasitic white noise)

The subject of this investigation is to see how much the estimation of the DR can be improved in the case the measured ACF is not smooth, rather it shows a scatter of the data around an ideal smooth curve. We shall interpret such a scatter as the presence of a white or broad-band noise, and will study the effect of eliminating this component by wavelet filtering, before estimating the DR. Accordingly, in the simulations, we will assume the real ACF having the following form:

$$ACF_{noise}(\tau) = ACF_{ideal}(\tau) + \zeta(\tau) \tag{10}$$

Here  $\zeta(\tau)$  is a Gaussian process, which is generated by a random number generator. After sampling, the train of random numbers will be normalized with a constant factor in order to change the root-mean-square (rms) of the “noise” to a desired value.

Wavelet filtering is an effective tool to remove unwanted Gaussian noise. The term filtering here refers to a truncating process in which the detailed (high frequency) wavelet coefficients, obtained by discrete wavelet transform, are discarded if their amplitude is less than a pre-set threshold, where after the modified coefficients are used in an inverse wavelet transform to obtain a “wavelet filtered” form of the signal.

A central issue here is a suitable choice, or calculation (preferably through an algorithmic procedure from the signal values themselves) of the threshold value. One can use either the same threshold at all levels of the multi-resolution analysis, called global thresholding; alternatively, one can use a different threshold value at each level, i.e. level dependent thresholding. Moreover, for a given threshold, one can use either soft thresholding (just deleting all coefficients under the threshold) or hard thresholding (decreasing the value of the remaining coefficients, whose minimum is equal to the threshold, with the threshold value). Details on these ques-

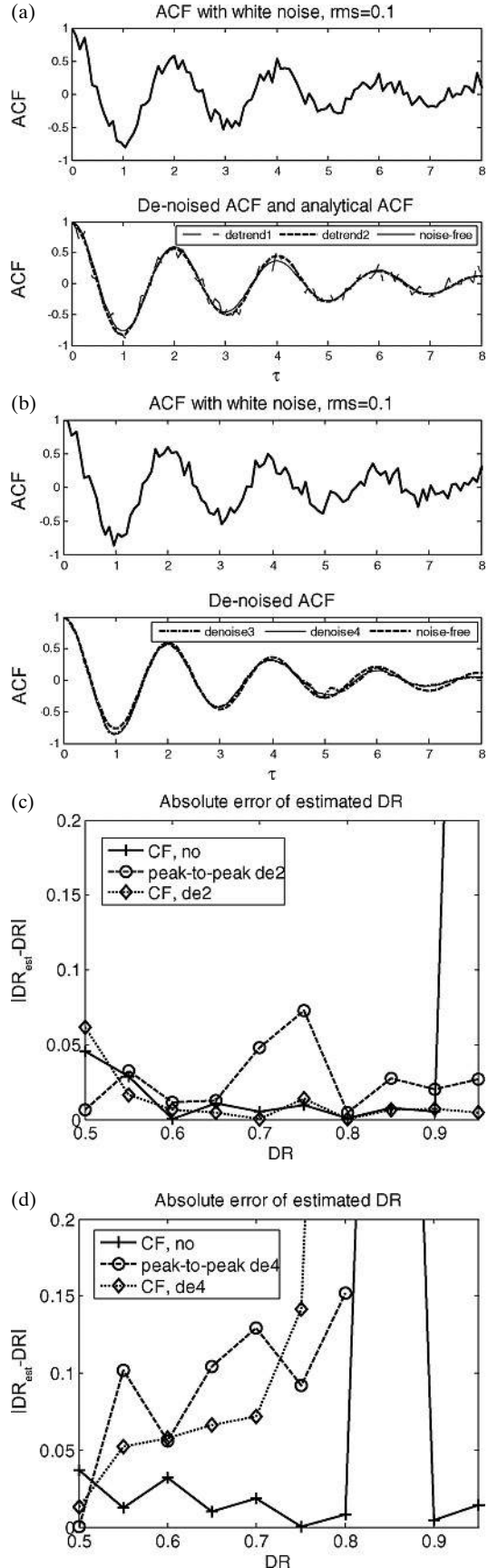


Fig. 6. In top of figure (a) the noisy signal with DR = 0.6 and f = 0.5 Hz is shown and in the bottom the noise-free and de-trended signals are shown. In figure (b) the same is shown except that the de-noising algorithms are used instead. In (c) and (d) the corresponding estimations of the decay ratios are shown. The estimation is based on both curve-fitting and peak-to-peak methods

tions can be found in [22]. Choosing the thresholding strategy that fits the problem best is usually an empirical process, achieved with trial and error. We have performed an extensive testing in this sense, and found that in the specific case treated here, the best results were obtained by soft, level dependent thresholding calculated by using Stein’s Unbiased Risk procedure [23] to achieve de-noising.

To perform the de-noising, equations (7) and (8) are modified to the following expressions:

$$denoise3(\tau) = wden(ACF_{noise}(\tau)) - A5(\tau) \tag{11}$$

and

$$denoise4(\tau) = deD4(\tau) + deD5(\tau) \tag{12}$$

where *wden* is the de-noising algorithm and *deD4* and *deD5* are the de-noised details at level 4 and 5.

Some quantitative results are shown in Fig. 6, which shows a “real” ACF containing added noise, together with the ideal (noise-free) ACF and the ACF:s after wavelet pre-processing. Actually we tested both the de-trending methods of Eqs. (7)–(8) (Fig. 6a) as well as the de-noising ones, Eqs. (11)–(12) (Fig. 6b). The motivation for the former is that although they are not specifically aimed at eliminating high frequency noise from the signal, they still act into this direction by amplifying the frequencies in the signal that are most relevant for the oscillation frequency of the instability. In these calculations, the decay ratio was chosen to be 0.6, the eigenfrequency to 0.5, and the added noise had an rms value of 0.1.

The results regarding the estimation of the decay ratio are seen in Fig. 6c and d, which show the absolute error of the estimation for the selected methods. It is seen that the second method, devised for trend elimination, has the best performance. This time this is valid both for the reconstruction of the ideal form of the ACF and the estimation of the decay ratio. This is due to the fact that no information about the signal is present in the lower level details and hence they can be removed without losing any information, whereas the white noise is present with a low weight at levels 4 and 5. It is somewhat unexpected that what regards the estimation of the DR, it is better to only use the details without any thresholding of the coefficients, which usually would be thought to be the natural way to de-noise a signal.

### 3.4 Elimination of both the trends and the white noise

As a last step, the de-trending and de-noising methods developed in the two previous section will be combined in order to wavelet pre-process an ACF which is corrupted by both trends and white noise. Hence the simulated signal with both trends and noise will have the form

$$ACF_{noise}(\tau) = \frac{ACF_{ideal}(\tau) + 0.1(2 - \tau) + e^{-0.5\tau} + 1 + \zeta(\tau)}{ACF_{noise}(\tau = 0)} \tag{13}$$

Due to the experience from the pure de-trending and de-noising cases treated in the foregoing, again all four algorithms were tested. As before, the DR was determined by using either the peak-to-peak method or the curve-fitting method from the wavelet processed signal.

The results are shown in Fig. 7 from the de-noising of an ACF with both trends and white noise added. In Fig. 7a the real ACF is shown, together with the ideal ACF as well as the de-trended and de-noised ACF using the best method, *detrend2* given by Eq. (8). In Fig. 7b the absolute error for the estimation of some decay ratios are shown; the peak-to-

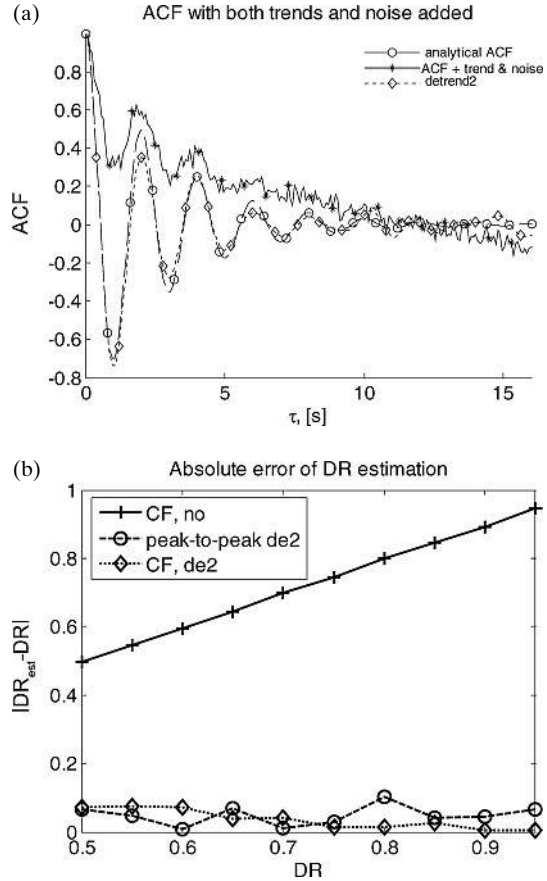


Fig. 7. In (a) an ACF with both trends and white noise are shown together with the original ACF and the de-noised ACF. In (b) the absolute error for the estimation of the decay ratio is shown

peak and curve-fitting method performed on the de-noised ACF, and the curve fitting method on the real ACF. The peak-to-peak method was not applied on the realistic ACF because it is cumbersome to apply that method to a noisy signal.

In this case now there is a significant advantage in using the wavelet pre-processing for the improvement of the estimation of the DR. It is interesting that here again, this improvement is achieved despite that fact that the form of the same wavelet de-trended and de-noised signal does not agree very well with the form of analytical ACF curve. Applied on the wavelet pre-processed ACF, both the CF and the peak-to-peak methods supply a much more accurate value of the DR than the curve-fitting performed on the realistic ACF containing both trends and noise. Since real-world ACFs taken from measurements are likely to be affected both by trends and scatter of data, the wavelet pre-processing could prove useful in improving the quality of the estimation of the DR. The experience gained here (both the negative and the positive ones) can be transferred to other areas of parameter estimation from measurements where deviations from the ideal expected signal form are present.

## 4 Using the continuous wavelet transform for the determination of the DR

Wavelet techniques can be used not only to improve the quality of the input data, such as the ACF, to other algorithms that calculate the DR, but can also be used for the determination of the DR directly from the raw time series signals or from

the ACF. By virtue of the capability of the wavelet transform to resolve both time and frequency dependence and to handle non-stationary processes, such techniques are even capable to calculate the instantaneous decay ratio during a transient change of the state of the system [18]. However, in this work, we will confine ourselves to the use of the continuous wavelet transform (CWT) for the determination of the DR in a quasi-stationary case, i.e. we are not going to follow up the time variation of the DR. Methods for achieving this latter have been reported by Staszewski [25, 26] and by Hera and Hou [27]. In all these works a complex continuous wavelet transform of the ACF is used to calculate the decay ratio of second order systems.

The essence of the method can be summarized as follows. Applying a progressive complex wavelet transform (containing no negative frequencies), such as the complex Morlet wavelet on the ACF

$$ACF(t) = A_0 e^{-\xi\omega_0 t} \cos(\phi(t)) \quad (14)$$

Then the wavelet transform can be approximated as [28, 29]

$$W(ACF)(a, b) \approx \frac{1}{2} A_0 e^{-\xi\omega_0 b} e^{i\phi(b)} G^*(a\phi'(b)) \quad (15)$$

From this, the modulus of the wavelet transform is calculated as

$$|W(ACF)(a, b)| \approx \frac{1}{2} A_0 e^{-\xi\omega_0 b} |G(a\phi'(b))| \quad (16)$$

Here,  $W(f)(a, b)$  is the wavelet transform of  $f$  and  $G$  is the Fourier transform of the analysing wavelet and from Eq. (3)  $\phi(b) = \omega_0 b + \varphi$  giving  $\phi'(b) = \omega_0$ .

The next step is to take the logarithm of Eq. (16) at the ridge of the transform, i.e. at  $a = a_0$  corresponding to the maximum value of the modulus of transform.

$$\ln |W(ACF)(a_0, b)| \approx -\xi\omega_0 b + \ln\left(\frac{1}{2} A_0 |G(a_0\phi'(b))|\right) \quad (17)$$

The second term on the right hand side is a constant at  $a_0$ , hence  $\xi\omega_0$  can be calculated from the slope of this curve. Further,  $\omega_0$  can be approximated with  $2\pi f_0$  corresponding to  $a_0$ . Therefore the decay ratio can be calculated as:

$$DR = \exp\left(\frac{\frac{d}{db} \ln |W(ACF)(a_0, b)|}{\omega_0} 2\pi\right) = \exp\left(\frac{\frac{d}{db} \ln |W(ACF)(a_0, b)|}{f_0}\right) \quad (18)$$

To illustrate the method, some applications are shown with simulated signals. An ideal ACF is used for this purpose with  $DR = 0.6$  and  $f = 0.5$  Hz. The logarithm of the modulus of the CWT for this ACF is shown in Fig. 8a, and the corresponding ridge at  $a_0$  is plotted in Fig. 8b. For better visibility the ridge is marked with a white line in Fig. 8a. Fig. 8b shows that for  $b$  between 10 and 25 s the ridge contains a linear section. Hence the derivative in Eq. (18) can be estimated as the constant slope of the ridge between these values of  $b$ .

For the quantitative analysis of the method of estimating the decay ratio, a test was run on analytically generated ACFs with decay ratios ranging from 0.3 to 0.95. Two different wavelets were used in the test, both of them being complex Morlet wavelets of the following form [22, 23]:

$$\psi(t) = \frac{1}{\sqrt{\pi F_b}} e^{2\pi F_c t} e^{-t^2/F_b} \quad (19)$$

Here  $F_b$  is the bandwidth parameter and  $F_c$  is the centre frequency parameter. In this paper the bandwidth parameter

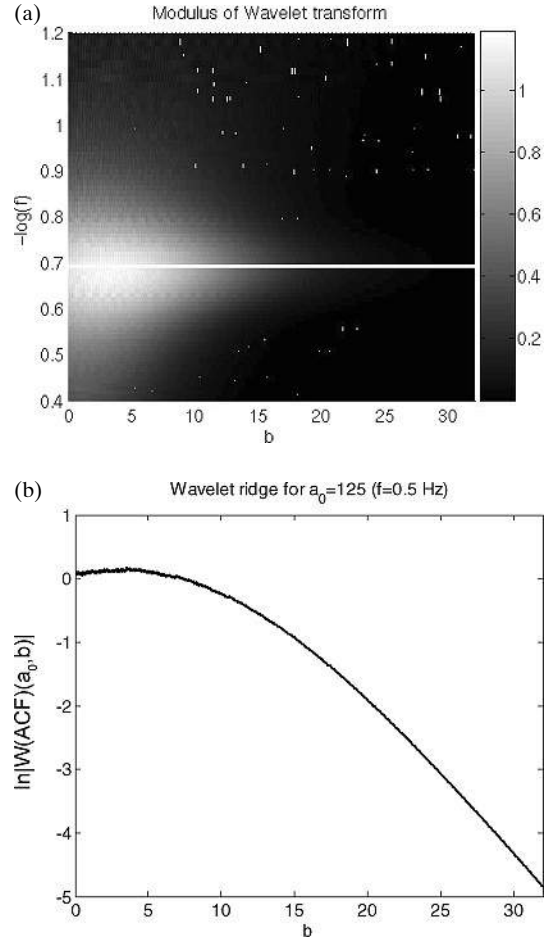


Fig. 8. (a) The modulus of the wavelet transform of an ACF with  $DR = 0.6$  and  $f = 0.5$  Hz with a white line showing the ridge. (b) Ridge corresponding to the white line in (a)

was set to unity and two different centre frequencies were used. Namely, 2 Hz for the first of the wavelets and 5 Hz for the second [25]. In the rest of the text these will be referred to as *cmor1-2* and *cmor1-5*, respectively. The features of the complex Morlet wavelet, i.e. its real and imaginary part, are shown in Fig. 9 where the *cmor1-2* wavelet is plotted. The width of the wavelet is governed by the bandwidth parameter and the oscillations are determined by the centre frequency parameter.

The quantitative results are shown in Fig. 10 for a “clean” (ideal) signal (Fig. 10a) and for a “realistic signal” containing added noise (Fig. 10b). It can be seen that the estimation of the DR from the clean ACF performs well for decay ratios larger than 0.7 for both wavelets. When the decay ratio is smaller, the *cmor1-5* wavelet increasingly overestimates it, whereas the *cmor1-2* wavelet estimates it correctly for all true DR value. At high DR values, which is the primary safety concern, both methods work satisfactorily.

In the case of the perturbed or “noisy” signal, the estimation of the decay ratio is still satisfactory for DR values higher than 0.7 for both wavelets (Fig. 10b). But for lower values of the DR, the accuracy of the estimation deteriorates fast, for both wavelets. It is remarkable that the error does not appear to be systematic, rather statistical in its character, in that with decreasing true DR, the deviation of the estimates is not a monotonic function. The truly problematic part is that in certain cases, while the true DR is about 0.3 or 0.6, the estimates predict a DR being close to unity. Although it appears that

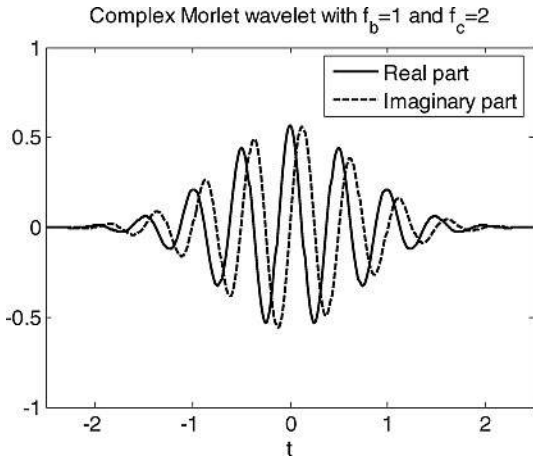


Fig. 9. Complex Morlet wavelet with  $F_b = 1$  and  $F_c = 2$

the errors lead to a conservative estimate (overestimation) of the DR, the crude overestimation can lead to false alarms if used in a monitoring system. Fortunately, this problem can actually be resolved, by not only calculating the derivative of the ridge according to Eq. (18), but also checking the magnitude and the form of the ridge from which the derivative was calculated, such as seen in Fig. 8b. From this information the reliability of the estimation of the DR can be determined. If the modulus of the continuous wavelet transform is low, and the linear section is short, such that the determination of the derivative becomes uncertain, this gives an indication that the estimation is unreliable and should be discarded (since this occurs only if the DR itself is low).

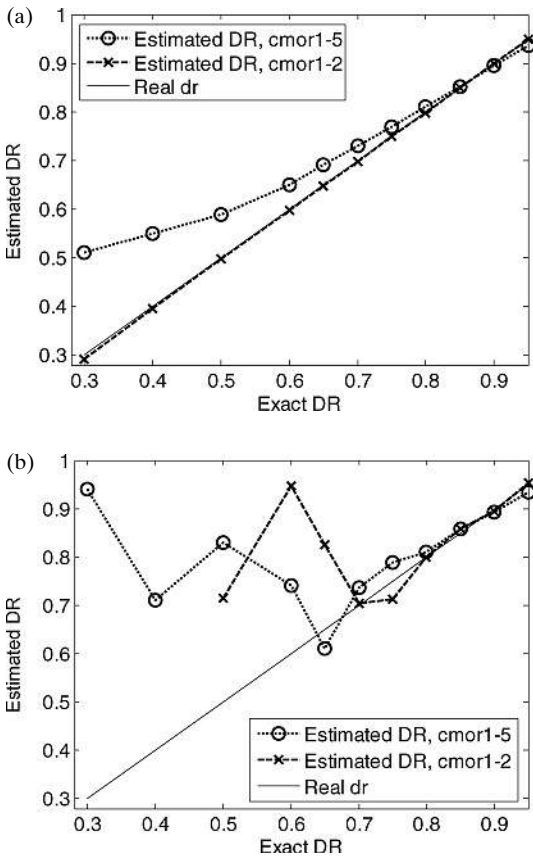


Fig. 10. Estimation of DR using continuous wavelets. In (a) the estimation is from an ideal ACF and in (b) from a “noisy” ACF with  $rms = 0.1$  for the noise

As was mentioned before, in some cases two different instability oscillations can occur with different weights and different DRs, but at the same or nearly the same frequency, such that they cannot be separated by frequency filtering methods. If the amplitude of the signal with the higher DR is smaller, the traditional method can return the lower DR, thereby missing the detection of the presence of an unstable component. There have been several methods reported how this problem can be tackled, both by pure signal processing methods using individual in-core detectors (LPRMs), and by using core physics knowledge to separate the two components based on their differing spatial form, employing several LPRM signals simultaneously. One can follow two possible strategies. The minimum goal is to detect the higher DR, even if the corresponding oscillation occurs with a lower amplitude than the competing, but stable, oscillation. The more ambitious strategy is to determine both DRs simultaneously, including of course the higher one.

The continuous wavelet method has some potential to achieve both goals, under certain circumstances. In the following we shall investigate this potential, both through simulations and on real data. First we investigate the case of dual oscillations of two instabilities with the same frequency. For this we consider an ideal signal in the form

$$ACF(\tau) = \frac{S_1 e^{-\xi_1 \omega_0 \tau} [\cos(\omega_0 \tau) + \xi_1 \sin(\omega_0 \tau)] + S_2 e^{-\xi_2 \omega_0 \tau} [\cos(\omega_0 \tau) + \xi_2 \sin(\omega_0 \tau)]}{S_1 + S_2} \quad (20)$$

Here  $\xi_i$  and  $S_i$ ,  $i = 1, 2$ , correspond to the two simultaneous processes,  $S_i$  being the amplitude. In the quantitative work, the  $\xi_i$  is chosen such that one has  $DR = 0.6$  for the first process (stable) and  $DR = 0.9$  for the second (unstable). The relative weight of the signals is determined by the ratio  $S_1/S_2$ . The result of the estimation of the DR with the continuous wavelet transform is shown in Fig. 11 where this ratio varies between 1 to 10. The two different wavelets yield a relatively good estimate of the unstable DR of 0.9 for all ratios, even when the amplitude of the stable signal is 10 times higher than that of the unstable one. In this respect the CWT method yields DR values closer to the unstable one than the traditional peak-to-peak method and the curve-fitting method, with the wavelet *cmor1-2* proving to be the better one of the two wavelets.

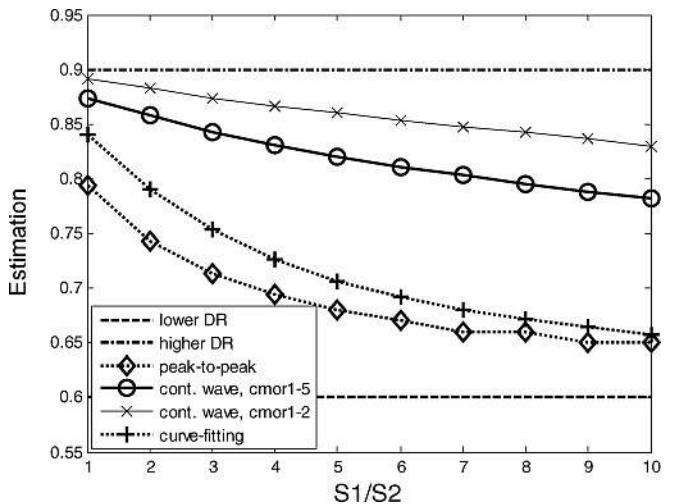


Fig. 11. Signal with two DR:s at the same time. Estimation of the DR with peak-to-peak, curve-fitting and complex wavelet methods. The ratio  $S1/S2$  indicates the relation of the strength between the two different DRs

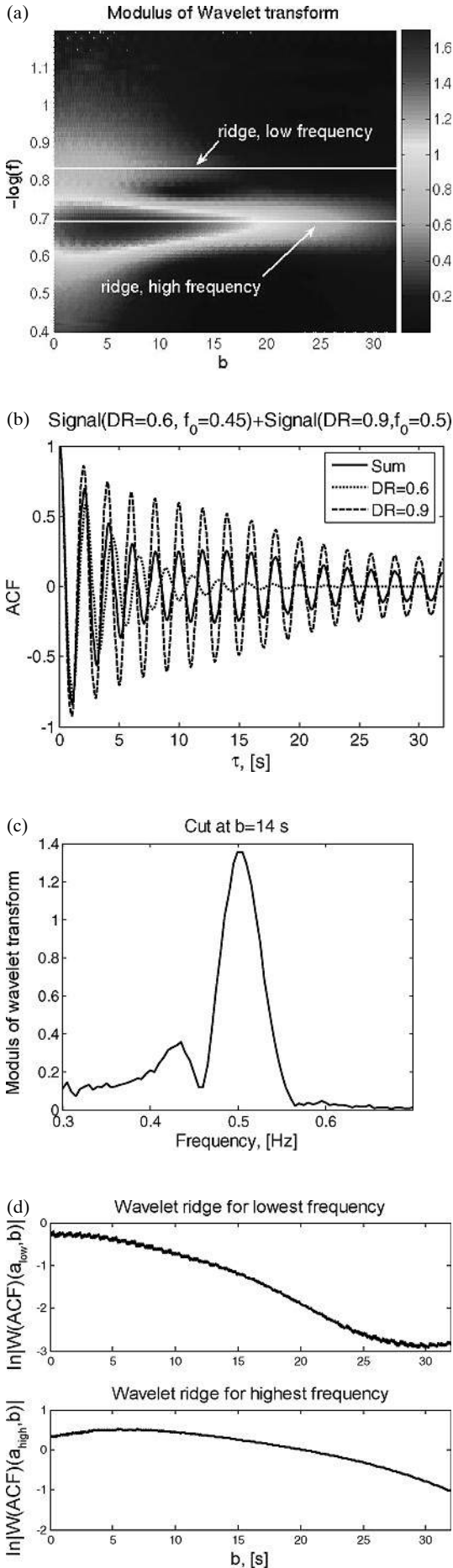


Table 2. Results of estimation (*cmor1-5*) with two frequencies and two DRs

low DR			high DR		
$f_0$	DR	DR <sub>est</sub>	$f_0$	DR	DR <sub>est</sub>
0.45	0.6	0.71	0.45	0.9	0.89
0.46	0.6	0.70	0.46	0.9	0.90
0.47	0.6	0.84	0.47	0.9	0.90

As long as the two simultaneous oscillations occur with exactly the same frequency, the CWT-based method has no chance to determine the two different DRs. However, if the frequencies of the two oscillations slightly differ, one can observe two ridges in the modulus maxima of the wavelet transform, and hence there is a possibility to determine the two different DRs. This is illustrated in Fig. 12, where the calculations were performed with the use of *cmor1-5* wavelet. The Figure shows the position of the ridges (white lines) on the plot of the modulus as well as the form of the ridges where the corresponding linear sections, to be used for the estimation of the corresponding DRs, can be seen.

Results of a quantitative investigation are shown in Table 2 for the same fixed DR values for the two oscillations, but with varying frequency difference between the two. These calculations were made with the *cmor1-5* wavelet, since with the *cmor1-2* it was not possible to resolve frequencies as close as 0.05 Hz. This is expected since higher centre frequency of the analysing wavelet will give better frequency resolution [29]. The results in the Table show that whereas the higher DR is estimated correctly for all frequency differences, the accuracy of the estimation of the low DR deteriorates fast when the two frequencies approach each other. This study suggests that if the frequencies are not closer than 0.03 Hz, it is possible to detect two ridges in the modulus of the wavelet transform. If the difference is 0.04 Hz or larger, it is also possible to estimate both decay ratios with good accuracy.

### 5 Ringhals benchmark

There are real measurement data available to test the performance of the wavelet methods. An instability event occurred in the Ringhals-1 NNP at the beginning of fuel cycle 14, where a stable global oscillation and an unstable regional (out-of-phase) oscillation occurred simultaneously. This event has been analysed with various methods in the past and is thought to be well understood [9, 19, 20, 30]. During start-up, there were a total of 9 measurements made at various positions of the power-flow map (see Fig. 13).

In each point  $36 \times 2$  LPRM signals were measured (36 LPRM strings at two axial elevations, upper = 2, and lower = 4) with a sampling frequency of 12.5 Hz and a length of about 11 min. The decay ratios for the different points in the power-flow

Fig. 12. In (a) the modulus of the wavelet transform of the ACF from (b) with two different DR:s with different frequency are shown. The white lines in a) indicate the position of the two ridges. In (c) a cross-sectional cut of the modulus, at  $b = 14$  s is shown. The two peaks indicate the two different frequencies present. In (d) the ridges from which the DR is estimated are shown. The parts of the ridges between 15 to 25 s, where it is straight are used for the estimation

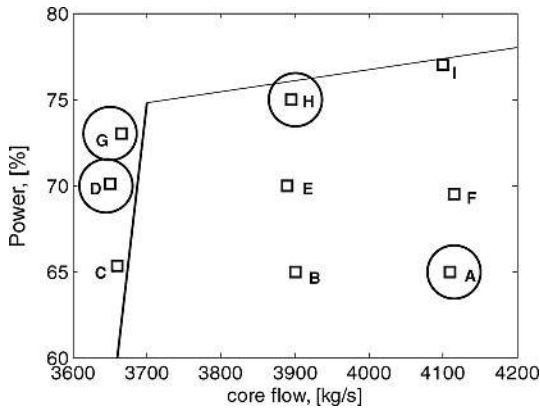


Fig. 13. Power-flow map of Ringhals-1 from the benchmark study at BOC-14

map have been estimated in several papers and reports. We have access to data from four of the measurements, namely A, D, G and H, which are marked with circles in Fig. 13. The Ringhals plant staff has made a calculation of the decay ratio for both the global and regional oscillations [20]. An alternative calculation for point D and H are found in van der Hagen et al. [9], where the DR is calculated in a number of different ways, we chose to use the DR calculated as the average DR from all LPRMs signals from both levels. The DR from these two calculations are shown in Table 3.

From these calculated reference values we choose to use the van der Hagen et al. [9] reference values for point D and H where the dual oscillation were the most apparent, and the Ringhals [20] values for point A and G where one of the modes dominated. For point A the only value available is the global one and for point G we choose to use the regional values since it is quite clear from all benchmarks and calculations of the DR that it is this values which is the correct one for this operating point.

Table 3. Reference decay ratio for the global and regional oscillations. Bold values are used as reference values

Operating point	Ringhals reference		van der Hagen reference	
	global	regional	global	regional
A	<b>0.3</b>	–	–	–
D	0.79	0.75	<b>0.72</b>	<b>0.83</b>
G	0.8	<b>0.99</b>	–	–
H	0.78	0.79	<b>0.7</b>	<b>0.94</b>

5.1 De-noising

First the de-noising method, described in Section 3, was applied to the measurements. We used the *denoise2*-method since it was the method which performed best on the simulated data. The DR is estimated from the de-noised ACF using the curve-fitting, by using the first 200 points of the ACF, and from the raw ACF using the peak-to-peak method using  $B3 = B2$ , see Fig. 1. Once the DR is estimated for each detector, the mean value and standard deviation is calculated for each of the two axial detector levels 2 and 4. In Table 4 the results are presented with the standard deviations as uncertainties. In some of the measurements some of the signals are unreliable (faulty), shown in parentheses in the Table for each operating point, hence they are not used in the estimation.

The de-noising algorithm is able to correctly estimate the DR in point G where it is close to unity, but on the other hand the peak-to-peak method is performing equally well. For the “middle” DR, points D and H, the de-noising is not able to separate the global and regional parts; in fact the method cannot estimate the DR of any of the two oscillations. For the

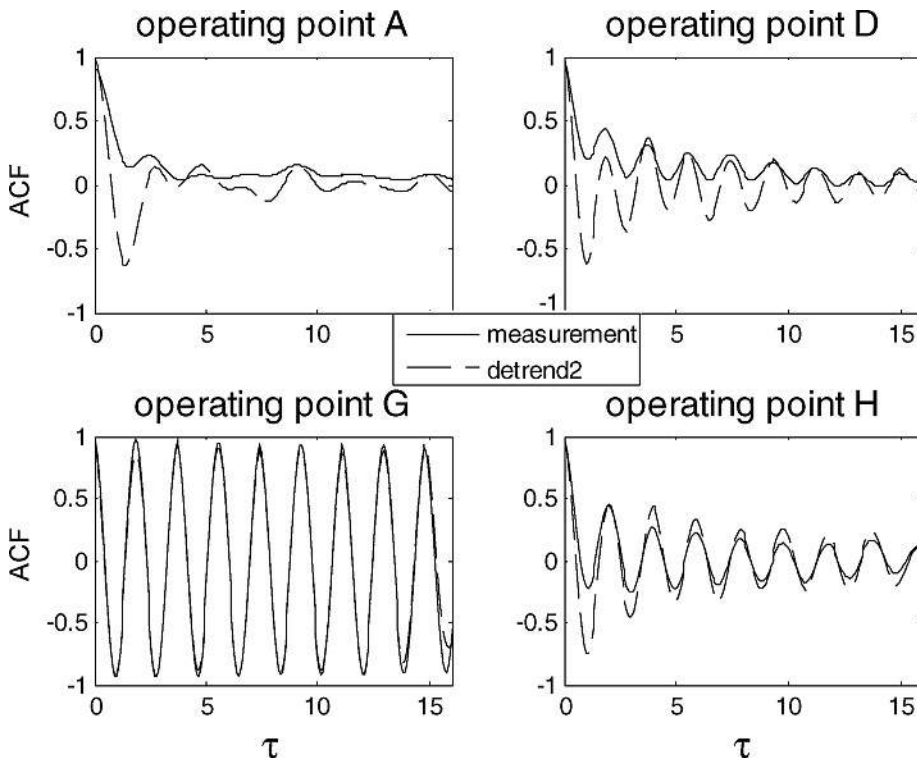


Fig. 14. Original and de-noised ACF from LPRM 36.4 for operating points, A, D, G and H from a measurement made at Ringhals-3

Table 4. Decay ratio estimated with the dmey wavelet and 200 points of the ACF using denoise2 from measurements taken at BOC-14, Ringhals-1

Operating point (String not used)	Reference DR global, regional	curve fitting		peak-to-peak	
		level 2	level 4	level 2	level 4
A (26)	0.30	0.20 ± 0.016	0.20 ± 0.027	–	–
D (12, 26)	0.72, 0.83	0.63 ± 0.11	0.62 ± 0.17	0.78 ± 0.053	0.75 ± 0.057
G (12, 26, 35)	0.99	0.98 ± 0.021	0.98 ± 0.014	0.97 ± 0.021	0.97 ± 0.017
H (12, 26, 33, 35)	0.7, 0.94	0.74 ± 0.039	0.75 ± 0.085	0.80 ± 0.032	0.78 ± 0.048

lowest DR, point A, the peak-to-peak method on the raw data is not working at all and the de-noising is underestimating the DR with about 50 %.

In Fig. 14 the original ACFs from LPRM 36.4 for all four operating points are shown together with the de-noised ACF using *denoise2*. Clearly, the higher the decay ratio is, the better the denoising is working. If the decay ratio is low, then the oscillations are mistaken as “noise” by the de-noising algorithm and the de-noising is not working well. It is also clear from the figure why the peak-to-peak method does not work in point A, since there are hardly any peaks present at all.

5.2 Continuous wavelet transform

Since at least two of the operating points from the Ringhals Benchmark consist of two different oscillations, the CWT method would be suitable for estimating the DR. Hence, this method is also applied to the measurements. The algorithm for estimating the DR from the measurements has to be made to work automatically compared to the algorithm used for the simulation due to the large number of data available. The algorithm also has to be tuned to fit the measurements. The phenomena of having to slightly modify the algorithm used

in simulations compared to the one used on real data has been experienced before by the present authors [31]. The new algorithm for determining the DR of the measurements by using the CWT goes as follows:

- determine  $a_0$  for the ridge of  $\ln|W(meas)(a, b)|$ ,
- determine which part of the ridge to use, an interval of  $b$  ( $\Delta b$  and  $b_0$ ),
- fit the ridge to a polynomial,  $Ab + B$  where  $A \approx -\xi\omega_0$ ,
- estimate the decay ratio by using  $A$ .

First the maximum modulus ridge has to be found, or in other words  $a_0$  of Eq. (18) has to be determined, where the modulus of the CWT of the measurement is represented as  $|W(meas)(a, b)|$ . This is done by calculating the maximum value for a curve  $\ln|W(meas)(a, b_n)|$  for a suitable  $b_n$  and then to use the corresponding  $a$  as  $a_0$ . From the previous section it is also clear that the maximum line of the modulus of the CWT of the ACF is not straight for all  $b$ . Hence an interval where the ridge is constant has to be chosen. In the case with the Ringhals measurements, an interval of 50 points or  $\Delta b = 4s$  is chosen. Then the starting point of the interval has to be decided. But one would like to use different starting points for different signals. Hence, all points in the interval  $b_0 = b(X)$  to  $b_0 = b(Y)$  are tested as starting points and the

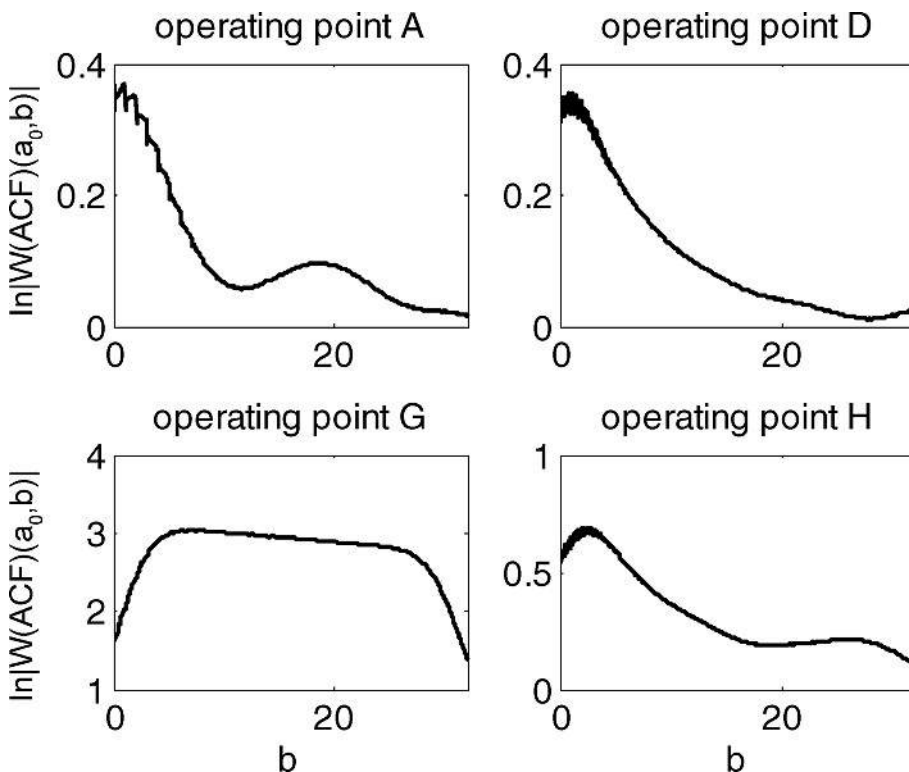


Fig. 15.  $\ln|W(meas)(a_0, b)|$  for all the measurement points used for determination of the linear interval used in the estimation of the decay ratio *cmor1-2*

one with least fitting error to the polynomial  $Ab + B$  is used. This can be summarised in the following equation,

$$J = \min_j \left( \sum_{i=1}^Y \sum_{j=X}^{49} [\ln |W(meas)(a_0, b(j+i)) - LS_j(i)|^2] \right) \quad (21)$$

Here  $LS_j$  is the least-square fitted polynomial,  $A_j b + B_j$ , starting at  $b_j$ . Once  $J$  is determined, the DR is estimated using Eq. (18) as

$$DR = \exp\left(\frac{A_j}{f_0} 2\pi\right) \quad (22)$$

The parameters  $X$  and  $Y$  in Eq. (21) are manually determined by visual inspection of one wavelet ridge for each operating point. From Fig. 15 it can be determined that  $X = 4s/12 \text{ Hz} = 50$  for all operating points and that  $Y = 16s/12 \text{ Hz} = 200$  for operating points D, G and H and  $Y = 8s/12 \text{ Hz} = 100$  for operating point A in order for  $\ln |W(meas)(a_0, b)|$  to be straight. It is obvious that one should use small  $b_0$  for oscillations with low DR since the ACF is dying away faster for smaller DRs. In the figure it is also possible to observe the well known edge effects of the wavelet transform [22]; in operating point G it is clearly visible as a sharp dip at the end of the curve.

According to Table 2 the continuous wavelet method should be able to separate dual oscillations with frequencies which are not closer than 0.3 Hz. In the measurement from Ringhals-1 the difference between the estimated frequencies of the global and regional oscillations is 0.3 Hz or less [20]. Hence, it is not possible to separate the two oscillations. But it could be possible to at least estimate the higher of the two decay ratios according to the discussion in the previous section and Fig. 11.

The estimated DRs, from BOC-14 at Ringhals-1, using the above described CWT method are shown in Table 5, both the *cmor1-2* and *cmor1-5* wavelets. The results presented in the Table are in agreement with the results of the simulations with two decay ratios present. Clearly, *cmor1-2* is better of estimating decay ratios lower than 0.6, such as in operating point A, as is seen in Fig. 10a. On the other hand, for the cases with dual oscillations, operating points D and H, both of the wavelets are at least estimating the DR to be closer to the higher value than the lower value, even though slightly underestimating the higher DR which is in agreement with Fig. 11. Both wavelets are equally suitable to estimate high DRs from single oscillations, such as in operating point G. Hence, the conclusion of the test of the CWT method on the measurements is that the result is in agreement with the simulations from the previous section.

Table 5. Comparison between DR calculated by wavelet ridge method and reference value. Measured signals from Ringhals-1 BOC-14

Operating point (String not used)	Reference DR global, regional	Mean DR	
		<i>cmor1-2</i>	<i>cmor1-5</i>
A (26)	0.30	0.433 ± 0.101	0.824 ± 0.051
D (12, 26)	0.72, 0.83	0.784 ± 0.110	0.794 ± 0.043
G (12, 26, 35)	0.99	0.992 ± 0.002	0.989 ± 0.003
H (12, 26, 33, 35)	0.7, 0.94	0.864 ± 0.038	0.895 ± 0.015

## 6 Conclusions

In this paper various methods of using wavelet methods for calculating the decay ratio have been tested. First an attempt was made to pre-process realistic ACF functions, before estimation of the DR, that deviate from ideal ones by containing both linear and exponential trends as well as white noise, by using discrete wavelet methods. The best de-trending/de-noising effect is achieved if the details at level 4 and 5 are used as a representation of the ACF. At these levels the frequency content around the pseudo-frequencies of the wavelet details corresponds well to the frequency of the instability oscillations.

A wavelet method based on the continuous transform for calculating the decay ratio was also tested. This method appears to work satisfactorily on ideal signals. The method can also be used to determine the higher of the two decay ratios in case of dual oscillations, i.e. with a high decay ratio and low amplitude superimposed on a process with lower decay ratio and higher amplitude. The wavelet based method is more effective than the traditional methods. Under some circumstances, it is also suitable for the simultaneous determination of the two different decay ratios.

(Received on 16 August 2006)

## References

- 1 Thie, J. A.: Dynamic behaviour of boiling reactors. ANL-5849, Argonne National Laboratory, 1959
- 2 March-Leuba, J.; Cacuci, D. G.; Perez, R. B.: Nonlinear dynamics and stability of boiling water reactors: part 1 – qualitative analysis. Nuclear Science and Engineering 93 (1986) 111
- 3 Konno, H.; Kanemoto, S.; Takeuchi, Y.: Parametric stochastic stability and decay ratio for a stochastic nonlinear BWR model below the Hopf bifurcation. Annals of Nuclear Energy 26 (1999) 1465
- 4 Analytis, G. Th.; Hennig, D.; Karlsson, J. K.-H.: The physical mechanism of core-wide and local instabilities at the Forsmark-1 BWR. Nuclear Engineering and Design 205 (2001) 91
- 5 Hotta, A.; Suzawa, Y.; Takeuchi, H.: Development of BWR regional instability model and verification based on Ringhals-1 test. Annals of Nuclear Energy. 24 (1997) 1403
- 6 Hotta, A.; Ninokata, H.: Numerical study on observed decay ratio of coupled neutronic-thermal hydraulic instability in Ringhals Unit 1 under random noise excitation. Journal of Nuclear Science and Technology 39 (2002) 138
- 7 Smed, T.; Lansäker, P.: The MATSTAB code for calculation of the decay ratio. Personal communication (1999)
- 8 van der Hagen, T. H. J. J.; Zboray, R.; de Kruijff, W. J. M.: Questioning the use of the decay ratio in BWR stability monitoring. Annals of Nuclear Energy. 27 (2000) 727
- 9 van der Hagen, T. H. J. J.; Pázsit, I.; Thomson, O.; Melkersson, B.: Methods for determination of the in-phase and out-of-phase stability characteristics of a boiling water reactor. Nuclear Technology 107 (1994) 193
- 10 Behringer, K.; Hennig, D.: A novel auto-correlation function method for the determination of the decay ratio in BWR stability analysis. Annals of Nuclear Energy 29 (2002) 1483
- 11 Pázsit, I.: Determination of reactor stability in case of dual oscillations. Annals of Nuclear Energy. 22 (1995) 377
- 12 van der Hagen, T. H. J. J.: Artificial neural networks versus conventional methods for boiling water reactor stability monitoring. Nuclear Technology. 109 (1995) 286
- 13 Tambouratzis, T.; Antonopoulos-Domis, M.: On-line stability monitoring of BWRs using artificial neural networks. Annals of Nuclear Energy. 26 (1999) 1287
- 14 Tsuji, M.; Shimazu, Y.: Evaluation of the Decay Ratio of BWRs using Singular Value Decomposition Method. Journal of Nuclear Science and Technology. 42 (2005) 169
- 15 Tsuji, M.; Michishita, H.; Shimazu, Y.: Stability monitoring for BWR based on Singular Value Decomposition Method using Artificial Neural Networks. Journal of Nuclear Science and Technology 42 (2005) 1054

- 16 *Tambouratzis, T.; Antonopoulos-Domis, M.*: Parameter estimation during a transient – application to BWR stability. *Annals of Nuclear Energy*. 31 (2004) 2077
- 17 *Antonopoulos-Domis, M.; Tambouratzis, T.*: System identification during a transient via wavelet multiresolution analysis followed by spectral techniques. *Annals Nuclear Energy* 25 (1998) 465
- 18 *Espinosa-Paredes, G.; Prieto-Guerrero, A.; Núñez-Carrera, A.; Amador-García, R.*: Wavelet-based method for instability analysis in boiling water reactors. *Nuclear Technology* 151 (2005) 250
- 19 *Pázsit, I. (editor)*: Investigation of regional instability in Ringhals-1. CTH-RF-100/RR-1. Chalmers University of Technology 1993
- 20 *Lefvert, T.*: Ringhals 1 stability benchmark, Final report. NEA/NSC/DOC(96)22 1996
- 21 *Thomson, O.; Garis, N. S.; Pázsit, I.*: Quantitative analysis of detector string impacting. *Nuclear Technology* 120 (1997) 71
- 22 *Addison, P.*: The Illustrated Wavelet Transform Handbook. Institute of Physics Publishing, London, 2002
- 23 *Matlab*. 2000. Wavelet Toolbox User's Manual. Matworks Inc.
- 24 *Pázsit, I.; Kitamura, Y.; Wright, J.; Misawa, T.*: Calculation of the pulsed Feynman-alpha formulae and their experimental verification. *Annals Nuclear Energy* 32 (2005) 896
- 25 *Staszewski, W. J.*: Identification of damping in modf systems using time-scale decomposition. *Journal of sound and vibration*. 203 (1997) 283
- 26 *Staszewski, W. J.*: Analysis of non-linear systems using wavelets. Proceedings of the Institution of Mechanical Engineers, Part C, *Journal of Mechanical Engineering*. 214 (2000) 1339
- 27 *Hera, A.; Hou, Z.*: Wavelet approach for damage detection using experimental data of ASCE benchmark Study. Proceedings of 16th ASCE Engineering Mechanics Conference, July 16–18, University of Washington, Seattle, 2003
- 28 *Carmona, R. A.; Hwang, W. L.; Torrèsani, B.*: Characterization of Signal by the Ridges of Their Wavelet Transforms. *IEEE Transactions on Signal Processing*. 45 (1997) 2586
- 29 *Delprat, N.; Escudé, B.; Guillemain, P.; Kronland-Martinet, R.; Tchamitchian, P.; Torrèsani, B.*: 1992. Asymptotic Wavelet and Gabor Analysis: Extraction of Instantaneous Frequencies. *IEEE Transactions on Information Theory* 28 (1992) 644
- 30 *Tsuji, M.; Shimazu, Y.*: Evaluation of the Decay Ratio of BWRs using Singular Value Decomposition Method. *Journal of Nuclear Science and Technology* 42 (2005) 169
- 31 *Sunde, C.; Pázsit, I.*: Investigation of detector tube impacting in the Ringhals-1 BWR. *International Journal of Nuclear Energy Science and Technology* 2 (2006) 185

#### The authors of this contribution

*Carl Sunde* and Prof. *Imre Pázsit*, Chalmers University of Technology, Department of Nuclear Engineering, 412 96 Göteborg, Sweden. E-mail: kalle@nephy.chalmers.se, E-mail: imre@nephy.chalmers.se

## Corrections of the proof

Where	Correction	Comment
Page 1, line 7 from bottom in the English Abstract	...in the ACF, is brings... should read as ...in the ACF, it brings...	Manuscript error
Page 1, right column, line 2 from bottom	...have been also been... should read as ...have also been...	Manuscript error
Page 2 below Equation 1	“and $\omega_0$ is” should read “and $\omega_0$ is”	
Page 2, third line in the last paragraph and thereafter	A2 = A1 should read A2/A1 B2 = B1 should read B2/B1 B3 = B2 should read B3/B2	Manuscript error
Page 2 right column 8th row from below	“3 <sup>rd</sup> ” should read “3rd”	Manuscript error
Page 4, caption of Fig. 3	“...different levels are shown. Levels 5 and 6...”	Manuscript error
Page 6, line 3 from bottom in second last paragraph	“where after” should be written as “whereafter”.	
Page 7, 3 <sup>rd</sup> line	...trial an error... should read ...trial and error...	Manuscript error
Page 7 Equation 13	“ $ACF_{noise}$ ” should read “ $ACF_{real}$ ”	Manuscript error
Page 8 above Equation 17	“ $\phi'(b)$ ” should read “ $\phi'(b)$ ”	Manuscript error
Page 8 Equation 17	“ $G(a_0\phi'(b))$ ” should read “ $G(a_0\omega_0)$ ”	Manuscript error
Page 8 Equation 19	“ $2\pi F_c$ ” should read “ $2\pi F_c t$ ”	Manuscript error
Page 9 Equation 20	The first “ $\xi_2$ ” should read “ $\xi_1$ ”	Manuscript error
Page 10. Table 2, fourth column	All values of the frequency $f_0$ should be 0.50	
Page 11 right column 7th row from the top	“B3=B2” should read “B3/B2”	Manuscript error
Page 12 right column 11 <sup>th</sup> row from above	“a0” should read “ $a_0$ ”	Manuscript error
Page 13 left column, around the middle	0.3 should be 0.03, on two places.	Manuscript error
Page 13, Ref. 10	The second authors should read as Hennig, D.	Manuscript error



# Paper IV

*Calculations of the neutron noise induced by shell-mode core-barrel vibrations  
in a 1-D, two-group, two-region slab reactor model*

C. Sunde, C. Demazière and I. Pázsit

Nuclear Technology **154**, 129 (2006).



# CALCULATION OF THE NEUTRON NOISE INDUCED BY SHELL-MODE CORE-BARREL VIBRATIONS IN A 1-D, TWO-GROUP, TWO-REGION SLAB REACTOR MODEL

FISSION REACTORS

**KEYWORDS:** *core-barrel vibrations, in-core neutron noise, shell-mode vibrations*

CARL SUNDE,\* CHRISTOPHE DEMAZIÈRE, and IMRE PÁZSIT  
*Chalmers University of Technology, Department of Nuclear Engineering  
SE-412 96 Göteborg, Sweden*

Received December 22, 2004

Accepted for Publication October 12, 2005

*The subject of this paper is the calculation of the in-core neutron noise induced by the shell-mode vibrations of the core barrel. The original motivation was to investigate whether an out-of-phase behavior can exist between the in-core and ex-core (ex-vessel) detectors lying at the same azimuthal position. To this end, a two-region two-group diffusion model was used in one dimension. The noise was calculated by representing the vibrations of the core barrel by a model developed earlier to describe control rod vibrations. It was found that such an out-of-phase behavior indeed exists, although only for in-core detector positions close to the core boundary. This behavior is due to the local com-*

*ponent of the noise, which is accounted for in a two-group treatment. The finding is in accordance with the experiment whose result prompted the present work. In addition to its effect on the phase, the local component also manifests itself by a large amplitude of the noise around the vibrating core boundary, i.e., in both the core and the reflector. The appearance and the properties of the local component of the neutron noise for core-barrel vibrations is the main finding of this paper. The results suggest that the efficiency of core-barrel vibrations can be enhanced if in addition to the ex-core detectors, the in-core detectors in the outermost fuel assemblies are used.*

## I. INTRODUCTION

The ex-core neutron noise induced by core-barrel vibrations has long been used to diagnose both beam-mode and shell-mode vibrations.<sup>1-12</sup> In particular, Ref. 5 gives a self-contained description of the principles of fluctuation analysis for the diagnostics of reactor cores, including the neutron noise induced by core-barrel vibrations. These are classified into various modes, which correspond to a Fourier-series expansion of the core boundary displacement as a function of the azimuthal angle. Mode 0 (uniform radial expansion/contraction) is absent, mode 1 is called the pendulum-like or beam-mode vibration, and mode 2 is called the shell-mode vibration. More details and illustrations can be found in Ref. 13.

The corresponding methods have undergone quite a long development stage and have become quite effective for the diagnostics of beam-mode (pendular) vibrations. By starting out with underlying models restricted to either unidirectional or isotropic vibrations, they have successively advanced to a stage of being able to treat arbitrary anisotropic two-dimensional (2-D) random motions. This way it became possible to monitor a change in the preferred directions and the amplitude of the vibrations simultaneously. Even reconstruction of the 2-D random motion of the core barrel has been performed with success in some cases, although it has less direct diagnostic value.

However, the quantitative diagnostics of shell-mode vibrations have not reached a similar state, at least not in Westinghouse-type reactors where there are four ex-core detectors with equal 90-deg spacing. Because the shell-mode vibrations, and hence also the neutron noise induced

\*E-mail: kalle@nephy.chalmers.se

by such vibrations, exhibit the same symmetry against rotations with 90 deg as the detectors, the information content in all detectors is equivalent; i.e., all ex-core detectors carry the same information. (The situation is different with reactor constructions such as the Eastern-European VVER-440, where three ex-core detectors are used with a 120-deg spacing, and in some Japanese reactors with five ex-core detectors.<sup>9</sup>) Hence, it is not possible to determine both the vibration amplitude and the direction from the detector signals. In particular, it is not possible to find out if a change in the signal amplitude is due to a change in the vibration amplitude or to a change in the direction of the vibrations.

In connection with the study of in-core neutron noise induced by fluctuating system boundaries,<sup>14</sup> originally considered for the description of the neutron noise induced by vibrating control rods, it was realized that core-barrel vibrations might also lead to in-core noise. For this reason we started using the in-core detector signals for the analysis of core-barrel vibrations as part of a collaborative research project between the Ringhals power plant and the Department of Nuclear Engineering (formerly the Department of Reactor Physics) at Chalmers University of Technology.<sup>15-18</sup> A compact solution for the radial and angular dependence for the in-core noise induced by core-barrel vibrations is given in Ref. 13. However, full confirmation of the theory was hindered by the low number of in-core detectors (a maximum of five movable in-core detectors at a time). In particular, during the evaluation of the only measurement in Ringhals Unit 3 (Ringhals-3) when both in-core and ex-core detectors were available, to have consistent interpretation it was necessary to assume that ex-core and in-core detectors lying on the same azimuthal position exhibited opposite phases.<sup>13</sup>

This latter statement, and the apparent contradiction that it implies, will be expounded here in some detail because it was this observation that prompted the present work. The theoretical results and experimental comparison are summarized in Fig. 1. It is shown in Ref. 13 that the angular and radial dependence of the in-core noise induced by shell-mode vibrations at the vibration eigenfrequency  $\omega$  can be given in a 2-D polar coordinate system  $r = (r, \varphi)$  as

$$\delta\phi(r, \varphi) = AJ_2(B(\omega)r)\cos 2(\varphi - \chi) , \quad (1)$$

where

$B(\omega)$  = dynamic buckling<sup>14</sup>

$J_2$  = Bessel function

$\chi$  = angle of the vibration axis.

As Eq. (1) shows, and as can also be expected by simple considerations, the induced noise has a rotational symmetry by 90 deg. In particular, the auto-power spectral density (APSD), given from Eq. (1) as

$$\begin{aligned} \text{APSD}_{\delta\phi}(r, \varphi) &= |AJ_2(B(\omega)r)|^2 \cos^2 2(\varphi - \chi) \\ &= \frac{1}{2}|AJ_2(B(\omega)r)|^2 [1 + \cos 4(\varphi - \chi)] , \end{aligned} \quad (2)$$

has four maxima (along the vibration axes) and four minima (nodal lines) in between, as shown in Fig. 1a. As a function of the polar angle, the phase changes sign whenever the nodal line is crossed; i.e., there is an out-of-phase relationship at the two sides of the nodal lines, as is seen from Eq. (1).

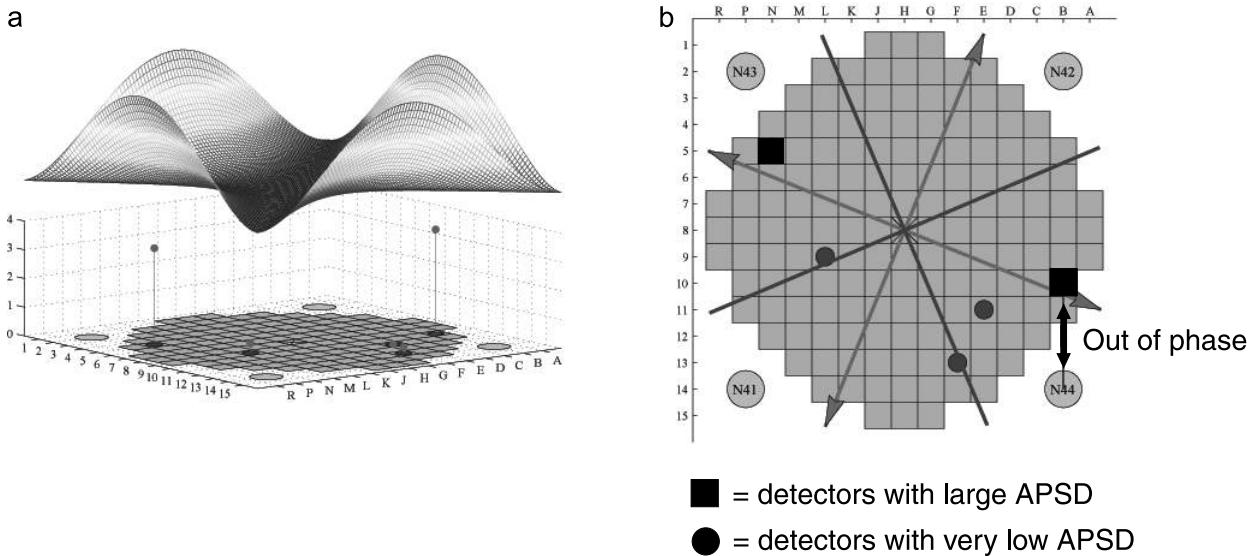


Fig. 1. (a) The structure of in-core noise induced by shell-mode vibrations and (b) evaluation of measurement from Ringhals-3.

If the model is applied equally to the in-core and the ex-core noise with the motivation that the ex-core noise arises from leakage neutrons that are related to the neutron flux close to the boundary, then the interpretation of the measurement, shown in Fig. 1b, becomes problematic. Basically, we wanted to determine only the direction of the vibrations by finding a suitable position of the vibration axes and the corresponding nodal lines that are consistent with the amplitudes of the APSDs and the phase relations. Because of the amplitudes of the APSDs (some small, some large, as seen in Fig. 1b), the direction of the vibrations had to be positioned as shown in Fig. 1b, indicated by the arrow lines. However, at the same time, the in-core detector B10 and the ex-core detector N44, at two different sides of the vibration axis but in between two nodal lines, showed an out-of-phase behavior, which contradicts the aforementioned model.

To resolve this apparent contradiction, it was argued in Ref. 13 that there should be an extra out-of-phase factor between the in-core and the ex-core detectors at the same azimuthal position. Naturally, the occurrence of such a phase factor cannot be explained within the simple theory that was used so far. However, a bare system was used in that theory. In real systems a reflector region is situated between the core and the ex-core (ex-vessel) detectors, whose thickness is also changing with oscillations of the core. This difference between the real situation and the simple nonreflected model opens the possibility of finding the out-of-phase factor in question.

The signal of the ex-core detectors is attributed to the variations of the attenuation of the outbound flux from the core, due to the variations in the reflector thickness. Hence, one does not expect a different behavior of the ex-core detector signals for a reflected system as compared to a bare one. However, regarding the in-core noise, one cannot exclude the possibility that the core-barrel vibrations, if treated in a reflected system, would lead to a structure of the neutron noise different than in a bare system. For instance, the outbound movement of the boundary in the non-reflected system means some multiplicative material added outside the static boundary, which then would lead to both an increase of reactivity and a local increase of the neutron flux. Both components would be in phase with the signal of the ex-core detectors. However, in a reflected system, an outbound movement of the core boundary means a decreasing reflector thickness, and, under certain conditions, possibly also a decrease of reactivity. Hence, it is not obvious whether or not such a movement will lead to an increase of the in-core flux, depending on the behavior of the reactivity with the core motion.

To take into account the effect of the reflector, one needs to use the two-group theory. The purpose of this paper is to investigate the in-core noise induced by core-barrel vibrations in reflected systems by the extension of the model used earlier. As it turns out, this not only will necessitate the use of the two-group theory but also lends the possibility of a simplification of the treatment of the

vibrating boundary. Namely, the vibrations of the free boundary required some sophisticated methods of treating boundary conditions at a moving free-vacuum boundary, since in diffusion theory one cannot make use of the existence of the flux outside the boundary. In the case of the vibrations of the core boundary in a reflected system, the oscillations of the boundary can be treated by adding or subtracting core material and subtracting or adding reflector material at either side of the boundary, respectively. This can be treated by a particularly simple model that was used for the description of vibrating control rods in the past.<sup>19,20</sup>

To make a first principal investigation of the possible change of the phase relationships by including a reflector, a one-dimensional (1-D) model was used in this work. Combined with the simple way of treating the core-barrel vibrations as a noise source, the present model allowed a fully analytic solution. The dependence of the amplitude and the phase of the noise throughout the whole core was readily calculated and studied. It turned out that not surprisingly, in the two-group treatment a strong local component, characteristic of that of an absorber of variable strength, is present at and around the core boundary. The large amplitude of this component suggests that it is practical to use in-core detectors as close to the core boundary as possible to be able to make an effective core-barrel vibration diagnostic.

The present exercise was appended with and compared to the results of fully numerical solutions of the same problem by using a so-called "noise simulator."<sup>21</sup> The noise simulator is a code for the calculation of the dynamic transfer function  $G(\mathbf{r}, \mathbf{r}', \omega)$  of real, inhomogeneous cores in the two-group theory, very much the same way as static in-core fuel management (ICFM) codes calculate the static flux in real cores. In particular, it is compatible with the input deck of ICFM codes, most notably the SIMULATE code,<sup>22</sup> which is used by most of the Swedish power utilities in core optimization and loading. The idea behind the development was to be able to perform spatial unfolding of localized or distributed noise sources by inverting the basic formula of linear noise theory, expressing the noise as a convolution of the transfer function with the noise source. Such inversion or unfolding procedures were performed in the past exclusively by using simple transfer or Green's functions for homogeneous systems, equivalent with the analytical model used in this paper. Although such models were used in a few singular cases with success in the past even in real cores, one cannot trust that such models would always work in reflected nonhomogeneous cores. With the present noise simulator, any measurement taken in Swedish power plants can be evaluated for spatial unfolding of the noise source.

The simulator was used with success in locating the channel-type instability in the Forsmark-1 boiling water reactor<sup>23</sup> and also for the explanation of a spatially dependent decay ratio in the same measurement.<sup>24</sup> However,

more testing of the applicability and the performance of the simulator was desirable. One special task in each application of the noise simulator is to find a proper representation of the noise source, since this is not an autonomous part of the simulator. While analytical models can use simplifications such as Dirac-delta functions and the like, in the noise simulator a numerical representation that is constrained with the discretization of the numerical algorithm is to be found. The present problem appeared to be a suitable exercise for yet another application of the noise simulator for a new type of noise source. Thus, the problem was solved by the use of the noise simulator. The amplitude and the phase across the core were calculated, and a good agreement was found with the results of the analytical method.

**II. CALCULATION OF THE NOISE INDUCED BY SHELL-MODE VIBRATIONS IN AN ANALYTICAL MODEL**

A 1-D model of a reflected reactor was selected for this study with a homogeneous central core and outer reflectors placed symmetrically around the core (see Fig. 2). The two-group diffusion theory will be used with corresponding cross sections and diffusion constants. A list of those, together with the numerical values used in the quantitative work, is given in the Appendix. Quantities in the fast and the thermal groups are labeled with subscripts 1 and 2, respectively. Superscripts *c* and *r* indicate whether the quantity belongs to the core or to the reflector. The same notation convention is used for the fast and thermal static flux in the core and in the reflector, and for the noise. One averaged group of delayed neutrons is used in the dynamic calculations. Vacuum boundary conditions are assumed at the outer boundary. A schematic view of the system is shown in Fig. 2.

To simplify the formalism, whenever practical, vector notations will be used where the two components belong to the fast and the thermal groups; e.g., the static flux in the core and the reflector can be written as

$$\vec{\phi}(x) = \begin{cases} \vec{\phi}^c(x) = \begin{bmatrix} \phi_1^c(x) \\ \phi_2^c(x) \end{bmatrix}, & -b \leq x \leq b \\ \vec{\phi}^r(x) = \begin{bmatrix} \phi_1^r(x) \\ \phi_2^r(x) \end{bmatrix}, & -a \leq x \leq -b, b \leq x \leq a \end{cases} \quad (3)$$

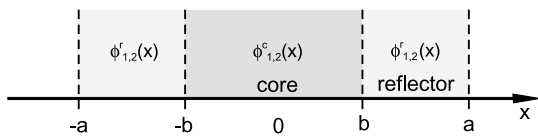


Fig. 2. One-dimensional core model with reflector.

The static fluxes are given by the solution of the static equations as well as by the boundary conditions at  $x = \pm a$  and the interface conditions at  $x = \pm b$ . Instead of using all these interface and boundary conditions, it is easier to notice that the static flux is symmetrical around the origin. Hence, it is simpler to seek a solution that is symmetric, i.e., that satisfies

$$\begin{aligned} \vec{\phi}^c(-x) &= \vec{\phi}^c(x), & -b \leq x \leq b \\ \vec{\phi}^r(-x) &= \vec{\phi}^r(x), & -a \leq x \leq -b, b \leq x \leq a \end{aligned} \quad (4)$$

and fulfills the interface conditions at  $x = b$

$$\begin{aligned} \vec{\phi}^r(x)|_{x=b_+} &= \vec{\phi}^c(x)|_{x=b_-} \\ D_1^r \frac{d}{dx} \phi_1^r(x)|_{x=b_+} &= D_1^c \frac{d}{dx} \phi_1^c(x)|_{x=b_-} \\ D_2^r \frac{d}{dx} \phi_2^r(x)|_{x=b_+} &= D_2^c \frac{d}{dx} \phi_2^c(x)|_{x=b_-} \end{aligned} \quad (5)$$

and the vacuum boundary conditions at the extrapolated boundary  $x = a$

$$\vec{\phi}^r(x)|_{x=a} = 0 \quad (6)$$

This way we need only consider the solution for  $x \geq 0$ . The solution to this standard problem is well known. The advantage of this treatment is that because of the symmetry of the shell-mode vibrations in this 1-D model, and hence that of the induced neutron noise, the same simplification can be applied in the dynamic case.

The material data were derived from a real core of Ringhals Unit 4 (Ringhals-4) condensed into the form of two-group cross sections, diffusion coefficients, and velocities and one-group delayed neutron data. These were taken from a SIMULATE calculation, then converted into equivalent 1-D data by modifying the absorption cross sections to account for the higher leakage in the three-dimensional (3-D) model than in the 1-D model used. These data were finally homogenized in the core and the reflector regions, respectively, to obtain a two-region reactor. Since the original data correspond to a core loading in the critical state, these data should yield a  $k_{eff}$  close to unity in the analytical calculations. To have rigorous criticality in the analytical calculations, the fission cross sections were readjusted after the criticality calculations as

$$\nu \Sigma_{f,i}^c = \frac{1}{k_{eff}} \nu \Sigma_{f,i}^{c(old)} \quad i = 1, 2 \quad (7)$$

We turn now to the calculation of the noise, induced by the shell-mode vibrations of the core. These will be treated by a method originally introduced for the treatment of control rod vibrations in a numerical work by Sanchis-Arnal et al.<sup>25</sup> and developed into an analytical tool under the name “ $\epsilon/D$  method” by one of the present

authors.<sup>19</sup> In that treatment, at the interface of the core and the reflector at  $x = b$ , a uniform description of the static cross sections over both the core and the reflector can be given for  $0 \leq x \leq a$  as

$$\Sigma_{\alpha,i}(x) = \{1 - H(x - b)\}\Sigma_{\alpha,i}^c + H(x - b)\Sigma_{\alpha,i}^r, \quad (8)$$

where  $\alpha = \{a, R, f\}$ ; i.e., it stands for the type of reaction (absorption, removal, or fission);  $i = \{1, 2\}$  stands for the energy group index; and  $H(x)$  is the unit step function. A similar form can easily be given for  $-a \leq x \leq 0$ , from simple symmetry considerations.

The vibrations of the boundary are described by a time-dependent amplitude  $\varepsilon(t)$  around the interface; i.e., one will have  $b(t) = b + \varepsilon(t)$ . Then, from Eq. (8), the time-dependent cross sections are given as

$$\begin{aligned} \Sigma_{\alpha,i}(x, t) = & \{1 - H(x - b - \varepsilon(t))\}\Sigma_{\alpha,i}^c \\ & + H(x - b - \varepsilon(t))\Sigma_{\alpha,i}^r. \end{aligned} \quad (9)$$

Likewise, the shell-mode vibrations imply that the interface at  $-b$  will fluctuate as  $-b(t) = -b - \varepsilon(t)$ . Then, the perturbation  $\delta\Sigma_{\alpha,i}(x, t)$ , defined as

$$\Sigma_{\alpha,i}(x, t) = \Sigma_{\alpha,i}(x) + \delta\Sigma_{\alpha,i}(x, t), \quad (10)$$

can be obtained from Eqs. (8), (9), and (10) with a one-term Taylor expansion as

$$\delta\Sigma_{\alpha,i}(x, t) = \varepsilon(t)\delta\Sigma_{\alpha,i}(b)[\delta(x - b) + \delta(x + b)], \quad (11)$$

where the notation

$$\delta\Sigma_{\alpha,i}(b) \equiv \Sigma_{\alpha,i}^c - \Sigma_{\alpha,i}^r \quad (12)$$

was introduced. Equation (11) shows that the perturbation of the cross sections obeys the same symmetry as the static cross sections; hence, the induced neutron noise also will be symmetric around the core center.<sup>a</sup> Therefore, it is sufficient to calculate the induced neutron noise  $\delta\bar{\phi}(x, t)$  for  $x \geq 0$  only. For reasons of symmetry, the argument  $b$  can be neglected in Eq. (12) in the notation of the perturbation.

From now on the treatment is rather standard and can be described as follows. Starting with the time-dependent two-group diffusion equations for the noise in the core and the reflector, splitting up the fluxes and the delayed

neutron precursors to static values and fluctuations, neglecting second-order terms, and eliminating the delayed neutron precursors by a temporal Fourier transform, one arrives at the noise equations in the frequency domain in the following form:

$$\hat{L}^c(x, \omega)\delta\bar{\phi}^c = \varepsilon(\omega)\delta(x - b)\hat{S}(x)\bar{\phi}^c \quad (13)$$

and

$$\hat{L}^r(x, \omega)\delta\bar{\phi}^r = \varepsilon(\omega)\delta(x - b)\hat{S}(x)\bar{\phi}^r. \quad (14)$$

Here, the following notations are used:

$$\begin{aligned} \hat{L}^c = & \begin{bmatrix} D_1^c \frac{d^2}{dx^2} - \tilde{\Sigma}_1^c & \nu\tilde{\Sigma}_{f,2}^c \\ \Sigma_R^c & D_2^c \frac{d^2}{dx^2} - \tilde{\Sigma}_{a,2}^c \end{bmatrix} \quad (\text{core}), \quad (15) \\ \hat{L}^r = & \begin{bmatrix} D_1^r \frac{d^2}{dx^2} - \tilde{\Sigma}_1^r & 0 \\ \Sigma_R^r & D_2^r \frac{d^2}{dx^2} - \tilde{\Sigma}_{a,2}^r \end{bmatrix} \quad (\text{reflector}), \end{aligned} \quad (16)$$

and

$$\hat{S} = \begin{bmatrix} \delta\tilde{\Sigma}_1 & -\left(1 - \beta + \frac{\lambda\beta}{\lambda + i\omega}\right)\nu\delta\Sigma_{f,2} \\ -\delta\Sigma_R & \delta\Sigma_{a,2} \end{bmatrix}, \quad (17)$$

with the further following shorthand notations:

$$\begin{cases} \tilde{\Sigma}_1^c = \left(\Sigma_{a,1}^c + \Sigma_R^c + \frac{i\omega}{v_1}\right) - \left(1 - \beta + \frac{\lambda\beta}{\lambda + i\omega}\right)\nu\Sigma_{f,1}^c \\ \tilde{\Sigma}_{f,2}^c = \left(1 - \beta + \frac{\lambda\beta}{\lambda + i\omega}\right)\Sigma_{f,2}^c \\ \tilde{\Sigma}_{a,2}^c = \Sigma_{a,2}^c + \frac{i\omega}{v_2} \\ \delta\tilde{\Sigma}_1 = \delta\Sigma_{a,1} + \delta\Sigma_R - \left(1 - \beta + \frac{\lambda\beta}{\lambda + i\omega}\right)\nu\delta\Sigma_{f,1} \\ \tilde{\Sigma}_1^r = \left(\Sigma_{a,1}^r + \Sigma_R^r + \frac{i\omega}{v_1}\right) \\ \tilde{\Sigma}_{a,2}^r = \Sigma_{a,2}^r + \frac{i\omega}{v_2}. \end{cases} \quad (18)$$

Explanations of all the parameters and the quantitative values used in the numerical work can be found in the Appendix. To make the solutions unique, one needs to

<sup>a</sup>It might be interesting to note that for the case of a vibrating central control rod, one would have  $\delta\Sigma_{\alpha,i}(-b) = -\delta\Sigma_{\alpha,i}(b)$  in contrast to Eq. (11), which leads to an antisymmetric noise distribution in the core.

specify the interface and boundary conditions of Eqs. (13) and (14). The boundary conditions for the noise will be the same as for the static flux in Eq. (6); i.e.,

$$\delta\vec{\phi}^r(x)|_{x=a} = 0 \quad (19)$$

However, the interface conditions will be modified because of the Dirac-delta function character of the perturbation, as expressed in Eqs. (13) and (14):

$$\delta\vec{\phi}^c(x, \omega)|_{x=b_-} = \delta\vec{\phi}^r(x, \omega)|_{x=b_+} \quad (20a)$$

$$D_1^r \frac{\partial}{\partial x} \delta\phi_1^r(x, \omega)|_{x=b_+} - D_1^c \frac{\partial}{\partial x} \delta\phi_1^c(x, \omega)|_{x=b_-} = \varepsilon(\omega)(S_{11}\phi_1(b) + S_{12}\phi_2(b)) \quad (20b)$$

and

$$D_2^r \frac{\partial}{\partial x} \delta\phi_2^r(x, \omega)|_{x=b_+} - D_2^c \frac{\partial}{\partial x} \delta\phi_2^c(x, \omega)|_{x=b_-} = \varepsilon(\omega)(S_{21}\phi_1(b) + S_{22}\phi_2(b)) \quad (20c)$$

On the right side of Eqs. (20b) and (20c), we did not indicate if the flux is taken from the core or the reflector because as Eq. (20a) also expresses, they are equal to each other at the interface.

A comparison of the static boundary conditions of Eqs. (5) and (6) with the dynamic conditions of Eqs. (19) and (20) shows that the number of conditions and the number of regions separated by interface conditions is the same for the static and the dynamic cases. The reason for this is that the perturbation is acting exactly on the interface. Hence, the degree of difficulty of solving the dynamic equations is the same as that of solving the static equations. In effect, the dynamic task is even simpler in the sense that because of the inhomogeneous terms on the right side of Eqs. (20b) and (20c) and the nonvanishing determinant of the matrix for the unknown flux coefficients (given shortly), the dynamic problem is not an eigenvalue problem; rather, it is the solution of a directly invertible nonsingular matrix equation. To illustrate this, one writes the solutions of Eqs. (13) and (14), taking the symmetry also into consideration, in the following form:

$$\begin{cases} \overline{\delta\vec{\phi}^r}(x, \omega) = \tilde{A}_3 \begin{bmatrix} 1 \\ \tilde{C}_\kappa(\omega) \end{bmatrix} \frac{\sinh(\tilde{\kappa}_1(|x| - a))}{\sinh(\tilde{\kappa}_1(b - a))} + \tilde{A}_4 \begin{bmatrix} 0 \\ 1 \end{bmatrix} \frac{\sinh(\tilde{\kappa}_2(|x| - a))}{\sinh(\tilde{\kappa}_2(b - a))} \\ \overline{\delta\vec{\phi}^c}(x, \omega) = \tilde{A}_1 \begin{bmatrix} 1 \\ \tilde{C}_\mu(\omega) \end{bmatrix} \cos(\tilde{\mu}x) + \tilde{A}_2 \begin{bmatrix} 1 \\ \tilde{C}_\eta(\omega) \end{bmatrix} \frac{\cosh(\tilde{\eta}x)}{\cosh(\tilde{\eta}b)} \end{cases} \quad (21)$$

where

$$\begin{cases} \tilde{\kappa}_1 = \sqrt{\frac{\tilde{\Sigma}_1^r}{D_1^r}} \\ \tilde{\kappa}_2 = \sqrt{\frac{\tilde{\Sigma}_{a,2}^r}{D_2^r}} \\ \tilde{C}_\kappa = \frac{\Sigma_R^r}{D_2^r(\tilde{\kappa}_2^2 - \tilde{\kappa}_1^2)} \end{cases} \quad (22)$$

and

$$\begin{cases} \tilde{\eta} = \sqrt{\frac{(D_1^c \tilde{\Sigma}_{a,2}^c + D_2^c \tilde{\Sigma}_1^c) + \sqrt{(D_1^c \tilde{\Sigma}_{a,2}^c - D_2^c \tilde{\Sigma}_1^c)^2 + \frac{4}{k} \nu \tilde{\Sigma}_{f,2}^c \Sigma_R^c D_1^c D_2^c}}{2D_1^c D_2^c}} \\ \tilde{\mu} = \sqrt{\frac{\sqrt{(D_1^c \tilde{\Sigma}_{a,2}^c - D_2^c \tilde{\Sigma}_1^c)^2 + \frac{4}{k} \nu \tilde{\Sigma}_{f,2}^c \Sigma_R^c D_1^c D_2^c} - (D_1^c \tilde{\Sigma}_{a,2}^c + D_2^c \tilde{\Sigma}_1^c)}{2D_1^c D_2^c}} \\ \tilde{C}_\eta = \frac{\Sigma_R^c}{\tilde{\Sigma}_{a,2}^c - D_2^c \tilde{\eta}^2} \\ \tilde{C}_\mu = \frac{\Sigma_R^c}{\tilde{\Sigma}_{a,2}^c + D_2^c \tilde{\mu}^2} \end{cases} \quad (23)$$

The unknown constants  $\tilde{A}_1$  through  $\tilde{A}_4$  can be determined from the equation that results from putting Eq. (21) into Eq. (20) and rearranging to obtain

$$\hat{M} \cdot \begin{bmatrix} \tilde{A}_1 \\ \tilde{A}_2 \\ \tilde{A}_3 \\ \tilde{A}_4 \end{bmatrix} = \varepsilon(\omega) \begin{bmatrix} 0 \\ 0 \\ S_{11}\phi_1^c(b) + S_{12}\phi_2^c(b) \\ S_{21}\phi_1^c(b) + S_{22}\phi_2^c(b) \end{bmatrix} \quad (24)$$

or

$$\hat{M} \cdot \tilde{A} = \varepsilon(\omega) \tilde{F} \quad (25)$$

where  $\hat{M}$  is given as

$$\begin{bmatrix} -\cos(b\mu) & -1 & 1 & 0 \\ -C_\mu \cos(b\mu) & -C_\eta & C_\kappa & 1 \\ \mu D_1^c \sin(b\mu) & -\eta D_1^c \tanh(b\eta) & \kappa_1 D_1^r \coth(\kappa_1(b-a)) & 0 \\ C_\mu \mu D_2^c \sin(b\mu) & -C_\eta \eta D_2^c \tanh(b\eta) & C_\kappa \kappa_1 D_2^r \coth(\kappa_1(b-a)) & \kappa_1 D_2^r \coth(\kappa_1(b-a)) \end{bmatrix} \quad (26)$$

The solution of Eq. (25) is given as

$$\tilde{A} = \varepsilon(\omega) \hat{M}^{-1} \tilde{F} \quad (27)$$

Substituting the solution expressed by Eq. (27) back into Eq. (21) yields the formal solution to the problem, which can then be evaluated numerically.

### III. ALTERNATIVE CALCULATION OF THE NOISE

As mentioned earlier, the noise was also calculated by the dynamic code developed at the Chalmers University of Technology Department of Nuclear Engineering<sup>21</sup> and referred to as the noise simulator. Although this simulator was primarily designed for handling 2-D cores, a 1-D version was also developed in the framework of this study so that the 1-D system described previously could be easily modeled. The fact that the system consists of a homogeneous core and an (obviously homogeneous) reflector meant that the requirements on the node resolution were rather mild. To be able to represent small amplitude vibrations of the core, a node size of 0.5375 cm was selected. This parameter was solely determined by the fact that the spatial extent of a perturbation cannot be smaller than one node, hence the small node size. This node resolution can only be achieved in 1-D systems (i.e., the node size in 2-D systems cannot typically be smaller than 8 cm because of excessive computational times).

The absolute value and the phase of the noise were calculated over the core by using the same static parameters as in the analytical model (see the Appendix) for a vibration of 0.5375-cm amplitude. The noise simulator also calculates the static flux by solving the static eigenvalue equation. It is an important aspect of any noise

calculation that the system is exactly critical (i.e., to an accuracy of a large number of decimal points) by applying the same spatial discretization algorithm as the one used in the dynamic calculations; otherwise, the asymptotic properties, such as the dominance of the point kinetic term at low frequencies, will not be reconstructed. Hence, the correct spatial behavior of the noise also will be incorrect. Because of this requirement, the noise simulator and the analytical method, although starting with the same static data set, need to make the eigenvalue calculation separately and modify the fission cross sections according to Eq. (7) each with their own  $k_{eff}$  value. This also gives an opportunity to compare the  $k_{eff}$  of the analytical model and the simulator. In the present calculations, one obtained  $k_{eff} = 1.0014629$  in the analytical model and  $k_{eff} = 1.0014594$  with the noise simulator.

Finally, in some cases comparisons were made with the calculations for the same problem by using the adiabatic approximation.<sup>26</sup> In the adiabatic approximation, the noise is calculated as the sum of a point kinetic (or reactivity) term, and the adiabatic fluctuation of the so-called shape function  $\psi(x, t)$ , which is defined in the flux factorization.<sup>27</sup> That is, the noise is written in the form

$$\delta\phi_i(x, t) = \delta P(t) \cdot \phi_{0,i}(x) + \delta\psi_i(x, t) \quad i = 1, 2 \quad (28)$$

where the first term on the right side is the point kinetic term with  $\phi_{0,i}(x)$  being the static flux and the second term is referred to as the space-dependent term.

In the adiabatic approximation, the functions  $\delta\psi_i(x, t)$  are determined from static calculations as the difference between the static eigenfunctions corresponding to the

perturbed and unperturbed states. The perturbed state corresponds to a static case when the core-reflector interface is at  $x = b + \varepsilon$ , whereas the unperturbed case is when  $\varepsilon = 0$ . Hence,

$$\delta\psi_i(x, \varepsilon) \approx \delta\psi_i^{ad}(x, \varepsilon) \equiv \psi_i(x, \varepsilon) - \phi_{0,i}(x) \quad (29)$$

where  $\psi_i(x, \varepsilon)$  are the static (normalized) shape functions corresponding to the boundary being at  $x = b + \varepsilon$ . The superscript *ad* stands for the adiabatic approximation. By letting  $\varepsilon$  depend parametrically on time,  $\varepsilon = \varepsilon(t)$ , one can write  $\delta\psi_i(x, \varepsilon(t)) = \delta\psi_i(x, t)$ . Since in the calculations only terms linear in  $\varepsilon$  were kept, one can easily switch to the frequency domain since all time dependence in the second term on the right side of Eq. (28) is contained in  $\varepsilon(t)$ :

$$\delta\psi_i(x, t) \approx \left. \frac{\partial \delta\psi_i(x, \varepsilon)}{\partial \varepsilon} \right|_{\varepsilon=0} \varepsilon(t) \quad (30)$$

In the concrete calculations by Sunde and Arzhanov,<sup>26</sup> the further simplification of the plateau frequency approximation was used, in which one assumes

$$G_0(\omega) \approx \frac{1}{\beta} \quad (31)$$

This leads finally to the form used in the numerical work as

$$\delta\phi_i(x, \omega) = \frac{1}{\beta} \delta\rho(\omega) \cdot \phi_{0,i}(x) + \delta\psi_i^{ad}(x, \omega) \quad (32)$$

Because of the application of the plateau frequency approximation, the frequency dependence of both terms on the right side of Eq. (32) is contained only in  $\varepsilon(\omega)$ , which means that  $\delta\phi_i(x, \omega)/\varepsilon(\omega)$  will be a real number. That is, the phase will take the values of either zero or  $\pm\pi$  only. This is a clear limitation of the adiabatic approximation with the plateau frequency approximation when investigating the behavior of the phase.

One advantage of the adiabatic approximation—which constituted a good part of the motivation for using it—is the fact that it easily allows accounting for the dilution of the core material with the “stretching” of the system during shell-mode vibrations. In the real case, unlike in the simple analytical model we assumed here, due to materials conservation, the distortion of the core means a redistribution of the material. That is, along the directions of the core expansion, the material density will decrease, and vice versa. In the simple 1-D case, this means that the macroscopic cross sections in the core will scale as  $b/(b + \varepsilon)$ , with a change of the boundary position by  $\varepsilon$ . Such an effect is very easy to incorporate in the adiabatic approximation, both in the reactivity and in the space-dependent term. On the other hand, in the full analytical model this would mean the appearance of a noise source that, in addition to the Dirac-delta one at

the core-reflector interface, also has a term uniformly distributed in the core. Such a case would be an order of magnitude more difficult to handle in the analytical model. Indeed, such calculations are made much easier in the noise simulator or in the adiabatic approximation. However, we disregard the dilution effect and only use the perturbation as defined at the beginning of this section. The calculations by Sunde and Arzhanov<sup>26</sup> showed that the dilution effect has only moderate influence on the solutions in the core and a negligible effect in regard to the local component, which is our main concern in this paper.

In all quantitative work, for the sake of comparison, the calculated values of  $\delta\phi_i(x, \omega)/\varepsilon(\omega)$  were calculated and are shown in Figs. 3 through 6.

#### IV. NUMERICAL WORK

Before turning to the comparison between the different methods of calculating the noise, we first investigate the amplitude and the phase of the noise as calculated in the analytical model for the system specified in the Appendix. The dimensions of the critical system are  $b = 161.25$  cm and  $a = 279.5$  cm. The result of such a calculation with the frequency of the shell-mode vibration set to 20 Hz is shown in Fig. 3. Figure 3 shows a large local component in the amplitude of both the fast and the thermal noise and in the phase of the thermal noise. The phase of the fast noise, on the other hand, remains smooth even at the boundary. The amplitude rises quite markedly for both the thermal and the fast flux close to the interface core/reflector.

The phase behavior of the thermal noise (and also the fine structure of the amplitude of the thermal noise, shown in Fig. 4) close to the interface is rather intricate and deserves a more detailed analysis. It is seen that in most parts of the core, the phase is negative, which is natural, but it is also relatively close to zero except close to the boundary. It is quite constant in the reflector, while it decreases in the core with increasing distance from the core boundary. This latter behavior is also self-explaining. It simply shows the physical effect of increasing phase lag with increasing distance between perturbation and response.

To understand the opposite phase behavior of the thermal noise close to the core-reflector interface, it is first necessary to know the reactivity coefficient of the oscillations; i.e.,

$$\alpha \equiv \left. \frac{\delta\rho}{\partial\varepsilon} \right|_{\varepsilon=0} \quad (33)$$

This can be calculated from either a simple perturbation formula using the perturbation as defined by Eq. (11) or from a static eigenvalue calculation performed in the

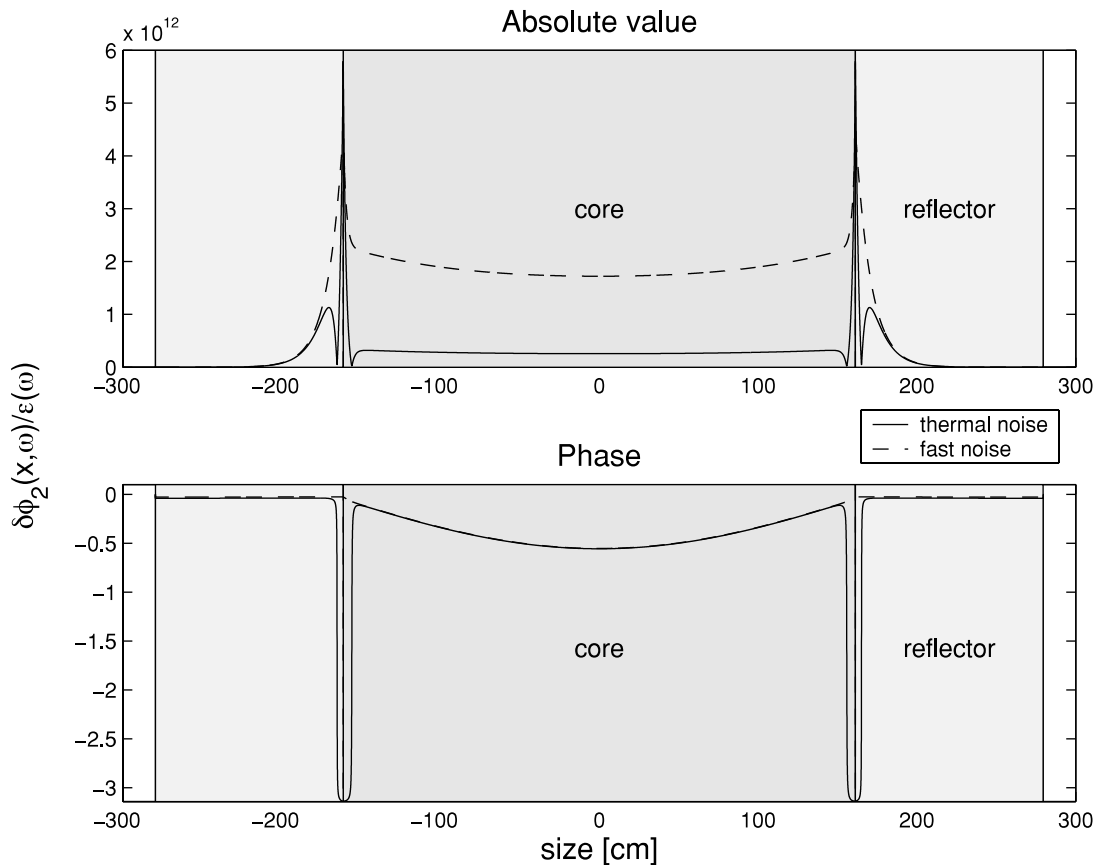


Fig. 3. Absolute value and phase of fast and thermal noise.

adiabatic approximation. These of course need to give the same value in the first order of  $\varepsilon$ . With the material and geometrical data of the system treated here, one obtains

$$\alpha = 4.95 > 0 \text{ pcm/cm} ; \quad (34)$$

i.e., the point kinetic term of the noise is in phase with the perturbation. Based on the calculations made in the adiabatic approximation,<sup>26</sup> where the shape function also is calculated separately, one can see that except close to the interface where the local component dominates, the noise is rather well described by the point kinetic term; i.e., the traditional space-dependent term is small. Hence, the phase is close to zero in those points.

It remains to be explained why a perturbation that has a positive reactivity effect leads to a decreasing thermal flux (i.e., a noise with opposite phase) only in the very neighborhood of the perturbation itself. However, this is also understandable. An increase of  $\varepsilon$  actually means adding a layer of core material at the boundary and replacing the reflector material there. The core material means increased production of fissions and hence fast neutrons, which is the ultimate reason for the in-

crease in reactivity, but this is achieved at the price of increased absorption of thermal neutrons. This is the reason for the out-of-phase behavior of the local thermal noise. The same facts also explain the fine spatial structure of the amplitude of the thermal noise close to the boundary (Fig. 4) where the close-to-zero value of the minimum of the amplitude corresponds to the crossing of its (otherwise dominating) real part from positive to negative. It is also seen that in accordance with the previous statement, the phase of the fast noise shows no local out-of-phase behavior. It remains smooth and close to zero everywhere.

One now can also check how the present results support the possibility of an out-of-phase behavior between an ex-core (ex-vessel) detector and an in-core detector, as described in Sec. I and in Ref. 13. Using vacuum boundary conditions at the outer edge of the reflector, an ex-vessel detector cannot be directly modeled in diffusion theory. It can be best approximated in the present model with a detector inside the reflector but close to its outer boundary. The data shown in Figs. 3 through 6 illustrate that an out-of-phase behavior can indeed exist between such an ex-core detector and an in-core one if the in-core detector is close to the core boundary.

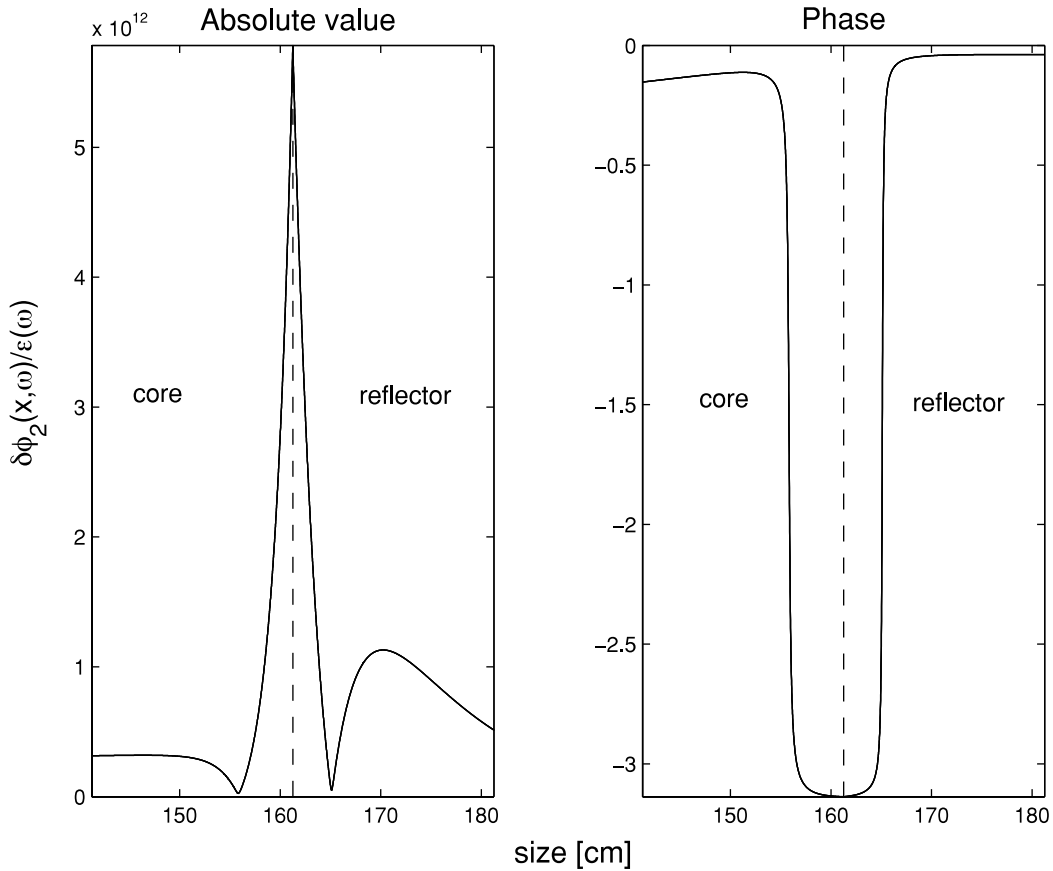


Fig. 4. Absolute value and phase (in radians) of the thermal noise at the interface between the core and the reflector.

A comparison with the measurement that prompted the recent work, shown in Fig. 1b, supports the validity of the results. Namely, the in-core detector in question was in the center position of an outermost fuel assembly, even if not exactly on the boundary. Unfortunately, the signals from the other in-core detectors had a low APSD at the shell-mode vibration frequency and supplied a nonreliable phase value, so a more thorough checking of the calculation results is not possible for the time being.

Of course the model used here contains several simplifications compared to reality, and the severity of the constraint this fact puts on the applicability of the results to a concrete case is not clear. One neglected effect, already mentioned, is the rearrangement (dilution) of the core density with the shell-mode vibrations. It was shown in the adiabatic calculations<sup>26</sup> that the dilution effect decreases the reactivity coefficient of the vibrations very significantly, to the extent that the magnitude of the ordinary (nonlocal) space-dependent component becomes dominating in the core. In such a case, an out-of-phase behavior can exist even between an ex-vessel detector and an in-core detector, which is not based on the local component, and hence, the in-core detector does not need

to be close to the core boundary. A final difference between the models and reality is that the detector, being situated within a fuel assembly, vibrates together with the core, and hence, the noise it measures is not the same as the one calculated in all the models used here. This effect actually could be calculated in the adiabatic approximation, which could be an interesting exercise. Finally, a more realistic description of the core-barrel vibrations requires a 2-D description. In two dimensions, the space-dependent component of the noise is, as a rule, enhanced compared with the point kinetic one, and this could also alter some of the conclusions of the present work. However, in this paper our main purpose was to perform a conceptual study and understanding of the basic phenomena rather than try to exactly reconstruct certain measurements. In later work the present investigations will be extended to two dimensions, alleviating some of the restrictions mentioned above.

It is interesting to compare the results of the analytical model with those of the noise simulator. Such a comparison is shown, now only for the thermal noise, in Fig. 5. It is seen that they agree with each other very well. The relative weight of the amplitude of the local components in the two models shows some disagreement,

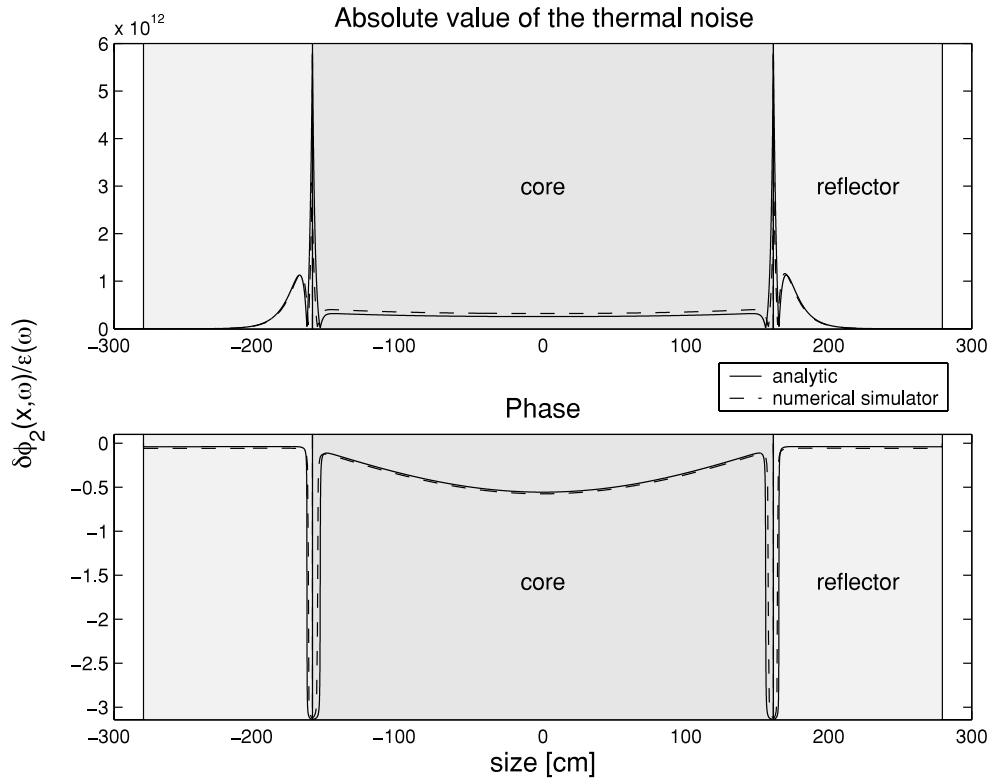


Fig. 5. Absolute value and phase of the thermal noise from both the analytical solution and the numerical simulator.

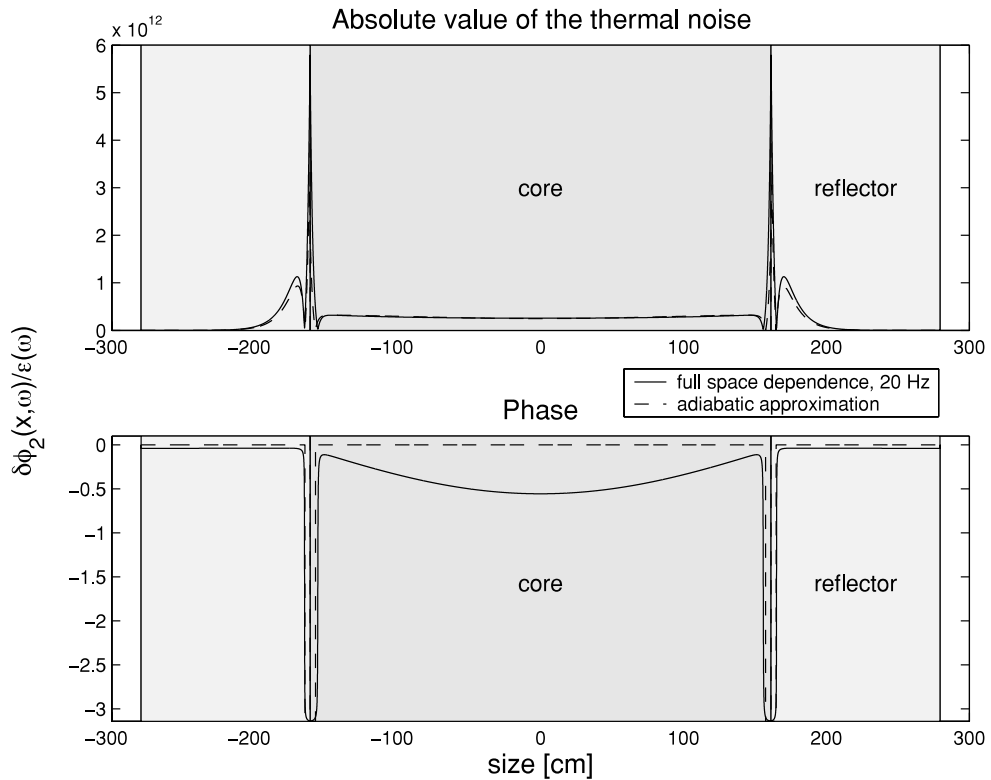


Fig. 6. Absolute values and phase of thermal noise calculated in the full analytical model and in the adiabatic approximation.

which is due to the fact that in the Dirac-delta function representation and in the finite node size perturbation of the cross sections, the internal magnitude of the perturbation of the various cross sections will not be exactly the same in the two models. The phase curves, on the other hand, agree very well. This serves as further confirmation of the validity of the results.

Also, a comparison with the calculations from the adiabatic approximation can be made, as shown in Fig. 6. Figure 6 illustrates well that while the amplitudes, as obtained from the two models, agree well qualitatively and quantitatively, the phase of the noise in the adiabatic approximation is reproduced only in a very coarse way (as a binary variable taking the values 0 or  $-\pi$ ). Hence, the phase is zero in this approximation in most parts of the reflector and in the core, except close to the core-reflector interface. The opposite-phase behavior around the core-reflector interface, though, is also correctly reproduced by the adiabatic approximation.

**V. CONCLUSIONS**

The present work constitutes the first calculation of the in-core and ex-core neutron noise induced by shell-mode core-barrel vibrations in a two-group treatment. Although the model used has several limitations, such as a 1-D treatment and no accounting for the change in material density during vibrations, certain aspects of the induced noise, most notably the strong local component at the core-reflector interface, were reconstructed correctly. Some measurements with in-core detectors close to the core boundary would be useful for checking the applicability of the results, and indeed such measurements are planned. Extension of the calculations to two dimensions constitutes no conceptual problem, and accounting for the effect of the vibration together with the core of the in-core detectors itself in the adiabatic approximation can be performed without difficulty. Such extensions are planned in future work.

**APPENDIX**

The following values of cross sections and diffusion coefficients were obtained from static SIMULATE-3 calculations in three dimensions corresponding to the Ringhals-4 pressurized water reactor (cycle 16, burnup 8.767 GWd/tonne HM) and then homogenized from three dimensions to one dimension. These data were finally homogenized for the core and the reflector regions, respectively. Note that the absorption cross section for the fast group in the core is negative. This is due to the homogenization from three dimensions to one dimension, which preserves the leakage rate in the directions not accounted for in the 1-D model.

$\Sigma_{a,1}^c = 0.0115 \text{ cm}^{-1}$	fast absorption cross section	} for the core	(A.1)
$\Sigma_{a,2}^c = 0.1019 \text{ cm}^{-1}$	thermal absorption cross section		
$\Sigma_R^c = 0.0151 \text{ cm}^{-1}$	removal cross section		
$\nu$	average number of neutrons per fission		
$\nu\Sigma_{f,1}^c = 0.0057 \text{ cm}^{-1}$	fast fission cross section times $\nu$		
$\nu\Sigma_{f,2}^c = 0.1425 \text{ cm}^{-1}$	thermal fission cross section times $\nu$		
$D_1^c = 1.4376 \text{ cm}$	fast diffusion coefficient		
$D_2^c = 0.3723 \text{ cm}$	thermal diffusion coefficient		
$v_1 = 1.82304 \times 10^7 \text{ cm/s}$	speed of fast neutrons		
$v_2 = 4.13067 \times 10^5 \text{ cm/s}$	speed of thermal neutrons		

$\Sigma_{a,1}^r = -0.0098 \text{ cm}^{-1}$	fast absorption cross section	} for the reflector	(A.2)
$\Sigma_{a,2}^r = 0.0284 \text{ cm}^{-1}$	thermal absorption cross section		
$\Sigma_R^r = 0.0238 \text{ cm}^{-1}$	removal cross section		
$D_1^r = 1.3116 \text{ cm}$	fast diffusion coefficient		
$D_2^r = 0.2624 \text{ cm}$	thermal diffusion coefficient		

$\beta = 0.00535$	effective delayed neutron fraction	} for the precursors	(A.3)
$\lambda = 0.08510$	decay constant of the delayed neutrons		

## REFERENCES

1. J. B. DRAGT and E. TÜRKCAN, "Borssele PWR Noise: Measurements, Analysis and Interpretation," *Prog. Nucl. Energy*, **1**, 293 (1977).
2. C. W. MAYO, "Detailed Neutron Noise Analysis of Pressurized Water Reactor Internal Vibrations," *Atomkernenergie*, **29**, 9 (1977).
3. D. WACH and R. SUNDER, "Improved PWR-Neutron Noise Interpretation Based on Detailed Vibration Analysis," *Prog. Nucl. Energy*, **1**, 309 (1977).
4. J. A. THIE, "Core Motion Monitoring," *Nucl. Technol.*, **45**, 5 (1979).
5. J. A. THIE, *Power Reactor Noise*, American Nuclear Society, La Grange Park, Illinois (1981).
6. F. ÅKERHJELM, R. ESPEFÄLT, and J. LORENZEN, "Surveillance of Vibrations in PWR," *Prog. Nucl. Energy*, **9**, 453 (1982).
7. T. BOGARD, T. KOZLOSKY, S. LOWENFELD, and N. SINGLETON, "Reactor Internals and Core Support Monitoring System," *Proc. 6th Symp. Nuclear Reactor Surveillance and Diagnostics (SMORN-VI)*, Gatlinburg, Tennessee, May 19–24, 1991, Organization for Economic Cooperation and Development/Nuclear Energy Agency (1991).
8. D. J. DAILEY and R. W. ALBRECHT, "In-Core/Ex-Core Neutron Noise Measurements to Examine Core Internal Vibrations in an Operating PWR," *Prog. Nucl. Energy*, **15**, 251 (1985).
9. S. YAMADA, T. SATO, and H. KANAMARU, "Five-Detector Method for Core-Barrel Motion Analysis," *Ann. Nucl. Energy*, **12**, 455 (1985).
10. R. SUNDER, M. BALEANU, K. KIENINGER, A. KOLBASSEFF, W. KUHN, and H. RÖSLER, "Experiences and Results with COMOS—An On-Line Vibration Analysis and Monitoring System," *Proc. 6th Symp. Nuclear Reactor Surveillance and Diagnostics (SMORN-VI)*, Gatlinburg, Tennessee, May 19–24, 1991, Organization for Economic Cooperation and Development/Nuclear Energy Agency (1991).
11. I. PÁZSIT, J. K.-H. KARLSSON, and N. S. GARIS, "Some Developments in Core-Barrel Vibration Diagnostics," *Ann. Nucl. Energy*, **25**, 1079 (1998).
12. J. K.-H. KARLSSON and I. PÁZSIT, "Final Report on the Research Project Ringhals Diagnostics and Monitoring, Stage 3: Analysis of Core Barrel Vibrations in Ringhals 2, 3 and 4 for Several Fuel Cycles," CTH-RF-135/RR5, Chalmers University of Technology (1998).
13. V. ARZHANOV and I. PÁZSIT, "Diagnostics of Core Barrel Vibrations by Ex-Core and In-Core Neutron Noise," *Prog. Nucl. Energy*, **43**, 151 (2003).
14. I. PÁZSIT and V. ARZHANOV, "Linear Reactor Kinetics and Neutron Noise in Systems with Fluctuating Boundaries," *Ann. Nucl. Energy*, **27**, 1385 (2000).
15. C. DEMAZIÈRE, V. ARZHANOV, J. K.-H. KARLSSON, and I. PÁZSIT, "Final Report on the Research Project Ringhals Diagnostics and Monitoring, Stage 4," CTH-RF-145/RR6, Chalmers University of Technology (1999).
16. C. DEMAZIÈRE, V. ARZHANOV, and I. PÁZSIT, "Final Report on the Research Project Ringhals Diagnostics and Monitoring, Stage 5," CTH-RF-156/RR7, Chalmers University of Technology (2000).
17. C. DEMAZIÈRE, V. ARZHANOV, and I. PÁZSIT, "Final Report on the Research Project Ringhals Diagnostics and Monitoring, Stage 6," CTH-RF-161/RR8, Chalmers University of Technology (2001).
18. C. DEMAZIÈRE, V. ARZHANOV, and I. PÁZSIT, "Final Report on the Research Project Ringhals Diagnostics and Monitoring, Stage 7," CTH-RF-167/RR9, Chalmers University of Technology (2002).
19. I. PÁZSIT, "Control Rod Models and Vibration Induced Noise," *Ann. Nucl. Energy*, **15**, 333 (1988).
20. I. PÁZSIT and J. KARLSSON, "On the Perturbative Calculation of the Vibration Noise by Strong Absorbers," *Ann. Nucl. Energy*, **24**, 449 (1997).
21. C. DEMAZIÈRE, "Development of a 2-D 2-Group Neutron Noise Simulator," *Ann. Nucl. Energy*, **31**, 647 (2004).
22. J. A. UMBARGER and A. S. DIGIOVINE, "SIMULATE-3, Advanced Three-Dimensional Two-Group Reactor Analysis Code, User's Manual," Studsvik of America (1992).
23. C. DEMAZIÈRE and I. PÁZSIT, "2-D 2-Group Neutron Noise Simulator and Its Application to Anomaly Localisation," *Proc. Int. Mtg. Mathematical Methods for Nuclear Applications (M&C 2001)*, Salt Lake City, Utah, September 9–13, 2001, American Nuclear Society (2001) (CD-ROM).
24. C. DEMAZIÈRE and I. PÁZSIT, "A Phenomenological Model for the Explanation of a Strongly Space-Dependent Decay Ratio," *Proc. Int. Mtg. Nuclear Mathematical and Computational Sciences (M&C 2003)*, Gatlinburg, Tennessee, April 6–10, 2003, American Nuclear Society (2003) (CD-ROM).
25. R. SANCHIS-ARNAL, G. VERDÚ MARTIN, and G. L. MUNOZ-COBO, "Detector Point of View of Reactor Internal Vibrations Under Gaussian Coloured Random Forces—The Problem of Fitting Neutron Noise Experimental Data," *Ann. Nucl. Energy*, **15**, 275 (1988).
26. C. SUNDE and V. ARZHANOV, "Calculation of the Neutron Noise Induced by Shell-Mode Core-Barrel Vibrations in a 1-D 2-Group 2-Region Slab Reactor," CTH-RF-173, Chalmers University of Technology (2003).
27. G. I. BELL and S. GLASSTONE, *Nuclear Reactor Theory*, Van Nostrand-Reinhold, New York (1970).



# Paper V

*Investigation of the neutron noise induced by shell-mode core-barrel vibrations in a reflected reactor*

C. Sunde, C. Demazière and I. Pázsit

Proc. Int. Top. Mtg. on Mathematics and Computing, Supercomputing, Reactor Physics and Nuclear and Biological Applications (M&C2005), Avignon, France, September 12-15, 2005, American Nuclear Society (2005).



## **INVESTIGATION OF THE NEUTRON NOISE INDUCED BY SHELL-MODE CORE-BARREL VIBRATIONS IN A REFLECTED REACTOR**

**C Sunde, C Demazière and I Pázsit**

Department of Reactor Physics  
Chalmers University of Technology  
412 96 Göteborg, Sweden  
kalle@nephy.chalmers.se; demaz@nephy.chalmers.se;  
imre@nephy.chalmers.se

### **ABSTRACT**

The subject of this work is the calculation of the in-core neutron noise, induced by the shell-mode vibrations of the core-barrel. The original motivation was to investigate whether an out-of-phase behaviour can exist between the in-core and ex-core (ex-vessel) detectors lying at the same azimuthal position. To this order a two-region two-group diffusion model was used in one dimension. The noise was calculated with three different methods: with a full space-frequency-dependent solution, with a numerical code (“noise simulator”), and in the adiabatic approximation. It was found that such an out-of-phase behaviour indeed exists for in-core detector positions very close to the core boundary, due to the local component of the noise. In addition to its effect on the phase, the local component also manifests itself by a large amplitude of the noise around the vibrating core boundary, i.e. both in the core and the reflector. On the other hand if the movement of the detector together with the core is accounted for, which is possible in the adiabatic approximation, the effects of the local component disappear. Recently performed measurements in a power reactor were unsuccessful to detect the predicted local component, presumably because in-core detectors are not close enough to the core boundary.

**KEYWORDS:** shell-mode core-barrel vibrations, in-core neutron noise, local component

### **1. INTRODUCTION**

The ex-core neutron noise, induced by core-barrel vibrations has long been used to diagnose both beam-mode and shell-mode vibrations [1]-[12]. The corresponding methods have undergone a quite long development stage, and became quite effective for the diagnostics of beam-mode (pendular) vibrations. The quantitative diagnostics of shell-mode vibrations, however, has not reached a similar state, at least not in Westinghouse-type reactors where there are four ex-core detectors with an equal  $90^\circ$  spacing. Due to the fact that the shell-mode vibrations, and hence also the neutron noise induced by such vibrations, exhibit the same symmetry against rotations with  $90^\circ$  as the detectors, the information content in all detectors is equivalent, i.e. all ex-core detectors carry the same information. Hence it is not possible to determine both the vibration amplitude and the direction from the detector signals. In particular it is not possible to find out if

the reason for a change in the signal amplitude is due to a change in the vibration amplitude or to a change in the direction of the vibrations.

In connection with the study of in-core neutron noise induced by fluctuating system boundaries [13], originally considered for the description of the neutron noise induced by vibrating control rods, it was realized that core-barrel vibrations might lead also to in-core noise. For this reason the present authors started using the in-core detector signals for the analysis of core-barrel vibrations as part of a collaborative research project between the Ringhals NPP and the Department of Reactor Physics at Chalmers University of Technology ([14] - [15]). A compact solution for the radial and angular dependence for the in-core noise, induced by core-barrel vibrations, was given in [16]. The full confirmation of the theory, however, was hindered by the low number of in-core detectors (a maximum of five movable in-core detectors at a time). In particular, during the evaluation of the only measurement in Ringhals-3 when both in-core and ex-core detectors were available, in order to have a consistent interpretation, it was necessary to assume that ex-core and in-core detectors lying on the same azimuthal position exhibited opposite phase [16].

However, in that theory a bare system was used. In real systems a reflector region is situated between the core and the ex-core (=ex-vessel) detectors, whose thickness is also changing with oscillations of the core. This difference between the real situation and the simple non-reflected model opens a possibility to find the out-of-phase factor in question. In order to take into account the effect of the reflector, one needs to use two-group theory. The purpose of this work is to investigate the in-core noise induced by core-barrel vibrations in reflected systems by the extension of the model used earlier. Vibrations of the core boundary in a reflected system can be treated by a particularly simple model that was used for the description of vibrating control rods in the past [18]-[19].

In order to make a first principal investigation of the possible change of the phase relationships by including a reflector, a one-dimensional model was used in this work. Combined with the simple way of treating the core-barrel vibrations as a noise source, the present model allowed a fully analytic solution. The dependence of the amplitude and phase of the noise throughout the whole core was readily calculated and studied.

The calculations in the analytical model were compared to the results of a fully numerical solution of the same problem by using a so-called noise simulator [20]. The noise simulator is a code for the calculation of the dynamic transfer function of real, inhomogeneous cores in two-group theory, very much the same way as static ICFM codes calculate the static flux in real cores. In particular, it is compatible with the input deck of ICFM codes, most notably SIMULATE, which is used by most of the Swedish power utilities in core optimization and loading. Finally, the calculations were compared with a calculation made by using the adiabatic approximation [21].

Finally it was investigated how the results are modified if the noise is detected in points which move together with the core while the latter vibrates. This might well be the case for in-core detectors which are situated in the central positions of fuel assemblies in a PWR. Such a calculation can be easily performed in the adiabatic approximation. The results show that if the

noise is measured in a system moving together with the core, the local component disappears, which result is understandable. In reality the extent of the movement of the detectors is not known, although the concurrent movement of the detectors with the core, even if not to full extent, is presumably closer to the case in reality.

## 2. CALCULATION OF THE NOISE INDUCED BY SHELL-MODE VIBRATIONS

A one-dimensional model of a reflected reactor is selected for this study with a homogeneous central core and outer reflectors placed symmetrically around the core (see Fig. 1). Two-group diffusion theory will be used with the corresponding cross sections and diffusion constants. A list of those, together with the numerical values used in the quantitative work is given in the Appendix. Quantities in the fast and thermal groups are labeled with the subscript 1 and 2, respectively. The superscript *c* and *r* indicates whether the quantity belongs to the core or the reflector. One averaged-group of delayed neutrons is used in the dynamic calculations.

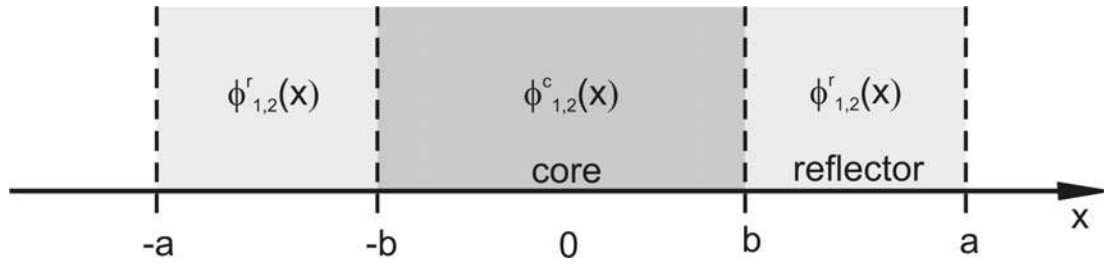


**Figure 1. 1-D core model with reflector**

The neutron noise induced by the shell-mode core-barrel vibrations is calculated from the usual time-dependent diffusion equations in two-group theory. Standard interface conditions and vacuum boundary conditions are used. In order to get a static critical system the fission cross sections are scaled with  $k_{eff}$ . The time-dependent equations can be solved by linearization and Fourier techniques in the usual manner. Then one ends up with the following expression for the noise in the frequency domain.

$$\hat{L}^c(x, \omega) \delta \bar{\phi}^c(x, \omega) = \varepsilon(\omega) \delta(x-b) \hat{S}(x) \bar{\phi}_0^c(x) \quad (1)$$

$$\hat{L}^r(x, \omega) \delta \bar{\phi}^r(x, \omega) = \varepsilon(\omega) \delta(x-b) \hat{S}(x) \bar{\phi}_0^r(x) \quad (2)$$

Here vector notations are used for the two energy groups, i.e.

$$\delta \bar{\phi} \equiv \begin{bmatrix} \delta \phi_1 \\ \delta \phi_2 \end{bmatrix}$$

etc., and the subscript 0 denotes the static flux. The matrices L and S contain different combinations of cross-sections and diffusion constants for the different groups and regions. The non-zero right hand side arises from the fact that the cross sections are time-dependent due to the

moving boundary between the core and the reflector. The cross sections were treated by a method, originally introduced for the treatment of control rod vibrations in a numerical work by Sanchis-Arnal et al. [17], and developed into an analytical tool under the name “ $\varepsilon/D$  method” by one of the present authors [18]. In that treatment, at the interface of the core and reflector at  $x = b$ , a uniform description of the static cross sections over both the core and reflector can be given as

$$\bar{\Sigma}_x(x) = \{1 - H(x - b)\} \bar{\Sigma}_x^c + H(x - b) \bar{\Sigma}_x^r \quad (3)$$

where the subscript  $x = \{\alpha, R, f\}$ , i.e. it stands for the type of reaction (absorption, removal or fission), and  $H(x)$  is the unit step function. A similar description is given at  $x = -b$ .

The vibrations of the boundary are described by a time-dependent amplitude  $\varepsilon(t)$  around the interface, i. e. one will have  $b(t) = b + \varepsilon(t)$  and likewise  $-b(t) = -b - \varepsilon(t)$ . Then, from a one-term Taylor expansion of Eq. (3) the time-dependent cross sections are given as

$$\bar{\Sigma}_x(x, t) = \bar{\Sigma}_x(x) + \varepsilon(t) \delta \bar{\Sigma}_x(b) [\delta(x - b) + \delta(x + b)] \quad (4)$$

where the notation

$$\delta \bar{\Sigma}_x(b) \equiv \bar{\Sigma}_x^c - \bar{\Sigma}_x^r \quad (5)$$

is introduced. Eq. (4) shows that the perturbation of the cross sections obeys the same symmetry as the static cross sections, hence also the induced neutron noise will be symmetric around the core centre\*. Therefore it is sufficient to calculate the induced neutron noise  $\delta \bar{\phi}(x, t)$  for  $x \geq 0$  only. For reasons of symmetry, the argument  $b$  can be neglected in Eq. (5) in the notation of the perturbation.

In order to make the solutions unique, one needs to specify the interface and boundary conditions to the above equations. The boundary conditions for the noise will be the same as for the static flux, i.e. vacuum boundary. The interface conditions will, however, be modified, due to the Dirac-delta function character of the perturbation and are as follows:

$$\left\{ \begin{array}{l} \delta \bar{\phi}^c(x, \omega) \Big|_{x=b_-} = \delta \bar{\phi}^r(x, \omega) \Big|_{x=b_+} \\ D_1^r \frac{\partial}{\partial x} \delta \bar{\phi}_1^r(x, \omega) \Big|_{x=b_+} - D_1^c \frac{\partial}{\partial x} \delta \bar{\phi}_1^c(x, \omega) \Big|_{x=b_-} = \varepsilon(\omega) [S_{11} \phi_{0,1}(b) + S_{12} \phi_{0,2}(b)] \\ D_2^r \frac{\partial}{\partial x} \delta \bar{\phi}_2^r(x, \omega) \Big|_{x=b_+} - D_2^c \frac{\partial}{\partial x} \delta \bar{\phi}_2^c(x, \omega) \Big|_{x=b_-} = \varepsilon(\omega) [S_{21} \phi_{0,1}(b) + S_{22} \phi_{0,2}(b)] \end{array} \right. \quad (6)$$

---

\* It might be interesting to note that for the case of a vibrating central control rod, one would have  $\delta \Sigma_{\alpha,i}(-b) = -\delta \Sigma_{\alpha,i}(b)$  in contrast to Eq. (4), which leads to an antisymmetric noise distribution in the core.

On the right hand side of the last two equations in Eq. (6) we did not indicate if the flux is taken from the core or the reflector; the reason is that, as the first equation also expresses, they are equal to each other at the interface. The solutions to Eqs. (1) and (2) with boundary and interface conditions and symmetry considerations are given as:

$$\begin{cases} \delta\bar{\phi}^r(x, \omega) = \tilde{A}_3 \begin{bmatrix} 1 \\ \tilde{C}_\kappa(\omega) \end{bmatrix} \frac{\sinh(\tilde{\kappa}_1(|x|-a))}{\sinh(\tilde{\kappa}_1(b-a))} + \tilde{A}_4 \begin{bmatrix} 0 \\ 1 \end{bmatrix} \frac{\sinh(\tilde{\kappa}_2(|x|-a))}{\sinh(\tilde{\kappa}_2(b-a))} \\ \delta\bar{\phi}^c(x, \omega) = \tilde{A}_1 \begin{bmatrix} 1 \\ \tilde{C}_\mu(\omega) \end{bmatrix} \cos(\tilde{\mu}x) + \tilde{A}_2 \begin{bmatrix} 1 \\ \tilde{C}_\eta(\omega) \end{bmatrix} \frac{\cosh(\tilde{\eta}x)}{\cosh(\tilde{\eta}b)} \end{cases} \quad (7)$$

where  $\tilde{C}_\kappa$ ,  $\tilde{C}_\mu$ ,  $\tilde{C}_\eta$ ,  $\tilde{\kappa}_1$ ,  $\tilde{\kappa}_2$ ,  $\tilde{\eta}$  and  $\tilde{\mu}$  are functions of the cross-sections, diffusion constants and the frequency,  $\omega$ . The unknown constants  $\tilde{A}_1 - \tilde{A}_4$  can be determined from the matrix equation that results from putting Eq. (7) into Eq. (6) and rearranging to obtain, in compact form:

$$\hat{M} \cdot \begin{bmatrix} \tilde{A}_1 \\ \tilde{A}_2 \\ \tilde{A}_3 \\ \tilde{A}_4 \end{bmatrix} = \varepsilon(\omega) \cdot \bar{F} \quad (8)$$

Here the matrix,  $\hat{M}$  is given by the l.h.s. of Eq. (6) and the vector,  $\bar{F}$ , by the r.h.s. of the same equation. This matrix equation is easily solved and the induced neutron noise in Eq. (7) can be evaluated numerically.

### 3. ALTERNATIVE CALCULATION OF THE NOISE

As mentioned earlier, the noise was also calculated by the dynamic code, developed at the Department ([20]), also referred to as the “noise simulator”. Although this simulator was primarily designed for handling 2-D cores, a 1-D version was also developed in the framework of this study so that the 1-D system described previously could be easily modelled. The fact that the system consists of a homogeneous core and homogenous reflector meant that the requirements on the node resolution were rather mild. In order to be able to represent small amplitude vibrations of the core, a node size of 0.5375 cm was selected. This parameter was solely determined by the fact that the spatial extent of a perturbation cannot be smaller than one node, hence the small node size. This node resolution can only be achieved in 1-D systems (i.e. the node size in 2-D systems cannot be smaller than typically 8 cm due to excessive computational times).

The absolute value and the phase of the noise were calculated over the core by using the same static parameters as in the analytical model (see the Appendix) for a vibration of 0.5375 cm amplitude. The noise simulator also calculates the static flux by solving the static eigenvalue equation. It is an important aspect of any noise calculation that the system is exactly critical (i.e. to an accuracy of a large number of decimal points) by applying the same spatial discretisation algorithm as the one used in the dynamic calculations, otherwise the asymptotic properties, such

as the dominance of the point kinetic term at low frequencies, will not be reconstructed. Hence also the correct spatial behaviour of the noise will be incorrect. Because of this requirement, the noise simulator and the analytical method, although starting with the same static data set, need to make the eigenvalue calculation separately and modify the fission cross sections each with their own  $k_{eff}$  value. This also gives an opportunity to compare the  $k_{eff}$  of the analytical model and the simulator. In the present calculations one obtained  $k_{eff} = 1.0014629$  in the analytical model, and  $k_{eff} = 0.0014594$  with the noise simulator.

Finally, in some cases comparisons were performed with the calculations made for the same problem by using the adiabatic approximation [21]. In the adiabatic approximation the noise is calculated as a point kinetic (or reactivity) term, and the adiabatic form of the so-called shape function [22]. That is, the noise is written in the form

$$\delta\bar{\phi}(x,t) = \delta P(t) \cdot \bar{\phi}_0(x) + \delta\bar{\psi}^{ad}(x,t) \quad (9)$$

where the first term on the right-hand-side is the point kinetic term, whereas the second one is referred to as the space-dependent term.

In the adiabatic approximation the functions  $\delta\bar{\psi}^{ad}(x,t)$  for various values of  $t$  are determined from static calculations, as the difference between the static eigenfunctions corresponding to the perturbed and unperturbed state. The perturbed state corresponds to a static case when the core-reflector interface is at  $x = b + \varepsilon(t)$ , whereas the unperturbed case is when  $\varepsilon = 0$ . If the system is in the so-called plateau region of the zero power reactor transfer function the noise in the frequency domain can be calculated as

$$\delta\bar{\phi}(x,\omega) = \frac{1}{\beta} \delta\rho(\omega) \cdot \bar{\phi}_0(x) + [\bar{\psi}(x,\varepsilon(\omega)) - \bar{\phi}_0(x)] \quad (10)$$

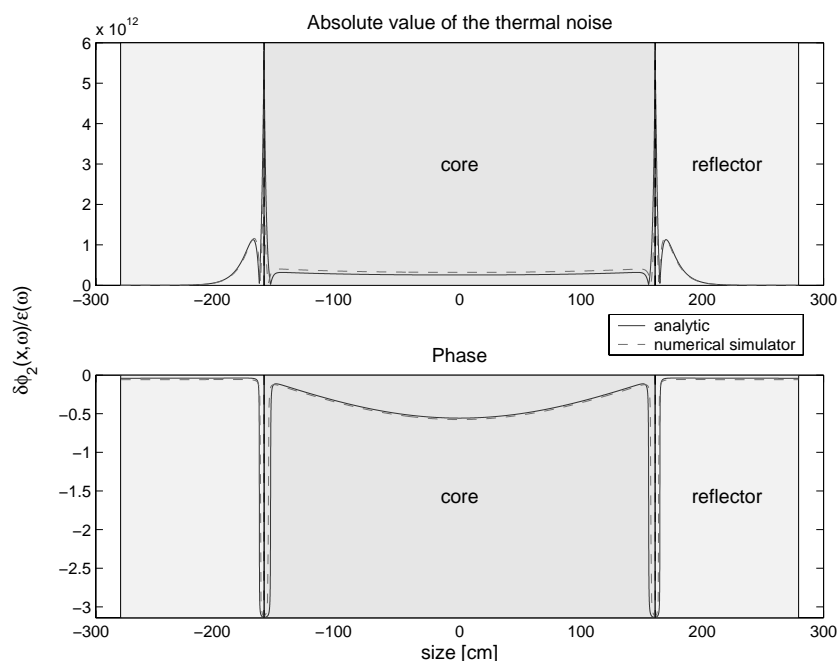
where  $\bar{\psi}(x,\varepsilon(\omega))$  are the static (normalised) shape functions corresponding to the boundary being at  $\varepsilon(\omega)$ . Due to the application of the plateau frequency approximation, the frequency dependence of both terms on the r.h.s. is contained only in  $\varepsilon(\omega)$ , which means that  $\delta\bar{\phi}(x,\omega)$  will be a real number. That is, the phase will take the values of either zero or  $\pm\pi$  only. This is a clear limitation of the adiabatic approximation with the plateau frequency approximation, when investigating the behaviour of the phase.

#### 4. NUMERICAL WORK

First, the noise was calculated both with the analytical expressions from Eqs. (1) - (2) and by the numerical simulator for the system specified in the Appendix. The dimensions of the critical system are  $b = 161.25$  cm and  $a = 279.5$  cm. The results of such calculations with the frequency of the shell-mode vibration set to 20 Hz, are shown in Fig. 2, with only the thermal noise present. It is seen that there is good agreement between the two different calculations. The relative weight of the amplitude in the two models show some disagreement, which is due to the fact that in the Dirac-delta function representation and in the finite node size perturbation of the cross sections, the internal magnitude of the perturbation of the various cross sections will not be exactly the same in the two models. The phase curves, on the other hand, agree very well. This agreement serves as a confirmation of the validity of the results.

A large local component in the amplitude and phase of the thermal noise is clearly visible in the figure. The phase behaviour of the thermal noise close to the interface is rather intricate and deserves a more detailed analysis. It is seen that in most parts of the core the phase is negative, which is natural, but also relatively close to zero except close to the boundary. It is quite constant in the reflector, while it decreases in the core with increasing distance from the core boundary. This latter behaviour is also self-explanatory, it just shows the physical effect of increasing phase lag with increasing distance between perturbation and response.

In order to understand the opposite phase behaviour of the thermal noise close to the core-reflector interface, it is necessary to know the reactivity coefficient  $\alpha$  of the oscillations.



**Figur 2. Absolute value and phase of the thermal noise from both the analytical solution and numerical simulator**

This can be calculated from either a simple perturbation formula using the perturbation as defined by Eq. (4), or from a static eigenvalue calculation, performed in the adiabatic approximation. These of course need to give the same value in first order of  $\epsilon$ . With the material and geometrical data of the system treated here, one obtains

$$\alpha = \frac{\partial \rho}{\partial \epsilon} = 4.95 > 0 \quad pcm/cm \quad (11)$$

i.e. the point kinetic term of the noise is in-phase with the perturbation. Based on the calculations made in the adiabatic approximation [21], where also the shape function is calculated separately, one can see that except close to the interface where the local component dominates, the noise is

rather well described by the point kinetic term, i.e. the traditional space-dependent term is small. Hence the phase is close to zero in those points. It remains to explain why a perturbation that has a positive reactivity effect leads to a decreasing thermal flux (i.e. a noise with opposite phase) just in the very neighbourhood of the perturbation itself. This is however also understandable. An increase of  $\epsilon$  actually means adding a layer of core material at the boundary and replacing the reflector material there. The core material means increased production of fissions and hence fast neutrons, which is the ultimate reason for the increase in reactivity; but this is achieved at the price of increased absorption of thermal neutrons. This is the reason of the out-of-phase behaviour of the local thermal noise. The same facts explain also the fine spatial structure of the amplitude of the thermal noise close to the boundary.

One can also check now how the present results support the possibility of an out-of-phase behaviour between an ex-core (ex-vessel) detector and an in-core detector, as described in the introduction and in [18]. Using vacuum boundary conditions at the outer edge of the reflector, an ex-vessel detector cannot be directly modelled in diffusion theory. It can be best approximated in the present model with a detector inside the reflector, but close to its outer boundary. The data shown in Fig. 2 illustrate that an out-of-phase behaviour can indeed exist between such an ex-core detector and an in-core one, if the in-core detector is close to the core boundary. A comparison with the calculations from the adiabatic approximation can be made, and it is shown in Fig. 3. The figure illustrates well that while the amplitudes, as obtained from the two models, agree qualitatively and quantitatively well, the phase of the noise, in the adiabatic approximation, is reproduced only in a very coarse way (as a binary variable taking the values 0 or  $-\pi$ ) which is a clear limitation. The opposite-phase behaviour around the core-reflector interface is though also correctly reproduced by the adiabatic approximation.

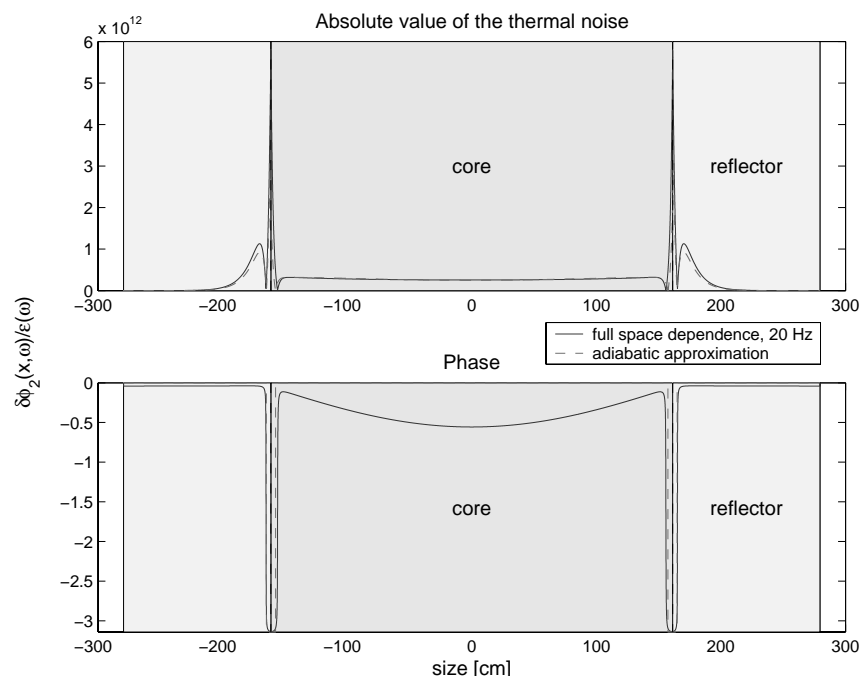


**Figure 3. Absolute value and phase of the thermal noise calculated in the full analytical model and in the adiabatic approximation.**

However, one advantage with the adiabatic approximation is the possibility to account for the possible movement of the detectors together with the core-barrel movements. So far the noise has been calculated considering the detectors being stationary in the core. But, it could also be possible for the detectors to move along with the vibration of the core-barrel itself. Then the noise measured by the detectors could be calculated by assuming a linear displacement of the static in-core positions,  $x$ , according to:

$$x_d = x + \frac{\varepsilon}{b} x \quad (12)$$

Then the measured neutron noise can be written as

$$\delta\bar{\phi}_{move}^c(x, t) = \bar{\phi}^c(x_d, t) - \bar{\phi}_0^c(x) = \left[ \bar{\phi}_0^c(x_d) + \delta\bar{\phi}^c(x_d, t) \right] - \bar{\phi}_0^c(x) \quad (13)$$

If the noise in the core is calculated using this expression the local behaviour completely disappears, i.e. there is no out-of-phase behaviour and no large amplitude of the noise at the boundary. The real situation in a reactor is probably something in between the two extremes of non-moving detectors and detectors that move completely together with the shell-mode vibrations of the core-barrel.

One should also bear in mind that the model used here contains several simplification compared to reality, and the influence of these simplifications on the accuracy of the results is not clear. One neglected effect is the re-arrangement (dilution) of the core density with the shell-mode vibrations. It was shown in the adiabatic calculations ([21]) that the dilution effect decreases the reactivity coefficient of the vibrations very significantly, to the extent that the magnitude of the ordinary (non-local) space dependent component becomes dominating in the core. In such a case an out-of-phase behaviour can exist even between an ex-vessel detector and an in-core detector, which is not based on the local component, and hence the in-core detector does not need to be close to the core boundary. Finally, a more realistic description of the core-barrel vibrations requires a 2-D description. In two dimensions, the space-dependent component of the noise is, as a rule, enhanced as compared to the point kinetic one, and this could also alter some of the conclusions of the present work. However, in this paper our main purpose was to perform a conceptual study and understanding of the basic phenomena, rather than trying to exactly reconstruct certain measurements.

## 5. MEASUREMENTS & CONCLUSIONS

Two measurements, specifically designed to detect the possible local component of the noise were performed at the Swedish PWR Ringhals-3 in March 2005. The five in-core detectors were placed in two different setups. One where they were aligned radial from the centre and out to the boundary and a second where all five detectors were placed in the outer most fuel assemblies, see Fig 4a). Since there is  $90^\circ$  rotational symmetry in the core for the neutron noise induced by the shell-mode vibrations it is possible to combine detectors from different quadrants to form a complete set of signals from one quadrant.

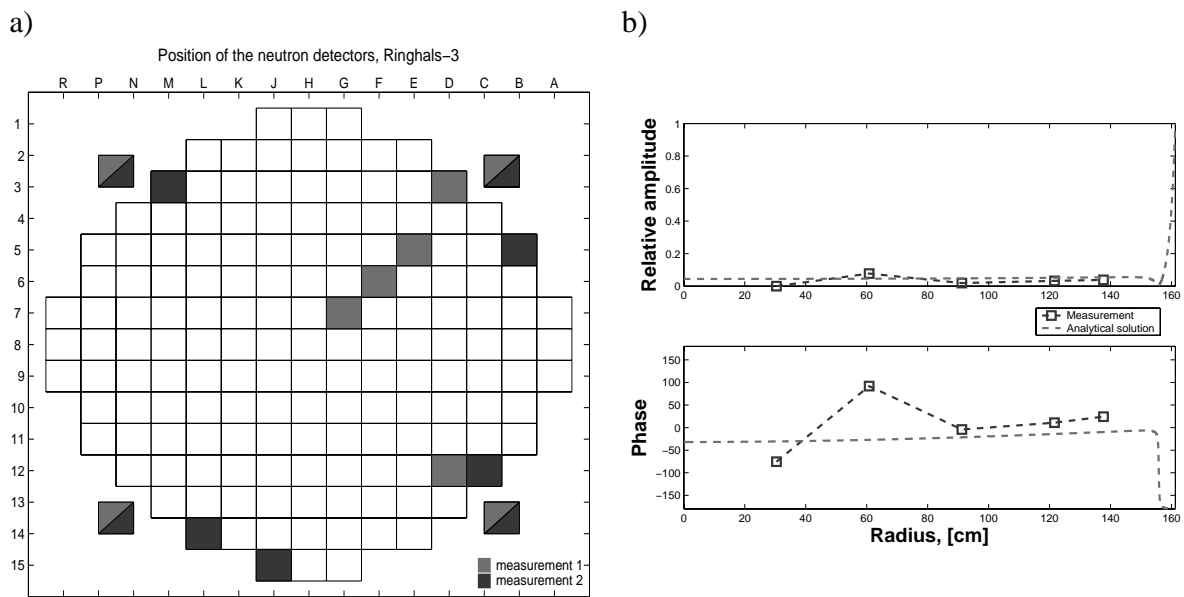


**Figure 4. a) Map of the Ringhals-3 core. The red squares indicate the position of the detectors in the first measurement and the blue squares are for the second measurement. b) Results from the first measurement with the analytical solution present.**

The analysis of the measurements showed that it is not possible to detect the large local component of induced in-core noise, see Fig 4b). This is due to the fact that it is not possible to place a detector close enough to the boundary where the local component is present. Hence, it is unfortunately no possibility to use the in-core noise when classifying the shell-mode core-barrel vibrations. For the same reasons, the comparison between measurements and calculations remain inconclusive concerning which solution is the one agreeing the most with the measurements, the one with the static detectors or with the moving detectors.

## REFERENCES

1. J. B. Dragt and E. Türkcan , “Borssele PWR noise: Measurements, analysis and interpretation“ *Prog. Nucl. Energy*, **1**, 293 (1977)
2. C. W. Mayo, “Detailed neutron noise analysis of pressurized water reactor internal vibrations” *Atomkernenergie*, **29**, 9 (1977)
3. D. Wach and R. Sunder, “Improved PWR-neutron noise interpretation based on detailed vibration analysis” *Prog. Nucl. Energy*, **1**, 309 (1977)
4. J. A. Thie, “Core Motion monitoring” *Nucl. Tech.*, **45**, 5 (1979)
5. J. A. Thie, “Power Reactor Noise” American Nuclear Society, La Grange Park, Illinois, USA, (1981)

6. F. Åkerhielm , R. Espefält and J. Lorenzen, “Surveillance of vibrations in PWR” *Prog. nucl. Energy*, **9**, 453 (1982)
7. T. Bogard, T. Kozlosky, S. Lowenfeld and N. Singleton, “Reactor Internals and Core Support Monitoring System“ *SMORN-VI*, Gatlinburg, Tennessee, USA (1991)
8. D. J. Dailey and R. W. Albrecht , “In-core/ex-core neutron noise measurements to examine core internal vibrations in an operating PWR” *Prog. Nucl. Energy*, **15**, 251 (1985)
9. S. Yamada, T. Sato and H. Kanamaru, “Five-detector method for core-barrel motion analysis” *Ann. nucl. Energy*, **12** , 455 (1985)
10. R. Sunder, M. Baleanu, K. Kieninger, A. Kolbasseff, W. Kuhn and H. Rösler, “Experiences and Results with COMOS - An On-Line Vibration Analysis and Monitoring System” *SMORN-VI*, Gatlinburg, Tennessee, USA (1991)
11. I. Pázsit, J. K.-H. Karlsson and N. S. Garis, “Some developments in core-barrel vibration diagnostics”. *Ann. nucl. Energy* **25**, 1079 - 1093 (1998)
12. J. K.-H. Karlsson, and I. Pázsit, “Final Report on the Research Project Ringhals Diagnostics and Monitoring, Stage 3: Analysis of core barrel vibrations in Ringhals 2, 3 and 4 for several fuel cycles.” CTH-RF-135/RR5, Chalmers University of Technology, Gothenburg, Sweden (1998)
13. I. Pázsit and V. Arzhanov, “Linear Reactor Kinetics and Neutron Noise in Systems with Fluctuating Boundaries” *Ann. Nucl. Energy*, **27**, 1385 (2000)
14. C. Demazière, V. Arzhanov, J. K.-H. Karlsson, and I. Pázsit, “Final Report on the Research Project Ringhals Diagnostics and Monitoring, Stage 4.” CTH-RF-145/RR6, Chalmers University of Technology, Gothenburg, Sweden (1999)
15. C. Demazière, V. Arzhanov and I. Pázsit, “Final Report on the Research Project Ringhals Diagnostics and Monitoring, Stage 7.” CTH-RF-167/RR9, Chalmers University of Technology, Gothenburg, Sweden (2002)
16. V. Arzhanov and I. Pázsit, “Diagnostics of Core Barrel Vibrations by Ex-Core and In-Core Neutron Noise”. *Prog. nucl. Energy* **43**, 151 - 158 (2003)
17. R. Sanchis-Arnal, G. Verdú Martín and G. L. Munoz-Cobo, “Detector point of view of reactor internal vibrations under Gaussian coloured random forces- The problem of fitting neutron noise experimental data” *Ann. nucl. Energy* **15**, 275 (1988)
18. I. Pázsit, “Control rod models and vibration induced noise.”, *Ann. nucl. Energy*, **15**, 333 (1988)
19. I. Pázsit and J. Karlsson, “On the perturbative calculation of the vibration noise by strong absorbers.” *Ann. nucl. Energy* **24**, 449 (1997)
20. C. Demazière, “Development of a 2-D 2-group neutron noise simulator.” *Ann. Nucl. Energy*, **31**, 647 (2004)
21. C. Sunde and V. Arzhanov “Calculation of the neutron noise induced by shell-mode core-barrel vibrations in a 1-D 2-group 2-region slab reactor.” CTH-RF-173, Chalmers internal report, Chalmers University of Technology, Gothenburg, Sweden (2003)
22. G. I. Bell and S. Glasstone, “Nuclear Reactor Theory” van Nostrand-Reinhold, New York, US (1970)

## APPENDIX

The following values of cross-sections and diffusion coefficients were obtained from static SIMULATE-3 calculations in 3-D corresponding to the Ringhals-4 PWR (cycle 16, burnup 8.767

GWd/tHM) and then homogenized from 3-D to 1-D. These data were finally homogenized for the core and the reflector regions, respectively. Note that the absorption cross section for the fast group in the core is negative, this is due do the homogenization from 3-D to 1-D which preserves the leakage rate in the directions not accounted for in the 1-D model.

$$\left\{ \begin{array}{l} \Sigma_{a,1}^c = 0.0115 \text{ cm}^{-1} \\ \Sigma_{a,2}^c = 0.1019 \text{ cm}^{-1} \\ \Sigma_R^c = 0.0151 \text{ cm}^{-1} \\ v \Sigma_{f,1}^c = 0.0057 \text{ cm}^{-1} \\ v \Sigma_{f,2}^c = 0.1425 \text{ cm}^{-1} \\ D_1^c = 1.4376 \text{ cm} \\ D_2^c = 0.3723 \text{ cm} \\ v_1 = 1.82304 \cdot 10^7 \text{ cm/s} \\ v_2 = 4.13067 \cdot 10^5 \text{ cm/s} \end{array} \right. \quad \text{for the core} \quad (14)$$

$$\left\{ \begin{array}{l} \Sigma_{a,1}^r = -0.0098 \text{ cm}^{-1} \\ \Sigma_{a,2}^r = 0.0284 \text{ cm}^{-1} \\ \Sigma_R^r = 0.0238 \text{ cm}^{-1} \\ D_1^r = 1.3116 \text{ cm} \\ D_2^r = 0.2624 \text{ cm} \end{array} \right. \quad \text{for the reflector} \quad (15)$$

$$\left\{ \begin{array}{l} \beta = 0.00535 \\ \lambda = 0.08510 \end{array} \right. \quad \text{for the precursors} \quad (16)$$

# Paper VI

*Beam mode core-barrel vibrations in the PWRs Ringhals 2-4*

M. Pázsit, C. Sunde and I. Pázsit

Proc. Int. Top. Mtg. Advances in Nuclear Analysis and Simulations (PHYSOR2006), Vancouver, Canada, September 10-14, 2006, American Nuclear Society (2006)



# Beam mode core-barrel vibrations in the PWRs Ringhals 2-4

Maria Pázsit, Carl Sunde\* and Imre Pázsit

*Department of Nuclear Engineering, Chalmers University of Technology,  
S-412 96 Göteborg, Sweden*

## Abstract

Analysis of core-barrel vibrations in the Swedish Ringhals PWRs has been performed by Chalmers since the early 1990's. In the first phase of this work, between 1991 and 1998, the evaluation method has been developed such that it made a consistent comparison between different measurements possible. A trend analysis showed that the beam mode amplitudes have steadily increased between 1991 and 1998 in all three plants.

This paper is to report on the second phase of the work, performed during 2005, on measurements made both before and after the summer outage 2005 in all three plants. During the summer outage, the hold-down spring in Ringhals-3 was replaced. The analysis shows that the vibration amplitudes increased in an accelerated rate between 1998 and 2005 in all three plants. In Ringhals 3, however, after the change of the hold-down spring, the beam mode amplitude has reverted to close its original level of 1991.

It became also clear that the extraction of the information from the vibration peaks needs to be refined and made less subjective. A new method of algorithmic peak separation was elaborated, which supplies more information than the previous analysis; it gives also the peak width in addition to peak amplitude and peak frequency, while also supplying more accurate estimates for the latter two.

**KEYWORDS:** *core-barrel vibrations, beam mode, peak estimation, trend analysis*

## 1. Introduction

In order to monitor the flow induced beam-mode core-barrel vibrations in a Pressurised Water Reactor, PWR, it is possible to use the ex-core detector signals [1]-[3]. From the Auto- and Cross-Power Spectral Densities (APSD and CPSD) of such signals, it is possible to gain knowledge about the vibration frequency and its relative amplitude. It could also be possible to calculate the absolute amplitude of the vibration but this has not been done in the present paper. It is especially important to monitor the change of the vibrations due to the power up-rate (increasing power and hence core flow), which is taking place in Sweden at the moment. It is also of interest to monitor the vibrations during a longer time period and make a trend analysis in order to determine the possibility of material fatigue and wear. Previously, a trend analysis was

---

\* Corresponding author, Tel. +46 (0) 31-772 30 86, Fax. +46 (0)31-772 30 79, E-mail: kalle@nephy.chalmers.se

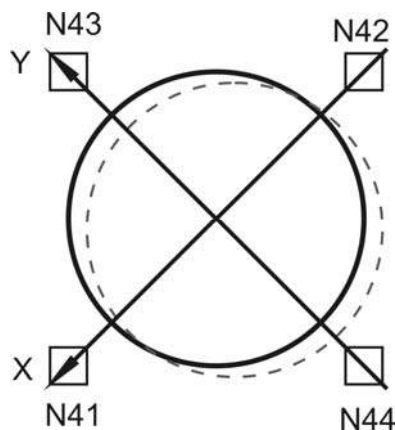
performed on measurements made during 1991-98 at the Swedish NPP Ringhals, but no new measurements were made since then until recently. Therefore, new measurement were taken during 2005 at all three PWR-units at Ringhals.

The work in this paper has three different objectives. The first objective is to compare the results of the recent analysis of the vibrations with those taken in the period 1991-98 [4]-[5], in order to follow up the development of the vibration characteristics in form of a trend analysis. The trend analysis will also be important in the future to monitor the change of vibrations due to the planned power up-rate in Ringhals 2-4. The results from the present analysis were compared to the previous results. The second objective is to investigate the changes of the properties of the core-barrel vibrations before and after the outage in the summer of 2005 in Ringhals-3. During the outage the hold-down springs were replaced to decrease the vibration amplitude. Thirdly a curve-fitting procedure was developed to better extract the information from the vibration peak by removing the influence of the background of the APSD. The curve-fitting also allows us to calculate the width of the peak which will give another parameter that can be used for characterizing material conditions.

## 2. Model of the induced noise

There are different vibration modes of the core-barrel as with every mechanical system. In the case with a core-barrel in PWR:s two vibration modes are of special interest, namely the first vibration mode, i.e. the beam-mode, and the second mode, which is called the shell-mode. In this paper we focus our attention on the first mode which is illustrated by the dashed circle in Fig.1. The beam-mode is also called the pendulum-mode since it executes a pendulum-like motion.

**Figure 1** Positions of the ex-core detectors relative to the core.



The different vibration modes of the core-barrel induce neutron noise, which can be monitored by the ex-core detectors. It is possible to separate the different modes by adding and subtracting the signals from the different detectors, since the modes have different symmetry properties. The beam-mode vibration has a  $180^\circ$  rotational symmetry whereas the shell-mode has  $90^\circ$  rotational symmetry. In Ref. 4 the following expressions were derived for the  $x$  and  $y$  components of the ex-core noise induced by the beam-mode vibrations:

$$\begin{aligned}\mu x(t) &= \frac{1}{2}[\delta\phi_1(t) - \delta\phi_2(t)], \\ \mu y(t) &= \frac{1}{2}[\delta\phi_3(t) - \delta\phi_4(t)].\end{aligned}\tag{1}$$

where the induced neutron noise,  $\delta\phi_n(t)$ , is measured at detector  $N4n$ ,  $n=1..4$ , respectively. Then by using the so-called  $k$ - $\alpha$  model for 2-D random anisotropic vibrations, it is possible to write the auto-spectra,  $S_{xx}$  and  $S_{yy}$ , of the  $x$  and  $y$  component as:

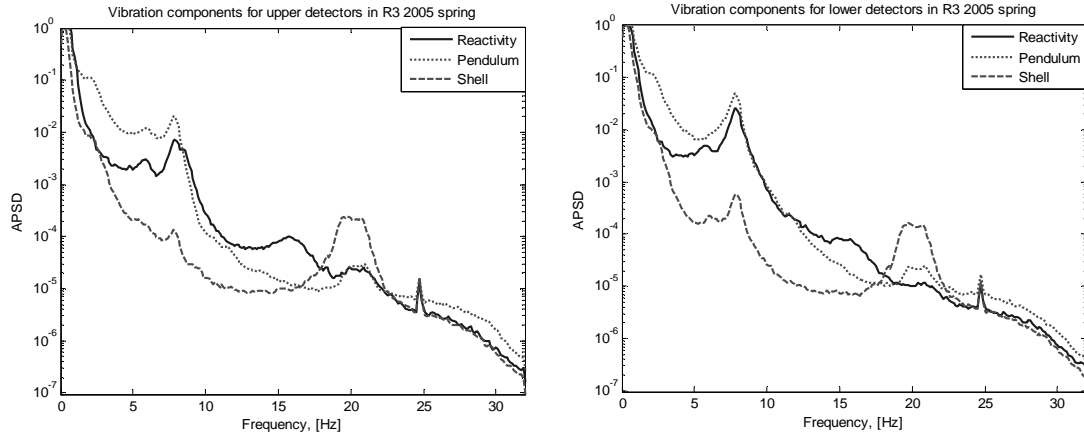
$$\begin{aligned}S_{xx}(f) &= |S(f)|^2 (1 + k \cos 2\alpha), \\ S_{yy}(f) &= |S(f)|^2 (1 - k \cos 2\alpha).\end{aligned}\tag{2}$$

Hence, it is possible to write the spectra,  $S(f)$  of the beam-mode vibration as:

$$APSD_{beam} = \frac{S_{xx}(f) + S_{yy}(f)}{2} = |S(f)|^2.\tag{3}$$

In Fig. 2 the spectra of the different vibration components are shown. It is clearly visible that the beam-mode has an eigenfrequency at around 8 Hz and it is separated from the shell-mode vibration which is at 20 Hz.

**Figure 2:** Spectra of the different components in the ex-core detectors.



### 3. Parameter estimation

In order to monitor the beam-mode vibration one can estimate the peak value and eigenfrequency of the peak from the APSD given in Fig. 2. This is also the procedure that was followed in the past for measurements made between 1991 and 1998 at Ringhals 2-4, [4]-[5]. The results from this analysis showed that the amplitude of the vibration peak had increased but the eigenfrequency remained roughly the same. In this paper we have continued the analysis by including measurements from 2005 for all three units. The estimation of the peak parameters were done in the same way as earlier. The results from this analysis are presented in the section

*Trend analysis* below. However, it is also possible to make a better estimation of the peak parameters by using curve-fitting procedures which will be described in the next chapter.

#### 4. Curve-fitting

In order to improve the estimation of vibration peaks in the spectra of the ex-core detectors, it is possible to use curve-fitting procedures. We start by assuming that the mechanical vibrations can be represented as the oscillations of a linear damped oscillator, driven by a white noise force,  $F(t)$ . Then the time-dependent equation for the induced noise,  $\delta\phi(t)$  can be written as

$$\delta\ddot{\phi}(t) + 2D\omega_0\delta\dot{\phi}(t) + \omega_0^2\delta\phi(t) = F(t). \quad (4)$$

From this it is possible to turn to the frequency domain by making a Fourier transformation and utilising  $\omega = 2\pi f$  and rescaling  $F(f)$  with  $1/(2\pi)^2$ :

$$\delta\phi(f) = \frac{F(f)}{-f^2 + 2iDf_0f + f_0^2} = H(f)F(f). \quad (5)$$

Finally, the Wiener-Khinchin theorem is used and the fact that the APSD from a white noise is a constant, [6]. Then one ends up with the following expression for the noise:

$$APSD_{\delta\phi}(f) = APSD_F(f)|H(f)|^2 = \frac{C^2}{(f^2 - f_0^2)^2 + 4D^2f^2f_0^2}. \quad (6)$$

Here,  $f_0$  is the eigenfrequency,  $D$  is the damping coefficient and  $C^2$  is a parameter proportional to the vibration amplitude. By calculating  $APSD_{\delta\phi}(f)$  using (1)-(3) from the measured signals, it is possible to fit the measured data to (6) with three unknown parameters  $C$ ,  $D$  and  $f_0$ . The fitting is done by using MatLab [7], with a least-square fitting algorithm. However, inspection of the measured spectra (c.f. Fig. 2) shows that the peaks are superimposed on a background that decreases with increasing frequency quite markedly. Hence one can expect to get a better estimate of the parameters if the actual fitting is done to the following equation:

$$APSD_{\delta\phi}(f) = \frac{\tilde{C}}{f^2 + \tilde{D}(f^2 - f_0^2)^2} + A_1f + A_2. \quad (7)$$

Here the two last terms on the r. h. s. are a simple linear term and a constant background, respectively. The following connections between the estimated parameters and the search parameters hold:

$$D^2 = \frac{1}{4\tilde{D}f_0^2}, \quad (8)$$

$$C^2 = \frac{\tilde{C}}{\tilde{D}}.$$

Initial values for the parameters to be estimated by the least-square fitting algorithm have to be given as inputs, Therefore, initial guesses of the amplitude, the full-width at half maximum (FWHM) and frequency of the peak is manually estimated from the APSD. From these parameters estimations of initial values for  $\tilde{C}$ ,  $\tilde{D}$  and  $f_0$  can be calculated. Also the frequency-range is given manually to the algorithm for each measurement, normally between 4 to

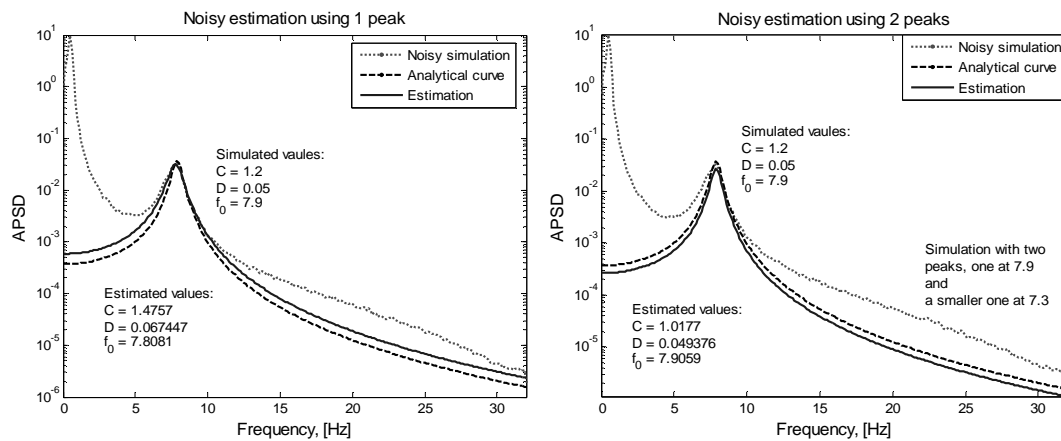
10 Hz. Once the parameters have been estimated it is possible to calculate the peak frequency,  $f_{peak}$ , the FWHM and the peak height,  $A_{peak}$ , according to the following expressions:

$$\begin{aligned}
 f_{peak} &= \sqrt{f_0^2(1-2D^2)}, \\
 f_{FWHM} &= f_0\sqrt{(1-2D^2) \pm 2D\sqrt{1-D^2}}, \\
 FWHM &= \Delta f_{FWHM}, \\
 A_{peak} &= \frac{C^2}{4f_0^4 D^2(1-D^2)}.
 \end{aligned} \tag{9}$$

#### 4.1. Simulations

A good practice to obtain an algorithm working satisfactorily is to test it on known data. Hence, the curve-fitting procedures are first tested on simulated signals corresponding to some realistic values of the parameters in (4). In simulations, it is also possible to investigate how a second peak with much lower amplitude but almost the same frequency as the beam-mode peak will influence the estimation of the parameters. It is also possible to investigate the influence of “noise” added to the signal spectra. In the left plot in Fig. 3 a simulated signal with some noise (dotted curve) is shown, corresponding to two vibrations, one with high amplitude which represents the beam-mode vibration and one with lower amplitude representing some other type of hypothetical vibration. The introduction of a second peak is prompted by observations of the spectra from the measurements. The curve for the beam-mode vibration is also shown as a dashed curve. In the right of Fig. 3 the solid curve is the fitted curve corresponding to the beam-mode vibration when two curves are used in the fitting algorithm, whereas to the left in Fig. 3 only one curve is used. The estimated values are also shown in the figures and as can be seen, the case with two fitted curves is much better at estimating the correct parameter values.

**Figure 3** Simulation of the beam-mode vibration with noise and another peak close. To the right two curves are used in the estimation and to the left only one.

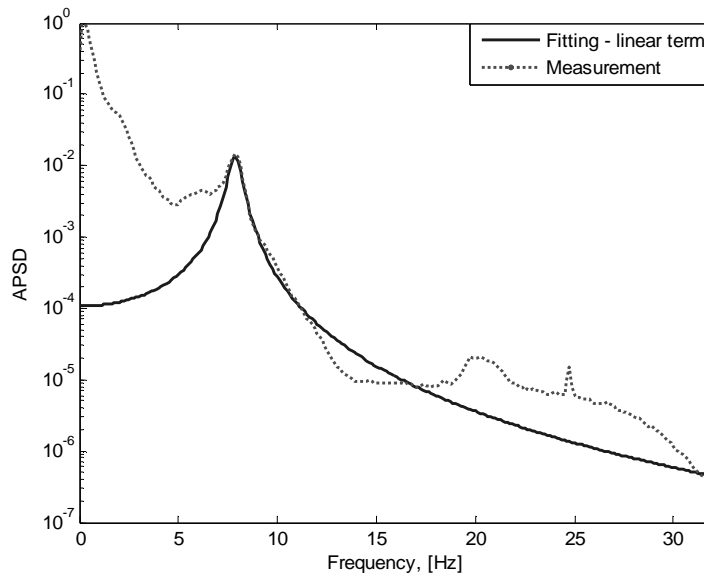


## 4.2. Measurements

In reality there are several peaks present in the spectrum, even if some of the peaks are removed by the adding and subtracting of the signals using equations (1)-(3). However, some peaks that are not due to the beam-mode core-barrel vibrations may remain in the spectra. Especially there may be a peak close the beam-mode peak which corresponds to the fuel assembly vibrations, [8]. Sometimes this second peak is visible and sometimes one can only see a broad single peak, due to two superimposed peaks. Hence, the best estimation of the beam-mode peak will be achieved if the broad peak is assumed to consist of two peaks. Then estimation to these two peaks can be made. One also has to consider the possibility of a superimposed background. If a linear trend is added to the fitting, as in (7), it is possible to estimate the parameters of the peak by eliminating the effect of the background.

This procedure was applied to the present measurements with good results. As an illustration, in Fig. 4 an APSD from the lower ex-core detectors in Ringhals-3 is shown together with the estimated peak.

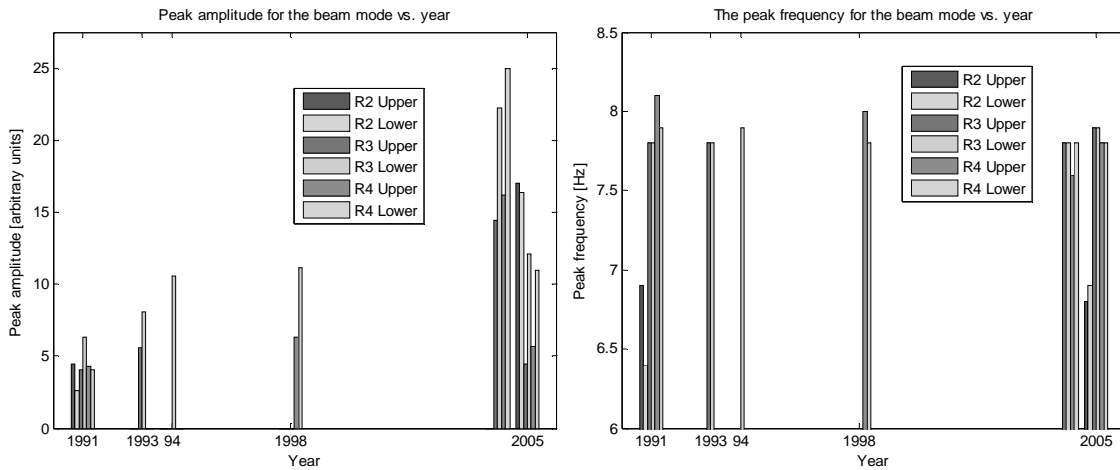
**Figure 4** APSD of lower ex-core detector signals from R3 with fitted curve without linear background term. Measurement made in autumn 2005.



## 5. Trend Analysis

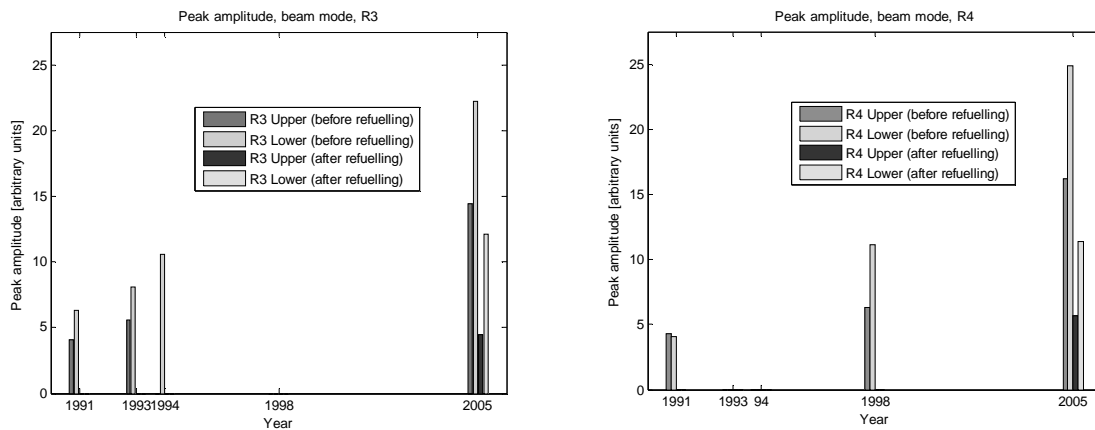
The trend analysis is based on both the manual “peak” method and the curve-fitting method. In the following figures the results from both analyses are presented. In Fig. 5 the result from the “peak” method trend analysis of the vibration amplitude is shown beginning at the year of 1991.

**Figure 5: Trend of the vibration peak amplitude and frequency.**



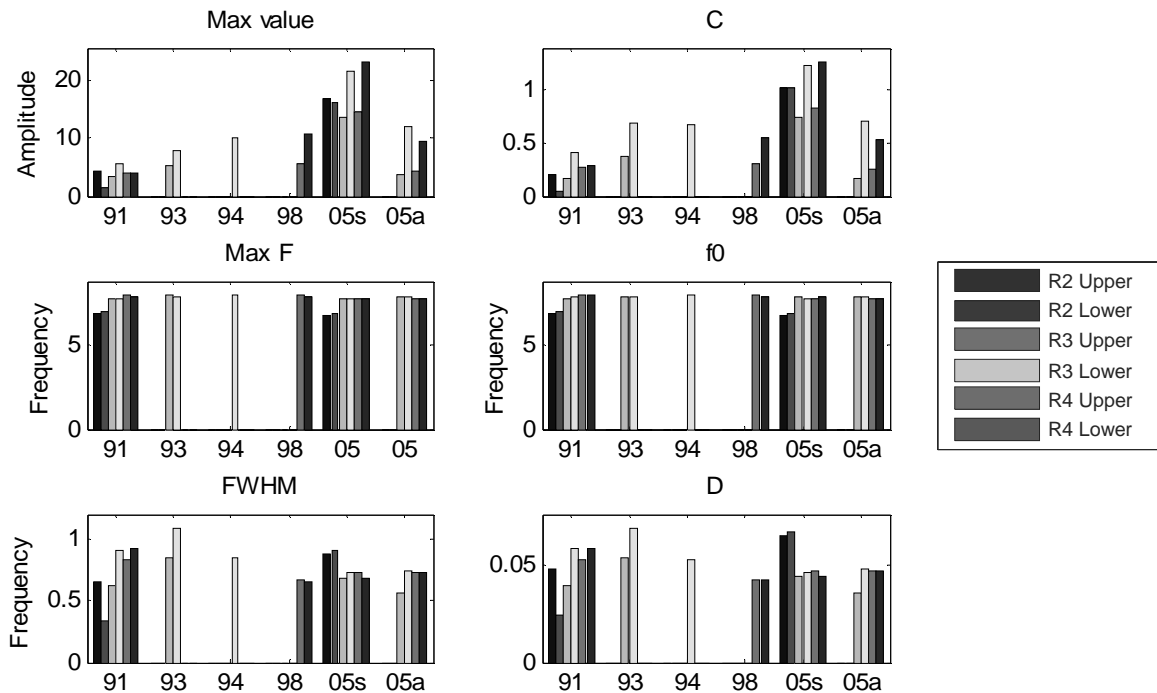
To make a more detailed analysis, the results before and after the re-fuelling in 2005 are shown in Fig. 6. Here it is clearly visible that the amplitude is decreasing in both Ringhals-3 and Ringhals-4.

**Figure 6: Amplitude before and after revision.**



The results from the curve-fitting analysis are shown in Fig. 7. There is good agreement between the two methods. It is also seen from the lowermost part of Fig. 7 that the additional information of the width,  $D$ , of the peaks does not seem to give any further information about the vibration properties.

**Figure 7:** Estimation of parameters from curve-fitting. 05s stands for 2005 spring and 05a stands for 2005 autumn.



## 6. Conclusions

The following conclusions can be made from the trend analysis given in the foregoing.

- The vibration amplitudes have increased for the beam mode (pendulum) for all units as compared to the previous values. The rate of increase appears to be somewhat faster for the period 1998-2005 than for the previous period, i.e. 1991-1998, and are about a factor 3 to 4 higher than in 1991;

- in general, the vibration frequency has decreased slightly for all reactor units. This change is not faster than in the previous period, and moreover it shows some statistical scatter, i.e. the trend is not completely monotonic. Nevertheless, it points into the same direction as the amplitude, i.e. it reflects a slight general weakening of the integrity of the core-barrel system against flow induced vibrations;

- the amplitude of the beam mode vibrations decreased significantly (by more than a factor 2) in R3 after refueling with the change of the hold down springs, compared to their values before re-fuelling. The amplitude values got down to a level comparable with those in the earliest measurements available to us, i.e. from 1991. Hence, it is possible to see the effect of the change of the hold down springs by monitoring the beam mode vibrations. However, the amplitude for

Ringhals-4 is also showing the same kind of behaviour. This is unexpected since there was no change of hold-down springs in this unit. The reasons for this change are not understood at the moment, and further measurements will be necessary to clarify the reason.

## **Acknowledgements**

The authors wish to thank the Ringhals power plant for financial support of this project and also for performing the measurements.

## **References**

- 1) J. A. Thie, "Core motion monitoring", Nucl. Tech. **45**, (1979)
- 2) V. Bauernfeind, "Vibration- and pressure signals as sources of information for an on-line vibration monitoring system in PWR power plants", Nucl. Engineering and Design **40**, (1977)
- 3) V. Bauernfeind, "Investigations on the vibrative excitation of PWR pressure vessel and internals by pressure noise analysis and model calculations", Progress in Nuclear Energy, **1**, (1977)
- 4) J. H-K. Karlsson and I. Pázsit, "Final Report on the Research Project Ringhals Diagnostics and Monitoring Stage 3", CTH-RF-135/RR-5, Chalmers University of Technology (1998)
- 5) I. Pázsit, J. Karlsson and N. S. Garis, "Some development in core-barrel vibration diagnostics", Ann. Nucl. Energy, **25**, 13 (1998)
- 6) I. Pázsit, "Determination of reactor stability in case of dual oscillations", Ann. Nucl. Energy, **22**, 6 (1995).
- 7) Users Guide MatLab, Mathworks Inc.
- 8) R. T. Wood and R. B. Perez, "Modeling and Analysis of Neutron Noise from an Ex-Core Detector at a Pressurized Water Reactor", Proceedings of SMORN VI, Gatlinburg, Tennessee, May 19-14 (1991)



# Paper VII

*Investigation of the validity of the point-kinetics approximation and of the break-frequency method in 2-D subcritical systems*

C. Sunde, C. Demazière and I. Pázsit

Proc. Joint Int. Top. Mtg. on Mathematics and Computing and Supercomputing in Nuclear Applications (M&C + SNA 2007), Monterey, California, April 15-19, 2007, American Nuclear Society (2007)



# **INVESTIGATION OF THE VALIDITY OF THE POINT-KINETIC APPROXIMATION AND OF THE BREAK-FREQUENCY METHOD IN 2-D SUBCRITICAL SYSTEMS**

**Sunde C, Demazière C and Pázsit I**

Department of Nuclear Engineering

Chalmers University of Technology

412 96 Göteborg, Sweden

kalle@nephy.chalmers.se; demaz@nephy.chalmers.se; imre@nephy.chalmers.se

## **ABSTRACT**

The accuracy and applicability of the break-frequency method for estimating the reactivity in a subcritical 2-D, 2-group reflected system with a distributed source is investigated for two different system sizes. The source is distributed according to the static thermal flux. This method could be useful in power reactor cores during loading conditions for determining the subcriticality. The validity of the point-kinetic approximation in the same systems is also tested. A neutron noise simulator is used to calculate the actual neutron noise induced by fluctuations of the source which is compared with the analytically calculated point-kinetic term. The break-frequency method is used to estimate the reactivity from the neutron noise calculated by the simulator. The conclusion of this work is that the point-kinetic approximation in general is not valid in 2-D, 2-group reflected systems and hence the break-frequency method is not valid either.

*Key Words:* point-kinetic, break-frequency, reactivity, reflected system, subcritical system

## **1. INTRODUCTION**

The validity of different methods for determining the reactivity in subcritical systems has been studied in 1-D one-group models and the methods are often based on the point-kinetic approximation. However, in 2-D, 2-group reflected systems much less is known about both the validity of methods for determining the reactivity and about the point-kinetic approximation. In this paper the break-frequency method [1], will be used to determine the reactivity in subcritical systems such as power reactors during loading. The advantage with the break-frequency method compared to other reactivity estimation methods is that there is no need for an external source. Instead an inherent source can be used, e.g. the neutrons from decay of fission products in a core during loading. Since, the break-frequency method is based on the point-kinetic approximation it is also important to investigate the validity of the point-kinetic approximation in subcritical systems.

An investigation of the validity of the source-modulation method has been performed in a subcritical 2-D, 2-group reflected system [2]. In the same paper the validity of the point-kinetic approximation was also investigated for the same system. However, the source in that paper was only placed in the centre and had no spatial distribution and only a few frequency points were investigated. In this work the investigation is extended to a source which is distributed in the whole core and the frequency range covers the whole part of interest for the transfer-function ( $10^{-4} - 10^4$  Hz). A spatially distributed source has been investigated in a paper by Demazière and Pázsit, [3], but in that case the focus was on the estimation of the Moderator Temperature Coefficient (MTC) in a critical reactor.

In this paper a so-called neutron noise simulator is used to calculate the neutron noise induced by a time-dependent source in a 2-D, 2-group heterogenous reflected system [4]. From the Auto Power Spectral Density (APSD) of the calculated neutron noise the reactivity can be estimated by using the break-frequency method. The source is assumed to be spatially distributed in the fast group with the distribution given by the static critical thermal flux of the system. Furthermore the time-dependence of the source fluctuation is assumed to be of a white noise character hence it is not possible to explicitly express the frequency dependence of the noise source. Finally, the numerically calculated neutron noise is compared with the analytical expression of the neutron noise in the point-kinetic approximation.

## 2. DERIVATION OF THE NEUTRON NOISE

In this section we start by deriving the time-dependent neutron noise in the 2-group diffusion approximation. The neutron flux will be divided into an amplitude factor and a shape function and linearisation techniques will be used in the derivation of the noise. The noise will then be expressed in the frequency domain. Finally, the expression for the neutron noise in the point-kinetic approximation will be derived. These derivations are following the derivations given in [2].

### 2.1. TIME-DEPENDENT DIFFUSION EQUATIONS

The system which will be treated in this paper is a 2-group subcritical system in the diffusion approximation including one group of delayed neutrons with a source in the fast group. The system will be used to model a power reactor in two dimensions. Hence, first the time-dependent diffusion equations are written down for the fast group

$$\begin{aligned} \frac{1}{v_1} \frac{\partial \phi_1}{\partial t}(\mathbf{r}, t) = \nabla \cdot [D_1(\mathbf{r}) \nabla \phi_1(\mathbf{r}, t)] + \nu \Sigma_{f,2}(\mathbf{r})(1 - \beta_{eff}) \phi_2(\mathbf{r}, t) \\ + \lambda C(\mathbf{r}, t) + \left[ \nu \Sigma_{f,1}(\mathbf{r})(1 - \beta_{eff}) - \Sigma_{a,1}(\mathbf{r}) - \Sigma_{rem}(\mathbf{r}) \right] \phi_1(\mathbf{r}, t) + S_1(\mathbf{r}, t), \end{aligned} \quad (1)$$

for the thermal group

$$\frac{1}{v_2} \frac{\partial \phi_2}{\partial t}(\mathbf{r}, t) = \nabla \cdot [D_2(\mathbf{r}) \nabla \phi_2(\mathbf{r}, t)] - \Sigma_{a,2}(\mathbf{r}) \phi_2(\mathbf{r}, t) + \Sigma_{rem}(\mathbf{r}) \phi_1(\mathbf{r}, t), \quad (2)$$

and for the precursor density

$$\frac{\partial C}{\partial t}(\mathbf{r}, t) = \beta_{eff} \left[ \nu \Sigma_{f,1}(\mathbf{r}) \phi_1(\mathbf{r}, t) + \Sigma_{f,2}(\mathbf{r}) \phi_2(\mathbf{r}, t) - \lambda C(\mathbf{r}, t) \right]. \quad (3)$$

Here the subscript 1 denotes the fast group and the subscript 2 the thermal group. All quantities have there usual meaning. Hence,  $\phi_1(\mathbf{r}, t)$  is the fast flux,  $\Sigma_x(\mathbf{r})$  are cross-sections and  $S_1(\mathbf{r}, t)$  is the time-dependent source in the fast group.

In order to solve these equations it is first assumed that it is possible to split the flux into an amplitude factor,  $P(t)$ , and a shape function,  $\psi(\mathbf{r}, t)$  as

$$\begin{bmatrix} \phi_1(\mathbf{r}, t) \\ \phi_2(\mathbf{r}, t) \end{bmatrix} = P(t) \times \begin{bmatrix} \psi_1(\mathbf{r}, t) \\ \psi_2(\mathbf{r}, t) \end{bmatrix}. \quad (4)$$

Since a new function is introduced, an additional normalisation condition needs to be used [5]:

$$\frac{\partial}{\partial t} \int \left[ \frac{1}{v_1} \phi_{1,0}^\dagger \psi_1(\mathbf{r}, t) + \frac{1}{v_2} \phi_{2,0}^\dagger \psi_2(\mathbf{r}, t) \right] d\mathbf{r}. \quad (5)$$

Here  $\phi_{i,0}^\dagger$  is the adjoint flux for the critical source-free system. Next, all the time-dependent terms are divided into their mean values,  $X_0(\mathbf{r})$  and fluctuating parts,  $\delta X(\mathbf{r}, t)$ , as:

$$X(\mathbf{r}, t) = X_0(\mathbf{r}) + \delta X(\mathbf{r}, t) \quad (6)$$

By using the above splitting, the flux can be written in vector form as

$$\begin{bmatrix} \phi_1(\mathbf{r}, t) \\ \phi_2(\mathbf{r}, t) \end{bmatrix} = \begin{bmatrix} \phi_1(\mathbf{r}) \\ \phi_2(\mathbf{r}) \end{bmatrix} + \begin{bmatrix} \delta\phi_1(\mathbf{r}, t) \\ \delta\phi_2(\mathbf{r}, t) \end{bmatrix} \quad (7)$$

and

$$\begin{cases} P(t) = P_0 + \delta P(t) \\ \begin{bmatrix} \psi_1(\mathbf{r}, t) \\ \psi_2(\mathbf{r}, t) \end{bmatrix} = \frac{1}{P_0} \begin{bmatrix} \phi_1(\mathbf{r}) \\ \phi_2(\mathbf{r}) \end{bmatrix} + \begin{bmatrix} \delta\psi_1(\mathbf{r}, t) \\ \delta\psi_2(\mathbf{r}, t) \end{bmatrix} \end{cases} \quad (8)$$

Here  $P_0 \psi_i(\mathbf{r}, t = 0)$  corresponds to the static subcritical flux,  $\phi_i(\mathbf{r})$ , given by

$$[\nabla \cdot \bar{D}(\mathbf{r}) \nabla + \bar{\Sigma}_{sub}(\mathbf{r})] \times \begin{bmatrix} \phi_1(\mathbf{r}) \\ \phi_2(\mathbf{r}) \end{bmatrix} = \begin{bmatrix} -S_1(\mathbf{r}) \\ 0 \end{bmatrix} \quad (9)$$

with

$$\bar{D}(\mathbf{r}) = \begin{bmatrix} D_1(\mathbf{r}) & 0 \\ 0 & D_2(\mathbf{r}) \end{bmatrix} \quad (10)$$

and

$$\bar{\Sigma}_{sub}(\mathbf{r}) = \begin{bmatrix} \nu\Sigma_{f,1}(\mathbf{r}) - \Sigma_{a,1}(\mathbf{r}) - \Sigma_{rem}(\mathbf{r}) & \nu\Sigma_{f,2}(\mathbf{r}) \\ \Sigma_{rem}(\mathbf{r}) & -\Sigma_{a,2}(\mathbf{r}) \end{bmatrix}. \quad (11)$$

If second-order terms are neglected, the neutron noise can be derived from Eqs. (7) - (8) as:

$$\begin{bmatrix} \delta\phi_1(\mathbf{r}, t) \\ \delta\phi_2(\mathbf{r}, t) \end{bmatrix} = \begin{bmatrix} \delta\phi_1^{pk}(\mathbf{r}, t) \\ \delta\phi_2^{pk}(\mathbf{r}, t) \end{bmatrix} + P_0 \times \begin{bmatrix} \delta\psi_1(\mathbf{r}, t) \\ \delta\psi_2(\mathbf{r}, t) \end{bmatrix}. \quad (12)$$

Here the point-kinetic term is expressed as:

$$\begin{bmatrix} \delta\phi_1^{pk}(\mathbf{r}, t) \\ \delta\phi_2^{pk}(\mathbf{r}, t) \end{bmatrix} = \frac{\delta P(t)}{P_0} \times \begin{bmatrix} \phi_1(\mathbf{r}) \\ \phi_2(\mathbf{r}) \end{bmatrix}. \quad (13)$$

Hence, the point-kinetic term has the same spatial dependence as the static flux of the subcritical system driven by a source.

## 2.2. DEFINITION OF THE SOURCE OF FLUCTUATIONS

Before we try to calculate the neutron noise numerically we need to specify the properties of the source term. Since, we want to model a power reactor core during loading conditions we assume that there is an inherent source present in the system. The inherent source neutrons are assumed to be coming from the decay of fission products which are produced during the static operation of the reactor. Hence, we make the simple assumption that the fission products, and thus the source, are distributed according to the static critical thermal flux,  $\phi_2^{cr,c}(\mathbf{r})$ , in the core. Furthermore it is assumed that all the source neutrons are born in the fast group. Hence the source is assumed to have the following properties:

$$S_1(\mathbf{r}, t) = \phi_2^{cr,c}(\mathbf{r}) + \delta S_1(\mathbf{r}, t). \quad (14)$$

where  $\delta S_1(\mathbf{r}, t)$  is a random white noise which cannot be given explicitly in the space-time domain.

However, it is possible to form the Cross-Power Spectral Density (CPSD) of the neutron noise  $\delta S_1(\mathbf{r}, t)$ . First, one assumes that the space-time correlations can be factorised into a temporal and a spatial component, where the temporal component is given by  $\delta(\tau)$ . For the spatial part, one also assumes that it can be further factorised into a fast decaying component as a function of the distance between two space points,  $e^{-\frac{|\mathbf{r}-\mathbf{r}'|}{l}}$ , and a much slower varying shape function,  $\sigma^2(\mathbf{r})$ . A more detail derivation of the CPSD for random white noise can be found in [3] where the final CPSD is given as

$$\begin{aligned} CPSD_{\delta S_1}(\mathbf{r}', \mathbf{r}'', \omega) &= \langle \delta S_1^*(\mathbf{r}', \omega) \delta S_1(\mathbf{r}'', \omega) \rangle \simeq \\ &\sigma^2(\mathbf{r}) e^{-\frac{|\mathbf{r}-\mathbf{r}'|}{l}} \simeq \sigma^2(\mathbf{r}) \delta(\mathbf{r}' - \mathbf{r}''), \end{aligned} \quad (15)$$

with

$$\mathbf{r} = \frac{\mathbf{r}' + \mathbf{r}''}{2}. \quad (16)$$

In the last step in the above equation it is assumed that the noise source is totally uncorrelated in space hence  $e^{-\frac{|\mathbf{r}-\mathbf{r}'|}{l}}$  is replaced with a  $\delta$ -function. As mentioned above we assume the noise source to be distributed as the critical thermal flux, hence

$$\sigma^2(\mathbf{r}) \sim (\phi_2^{cr,c})^2(\mathbf{r}). \quad (17)$$

Now, when the properties of the source are known, it is possible to calculate the neutron noise in the frequency domain.

## 2.3. NEUTRON NOISE IN THE FREQUENCY DOMAIN

The neutron noise can be derived in the frequency domain by first expressing all time-dependent quantities according to Eq. (6). Then the static solution is subtracted from the dynamic equations, Eqs. (1-3), and a temporal Fourier-transform is performed. The next step is to insert the expression for the precursor into the two equations for the flux. If all this is done one ends up with the following expression for the neutron noise in the frequency domain

$$[\nabla \cdot \bar{D}(\mathbf{r})\nabla + \bar{\Sigma}_{dyn}(\mathbf{r}, \omega)] \times \begin{bmatrix} \delta\phi_1(\mathbf{r}, \omega) \\ \delta\phi_2(\mathbf{r}, \omega) \end{bmatrix} = - \begin{bmatrix} \delta S_1(\mathbf{r}, \omega) \\ 0 \end{bmatrix} \quad (18)$$

with

$$\bar{\Sigma}_{dyn}(\mathbf{r}) = \begin{bmatrix} -\Sigma_1(\mathbf{r}, \omega) & \nu\Sigma_{f,2}(\mathbf{r}) \times \left(1 - \frac{i\omega\beta_{eff}}{i\omega + \lambda}\right) \\ \Sigma_{rem}(\mathbf{r}) & -\left(\Sigma_{a,2}(\mathbf{r}) + \frac{i\omega}{v_2}\right) \end{bmatrix} \quad (19)$$

and

$$\Sigma_1(\mathbf{r}, \omega) = \Sigma_{a,1}(\mathbf{r}) + \frac{i\omega}{v_1} + \Sigma_{rem}(\mathbf{r}) - \nu\Sigma_{f,1}(\mathbf{r}) \times \left(1 - \frac{i\omega\beta_{eff}}{i\omega + \lambda}\right). \quad (20)$$

A numerical noise-simulator, which has been developed at the Department of Nuclear Engineering, Chalmers University of Technology, is able to numerically solve this matrix-equation, on a nodal grid, for the neutron noise [4]. However, it is only possible to solve the matrix-equation if the temporal Fourier transform of the noise source can be given explicitly. But, in this paper the time-dependence of the noise source is assumed to be a random white noise and thus it can not be given explicitly in either the time- or the frequency-domain. Hence, we need to use the CPSD properties of the source.

In order to solve Eq. (18) and utilising the CPSD properties of the source the technique of Green's function is used. For a system of differential equations the Green's operator,  $\mathbf{G}$ , is used and the solution to Eq. (18) can formally be written as

$$\begin{bmatrix} \delta\phi_1(\mathbf{r}, \omega) \\ \delta\phi_2(\mathbf{r}, \omega) \end{bmatrix} = \int \mathbf{G}(\mathbf{r}, \mathbf{r}', \omega) \times \begin{bmatrix} \delta S_1(\mathbf{r}', \omega) \\ 0 \end{bmatrix} d\mathbf{r}', \quad (21)$$

where  $\mathbf{G}$  is the solution to:

$$\mathbf{M} \times \mathbf{G} = -\mathbf{I}. \quad (22)$$

Here  $\mathbf{I}$  is the identity matrix and  $\mathbf{M}$  is the matrix on the left hand side in Eq. (18). By using Eq. (21) and the CPSD properties of the source it is possible to calculate the APSD of the neutron noise as

$$\begin{aligned} \begin{bmatrix} APSD_{\delta\phi_1}(\mathbf{r}, \omega) \\ APSD_{\delta\phi_2}(\mathbf{r}, \omega) \end{bmatrix} &= \begin{bmatrix} \delta\phi_1^*(\mathbf{r}, \omega)\delta\phi_1(\mathbf{r}, \omega) \\ \delta\phi_2^*(\mathbf{r}, \omega)\delta\phi_2(\mathbf{r}, \omega) \end{bmatrix} = \\ &= \begin{bmatrix} \iint G_{11}^*(\mathbf{r}, \mathbf{r}', \omega)\delta S_1(\mathbf{r}', \omega)G_{11}(\mathbf{r}, \mathbf{r}'', \omega)\delta S_1(\mathbf{r}'', \omega) d\mathbf{r}' d\mathbf{r}'' \\ \iint G_{12}^*(\mathbf{r}, \mathbf{r}', \omega)\delta S_1(\mathbf{r}', \omega)G_{12}(\mathbf{r}, \mathbf{r}'', \omega)\delta S_1(\mathbf{r}'', \omega) d\mathbf{r}' d\mathbf{r}'' \end{bmatrix} = \\ &= \begin{bmatrix} \int G_{11}^*(\mathbf{r}, \mathbf{r}', \omega)G_{11}(\mathbf{r}, \mathbf{r}', \omega)(\phi_2^{cr,c})^2(\mathbf{r}') d\mathbf{r}' \\ \int G_{12}^*(\mathbf{r}, \mathbf{r}', \omega)G_{12}(\mathbf{r}, \mathbf{r}', \omega)(\phi_2^{cr,c})^2(\mathbf{r}') d\mathbf{r}' \end{bmatrix}. \end{aligned} \quad (23)$$

Since in this paper we are interested in validating the break-frequency method for reactivity estimations in a real power reactor, the APSD of the thermal noise is the part of interest. This is due to the fact that neutron detectors in a power reactor normally measure the thermal flux and we want to model realistic measurements.

The noise-simulator developed at the Department, [4], is able to calculate the Green's function and also the static and adjoint static fluxes needed for the calculation of the APSD. Hence, this tool is used in the forthcoming part of this paper to numerically calculate the APSD of the neutron noise.

## 2.4. POINT-KINETIC APPROXIMATION

Once the APSD of the neutron noise is calculated, a comparison with the point-kinetic approximation of the neutron noise expressed in Eq. (13) can be made in order to validate if the system behaves according to point-kinetics. It is possible to calculate the point-kinetic APSD analytically by first transforming Eq. (13) into the frequency domain with a temporal Fourier transform,

$$\begin{bmatrix} \delta\phi_1^{pk}(\mathbf{r}, \omega) \\ \delta\phi_2^{pk}(\mathbf{r}, \omega) \end{bmatrix} = \frac{\delta P(\omega)}{P_0} \times \begin{bmatrix} \phi_1(\mathbf{r}) \\ \phi_2(\mathbf{r}) \end{bmatrix}. \quad (24)$$

In [5] an equation system for  $P(t)$  is derived by first multiplying the dynamic subcritical equations of the flux, Eqs. (1)-(2), with the adjoint static eigenfunctions,  $\phi_{1,0}^\dagger$  and  $\phi_{2,0}^\dagger$ , for the source-free system, respectively. Then the static adjoint equations are multiplied with the time-dependent flux given in factorised form by Eq. (4). Next these equations are subtracted from each other and an integration over the whole system volume is made. Finally the normalisation condition given by Eq. (5) is used. The equation for the precursors, Eq. (3), is then multiplied with  $\phi_{1,0}^\dagger$  and integrated over the system volume. The final result is

$$\begin{cases} \frac{dP}{dt}(t) = \frac{\rho_0 - \beta_{eff}}{\Lambda(t)} P(t) + \lambda c(t) + q(t) \\ \frac{dc}{dt}(t) = \beta_{eff} \frac{P(t)}{\Lambda(t)} - \lambda c(t) \end{cases} \quad (25)$$

with the following functions

$$\begin{cases} \Lambda(t) = \frac{1}{F(t)} \int \left[ \frac{1}{v_1} \phi_{1,0}^\dagger(\mathbf{r}) \psi_1(\mathbf{r}, t) + \frac{1}{v_2} \phi_{2,0}^\dagger(\mathbf{r}) \psi_2(\mathbf{r}, t) \right] d\mathbf{r} \\ c(t) = \frac{\int \phi_{1,0}^\dagger(\mathbf{r}) C(\mathbf{r}, t) d\mathbf{r}}{\Lambda(t) F(t)} \\ q(t) = \frac{\int \phi_{1,0}^\dagger(\mathbf{r}) S_1(\mathbf{r}, t) d\mathbf{r}}{\Lambda(t) F(t)} \\ F(t) = \int \left[ \nu \Sigma_{f,1}(\mathbf{r}, t) \phi_{1,0}^\dagger(\mathbf{r}) \psi_1(\mathbf{r}, t) + \nu \Sigma_{f,2}(\mathbf{r}, t) \phi_{1,0}^\dagger(\mathbf{r}) \psi_2(\mathbf{r}, t) \right] d\mathbf{r} \end{cases} \quad (26)$$

and

$$\rho_0 = \frac{k_{eff} - 1}{k_{eff}}. \quad (27)$$

If Eq. (25) is considered in a static state one arrives at

$$P_0 = -\frac{\Lambda_0}{\rho_0} q_0. \quad (28)$$

If one then removes the static equation from Eq. (25) and assumes that  $\delta\Lambda(t) \ll \Lambda_0$  and performs a temporal Fourier-transform, the following is obtained for the amplitude factor:

$$\delta P(\omega) = \frac{\Lambda_0}{i\omega \left( \Lambda_0 + \frac{\beta_{eff}}{i\omega + \lambda} \right) - \rho_0} \delta q(\omega) = \frac{\Lambda_0}{G_0^{-1}(\omega) - \rho_0} \delta q(\omega) \quad (29)$$

with

$$G_0 = \frac{1}{i\omega \left( \Lambda_0 + \frac{\beta_{eff}}{i\omega + \lambda} \right)}. \quad (30)$$

The next step is to form the APSD of the point-kinetic term by utilising Eq. (24) and by using the CPSD of the source,

$$\begin{aligned} \begin{bmatrix} APSD_{\delta\phi_1^{pk}}(\mathbf{r}, \omega) \\ APSD_{\delta\phi_2^{pk}}(\mathbf{r}, \omega) \end{bmatrix} &= \begin{bmatrix} (\delta\phi_1^{pk})^*(\mathbf{r}, \omega) \delta\phi_1^{pk}(\mathbf{r}, \omega) \\ (\delta\phi_2^{pk})^*(\mathbf{r}, \omega) \delta\phi_2^{pk}(\mathbf{r}, \omega) \end{bmatrix} = \frac{\delta P^*(\omega) \delta P(\omega)}{P_0^2} \times \begin{bmatrix} \phi_1^2(\mathbf{r}) \\ \phi_2^2(\mathbf{r}) \end{bmatrix} = \\ \iint \left( \frac{\rho_0}{G_0^{-1}(\omega) - \rho_0} \frac{\phi_{1,0}^\dagger(\mathbf{r}) \delta S_1(\mathbf{r}, \omega)}{\phi_{1,0}^\dagger(\mathbf{r}) \phi_2^{cr,c}(\mathbf{r})} \right)^* &\left( \frac{\rho_0}{G_0^{-1}(\omega) - \rho_0} \frac{\phi_{1,0}^\dagger(\mathbf{r}') \delta S_1(\mathbf{r}', \omega)}{\phi_{1,0}^\dagger(\mathbf{r}') \phi_2^{cr,c}(\mathbf{r}')} \right) d\mathbf{r}' d\mathbf{r} \begin{bmatrix} \phi_1^2(\mathbf{r}) \\ \phi_2^2(\mathbf{r}) \end{bmatrix} = \\ \left\{ \delta S_1(\mathbf{r}, t) \delta S_1(\mathbf{r}', t) = (\phi_2^{cr,c})^2(\mathbf{r}') \delta(\mathbf{r} - \mathbf{r}') \right\} &= \\ \left( \frac{\rho_0}{G_0^{-1}(\omega) - \rho_0} \right)^* \left( \frac{\rho_0}{G_0^{-1}(\omega) - \rho_0} \right) &\begin{bmatrix} \phi_1^2(\mathbf{r}) \\ \phi_2^2(\mathbf{r}) \end{bmatrix}. \end{aligned} \quad (31)$$

The static part of the source is expressed through Eq. (26) as

$$q_0 = \frac{\int [\phi_{1,0}^\dagger(\mathbf{r}) S_1(\mathbf{r}) d\mathbf{r}]}{\Lambda_0 F_0} = \frac{\int \phi_{1,0}^\dagger(\mathbf{r}) \phi_2^{cr,c}(\mathbf{r})}{\Lambda_0 F_0} \quad (32)$$

and the frequency-dependent part of the source is estimated as

$$\delta q(\omega) \approx \frac{\int [\phi_{1,0}^\dagger(\mathbf{r}) \delta S_1(\mathbf{r}, \omega) d\mathbf{r}]}{\Lambda_0 F_0} \quad (33)$$

by linearisation of the denominator. Now the analytical point-kinetic APSD can be compared with the APSD calculated for different positions in the system by the numerical simulator. From the APSD the reactivity can be estimated by using the break-frequency method which will be described in the next section.

### 3. BREAK-FREQUENCY METHOD

There are a number of methods for determining the reactivity in subcritical systems. Most of the methods use an external source, but there is one method which does not use an external source, namely the break-frequency method [1]. In this paper the focus is on the estimation of the reactivity in a core during loading and since it is practical not to use an external source we have chosen the break-frequency method. However, the break-frequency method is based on the assumption that the point-kinetic approximation is valid. Hence, we will investigate whether or not this is true in a power reactor core during loading conditions. According to Eq. (31), the frequency-dependence of the APSD for the point-kinetic part is governed by

$$G_\rho(\omega) = \frac{1}{G_0^{-1}(\omega) - \rho_0} = \frac{1}{i\omega \left( \Lambda_0 + \frac{\beta_{eff}}{i\omega + \lambda} \right) - \rho_0}. \quad (34)$$

At high frequencies where  $\omega \gg \lambda$  one can write

$$G_\rho(\omega) \approx \frac{1}{i\omega\Lambda_0 + \beta_{eff} - \rho_0} = \frac{\Lambda_0}{i\omega + \frac{\beta_{eff} - \rho_0}{\Lambda_0}} = \frac{\Lambda_0}{i\omega + \omega_{break}}. \quad (35)$$

Here  $\omega_{break} = (\beta_{eff} - \rho_0)/\Lambda_0$  is the so-called break-frequency and if one can estimate the break-frequency the reactivity can be estimated as

$$\rho_0 = \beta_{eff} - \omega_{break}\Lambda_0. \quad (36)$$

Both  $\beta_{eff}$  and  $\Lambda_0$  are determined from the material data of the reactor. From this it is possible to get an estimate of the break-frequency by using curve-fitting methods. If  $\sqrt{APSD_{\delta\phi_2}(\mathbf{r}, \omega)/\phi_2^2(\mathbf{r})}$  is plotted against the frequency one can fit  $H(\omega) = |A/(\omega_{break} + i\omega)|$  to the high frequency part of the curve and get a good estimate of the break-frequency, if the system is behaving according to point-kinetics. We are also interested in comparing the actual neutron noise with the point-kinetic approximation. Hence, both the point-kinetic APSD (analytical),

$$\sqrt{\frac{APSD_{\delta\phi_2^{pk}}(\mathbf{r}, \omega)}{\phi_2^2(\mathbf{r})}} = \text{abs}\left(\frac{\rho_0}{G_0^{-1}(\omega) - \rho_0}\right) \quad (37)$$

and the APSD from the neutron noise (numerical),

$$\sqrt{\frac{APSD_{\delta\phi_2}(\mathbf{r}, \omega)}{\phi_2^2(\mathbf{r})}} \quad (38)$$

will be calculated and compared with each other. The reactivity will also be estimated at different positions in the core by using the spatial dependent APSD of the simulated neutron noise.

#### 4. INVESTIGATION OF THE VALIDITY OF THE BREAK-FREQUENCY METHOD

Before the validity of the break-frequency method is investigated, the system used in the investigation needs to be specified. As mentioned, the purpose of this work is to evaluate the estimation of the reactivity in a power reactor during loading. In the following section the system will be described in details and the reactivity will be estimated, for systems with different subcriticalities, using the break-frequency method.

##### 4.1. DEFINITION OF THE SYSTEM

The diffusion approximation is used in a 2-group, 2-region system in 2 dimensions. This type of system can be handled numerically by the noise-simulator. The nodalisation of the system used by the noise-simulator is shown in Fig. 1a). The size of the system is 32 by 32 nodes each node is 10.75 cm wide. The size of the nodes are determined by the size of a node in the In-Core Fuel Management code SIMULATE-3, representing the PWR Ringhals-3, from which the cross-sectional data are taken. In SIMULATE-3 each node is 21.5 cm wide and for better resolution every node in SIMULATE-3 is divided into four nodes in the noise-simulator, thus 10.75 cm.

The source properties have been described above in subsection 2.2. Now when the system is specified, the spatial distribution of the source can be calculated as being equal to the static thermal flux in the core. In Fig. 1b) the source distribution is shown for a system corresponding to a conventional light water reactor with a diameter of about 3.5 metres, i.e. the critical flux in the core from a static calculation by the neutron noise simulator.

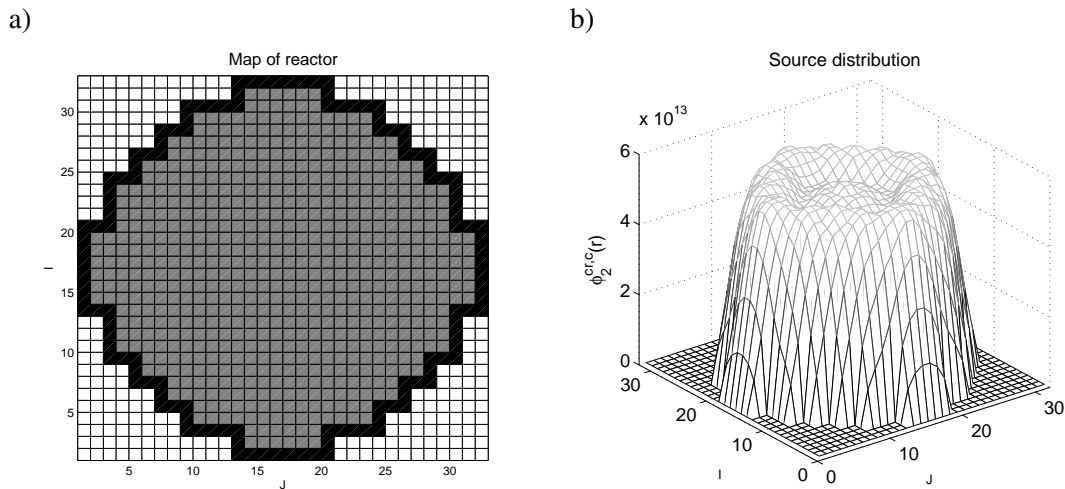


**Figure 1.** a): Nodal map of the system used by the noise-simulator. Gray squares denotes core nodes and black square denotes reflector nodes. b): Spatial source distribution for a system corresponding to a conventional light water reactor

## 4.2. ESTIMATION OF THE REACTIVITY

By using the system described above, the break-frequency method is used to estimate the reactivity from the APSD of the neutron noise. In order to investigate the validity of the break-frequency method for different subcriticalities, the subcriticality of the system is modified by adjusting the fission cross-section. Four different subcriticalities are investigated, namely, -200 pcm, -1395 pcm, -6205 pcm and -12278 pcm. These subcriticalities correspond to the following values of  $k_0$ : 0.99801, 0.98624, 0.94158 and 0.89065 respectively.

To map the radial behaviour, 16 different detector positions placed radially in the system are modelled by simply taking the calculated APSD of the thermal neutron noise at the corresponding nodal position as an estimate of the detector signal. In each position the reactivity is estimated by using the break-frequency method.

In Fig. 2a)-b), the square-root of the APSD (Eq. (38)) is shown for two different reactivities (-12278 pcm and -200 pcm) at 16 simulated detector positions. As a reference, the APSD of the point-kinetic term, Eq. (37), is also shown in the figures as a dashed line. In Fig. 2c)-d) the relative error between the APSD from the simulations and the point-kinetic APSD is shown for four different radial positions. Clearly, there is a big difference between the point-kinetic approximation and the numerical simulated values for all detector positions.

In Fig. 3a) the result from the estimation of the reactivity with the break-frequency method is shown. Generally, there is a large error in the estimation of the reactivity for all positions and all reactivities. However, it can be noted that at some point in between the centre and the reflector, the estimation is almost perfect. However, this position is changing with the reactivity. Hence, it is not possible to use this position for the determination of the reactivity.

It could also be of interest to investigate if a smaller system is better approximated by the point-kinetics.

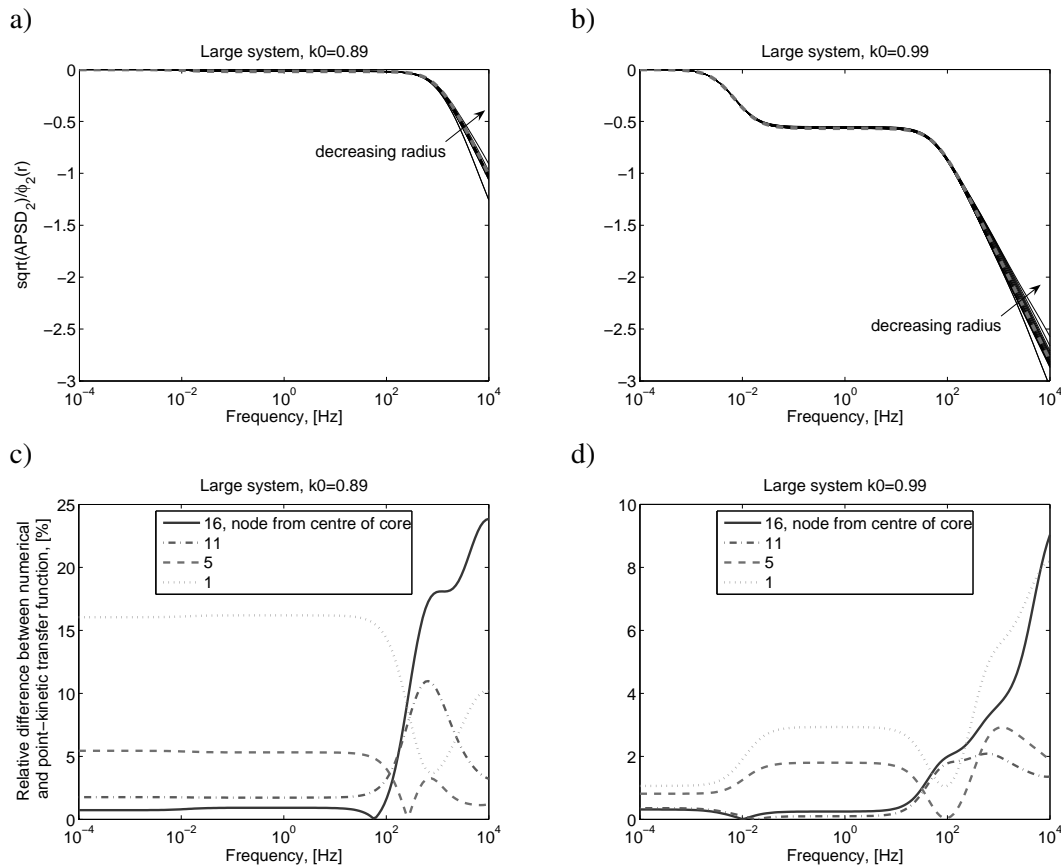


**Figure 2.** In a) and b) the transfer function for two of the reactivities and 16 different detector positions are shown. The point-kinetic transfer function is also shown as a reference. In c) and d) the relative error between the transfer function from the simulator and the point-kinetic approximation is shown for the same two reactivities. Only four radial positions are plotted for better visibility.

Therefore, the size of each node in the system was reduced by a factor of three and the total size of this smaller core it then about 1 m. In Fig. 3b) the relative error of the estimation of the reactivity for different radial positions is shown. The result is appreciably better than that for the larger system, even if the desired accuracy is higher than what was achieved.

## 5. CONCLUSIONS

The quantitative results in this paper show that the break-frequency method supplies relatively rough estimates of the subcritical reactivity when used in large subcritical power reactor cores during loading conditions for determining the reactivity. One reason for this is the fact that the point-kinetic approximation is not valid in large loosely coupled systems. On the other hand, the method still might be used for safety purposes, to indicate the margins for criticality. As long as the method is conservative, an accuracy of 10-20% is acceptable. This criterion is fulfilled in nearly all measurement positions in the small core, and in a significant portion of the available positions, see Fig.3a), in the large system.

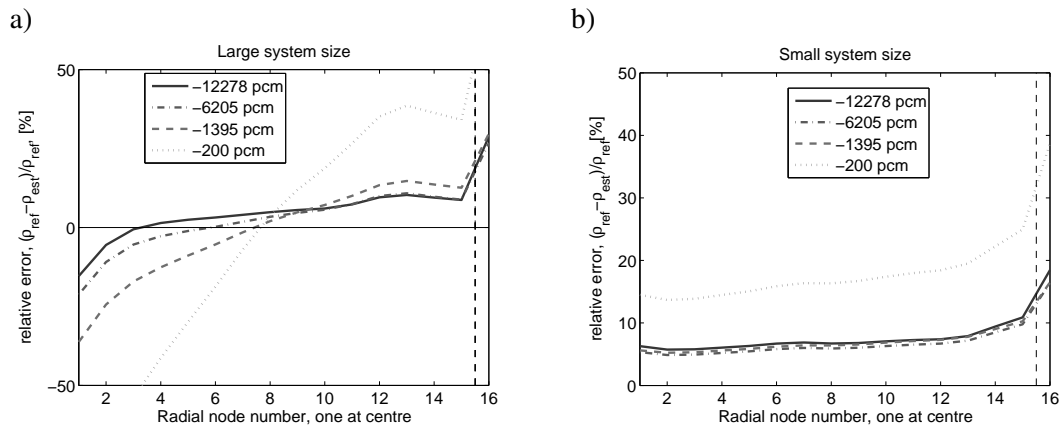


**Figure 3.** Large system: The relative error of the estimation of the reactivity using the break-frequency method. Node point 16 is in the reflector and 1 is centre of the core. a) Large system and b) small system.

### ACKNOWLEDGEMENTS

This work was supported by the Swedish Nuclear Power Inspectorate, SKI, contract number SKI 2005/1199-20050513.

### REFERENCES

- [1] J. T. Mihalczo, E. D. Blakeman, G.E. Ragan, E. B. Johnson and Y. Hachiya, "Dynamic Subcriticality Measurements Using the  $^{252}\text{Cf}$ -Source-Driven Noise Analysis Methods," *Nuclear Science and Engineering*, **104**, pp. 314-338 (1989).
- [2] C. Demazière, I. Pázsit and J. Wright, "Investigation of the validity of the point-kinetic approximation for subcritical heterogeneous system in 2-group diffusion theory for measurement of the reactivity in ADS," *Proceedings of GLOBAL*, Tsukuba, Japan, Oct 9-13 September (2005).
- [3] C. Demazière and I. Pázsit, "Theoretical investigation of the MTC noise estimate in 1-D homogenous systems," *Annals of Nuclear Energy*, **29**, pp. 75-100 (2002).
- [4] C. Demazière, "Development of a 2-D 2-group neutron noise simulator," *Annals of Nuclear Energy*, **31**, pp. 647-680 (2004).
- [5] G. I., Bell and S. Glasstone, 1970. *Nuclear Reactor Theory*, Van Nostrand Reinhold Company, New York (1970).